Raman spectroscopy: from ferroelastic domain identification to strain tuning

Kumulative Habilitationsschrift

Cameliu Constantin Himcinschi

Freiberg 2020

Raman spectroscopy: from ferroelastic domain identification to strain tuning

Von der Fakultät für Chemie und Physik (Fakultät 2)

der TU Bergakademie Freiberg

angenommene

kumulative Habilitationsschrift

zur Erlangung des akademischen Grades

doctor rerum naturalium habilitatus

Dr. rer. nat. habil.

vorgelegt

von Dr. rer. nat. Cameliu Constantin Himcinschi

geboren am 29.06.1974 in Blaj

eingereicht am 29.01.2020

Gutachter: Prof. Dr. Johannes Heitmann, TU Bergakademie Freiberg

Prof. Dr. Marin Alexe, University of Warwick

Prof. Dr. Jean Geurts, Julius-Maximilians-Universität Würzburg

Tag der Verteidigung: 10.09.2020

Contents

Appendix

Raman spectroscopy: from ferroelastic domain identification to strain tuning

1. Introduction

The atoms in a solid oscillate around their equilibrium positions at given finite temperature. These lattice vibrations, or phonons, are responsible for the fundamental properties of solid state materials such as heat capacity, thermal conductivity, lattice expansion, phase transitions, etc. In the particular case of multiferroic perovskite materials the lattice vibrations are considered to be one of the most fundamental keys in controlling the functional properties. On the other hand, the phonon frequencies count as material fingerprints, i.e. they have specific values for a given chemical composition and for a given crystal structure, and, thanks to their symmetry, they obey well defined optical selection rules. The lattice vibrations are commonly investigated by Raman spectroscopy and infrared spectroscopy and the corresponding Raman and infrared spectra can be used for material identification. Moreover, given the sensitivity of the phonon frequencies with respect to the structural parameters, the measured vibrational spectra (Raman or infrared) carry information related to the presence of structural defects or strain in the investigated solids.

Despite of enormous amount of research the assignment of the phonons symmetry in multifunctional materials, such as multiferroic $BiFeO_3$ (BFO), is still controversial, due to the polar character and the mixed symmetry of the oblique vibrational modes. We proposed for the first time a method based on the Raman tensor formalism, which allows an assignment of the BFO Raman modes of pure as well as mixed character/symmetries. Relying on the assignment done for crystals, it is shown that Raman spectroscopy is a powerful tool for the investigation of ferroelastic domain formation in multiferoic crystals and thin films.

Another major finding of this *Habilitation* thesis is (besides the ferroelastic domain orientation) that Raman spectroscopy is able to probe the tilt of the domain walls between the ferroelastic domains with respect to the sample surface. This knowledge was achieved by performing line scans using different excitation wavelengths. When employing several excitation wavelengths in the Raman spectroscopy experiment, one can gain depth information due to the different corresponding penetration depth of light.

An important direction of the Habilitation deals with the exploitation of strain in materials for tuning various material properties. In silicon by example, induced strain provides enhanced carrier mobility compared to the unstrained counterparts. In ferroelectric or multiferroic materials one can change the electric polarisation by changing the strain and thereby enhance or reduce the ferroelectricity. Generally, strain engineering has recently become a powerful method to vary the physical properties of complex multifunctional oxide thin films [Mar12] having a perovskite or spinel structure. However, the modification of perovskite structure induced by strain is difficult to be observed by means of classical X-ray diffraction experiments due to the poor in-plane sensitivity. Raman spectroscopy can detect even subtle structural modifications, in particular slight deviations from the cubic structure as occurring in the class of oxides with perovskite structure. The structural changes induced by strain can alter the crystal symmetry having a significant effect on the Raman spectrum. We show that Raman spectroscopy is a viable, non-destructive, and sensitive method which allows to study the strain in such material systems based on the exploration of the frequency range of the lattice vibrations. This cumulative *Habilitation* thesis summarizes several examples related to the quantitative determination of strain by Raman spectroscopy, the investigation of coupling phenomena induced by epitaxially, mechanically or piezoeletrically applied strain, as well as the understanding of temperature induced phase transitions which are intimately related to specific phonon modes.

Figure 1 presents a schematic representation of the own contribution to the progress in the application capabilities of Raman spectroscopy. The Raman tensor formalism was applied for the first time for unambiguous polar phonon assignment in multiferroics. Once the phonon assignment is clarified, Raman spectroscopy can be applied to the imaging of nano- and macro-domains and domain walls in multiferroics. Furthermore, phase transitions and orbital ordering can be monitored as a function of temperature by Raman spectroscopy. On the other hand, once the mode assignment is clear and after a careful calibration, the applied strain can be determined quantitatively as it was shown in the case of anisotropic strain for the elemental semiconductor silicon or in the case of epitaxially or piezolectrically applied strain in the case of the structurally more complex multiferroic materials.

The cumulative *Habilitation* is based on sixteen published scientific articles in which the candidate was significantly involved. The list of these publications and the candidate's own contribution to each publication can be found on the page 23.

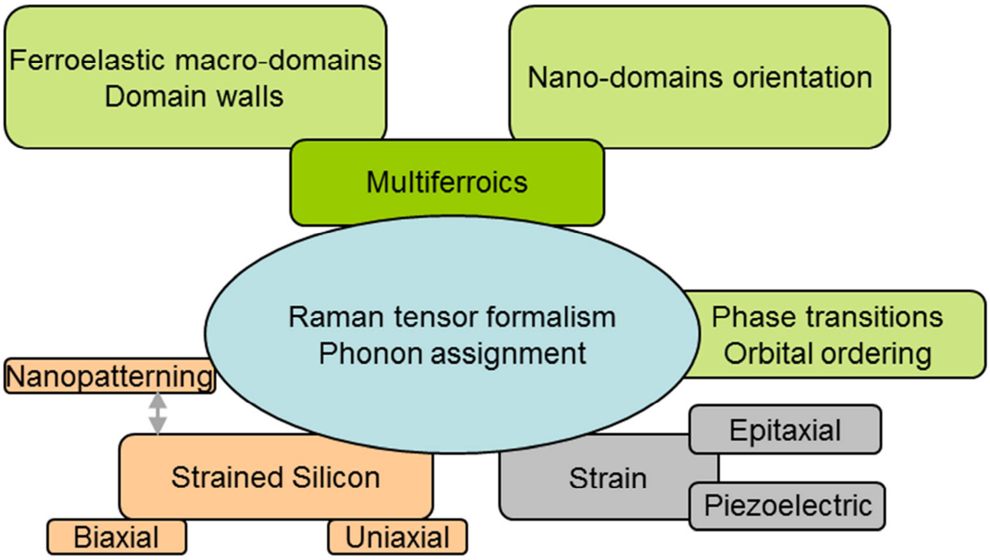

Figure 1. Schematic representation of the topics addressed in this cumulative *Habilitation* thesis.

The ferroelectric and multiferroic samples investigated were grown by pulsed laser deposition in the groups of Dr. Ionela Vrejoiu (Universität zu Köln, MPI Halle) Prof. Dr. Marin Alexe (University Warwick, MPI Halle) and Prof. Dr. Kathrin Dörr (MLU Halle). The strained Si samples were prepared by the candidate during his Postdoc period at MPI Halle.

The Raman measurements were performed by the candidate at TUBA Freiberg and MPI Halle (strained Si part). Ellipsometric measurements were performed by the candidate at TU Chemnitz (group of Prof. Dietrich R.T. Zahn) or at BESSY Berlin. Some of the XRD measurements were performed in the group of Prof David Rafaja (TUBA Freiberg).

2. Motivation

Multiferroic materials that simultaneously show polarization and magnetization ordering are envisaged to play a significant role in developing devices with large magnetoelectric coupling, i.e. devices in which the polarization and the magnetization can be controlled by applying a magnetic or electric field, respectively.[Ram07] Materials naturally showing occurrence of multiferroism are, however, rather rare. For example, in multiferroic materials with perovskite ABO_3-structure the multiferroism is hindered by the competition between exhibiting ferromagnetism and ferroelectricity (the former requires partially filled d orbitals whereas the latter empty d orbitals).[Spa05] One exception is the case of bismuth perovskites, which are regarded as good candidates for room temperature (RT) multiferroism.

Bismuth ferrite (BFO) is a rare case of a single phase RT multiferroic with ferroelectric Curie temperature T_c~1100 K and antiferromagnetic Néel temperature T_N~640 K, well above RT.[Fis80] Multiferroic epitaxial BFO films may find potential applications in non-volatile ferroelectric memories or novel multiple state memories as well as in devices based on magnetoelectric effects.[Chu08, Cat09] Another interesting candidate for intrinsic multiferroism is $BiCrO_3$ (BCO). The magnetism and ferroelectricity of BCO are still debated because of the lack of definite crystal structural information, which is an important prerequisite for understanding its properties. Polycrystalline BCO shows a structural transition from monoclinic to orthorhombic symmetry at 420 K.[Bel07] On the other hand, Hill *et al.* [Hil02] predicted that BCO should have a G-type antiferromagnetic ground state and antiferroelectric structural distortion on the basis of the hypothetically cubic crystal structure.

The growth of high-quality single crystalline thin films of multiferroics is essential for the study of their intrinsic fundamental physical properties, undisturbed by extrinsic contributions from parasitic phases and extended structural defects, and finally for their incorporation into practical devices.[Ram10] For example, artificial lattices of BFO/BCO were found to show ferrimagnetic interactions due to the Fe-Cr alternating ordering in (111) planes, although BFO and BCO are antiferromagnets.[Ich08]

Strain engineering was established as valuable method to tune the physical and functional properties of complex oxides [Ope11]. The usual way to induce different strain in thin films is the growth of films having different thickness on single crystal substrates with a certain lattice mismatch. This approach was successfully applied for engineering the magnetoelectric properties in complex multifunctional oxides. The structural modification induced by strain is difficult to follow. Raman spectroscopy is a suitable non-invasive methods which has been established for the detection of subtle structural changes, in particular slight deviations from cubic structure as occurring in the class of oxides with perovskite [Pez13, Bee12, Kre03, Ten08, Bea07 ,Pal08, Iss10, Her07, Lah09] and spinel [Iva10, Ili11, Fri11] structure. Raman spectroscopy has found increasing application for the characterization of ferroelectric thin films, because the ferroelectric phase transition is intimately related to specific phonon modes. For example, an increase in the number of Raman peaks may reflect a space group with lower symmetry as it was observed in the case of BFO films when the symmetry changed from tetragonal to monoclinic [Bea07, Pal08]. Recently, Raman spectroscopy was employed to show that the strain can completely modify the magnonic response of BFO [San13]. It should be mentioned that there is a series of extrinsic factors, e.g., the crystalline quality of the substrates, the growth method, stoichiometry (oxygen content), or the growth induced disorder which can affect the epitaxy and the substrate-film strain transfer. By applying piezoelectric strain it is possible to obtain a quantitative correlation between strain and the shift of the Raman-active phonons, ruling out the influence of extrinsic factors (growth conditions or crystalline quality of substrates). The lattice strain can be reversibly modulated using the piezoelectric effects of the substrate and for films that are epitaxialy grown, this strain can be transferred to the epitaxial films.

In order to extract information related to structural properties and their changes upon strain, the correlation between a measured Raman spectrum and the corresponding material/phase has to be established first. In ref **[Him19]** a decisive contribution to the clarification of the Raman mode assignment of BFO has been presented. The main achievements are shortly summarized in **3.1.**

In addition to the material/phase fingerprint, the Raman spectra are sensitively influenced by the measurement conditions such as excitation wavelength or measurement geometry. An example on how these effects can be exploited for extracting information about ferroelastic macro-domain and domain walls is shortly discussed in **3.2**. The application of Raman spectroscopy to the orientation determination for small (nano) domains to the case of BFO and BCO epitaxial films is addressed in **3.3**.

For resonant Raman spectroscopy investigations, the knowledge about the bandgap of the material is important (**3.4.**). The complex dielectric function was determined for the first time by us for some of the materials under study. For example, the dielectric function of BCO thin films was determined in the energy range of 0.73–9.8 eV using spectroscopic ellipsometry. By analysing the absorption onset region, it was shown that BCO is an indirect bandgap material **[Him13]**.

On the other hand, we have demonstrated on two examples ($BiCrO_3$ and $LaVO_3$) the strength of Raman spectroscopy in the monitoring of phase transitions or orbital ordering induced by temperature (**3.5.**).

Strained silicon (sSi) enables the enhancement of the carrier mobilities compared to bulk Si. Since the band gap engineering in such devices is almost exclusively based on the induced strain approach, it is very important that the strain in the Si layer is retained during various processing steps. Consequently, the behaviour of the strained state of sSi layers after nanopatterning is of significant technological importance. Raman spectroscopy has become an important non-destructive tool for investigation of strain in silicon films and Si based microelectronics. Moreover due to continuing miniaturization of the microelectronic devices, the use of short wavelength UV lasers for Raman spectroscopy has been proven to have significant advantages over the conventional visible lasers due to the short penetration depth and therefore surface-near probing of the material.

A significant part of this habilitation thesis was dedicated to the correlation between the effect of strain induced either by epitaxy or by using a piezolelectric substrate and the corresponding effects on the Raman spectra. Four studies were dedicated to the investigation of strain in BFO films, one article addressed strain in spinel films and other five papers were dedicated to strained silicon. These results are shortly summarized in **3.4.** for the BFO and spinel case and in **3.6.** and **3.7.** for the silicon case.

3. Results

3.1. Raman tensor formalism: assignment of the BFO polar modes [Him19]

[Him19] **C. Himcinschi**, J. Rix, C. Röder, M. Rudolph, M.-M. Yang, D. Rafaja, J. Kortus, and M. Alexe
Ferroelastic domain identification in $BiFeO_3$ crystals using Raman spectroscopy
Scientific Reports 9, 379_1_9 (2019) **doi: 10.1038/s41598-018-36462-5**

Although a lot of research was devoted to the properties of BFO, one of the most fundamental aspects, the lattice vibration, in particular the assignment of the phonons symmetry is still controversial, due to the polar character and the mixed symmetry of the oblique modes.

A full assignment of the modes considering mixed symmetry LO/TO and mixed character A1/E was done by Hlinka *et al.* [Hli11] based on the dispersion of phonons frequency on the angle θ (angle between the phonon propagation and the optic axis) [Hli11]. This method (ref. [Hli11]) is based on the phonon frequency variation with the angle between the crystal optic axis and the laser beam in randomly oriented crystalline grains.

We present in our paper [Him19] for the first time a method based on the Raman tensor formalism, which allows an assignment of the BFO Raman modes of pure as well as mixed character/symmetries. It should be mentioned that in literature the Raman tensor approach was only applied until now for pure (not mixed) modes. This restriction corresponds to the case $\theta = 0°$ (where θ is the angle between the phonon propagation and optic axis), *i.e.* the case of $(111)_{pc}$ oriented BFO. Most of the samples/films investigated in literature were, however, $(001)_{pc}$ oriented BFO corresponding to $\theta = 54.7°$, which leads to an incorrect interpretation, because in this case mixed character/symmetry of the modes needs to be considered. The method presented in our paper [Him19] analyses the in-plane (*i.e.* in the crystal surface plane) variation of the Raman intensities upon azimuthal rotation of a single crystal instead of the phonon frequency dispersion (which was reported in ref. [Hli11]). Since it is based on the Raman intensity analysis, the Raman tensor method presented here is highly sensitive to the in-plane orientation of the optic axis projection onto the sample surface for any angle θ between the phonon propagation (laser beam direction) and the optic axis. We present a general approach based on numerical simulations using the Raman tensor formalism combined with polarisation and azimuthal angle-dependent Raman measurements that is capable to identify the polar modes of mixed symmetries in a $(001)_{pc}$ oriented BFO single crystal unambiguously. This method can easily be extended to any crystal orientation.

In Figure 2, the azimuthal dependence of the intensity of the ordinary $\mathbf{E}_{\mathrm{TO}}$ modes and of extraordinary modes with mixed symmetries: $\mathbf{E}_{\mathrm{TO}}\leftrightarrow\mathbf{E}_{\mathrm{LO}}$, $\mathbf{E}_{\mathrm{TO}}\leftrightarrow\mathbf{A}_{\mathbf{1}\mathrm{TO}}$, $\mathbf{A}_{\mathbf{1}\mathrm{LO}}\leftrightarrow\mathbf{A}_{\mathbf{1}\mathrm{TO}}$, and $\mathbf{A}_{\mathbf{1}\mathrm{LO}}\leftrightarrow\mathbf{E}_{\mathrm{LO}}$ obtained by Raman tensor formalism simulations are shown to be in good agreement with the polar dependence of the experimentally measured peak areas for both parallel and cross polarisation.

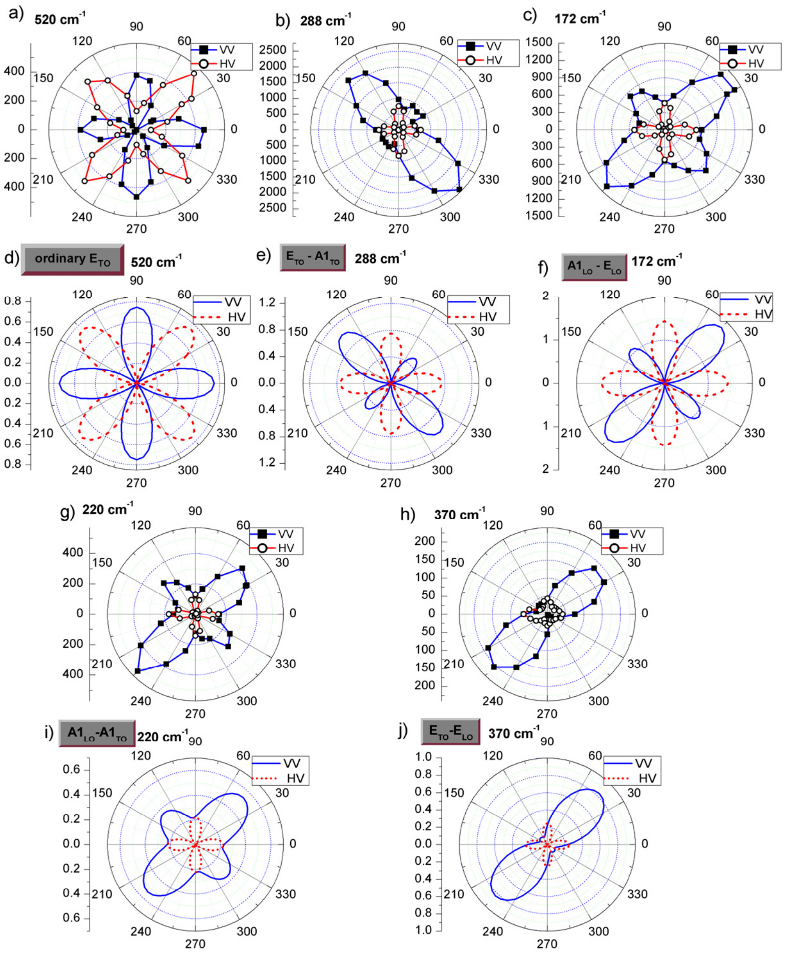

Figure 2. (taken from [Him19]) Polar plots of the azimuthal angle dependence of the measured peak areas for the $BiFeO_3$ modes at 520 cm^{-1} (a), 288 cm^{-1} (b), 172 cm^{-1} (c) 220 cm^{-1} (g) and 370 cm^{-1} (h) and the simulated intensity dependence using Raman tensor formalism for the ordinary E_{TO} (d), $E_{TO}\leftrightarrow A1_{TO}$ (e), $A1_{LO}\leftrightarrow E_{LO}$ (f), $A1_{LO}\leftrightarrow A1_{TO}$ (i) and $E_{TO}\leftrightarrow E_{LO}$ (j) mixed modes in the case of an $(001)_{pc}$ BFO scattering surface, for parallel (continuous line) and crossed (dashed line) polarisation configurations.

3.2. Resonant / non-resonant Raman spectroscopy on BFO: information about ferroelastic macro-domain and domain walls [Him19]

[Him19] **C. Himcinschi**, J. Rix, C. Röder, M. Rudolph, M.-M. Yang, D. Rafaja, J. Kortus, and M. Alexe
Ferroelastic domain identification in $BiFeO_3$ crystals using Raman spectroscopy
Scientific Reports 9, 379_1_9 (2019) **doi: 10.1038/s41598-018-36462-5**

For an accurate assignment of the phonon modes, Raman spectroscopy should be performed using a laser excitation energy which does not match any electronic transition in the studied material. In the case of resonant Raman spectroscopy, i.e. when the laser energy is resonant with an electronic transition energy, a breakdown of selection rules was observed in Raman scattering. [Mar71] This leads to effects such as occurrence of anomalous multiple-phonon lines or the appearance of Raman-allowed phonon lines in a forbidden polarization configuration. [Wil73] In order to exclude any ambiguity in the interpretation of the mode character we focused on the comparison of the Raman tensor formalism predictions with azimuthal dependent measurements performed under off-resonant conditions using the 633 nm (1.96 eV) laser line (see Figure 3). Once the mode characters have been unambiguously determined, we took advantage of the different penetration depths of the two laser lines in BFO (76 nm @442 nm and 7µm @633 nm) and performed line scans using both excitations in order to win depth information.

By performing line scans using different excitation wavelengths we demonstrated that Raman spectroscopy is able to probe tilting of the domain walls between the ferroelastic domains with respect to the sample surface (as shown in Figure 4 of the paper [Him19]). An advantage of Raman mapping/line scans performed at different excitation wavelengths (having different light penetration depths in BFO) with respect to other techniques such as XRD or polarisation microscopy is the depth sensitivity of the information regarding the tilt of the domain walls relative to the surface.

The sensitivity of the Raman signal to the ferroelastic domain orientation on one hand, combined with the variable depth information when using appropriate laser wavelengths for excitation on the other hand, provide a unique advantage when using Raman spectroscopy for domain imaging. Raman spectroscopy can be used to image the ferroelectric domains and at the same time to gain additional depth information regarding the tilt of the domain walls relative to the surface.

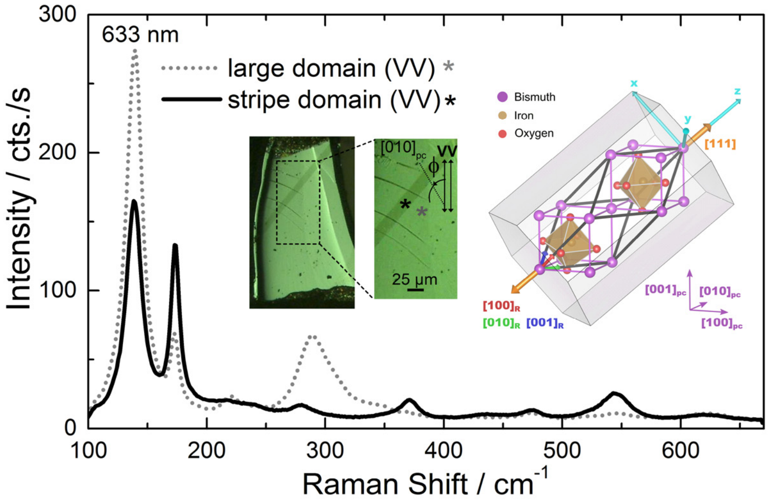

Figure 3. (taken from [Him19]) Typical BFO Raman spectra measured in parallel polarisation using the 633 nm excitation line on the two types of ferroelastic domains (as seen in inset in the polarisation microscopy image). The unit cell and the relation of the pseudo-cubic and rhombohedral crystallographic axes are shown on the right side of the figure.

3.3. Raman spectroscopy on BFO and BCO epitaxial films: orientation of small (nano) domains [Tal12, Tal15]

[Tal12] A. Talkenberger, **C. Himcinschi**, T. Weißbach, K. Vijayanandhini, I. Vrejoiu, C. Röder, D. Rafaja, and J. Kortus
Raman spectroscopic and X-ray diffraction investigations of epitaxial BiCrO$_3$ thin films
Thin Solid Films 520, 4590–4594 (2012) doi: 10.1016/j.tsf.2011.10.196
[Tal15] A. Talkenberger, I. Vrejoiu, F. Johann, C. Röder, G. Irmer, D. Rafaja, G. Schreiber, J. Kortus and **C. Himcinschi**
Raman spectroscopic investigations of epitaxial BiFeO$_3$ thin films on rare earth scandate substrates
J. Raman Spec. 46, 1245 (2015) doi: 10.1002/jrs.4762

With the knowledge of the phonon symmetry we performed polarisation dependent Raman measurements (in parallel and cross polarisation configuration) for the BFO film deposited on different scandate subtrates. [Tal15] In this case the samples were thin films consisting of thin ferroelastic domains (ca. 150 nm in lateral direction) having different crystallographic orientations. The laser focus was about 2 µm, so that several tens of domains were measured simultaneously. Consequently, the measured intensity and its dependence on the azimuthal angle are averaged over several domains. However, remarkable is the 90 degree periodicity of the peaks position (Figure 2b, in [Tal15]) and of the full width at half maximum (Figure 2c, in [Tal15]) mode for both parallel (vv) and cross (hv) polarisation. For both polarisations the four maxima in positions correspond to the minima in FWHM. Such a behaviour can be explained considering a twin family of crystals with a very well defined orientation to each other. Simulations of the Raman intensity as a function of the azimuthal angle, taking into account the symmetry of the Raman tensor, showed that the behaviour of the peak position and FWHM can be reproduced considering the presence of two ferroelastic domains in the films. Formation of two families of domains was also experimentally confirmed by XRD and visualised using piezoelectric force microscopy.

To determine the structural properties of BCO films we used a similar procedure as the one presented in [Him19] based on Raman tensor formalism. The epitaxial relation between films and substrates was verified by using polarisation dependent Raman spectroscopic experiments and theoretical calculations based on symmetry. [Tal12] In order to obtain information about the crystal structure of the films, about their quality, and about the mutual crystallographic orientation between the films and the substrates, complementary investigations by means of high resolution X-ray diffraction and pole figure measurements were performed on epitaxial BCO thin films grown on $NdGaO_3$ (110)- and $(LaAlO_3)_{0.3}$-$(Sr_2AlTaO_6)_{0.7}$ (100)-oriented substrates. These studies confirmed the findings of Raman spectra analysis, including the fact that the monoclinic (111) plane of BCO was found to be parallel to the substrate surface.

3.4. Strain influence on optical properties of BFO films: from epitaxial to piezoelectric strain [Him10a, Him10b, Him15, Him16]

[Him10a] **C. Himcinschi**, I. Vrejoiu, M. Friedrich, E. Nikulina, L. Ding, C. Cobet, N. Esser, M. Alexe, D. Rafaja, and D.R.T Zahn
Substrate influence on the optical and structural properties of pulsed laser deposited $BiFeO_3$ epitaxial films
J. Appl. Phys. 107, 123524_1-5 (2010) **DOI: 10.1063/1.3437059**
[Him10b] **C. Himcinschi**, I. Vrejoiu, M. Friedrich, L. Ding, C. Cobet, N. Esser, M. Alexe, and D.R.T Zahn
Optical characterisation of $BiFeO_3$ epitaxial thin films grown by pulsed-laser deposition
physica status solidi c 7, 296-299 (2010) **DOI: 10.1002/pssc.200982414**
[Him15] **C. Himcinschi**, A. Bhatnagar, A. Talkenberger, M. Barchuk, D.R.T. Zahn, D. Rafaja, J. Kortus, and M. Alexe
Optical properties of epitaxial $BiFeO_3$ thin films grown on $LaAlO_3$

Appl. Phys. Lett. 106, 012908_1-5 (2015) **doi: 10.1063/1.4905443**
[Him16] C. Himcinschi, E.J. Guo, A. Talkenberger, K. Dörr, and J. Kortus
Influence of piezoelectric strain on the Raman spectra of $BiFeO_3$ films deposited on PMN-PT substrates
Appl. Phys. Lett. 108, 042902 (2016) **doi: 10.1063/1.4940973**

Epitaxial thin films of bismuth ferrite deposited by pulsed laser deposition on $SrTiO_3$ (STO) (100), $DyScO_3$ (DSO) (110), $TbScO_3$ (TSO) (110) and $LaAlO_3$ (LAO) (100) were investigated by ellipsometry and Raman spectroscopy in order to check the influence of the epitaxial strain on the dielectric function and on the phonon modes. [Him10a, Him10b, Him15]

The Raman spectra revealed a clear blue shift of the BFO modes when going from the films deposited on DSO to those deposited on STO or when decreasing the film thickness. [Him10b] The blue shift of the Raman peaks indicates an increase of compressive strain in the films. This means that the BFO films deposited on STO have a higher compressive strain than those deposited on DSO. These results confirm the behavior observed in the dielectric function and the bandgap for these BFO films. [Him10a, Him10b] The thin films are more compressed than the thick ones, a fact which can be well understood considering the lattice mismatch between the BFO films and the STO and DSO substrates. These findings were supported by the results of complementary XRD measurements. [Him10b]

On the other hand, highly strained (tetragonal-like) and nearly pseudomorphic (rhombohedral) BFO films were PLD deposited on LAO and TSO respectively. [Him15] The symmetry of the tetragonal-like BFO films was analysed based on polarisation dependent Raman measurements and on the comparison with Raman spectra measured for rhombohedral films deposited on TSO. The evaluation of ellipsometric spectra revealed that the films deposited on LAO are optically less dense and the dielectric function is blue-shifted by 0.3 eV as compared to the rhombohedral films. Bandgaps of 3.10 eV and 2.80 eV were determined for the films deposited on $LaAlO_3$ and $TbScO_3$, respectively. The shift in the optical bandgap and dielectric function is nearly preserved also for thicker films, which indicates that the tetragonal structure is formed even in films with thicknesses above 100 nm as also confirmed by XRD investigations. [Him15]

By employing piezoelectric single crystal substrates (as for example $[Pb(Mg_{1/3}Nb_{2/3})O_3]$-$PbTiO_3$ (PMN-PT)), the strain in both substrate and film can be simultaneously modified by using an external electric field, so that extrinsic factors, which could affect the film strain (growth conditions, different thicknesses, different substrates quality), are excluded. The lattice strain can then be reversibly modulated using the piezoelectric effects of the substrate and if the films are epitaxialy grown, this strain can be transferred to the epitaxial films. (1-x)PMN-xPT with a concentration near to the morphotropic phase boundary x=0.3 possesses excellent piezoelectric activity. The strain can be effectively transferred to the films in the case of an efficient elastic coupling at the interface substrate/film using a structure as schematically shown in figure 4 [Him16]. The lattice parameters change linearly with the electric field applied and the effect is reversible. Using the lattice parameters measured by XRD and the Poisson ratio for BFO, the relative volume change induced by strain was determined. Using the shifts of the phonons measured by Raman and the relative volume change as determined by XRD we calculated for the first time the Grüneisen parameters for BFO films. [Him16] The method of piezoelectrically induced strain allows one to directly obtain a quantitative correlation between the strain and the shift of the Raman-active phonons. This is a prerequisite for making Raman scattering a strong tool to probe the strain coupling in multiferroic nanostructures.

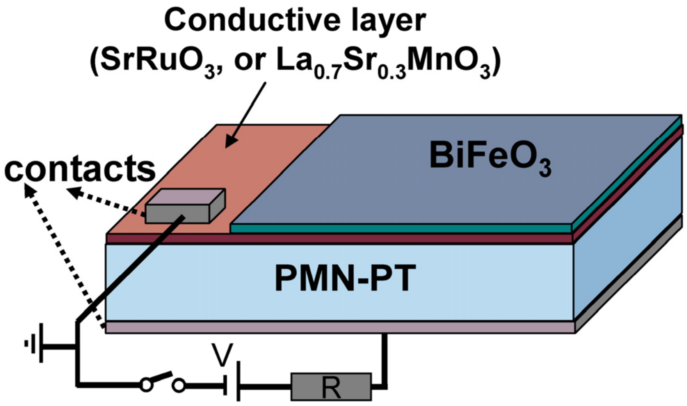

Figure 4. (taken from [Him16]) Schematic diagram of the BFO /buffer /piezo-PMN-PT structure used for Raman measurements and for the determination of Grüneisen parameters.

3.5. Raman spectroscopy: phase transition and orbital ordering [Him11, Him13, Vre16, Vre17]

[Him11] **C. Himcinschi**, I. Vrejoiu, T. Weißbach, K. Vijayanandhini, A. Talkenberger, C. Röder, S. Bahmann, D. R. T. Zahn, A. A. Belik, D. Rafaja, and J. Kortus
Raman spectra and dielectric function of $BiCrO_3$: Experimental and first-principles studies
J. Appl. Phys. 110, 073501_1-8 (2011) **doi:10.1063/1.3642985**
[Him13] **C. Himcinschi**, I. Vrejoiu, G. Salvan, M. Fronk, A. Talkenberger, D.R.T. Zahn, D. Rafaja, and J. Kortus
Optical and magneto-optical study of nickel and cobalt ferrite epitaxial thin films and submicron structures
J. Appl. Phys. 113, 084101_1-8 (2013) **doi: 10.1063/1.4792749**
[Vre16] I. Vrejoiu, **C. Himcinschi**, L. Jin, C.-L. Jia, N. Raab, J. Engelmayer, R. Waser, R. Dittmann and P. H. M. van Loosdrecht
Probing orbital ordering in $LaVO_3$ epitaxial films by Raman scattering
APL Mater. 4, 046103 (2016) **doi: 10.1063/1.4945658**
[Vre17] I. Lindfors-Vrejoiu, L. Jin, **C. Himcinschi**, J. Engelmayer, F. Hensling, C.-L. Jia, R. Waser, R. Dittmann and P.H.M. van Loosdrecht
Structure and orbital ordering of ultrathin $LaVO_3$ probed by atomic resolution electron microscopy and Raman spectroscopy
physica status solidi (rrl) 11, 1600350 (2017) **doi: 10.1002/pssr.201600350**

Structural changes induced by phase transitions alter the crystal symmetry, which determines the number of Raman peaks, their relative intensity and polarisation dependence in the Raman spectra. Temperature-dependent Raman spectroscopy was employed to study the structural phase transition in polycrystalline BCO and to determine the transition temperature. [Him11] The measured Raman modes can be correlated to a reversible phase transition from the “low-temperature” monoclinic to the “high temperature” orthorhombic phase (see figure 5). This phase transition was confirmed by in situ powder X-ray diffraction investigations.

Further, we exemplified how Raman spectroscopy can be used as a tool to probe phase transitions such as orbital ordering in the case of 3d transition metal oxides. [Vre16, Vre17] Miyasaka *et al.* [Miy05, Miy06] showed that it is possible to measure orbital excitation bands in single crystals of vanadium oxides using resonant Raman spectroscopy. These bands were assigned to orbiton processes and are sometimes difficult to distinguish from phonons, the resonance of the excitation line to the mode transition being one of the prerequisites for distinction. In our case [Vre16, Vre17] the phase transition to orbital ordering for $LaVO_3$ thin films grown on different crystalline substrates was evaluated by Raman spectroscopy. For this purpose, temperature-dependent measurements were carried out in the range from

90 K to 300 K using resonant excitation. The dependence of the orbital ordering on the film orientation on the different substrates was addressed.

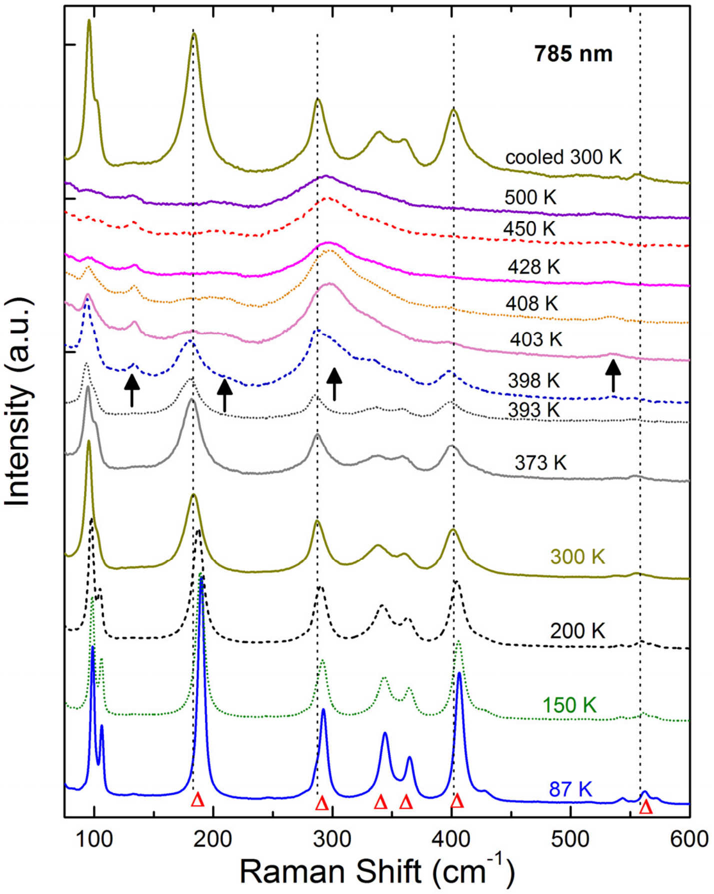

Figure 5. (taken from [Him13]) Temperature dependence of the Raman spectra of BCO from 87K up to 500K, illustrating the reversible phase transition from the monoclinic to the high temperature orthorhombic phase.

Another example relates to the crystalline structure in $NiFe_2O_4$ and $CoFe_2O_4$ thin films and sub-micron structures which were investigated by Raman spectroscopy. In these cases we evidenced a strain induced symmetry lowering. [Him13] A larger number of phonon bands was observed in the polarization dependent Raman spectra of the ferrite films than expected for the cubic spinel structures. This is explained by short range ordering of the Ni^{2+} (or Co^{2+}) and Fe^{3+} cations at the octahedral sites inducing a lowering of the symmetry. The same behaviour was also observed in the Raman spectra measured for the submicron structures, suggesting the same cation distribution as in the films.

3.6. Characterization of strained Si after nano-pattering using UV Raman spectroscopy [Him06, Him07c]

[Him06] **C. Himcinschi**, I. Radu, R. Singh, W. Erfurth, A. Milenin, M. Reiche, S.H. Christiansen, and U. Gösele
Relaxation of strain in patterned strained silicon investigated by UV Raman spectroscopy
Materials Science Engineering B 135, 184-187 (2006) DOI: 10.1016/j.mseb.2006.08.023
[Him07c] **C. Himcinschi**, R. Singh, I. Radu, A.P. Milenin, W. Erfurth, M. Reiche, U. Gösele, S.H. Christiansen, F. Muster, and M. Petzold
Strain relaxation in nanopatterned strained silicon round pillars
Applied Physics Letters 90, 021902 (2007) DOI: 10.1063/1.2431476

Biaxially tensile strained silicon on wafer level has been widely explored for performance enhancement since, in this case, the strain engineering in the silicon channel was successfully carried out by established heteroepitaxial growth processes. Biaxial tensile strain of the order of ~1% in silicon increases the electron and hole mobilities due to the effective mass reduction and the band structure modification induced by strain. To achieve biaxial tensile strain, a thin silicon layer is epitaxially and pseudomorphically grown on a thick relaxed SiGe layer that itself is epitaxially deposited and plastically relaxed on a Si(100) wafer. Subsequently, the thin strained Si layer can be transferred onto silicon oxide using the Smart-Cut© [Bru94] technology resulting in the so called strained Si on insulator (sSOI). With this approach tensile strain around 1% in the Si layer could be realized.

However, due to the miniaturization of the microelectronic devices the strained Si layers have to withstand various processing steps. The strain retention in the layers and structures after all these processing steps is an essential issue. One of the most critical processing steps with regard to the strain retention is the nano-patterning. It is, therefore, of significant technological importance to define a method that is able to monitor the behavior of the strain state of strained Si (sSi) layers after nanopatterning.

The strain in periodic arrays of sSi round nano-pillars fabricated on sSi layers deposited on SiGe virtual substrates was determined using high-resolution UV micro-Raman spectroscopy. [Him07c] The strain was found to relax significantly upon nanostructuring: from 0.9% in the unpatterned sSi layer to values between 0.22% and 0.57% in the round sSi pillars with diameters from 100 nm up to 500 nm.

[Him07c] Similar relaxation of the strain was proved by means of UV Raman spectroscopy in the case of patterning the strained Si ion rectangular pillars [Him06]. We found that the strain relaxation is mediated by the large free surface area at the edges of the pillars. The strain relaxation depends on the nanopattern size and geometry and should be considered in designing the chips since it critically influences the strain engineering.

3.7. Method for obtaining uniaxial strain at wafer level in tension and compression [Him07a, Him07b, Him08]

[Him07a] **C. Himcinschi**, M. Reiche, R. Scholz, S.H. Christiansen, and U. Gösele
Compressive uniaxially strained silicon on insulator by prestrained wafer bonding and layer transfer
Applied Physics Letters 90, 231909 (2007) **DOI: 10.1063/1.2747182**
[Him07b] **C. Himcinschi**, I. Radu, F. Muster, R. Singh, M. Reiche, M. Petzold, U. Gösele, and S.H. Christiansen
Uniaxially strained silicon by wafer bonding and layer transfer
Solid State Electronics 51, 226-230 (2007) **DOI: 10.1016/j.sse.2007.01.018**
[Him08] **C. Himcinschi**, R. Sing, O. Moutanabbir, R. Scholz, M. Reiche S.H. Christiansen, U. Gösele, and D.R.T. Zhan
Etching-back of uniaxially strained silicon on insulator investigated by spectroscopic ellipsometry
physica status solidi (a) 205, 841-844 (2008) **DOI: 10.1002/pssa.200777753**

The biaxial strain leads to substantial mobility enhancement for electrons [Cur01], but the enhancement of the hole mobility in the case of biaxial strained silicon is minor. Uniaxial straining was proposed as an alternative method for hole mobility enhancement. Even uniaxial strain below 0.05% yields to mobility enhancement of up to 15% [Hau03]. The amount of uniaxial strain at wafer level, which can be obtained in 200 mm wafers is smaller than 1%, of the order of 0.05-0.1% [Him07a]. However, this strain can result in a mobility enhancement of more than 35% in SOI and bulk MOSFETs [Bel01].

We proposed an approach that allows to create uniaxial strain flexibly in tension [Him07a] or compression [Him07b] on wafer level by exploiting mechanical straining of the material upon bending (see figure 6). For mechanical uniaxial straining, two wafers were bent over a cylinder (bending over a sphere would lead to biaxial strain), following the concept introduced first by Belford *et al.* [Bel02]. The bent wafers are brought into contact via direct wafer bonding and covalent bonds across the bonded interface form upon annealing in the bent state. By thinning one of the wafers, using the Smart-Cut© process, to less than 1 µm thickness the bonded pair assumes an almost flat surface and substantial strain is transferred to the thinned wafer. [Him08] This strain is essentially uniaxial and can be exploited in devices.

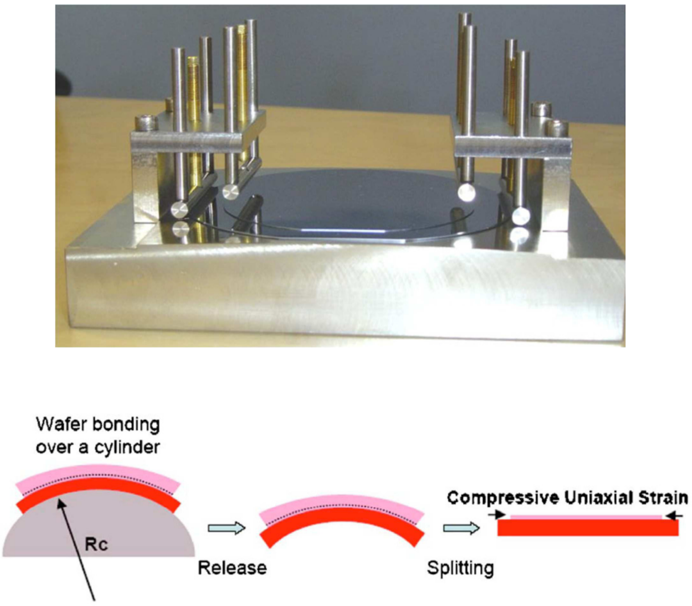

Figure 6. (taken from [Him07a, Him07b]) The bonding set-up and the schematic drawing of the concept for realising uniaxial compressive strain at wafer level.

UV-Raman spectroscopy was employed to determine the strain in the thin transferred layer as a function of radius of curvature of the initial bending. The strain values, as determined from Raman spectroscopy, can be controlled by varying the curvature radius of the bending cylinder used for bending the wafers before bonding. A maximum compressive uniaxial strain of 0.1% was obtained for a radius of curvature of 0.5 m.

4. Summary

The main results presented in this cumulative habilitation thesis are summarized in the following.

A method relying on the Raman tensor formalism, which allows an assignment of the $BiFeO_3$ (BFO) Raman modes having pure as well as mixed character /symmetries is proposed. Based on the Raman mode assignment, a novel procedure for the identification of the ferroelastic domains in multiferroic materials using Raman spectroscopy mapping is presented. This method takes advantage of the sensitivity of some mixed Raman modes of BFO to the arrangement (in-plane orientation) of the ferroelastic domains.

Raman studies have confirmed the very good epitaxy of the tetragonal-like BFO films grown on $LaAlO_3$ substrates, as indicated by the remarkable azimuthal / polarisation dependence of the Raman spectra. The larger number of phonons observed in the spectra of tetragonal-like BFO films as compared with that of rhombohedral BFO films is consistent with a Cc monoclinic structure, with a large tetragonal c/a ratio. The changes of the structures seen in Raman spectroscopy are accompanied by changes in optical properties: the dielectric function and the bandgap of tetragonal-like BFO films are blue shifted by ca. 0.3 eV as compared with the relaxed films.

Grüneisen parameters for BFO epitaxial thin films have been determined from the relative volume change and the relative shifts of the Raman modes induced by the piezoelectric strain and related to the anharmonicity of the vibrations.

Raman spectrum of $BiCrO_3$ (BCO) and its assignment based on symmetry considerations was reported for the first time. Temperature-dependent Raman spectroscopy and X-ray diffraction measurements were employed to study the structural phase transition between monoclinic and orthorhombic phases in polycristalline BCO and to determine the transition temperature, contributing to solve the structural controversies for this material. The epitaxial relation between BCO films and different substrates was determined by using polarisation-dependent Raman measurements corroborated with simulations dependent on crystal symmetry, and with X-ray diffraction and pole figure results. On the other hand, the dielectric function and the band gap of BCO films were determined for the first time from spectroscopic ellipsometry results.

The crystalline structure in $NiFe_2O_4$ (NFO) and $CoFe_2O_4$ (CFO) thin films and sub-micron structures was investigated by Raman spectroscopy and thereby a strain induced symmetry lowering was evidenced. The band gap as well as the diagonal and the off-diagonal components of the dielectric function of ferrimagnetic NFO and CFO epitaxial thin films were determined in the spectral range from 0.7 eV (diagonal) and from 1.7 eV (off-diagonal) to 5 eV by combining spectroscopic ellipsometry and magneto-optical Kerr effect measurements.

Raman spectroscopy was successfully applied as a tool to probe also other types of phase transitions such as orbital ordering in the case of 3d transition metal oxides. The transition to orbital ordering in epitaxial $LaVO_3$ films grown by PLD was probed and evidenced by temperature-dependent measurements.

A method of producing uniaxial strain in Si wafers based on mechanical bending and bonding of Si wafers, followed by thinning one of the wafers by ion-implantation induced splitting (known as the smart-cut process), was proposed. This method allows to create uniaxial strain flexibly in tension or compression on wafer level and UV-Raman spectroscopy can be employed to determine the strain in the thin transferred layer.

The relaxation of the strain in strained silicon nanostructures of different dimensions and different shapes was analysed by means of UV Raman spectroscopy.

5. List of the papers on which this cumulative Habilitation is based

The cumulative *Habilitation* is based on sixteen published scientific articles in which the candidate was significantly involved. The candidate's own contribution to each publication is indicated after the list.

[Him19] **C. Himcinschi**, J. Rix, C. Röder, M. Rudolph, M.-M. Yang, D. Rafaja, J. Kortus, and M. Alexe
Ferroelastic domain identification in $BiFeO_3$ crystals using Raman spectroscopy
Scientific Reports 9, 379_1_9 (2019) **doi: 10.1038/s41598-018-36462-5**

[Vre17] I. Lindfors-Vrejoiu, L. Jin, **C. Himcinschi**, J. Engelmayer, F. Hensling, C.-L. Jia, R. Waser, R. Dittmann and P.H.M. van Loosdrecht
Structure and orbital ordering of ultrathin $LaVO_3$ probed by atomic resolution electron microscopy and Raman spectroscopy
physica status solidi (rrl) 11, 1600350 (2017) **doi: 10.1002/pssr.201600350**

[Him16] **C. Himcinschi**, E.J. Guo, A. Talkenberger, K. Dörr, and J. Kortus
Influence of piezoelectric strain on the Raman spectra of $BiFeO_3$ films deposited on PMN-PT substrates
Appl. Phys. Lett. 108, 042902 (2016) **doi: 10.1063/1.4940973**

[Vre16] I. Vrejoiu, **C. Himcinschi**, L. Jin, C.-L. Jia, N. Raab, J. Engelmayer, R. Waser, R. Dittmann and P. H. M. van Loosdrecht
Probing orbital ordering in $LaVO_3$ epitaxial films by Raman scattering
APL Mater. 4, 046103 (2016) **doi: 10.1063/1.4945658**

[Him15] **C. Himcinschi**, A. Bhatnagar, A. Talkenberger, M. Barchuk, D.R.T. Zahn, D. Rafaja, J. Kortus, and M. Alexe
Optical properties of epitaxial $BiFeO_3$ thin films grown on $LaAlO_3$
Appl. Phys. Lett. 106, 012908_1-5 (2015) **doi: 10.1063/1.4905443**

[Tal15] A. Talkenberger, I. Vrejoiu, F. Johann, C. Röder, G. Irmer, D. Rafaja, G. Schreiber, J. Kortus and **C. Himcinschi**
Raman spectroscopic investigations of epitaxial $BiFeO_3$ thin films on rare earth scandate substrates
J. Raman Spec. 46, 1245 (2015) **doi: 10.1002/jrs.4762**

[Him13] **C. Himcinschi**, I. Vrejoiu, G. Salvan, M. Fronk, A. Talkenberger, D.R.T. Zahn, D. Rafaja, and J. Kortus
Optical and magneto-optical study of nickel and cobalt ferrite epitaxial thin films and submicron structures
J. Appl. Phys. 113, 084101_1-8 (2013) **doi: 10.1063/1.4792749**

[Tal12] A. Talkenberger, **C. Himcinschi**, T. Weißbach, K. Vijayanandhini, I. Vrejoiu, C. Röder, D. Rafaja, and J. Kortus
Raman spectroscopic and X-ray diffraction investigations of epitaxial $BiCrO_3$ thin films
Thin Solid Films 520, 4590–4594 (2012) **doi: 10.1016/j.tsf.2011.10.196**

[Him11] **C. Himcinschi**, I. Vrejoiu, T. Weißbach, K. Vijayanandhini, A. Talkenberger, C. Röder, S. Bahmann, D. R. T. Zahn, A. A. Belik, D. Rafaja, and J. Kortus

Raman spectra and dielectric function of $BiCrO_3$: Experimental and first-principles studies
J. Appl. Phys. 110, 073501_1-8 (2011) **doi:10.1063/1.3642985**

[Him10a] **C. Himcinschi**, I. Vrejoiu, M. Friedrich, E. Nikulina, L. Ding, C. Cobet, N. Esser, M. Alexe, D. Rafaja, and D.R.T Zahn
Substrate influence on the optical and structural properties of pulsed laser deposited $BiFeO_3$ epitaxial films
J. Appl. Phys. 107, 123524_1-5 (2010) **DOI: 10.1063/1.3437059**

[Him10b] **C. Himcinschi**, I. Vrejoiu, M. Friedrich, L. Ding, C. Cobet, N. Esser, M. Alexe, and D.R.T Zahn
Optical characterisation of $BiFeO_3$ epitaxial thin films grown by pulsed-laser deposition
physica status solidi c 7, 296-299 (2010) **DOI: 10.1002/pssc.200982414**

[Him08] **C. Himcinschi**, R. Sing, O. Moutanabbir, R. Scholz, M. Reiche S.H. Christiansen, U. Gösele, and D.R.T. Zhan
Etching-back of uniaxially strained silicon on insulator investigated by spectroscopic ellipsometry
physica status solidi (a) 205, 841-844 (2008) **DOI: 10.1002/pssa.200777753**

[Him07a] **C. Himcinschi**, M. Reiche, R. Scholz, S.H. Christiansen, and U. Gösele
Compressive uniaxially strained silicon on insulator by prestrained wafer bonding and layer transfer
Applied Physics Letters 90, 231909 (2007) **DOI: 10.1063/1.2747182**

[Him07b] **C. Himcinschi**, I. Radu, F. Muster, R. Singh, M. Reiche, M. Petzold, U. Gösele, and S.H. Christiansen
Uniaxially strained silicon by wafer bonding and layer transfer
Solid State Electronics 51, 226-230 (2007) **DOI: 10.1016/j.sse.2007.01.018**

[Him07c] **C. Himcinschi**, R. Singh, I. Radu, A.P. Milenin, W. Erfurth, M. Reiche, U. Gösele, S.H. Christiansen, F. Muster, and M. Petzold
Strain relaxation in nanopatterned strained silicon round pillars
Applied Physics Letters 90, 021902 (2007) **DOI: 10.1063/1.2431476**

[Him06] **C. Himcinschi**, I. Radu, R. Singh, W. Erfurth, A. Milenin, M. Reiche, S.H. Christiansen, and U. Gösele
Relaxation of strain in patterned strained silicon investigated by UV Raman spectroscopy
Materials Science Engineering B 135, 184-187 (2006) **DOI: 10.1016/j.mseb.2006.08.023**

5.1. Description of own contribution

[Him19] The candidate had the idea of the paper, wrote the manuscript (except the EBSD part), performed part of the Raman measurements and analysed the Raman mapping data.

[Vre17] The candidate performed and analysed the Raman spectroscopy measurements contributing in writing the Raman part of the manuscript.

[Him16] The candidate had the idea of the article, wrote the manuscript, performed the Raman measurements and analysed part of the Raman data.

[Vre16] The candidate performed and analysed the Raman spectroscopy measurements contributing in writing the Raman part of the manuscript.

[Him15] The candidate had the idea of the paper, wrote the manuscript, designed and performed the Raman measurements under electric field and analysed part of the Raman data.

[Tal15] The candidate had the idea of the project, assisted and guided A. Talkenberger in the measurements and analysis the Raman measurements and in elaborating the manuscript.

[Him13] The candidate had the idea of the article, wrote the manuscript, performed and analysed the ellipsometry measurements and part of the Raman spectroscopy data.

[Tal12] The candidate had the idea of the project, assisted and guided A. Talkenberger in the measurements and analysis the Raman measurements and contribute in writing part of the manuscript.

[Him11] The candidate had the idea of the article, wrote the manuscript, performed and analysed the ellipsometry measurements and part of the Raman spectroscopy data.

[Him10a] The candidate had the idea of the article, wrote the manuscript, performed and analysed the Raman measurements, applied for and performed the ellipsometry measurements at BESSY.

[Him10b] The candidate had the idea of the paper, wrote the manuscript, performed the ellipsometry measurements and analysed them.

[Him08] The candidate had the idea of the paper, wrote the manuscript, performed the ellipsometry measurements and analysed them.

[Him07a] The candidate designed the uniaxial bonding set-up, had the idea of the paper, wrote the manuscript, performed part of the bonding experiments, and performed the Raman measurements and their evaluation.

[Him07b] The candidate designed the uniaxial bonding set-up, had the idea of the paper, wrote the manuscript, performed part of the bonding experiments, and performed the Raman measurements and their evaluation.

[Him07c] The candidate proposed the project had the idea of the paper, wrote the manuscript, performed and analysed the Raman spectroscopy measurements.

[Him06] The candidate proposed the project had the idea of the paper, wrote the manuscript, performed and analysed the Raman spectroscopy measurements.

6. References

[Bea07] H. Bea, M. Bibes, S. Petit, J. Kreisel, and A. Barthelemy, Phil. Mag. Lett. 87, 165, (2007).

[Bee12] C. Beekman, A.A. Reijnders, Y.S. Oh, S.W. Cheong, and K.S. Burch, Phys Rev B 86, 020403 (2012).

[Bel01] R. E. Belford, J. Electron. Mater. 30, 807 (2001).

[Bel02] R. Belford, US patent US6,455,397 B1, Sept, 24, (2002).

[Bel07] A.A. Belik, S. Ikubo, K. Kodama, N. Igawa, and E. Muromachi Chem. Mat. 46, 8746 (2007).

[Bru94] M. Bruel, US Patent, US 5374564, Process for the production of thin semiconductor material films, 20 December 1994

[Cat09] G. Catalan and J.F. Scott, Advanced Materials 21, 2463 (2009).

[Chu08] Y-H. Chu et al., Nature Materials 7, 478 (2008).

[Cur01] M.T. Currie, C.W. Leitz, T.A. Langdo, G. Taraschi, E.A. Fitzgerald, J. Vac.

Sci. Technol. B 19 (2001) 2268.

[Fis80] P. Fischer, M. Polomska, I. Sosnowska,M. Szymanski, J. Phys. C 13, 1931 (1980).

[Fri11] D. Fritsch and C. Ederer, Appl. Phys. Lett. 99, 081916 (2011).

[Hau03] M. Haugerud, L. A. Bosworth, and R. E. Belford, J. Appl. Phys. 94, 4102 (2003).

[Her07] P. Hermet, M. Goffinet, J. Kreisel, and Ph. Ghosez, Phys. Rev. B 75, 220102(R) (2007).

[Hil02] N.A. Hill, P. Bättig, and C. Daul J. Phys. Chem. B 106, 3383 (2002)

[Hli11] J. Hlinka, J. Pokorny, S. Karimi, and I.M. Reaney, Phys. Rev. B 83, 020101(R) (2011).

[Ich08] N. Ichikawa, Appl. Phys. Exp. 1, 101302 (2008).

[Ili11] M.N. Iliev, D. Mazumdar, J.X. Ma, A. Gupta, F. Rigato, and J. Fontcuberta, Phys. Rev. B 83, 014108 (2011).

[Iss10] S. Issing, F. Fuchs, C. Ziereis, E. Batke, A. Pimenov, Y. Vu. Ivanov, A.A. Mukhin, and J. Geurts, The European Physical Journal B 73, 253 (2010).

[Iva10] V.G. Ivanov, M.V. Abrashev, M.N. Iliev, M.M. Gospodinov, J. Meen, and M.I. Aroyo, Phys. Rev. B 82, 024104 (2010).

[Kre03] J. Kreisel and P. Bouvier, J. Raman Spectrosc. 34, 524, (2003).

[Lah09] A. Lahmar, S. Habouti, M Dietze, C.H. Solterbeck, and M. Es-Souni, Appl. Phys. Lett. 94, 012903 (2009).

[Mar12] L.W. Martin, and D.G. Scholm, Current Opinion Solid State Mat. Sci. **16**, 199 (2012).

[Mar71] R.M. Martin, and T.C. Damen, Phys. Rev. Lett. 26, 86 (1971).

[Miy05] S. Miyasaka, S. Onoda, Y. Okimoto, J. Fujioka, M. Iwama, N. Nagaosa, and Y. Tokura, Phys. Rev. Lett. 94, 076405 (2005)

[Miy06] S. Miyasaka, J. Fujioka, M. Iwama, Y. Okimoto, and Y. Tokura, Phys. Rev. B 73, 224436 (2006)

[Ope11] M. Opel, S. Geprägs, E.P. Menzel, A. Nielsen, D. Reisinger, K.-W. Nielsen, A. Brandlmaier, F.D. Czeschka, M. Althammer, M. Weiler, S.T.B. Goennenwein, J. Simon, M. Svete, W. Yu, S.-M. Hühne, W. Mader, R. Gross, Phys. Status Solidi A 208, 232 (2011)

[Pal08] R. Palai, R.S. Katiyar, H. Schmid, P. Tissot, S.J. Clark, J. Robertson, S.A.T. Redfern, G. Catalan, and J.F. Scott, Phys Rev. B 77, 0140110 (2008).

[Pez13] G. Pezzotti, J. Appl. Phys. 113, 211301 (2013).

[Ram07] R.Ramesh and N.A. Spaldin, Nature Materials 6, 21 (2007).

[Ram10] S. Ramanathan (ed), Thin Film Metal-Oxides Fundamentals and Applications in Electronics and Energy, in Chapter 3: J. Lu, K.G. West and S.A. Wolf, Novel Magnetic oxide thin films, Springer (2010).

[San13] D Sando, A Agbelele, D Rahmedov, J Liu, P Rovillain, C Toulouse, I C Infante, A P Pyatakov, C Deranlot, S Lisenkov, D Wang, J-M Le Breton, M Cazayous, A Sacuto, J Juraszek, A K Zvezdin, L Bellaiche, B Dkhil, A Barthélémy, and M Bibes, Nature Materials 12, 641 (2013).

[Spa05] N.A. Spaldin and M. Fiebig, Science 309, 391 (2005).

[Ten08] D.A. Tenne, and X.X. Xi, J. Am. Ceram. Soc. 91, 1820 (2008).

[Wil73] P.F. Williams, and S.P.S. Porto, Phys. Rev. B 8, 1782 (1973).

www.nature.com/scientificreports

SCIENTIFIC REPORTS

OPEN

Ferroelastic domain identification in $BiFeO_3$ crystals using Raman spectroscopy

Received: 25 April 2018
Accepted: 23 November 2018

Cameliu Himcinschi[1], Jan Rix[1], Christian Röder[1], Martin Rudolph[2], Ming-Min Yang[3], David Rafaja[2], Jens Kortus[1] & Marin Alexe[3]

Multiferroic $BiFeO_3$ crystals were investigated by means of micro-Raman spectroscopy using the laser wavelengths of 442 nm (resonant conditions) and 633 nm (non-resonant conditions). The azimuthal angle dependence of the intensity of the Raman modes allowed their symmetry assignment. The experimental data are consistent with a simulation based on Raman tensor formalism. Mixed symmetries were taken into account, considering the orientation of the crystal optic axis along a pseudo-cubic <111> direction. The strong anisotropic intensity variation of some of the polar Raman modes was used for line scans and mappings in order to identify ferroelastic domain patterns. The line scans performed with different excitation wavelengths and hence different information depths indicate a tilt of the domain walls with respect to the sample surface. The domain distribution found by Raman spectroscopy is in very good agreement with the finding of electron back scattering diffraction.

Due to its multiferroic properties at room temperature, the visible-light photovoltaic effect, and related potential applications, $BiFeO_3$ (BFO) attracts a lot of scientific interest[1–4]. Under ambient conditions, BFO crystallizes in the trigonal space group (SG) ***R3c*** with the rhombohedral lattice parameters a = 5.6343 Å and α = 59.348°, or alternatively hexagonal lattice parameters a = 5.5876 Å and c = 13.867 Å[5,6]. Neglecting the mutual rotation of neighbouring FeO_6 octahedrons, the crystal structure of BFO can be approximated by a sheared perovskite structure (see the inset on the right-hand side of Fig. 1) that was reported by Tomashpolskii *et al.*[7] to crystallize in the space group ***R3m*** and with the lattice parameters a = 3.962 Å and α = 89.4°. The sheared perovskite structure is frequently reported as a pseudo-cubic (pc) structure of BFO[5]. In the pseudo-cubic structure, the polarisation axis is parallel to a crystallographic direction <111>, which is thus the polar (i.e. optic) axis. In such a case, four variants of ferroelastic domains and eight degenerated states for the electric polarisation (eight variants of ferroelectric domains taking also the polarisation orientation into account) are expected[8,9]. The knowledge and the control of the domain configurations are essential for the field of "domain engineering" which is striving for tuning the functionalities of devices based on BFO[10,11]. Raman scattering yields information on lattice dynamics. Thus, it is an established method to detect subtle structural changes in BFO[12–15]. For the BFO with the space group ***R3c***, group theory predicts 27 optical phonon modes $\Gamma_{opt,R3c} = 4A_1 + 5A_2 + 9E$. The $\mathbf{A_1}$ and doubly degenerated **E** modes are both Raman and IR active, while the $\mathbf{A_2}$ modes are silent. This means that 13 modes are observable by Raman spectroscopy from $(111)_{pc}$ BFO scattering surface[16–18]. The Raman tensors of the Raman modes are given by[19]:

$$A_1(z) = \begin{pmatrix} a & & \\ & a & \\ & & b \end{pmatrix},\ E(x) = \begin{pmatrix} & c & d \\ c & & \\ d & & \end{pmatrix},\ E(y) = \begin{pmatrix} c & & \\ & -c & d \\ & d & \end{pmatrix} \tag{1}$$

The modes are polarised along the directions x, y, or z, as shown the inset on the right-hand side of Fig. 1; z denotes the optic axis parallel to the $[111]_{pc}$ direction; $y||\sigma_v||[1\bar{2}1]_{pc}$. $\mathbf{A_1}$ and **E** are polar modes, thus, due to the macroscopic electric field, they split into longitudinal optical (LO) and transversal optical (TO) modes with different frequencies. According to the group theory, polar phonon modes with A_1 symmetry are polarised along the z-direction (i.e. optic axis $//(111)_{pc}$), while in the case of vibrations with E symmetry, the atomic displacement is

[1]Institute of Theoretical Physics, TU Bergakademie Freiberg, D-09596, Freiberg, Germany. [2]Institute of Materials Science, TU Bergakademie Freiberg, D-09596, Freiberg, Germany. [3]Department of Physics, University of Warwick, Coventry, CV4 7AL, United Kingdom. Correspondence and requests for materials should be addressed to C.H. (email: himcinsc@physik.tu-freiberg.de)

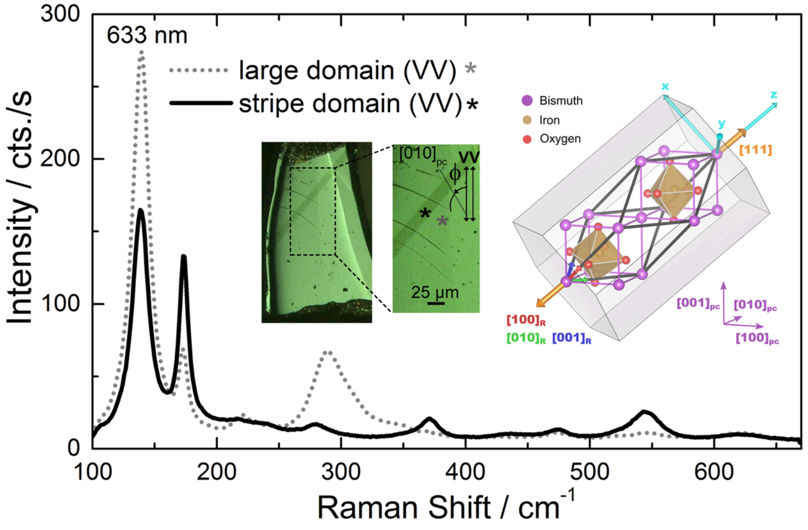

Figure 1. Typical Raman spectra measured in parallel (VV) polarisation using the 633 nm excitation line on the stripe domain (continuous line) and on the large domain (dotted line) of a $(001)_{pc}$ BFO crystal shown in the middle inset of the figure (polarisation microscopy image). Right inset: Alternative structural descriptions of BFO and their crystallographic relationship, using VESTA program[44]. Thick black lines terminate the rhombohedral unit cell (*R3c*). The unit cells plotted in purple and filled by the atoms are pseudo-cubic (*R3m*). The orange arrows mark the polarisation axis. The orthogonal (x,y,z) axes used for the Raman tensors are plotted in cyan. The gray object is an extended hexagonal elementary cell according to Doig *et al.*[45].

perpendicular to the z-axis. The frequency of the polar modes depends on the direction of the phonon propagation with respect to the optic axis, so that a directional dispersion occurs[20–22]. For this reason the oblique modes (propagating along a direction which forms an angle θ with the $[111]_{pc}$ optic axis) have usually a mixed symmetry character[23,24]. Consequently, due to the LO/TO splitting 22 modes should be observed by Raman spectroscopy from scattering surfaces different from $(111)_{pc}$. This is also the case for backscattering from the $(001)_{pc}$ oriented surface of BFO, for which θ = 54.7°. Unfortunately, this aspect was neglected in some of the Raman analyses performed on the $(001)_{pc}$ oriented BFO, which yielded to some controversies in the mode assignments[25–28]. A full assignment of the modes considering mixed symmetry LO/TO and mixed character A_1/E was done by Hlinka *et al.* based on dispersion of phonons frequency on the angle θ (angle between the phonon propagation and the optic axis)[24]. The method presented in ref.[24] is based on the phonon frequency variation with the angle between the crystal optic axis and the laser beam in randomly oriented crystalline grains.

In this work we present a method based on the Raman tensor formalism, which allows an assignment of the BFO Raman modes of pure as well as mixed character/symmetry. It should be mentioned that the Raman tensor approach was only applied until now for pure (not mixed) modes. This restriction corresponds to the cases θ = 0° and θ = 90° (where θ is the angle between the phonon propagation and optic axis), *i.e.* the case of $(111)_{pc}$ oriented BFO. Most of the samples/films investigated in literature were, however, $(001)_{pc}$ oriented BFO corresponding to θ = 54.7°, which leads to an incorrect interpretation, because in this case mixed character/symmetry of the modes needs to be considered. The method presented in this work analyses the in-plane (*i.e.* in the crystal surface plane) variation of the Raman intensities upon azimuthal rotation of a single crystal instead of the phonon frequency dispersion (which was reported in ref.[24]). Since it is based on the Raman intensity analysis, the Raman tensor method presented here is highly sensitive to the in-plane orientation of the optic axis projection onto the sample surface for any angle θ between the phonon propagation (laser beam direction) and the optic axis. Using the 180° periodicity of the azimuthal angular dependence of the intensity of some BFO Raman modes, this method allows for identification of the ferroelastic domains. Thanks to the sensitivity of the Raman signal to the domain orientation that is combined with the depth information when using two appropriate laser wavelengths for excitation, Raman spectroscopy can be used for domain imaging in BFO, as an alternative to other methods such as birefringence[29] or circular dichroism photoemission[30].

Material and Methods

The samples investigated in this work were 150 µm thick $(001)_{pc}$ oriented BFO crystals containing macroscopic ferroelastic domains. The crystals were grown in $Bi_2O_3 + B_2O_3$ flux using a method similar to that originally proposed by Kubel and Schmid[31]. The top solution crystals were harvested and polished parallel to the $(001)_{pc}$ surface. The final polishing was performed using a SiO_2 colloidal solution diluted with water in a 1:1 ratio in order to remove residual mechanical strain.

Raman spectroscopy. Raman spectroscopic measurements were performed in backscattering geometry at room temperature using Horiba Jobin Yvon HR 800 spectrometers equipped with 2400 mm^{-1} or 1800 mm^{-1} gratings. The 442 nm line of a HeCd laser and the 633 nm line of a HeNe laser were used for excitation. The light was focused and collected through a 50x magnification objective (about 2 µm focus diameter). The laser power was kept below 1.5 mW in order to avoid changes in the Raman spectra induced by laser heating. The light of the incident and scattered beam was polarised either parallel (VV) or perpendicular (HV) to each other.

Electron backscatter diffraction. The distribution of ferroelastic domains was verified by electron backscatter diffraction (EBSD) measurements that were performed on a scanning electron microscope (Zeiss LEO 1530 GEMINI) operating at an acceleration voltage of 20 kV. The Kikuchi patterns were recorded with a Nordlys II detector (Oxford Instruments) at the step size of 0.2 µm, and subsequently indexed by the HKL Channel 5 software. For indexing, the crystal structure suggested by Moreau *et al.*[6] was used. The EBSD measurements confirmed the almost single-crystalline nature of the BFO crystals and their orientation $(001)_{pc}$ parallel with the sample surface. Because of the pseudo-cubic symmetry of BFO and the centrosymmetry of the EBSD patterns, EBSD cannot distinguish easily between the orientation variants, which are mutually rotated about approximately 90°, 180° or 270° around the axis perpendicular to the sample surface[32]. Still in this particular case, the EBSD measurement was able to trace the local orientation of the polarisation axis through the elastic distortion of the crystal structure that is caused by the polarisation/ferroelastic effect. Thus, the smallest mean angular deviation (MAD) between the measured and simulated Kikuchi patterns of BFO was utilized as a decision criterion for the respective orientation variant and for the corresponding orientation of the polarisation axis.

Results and Discussions

Raman spectroscopy. Assignment of the oblique phonon modes. The inset in the middle of Fig. 1 shows a polarisation optical microscopy image of one of the BFO crystals (ca. 250 µm × 500 µm) investigated in this work, presenting two large homogeneous ferroelastic domains: a dark diagonal stripe and the remainder of the sample (further denoted as large domain). The optical contrast between the two domains is due to different orientations of the spontaneous electric polarisation. In both cases the spontaneous polarisation lies along a $<111>_{pc}$ diagonal, but the two polarisation projections on the sample surface are forming an angle of 90° with one another. The contrast of the image can be reverted by rotating the sample by 90° around the surface normal under the polarisation microscope and keeping the polariser and the analyser of the polarisation microscope fixed. Piezoresponse force microscopy (see Supplementary Material, Fig. 1s) indicates that for both domains the polarisation points downwards along $<111>_{pc}$ diagonal, which means that 71° domain walls should be formed[31,33,34].

Figure 1 shows characteristic Raman spectra measured on the two different domain regions, which are marked by asterisks in the inset, with the analyser being parallel to the polarisation of the incident light (VV). The spectra were excited with a laser line of 633 nm, which ensures non-resonant conditions and a relatively high integrated intensity of the first order Raman signal at room temperature[35]. On one hand the 633 nm excitation allows the use of the Raman tensor formalism for the assignment of Raman modes. On the other hand, the penetration depth of the laser light is very large because of the low extinction coefficient $k = 1.2 \times 10^{-4}$ [36,37]. Thus, BFO is nearly transparent for the 633 nm light; the excited volume is actually given by the focus depth (~7 µm). The Raman spectra measured on the stripe domain and on the remainder of the sample (large domain) have very different relative intensities. However, considering a flat $(001)_{pc}$ scattering surface of the sample (as in our case), one expects for both types of domains the same angle $\theta = 54.7°$ formed by the direction of laser light propagation and the optic axis. This is confirmed by the fact that the peaks have the same frequency position, as no angular dispersion is expected in this case[22,24]. Therefore the differences between the spectra are given by the different in-plane orientation of the optic axis in the two types of domains. In order to check this in detail Raman measurements have been performed by rotating the sample azimuthally around the laser beam direction (keeping the measurement point) every 15° for both parallel (VV) and crossed (HV) polarisation configurations, and on both types of domains.

Figure 2a) shows the spectra measured in HV polarisation configuration on the azimuthally rotated stripe domain. It can be seen that most of the Raman modes show a 90° periodicity of the intensity as a function of azimuthal rotation angle ϕ'. The azimuthal rotation angle $\phi = \phi' + 30°$ is the angle between the $[010]_{pc}$ BFO crystal direction and the direction of the polarisation of the incident laser light. For $\phi = 0°$ the $[010]_{pc}$ BFO crystal direction is parallel to the polarisation of the light. In order to obtain the intensity angular dependence of the modes each spectrum has been fitted using Lorentzian functions. In Fig. 2b) the fit obtained for the first spectrum in Fig. 2a), measured for $\phi' = 0°$ and HV polarisation, is shown as an example. The same procedure was applied for all rotation angles, both HV and VV polarisation configurations, and both domains. In all cases the peak areas depend periodically on the azimuthal angle. Exemplarily, the polar dependence of the peak areas for the peaks located at 520 cm^{-1}, 288 cm^{-1}, 172 cm^{-1}, 220 cm^{-1} and 370 cm^{-1} is plotted in Fig. 3a–c,g and h) respectively, for both VV (squares) und HV (circles) polarisation configurations and for the measurements performed on the stripe domain. We chose to present these modes because they have a high enough intensity for both polarisation configurations. Moreover, their positions are well separated from that of neighbouring modes. The peak area of the modes at 172 cm^{-1}, 288 cm^{-1}, and 370 cm^{-1} shows a 180° periodicity for VV polarisation and a 90° periodicity for HV polarisation. In case of the 520 cm^{-1} mode a periodicity of 90° was obtained for both polarisation configurations. The polar dependence of the intensity of the peaks when measuring on the large domain is rotated by 90° as compared with the measurements on the stripe domain. A comparison of the intensity for the modes at 138 cm^{-1} and at 370 cm^{-1} on stripe and large domains is exemplarily shown in the Fig. 2s in the Supplementary material. The anisotropic behaviour (180° periodicity) of the intensity allows us to distinguish between the macroscopic ferroelastic domains as will be shown in the line scans and maps discussed in the next section of the paper.

As mentioned above, for a $(001)_{pc}$ scattering surface the laser beam direction has an angle of $\theta = 54.7°$ with respect to the direction of the spontaneous polarisation, which is along a $< 111 >_{pc}$ direction (parallel to the optic axis). In this case, as discussed in the introduction, the polar $\mathbf{E}$ and $\mathbf{A_1}$ modes show a directional dispersion as

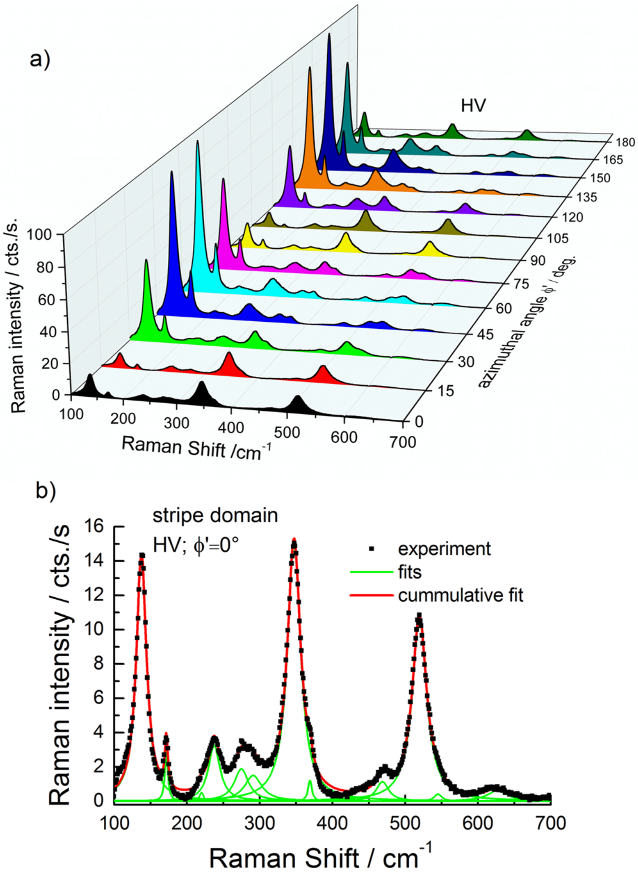

Figure 2. (**a**) Raman spectra measured in crossed (HV) polarisation on the stripe domain for different azimuthal rotation angles ϕ'. (**b**) Example of spectrum evaluation (fit) for $\phi' = 0°$.

function of θ[24]. Besides the ordinary $\mathbf{E}_{\mathrm{TO}}$ modes, whose frequencies are independent on the angle θ, there are four types of extraordinary modes with mixed symmetries: $\mathbf{E}_{\mathrm{TO}}\leftrightarrow\mathbf{E}_{\mathrm{LO}}$, $\mathbf{E}_{\mathrm{TO}}\leftrightarrow\mathbf{A}_{\mathrm{1TO}}$, $\mathbf{A}_{\mathrm{1LO}}\leftrightarrow\mathbf{A}_{\mathrm{1TO}}$, and $\mathbf{A}_{\mathrm{1LO}}\leftrightarrow\mathbf{E}_{\mathrm{LO}}$[38]. For the assignment of these oblique phonon modes the mixed character of the modes which correspond to $\theta = 54.7°$ should be taken into account.

The Raman tensor formalism allows for consideration of mixed phonon mode character based on a unit vector of phonon polarisation (cf. Yang *et al.*[39] and Talkenberger *et al.*[38]). For calculation of the Raman scattering intensity as function of the azimuthal angle, equation (9) from Talkenberger *et al.*[38] and the corresponding Raman tensors (equation 1) were used. The unit vectors of incident and scattered light as well as the phonon polarisation of ordinary and extraordinary modes were expressed with respect to the crystal (x,y,z) coordinate system assuming backscattering geometry. Using the method described above the azimuthal dependence of the intensity of all symmetries: ordinary E_{TO}, $\mathrm{E}_{\mathrm{TO}}\leftrightarrow\mathrm{A}_{\mathrm{1TO}}$, $\mathrm{A}_{\mathrm{1LO}}\leftrightarrow\mathrm{E}_{\mathrm{LO}}$, $\mathrm{A}_{\mathrm{1LO}}\leftrightarrow\mathrm{A}_{\mathrm{1TO}}$ and $\mathrm{E}_{\mathrm{TO}}\leftrightarrow\mathrm{E}_{\mathrm{LO}}$ were simulated for both VV and HV polarisation configurations in agreement with the experimental data as shown in Fig. 3d–f,i,j), respectively. It should be mentioned that each specific vibration has unique tensor elements. For their accurate determination, crystals with several differently oriented scattering surfaces would be needed. However, using the values of the Raman tensor elements given in the Table 1, a very good agreement between the simulated and the experimental data could be obtained for all five symmetries as shown in Fig. 3. At a closer look, when comparing experimental and simulated data, one can see that some of the experimental curves in parallel polarisation are not going to zero intensity as some of the simulated curves do. Possible reasons for this may be: the used angular step size of 15° could skip the very narrow minimum in intensity, the correlation errors in the fitting procedures (especially for neighbouring modes), a slight tilt of the sample surface, and/or polarisation leakages which are softening the selection rules. Nevertheless, our method allows a clear assignment of mixed symmetries of most of the BFO modes in the case of $(001)_{\mathrm{pc}}$ scattering surfaces. The azimuthal dependence of the 220 cm^{-1} and the 172 cm^{-1} modes looks similar. In this case the phonon dispersion (where only one mode at 220 cm^{-1} has $\mathrm{A}_{\mathrm{1LO}}$-$\mathrm{A}_{\mathrm{1TO}}$ mixed symmetry)[24,38], has to be used to distinguish between their symmetry. It should be mentioned that for all the modes mentioned in Table 1 the same symmetry assignment was found as expected from the dispersion curves from Hlinka *et al.*[24] for $\theta = 54.7°$ which corresponds to our $(001)_{\mathrm{pc}}$ oriented BFO.

Imaging of the ferroelastic domains. Using the 180° periodicity of the azimuthal angle dependence of the modes at 138 cm^{-1} ($\mathbf{E}_{\mathrm{TO}}\leftrightarrow\mathbf{A}_{\mathrm{1TO}}$) and 172 cm^{-1} ($\mathbf{A}_{\mathrm{1LO}}\leftrightarrow\mathbf{E}_{\mathrm{LO}}$) one can now use Raman spectroscopy for a quick distinction between different domains. A Raman spectroscopic line scan was realised along a 54 µm line crossing

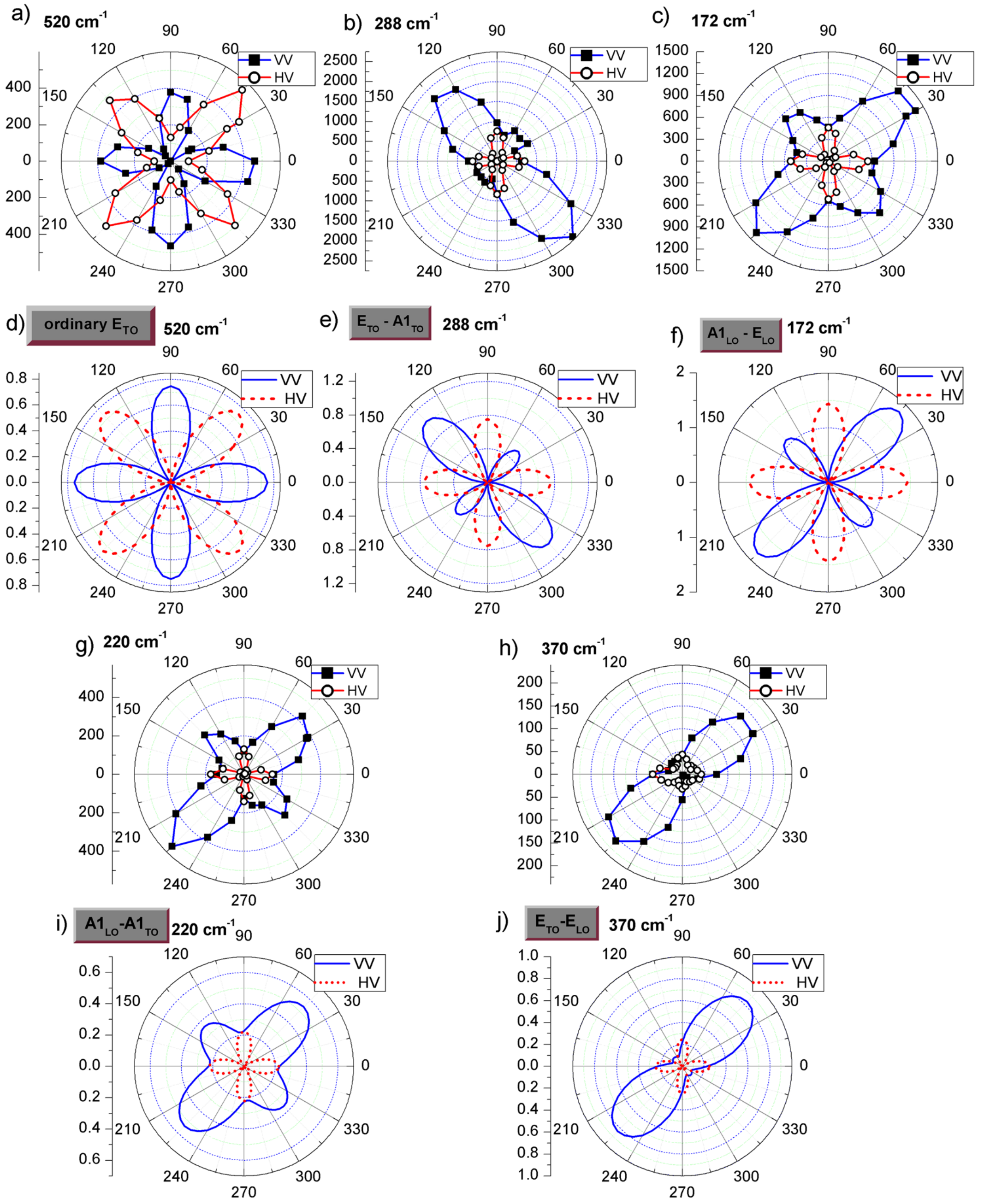

Figure 3. Polar plots of the azimuthal angle (ϕ) dependence of the peak areas for the modes at 520 cm^{-1} (**a**), 288 cm^{-1} (**b**), 172 cm^{-1} (**c**) 220 cm^{-1} (**g**) and 370 cm^{-1} (**h**) measured on the stripe domain using parallel (squares) and crossed (circles) polarisation configurations. Simulated intensity dependence using Raman tensor formalism for the ordinary E_{TO} (**d**), $E_{TO}\leftrightarrow A1_{TO}$ (**e**), $A1_{LO}\leftrightarrow E_{LO}$ (**f**), $A1_{LO}\leftrightarrow A1_{TO}$ (**i**) and $E_{TO}\leftrightarrow E_{LO}$ (**j**) mixed modes in the case of an $(001)_{pc}$ BFO scattering surface, for parallel (continuous line) and crossed (dashed line) polarisation configurations.

the stripe domain, with measurements done every 3 μm as can be seen in the inset of Fig. 4a). In the same figure, the Raman spectra measured with the 442 nm excitation line in parallel polarisation (VV) are shown. The grey dotted spectra correspond to points measured on the large domain, while the black continuous spectra are measured on the stripe domain. The 442 nm (2.81 eV) excitation line is slightly above the BFO bandgap of ~2.75 eV which means that near-resonant Raman scattering can be observed when using this line. In such conditions a breakdown of selection rules can occur which can affect the intensity of the modes[40–42]. In order to exclude any ambiguity in the interpretation of the mode characters, the Raman tensor formalism combined with azimuthal dependent measurements was only applied for the case of off-resonant measurement performed with 633 nm (1.96 eV). Once the mode characters have been unambiguously determined, one can take advantage of the different penetration depth of the two laser lines in BFO (76 nm @442 nm and 7 μm @633 nm)[37]. Thus, line scan

Symmetry	**Modes**	**Tensor elements**
Ordinary $\mathbf{E_{TO}}$	520 cm^{-1}, 237 cm^{-1}, 347 cm^{-1}	$c_{TO} = 0.2$, $d_{TO} = 1.2$
$\mathbf{E_{TO}\text{-}A_{1TO}}$	288 cm^{-1}, 138 cm^{-1}, 545 cm^{-1}	$a_{TO} = -1.1$, $b_{TO} = 0.6$ $c_{TO} = 0.2$, $d_{TO} = 1.2$
$\mathbf{A_{1LO}\text{-}E_{LO}}$	172 cm^{-1}, 470 cm^{-1}, 620 cm^{-1}	$a_{LO} = 0.4$, $b_{LO} = 0.4$ $c_{LO} = 1.0$, $d_{LO} = 1.7$
$\mathbf{A_{1LO}\text{-}A_{1TO}}$	220 cm^{-1}	$a_{LO} = -1.0$, $b_{LO} = 1.0$, $a_{TO} = 0.2$, $b_{TO} = 1.2$
$\mathbf{E_{TO}\text{-}E_{LO}}$	370 cm^{-1}, 432 cm^{-1}	$c_{LO} = 0.2$, $d_{LO} = 1.0$, $c_{TO} = -0.5$, $d_{TO} = 0.9$

Table 1. The modes and their assigned symmetry. The tensor elements correspond to the phonon modes for which the simulations were shown in Fig. 3 (the first mode in each table line).

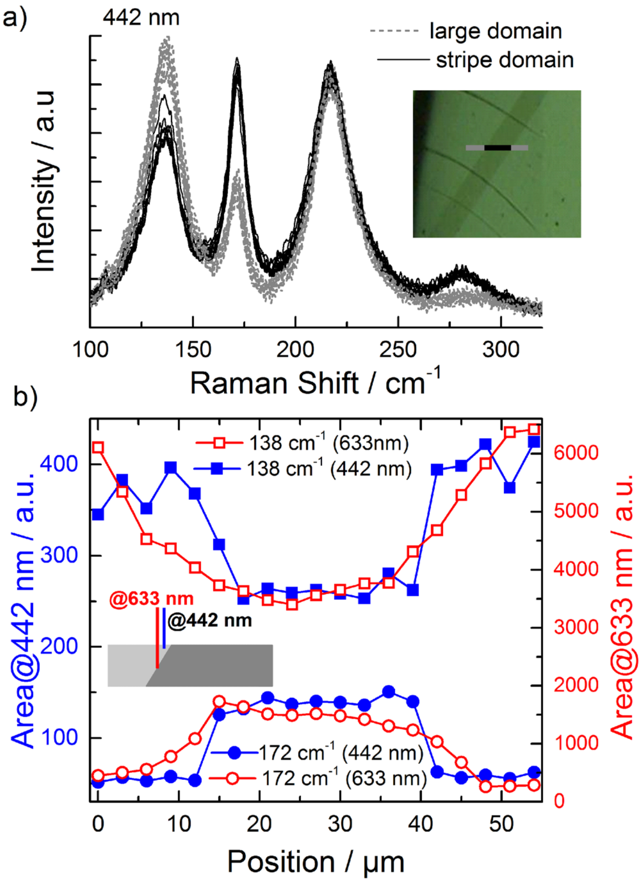

Figure 4. (**a**) Raman spectra measured using 442 nm in a line scan crossing the stripe domain. The spectra measured on the large domain are plotted by dashed lines, and those measured on the stripe domain by continuous lines. (**b**) The peak areas of the 138 cm^{-1} and 172 cm^{-1} modes show well separated stripe and large domains when measuring with 442 nm excitation line (full symbols). The interface region shows a continuous change in the peak areas when measuring with 633 nm excitation line (open symbols). The inset shows schematically the interface between the two domain types.

measurements were performed using both excitations in order to obtain depth information on the domain walls. Considering the low penetration depth of the light for 442 nm excitation these measurements are very sensitive to the surface of the sample. The spectra have been evaluated using a similar fitting procedure as for the azimuthal angle dependent measurements. In Fig. 4b) the peak areas for the modes at 138 cm^{-1} and 172 cm^{-1} are plotted by full symbols. It can be seen that the intensities (as peak areas) of these two peaks can be used to identify the two types of ferroelastic domains showing a sharp interface (in the limit of the 3 µm steps) between them.

The same measurement procedure was carried out in addition using the 633 nm laser as an excitation source. As discussed previously, the extinction coefficient is very low for this wavelength, thus the information depth is given by the focus depth (~7 µm). Under such conditions, the information obtained from the experiment is not limited to the surface of the sample, but stems also from the “bulk”. For this reason, the transition at the domain wall between the intensities (as peak areas) of the two Raman modes measured with 633 nm (open symbols in

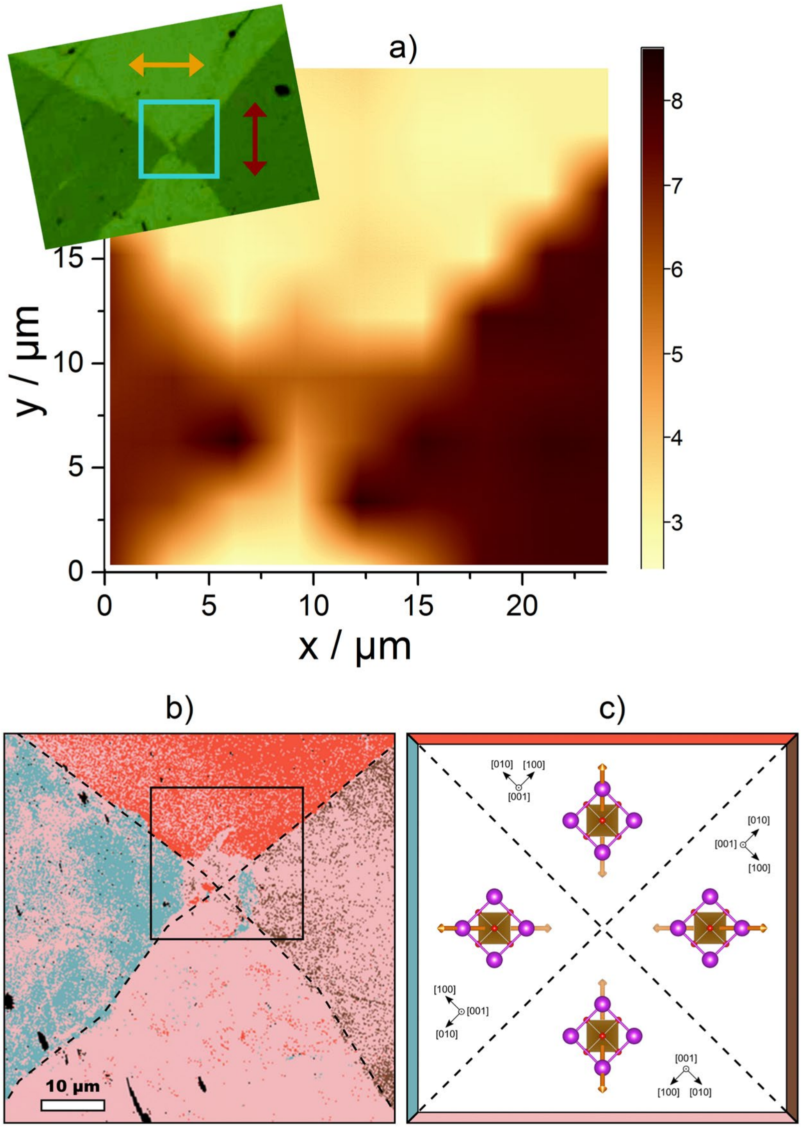

Figure 5. (**a**) Intensity of the 172 cm^{-1} mode shown as Raman map on an area of 24 µm × 24 µm (3 µm steps) indicated by the square in the polarisation microscopy image (in the top-left side). The arrows indicate the projections of the spontaneous polarisation on the sample surface. (**b**) Local EBSD map and (**c**) the corresponding idealized schematic domain structure. The domain boundaries are highlighted by dashed lines. The area marked in (**b**) by black square corresponds to the Raman map presented in (**a**). All four domains contain regions with crystallographically equivalent orientations. Different colours of the spots (red, brown, pink and blue) result from different local rhombohedral distortions that are associated with different orientations of the polarisation axis. The polarisation axes are depicted by orange arrows in figure (**c**), where also the dominant orientation variants are illustrated.

Fig. 4b)) is not as sharp as for the 442 nm excitation. This indicates that the interfaces between the two neighbouring domains are not vertical but inclined, as schematically shown in the inset of the figure. Such inclined domain walls are typically formed in the case of so called 71° domain pattern[10,34,43], as was confirmed by piezoresponse force microscopy (Fig. 1s, Supplementary Material). Thus, the Raman spectroscopy offers not only a tool for distinguishing between differently oriented ferroelastic domains in BFO crystals, but is also capable to supply information about the depth profile and shape of the domain interfaces if different excitation wavelengths are used.

The Raman line scans can easily be extended to two-dimensional Raman mapping. In the upper left part of the Fig. 5a) macroscopic ferroelastic domains forming a diagonally tiled structure are revealed by polarised light microscopy on another BFO sample. The arrows in the polarisation microscopy image correspond to the projection of the spontaneous polarisation for the two domain types on the sample surface and they are perpendicular to each other. Raman mapping on this sample was carried out on an area of 24 µm × 24 µm indicated by the square, with a step size of 3 µm between measurements using the 442 nm laser for excitation. Each single Raman spectrum was fitted as described previously. The integral intensity (peak area) of the 172 cm^{-1} peak, that shows 180° periodicity of the azimuthal angle dependence in VV polarisation in Fig. 3c), is plotted in the Fig. 5a) as a map. In the intensity map a very clear distinction between the two types of domains can be seen. The shape of the Raman map is very similar compared to that of the polarisation microscopy image, which shows again the capability of Raman spectroscopy to distinguish between different ferroelastic domains.

The results of the optical polarisation microscopy and the Raman map (Fig. 5a)) were supported by local EBSD measurements (Fig. 5b)). As the smallest MAD value was employed as the main criterion for the selection of the respective orientation variant by means of EBSD, the different colours stand for different local rhombohedral distortions of the pseudo-cubic cell of BFO that are associated with different macroscopic orientations of the polarisation axis $[111]_{pc}$. Generally, four different orientations of BFO were detected in the examined area (red, brown, pink and blue, see Fig. 5b)), which were assigned to domains with idealized orientations as shown in Fig. 5c). These domains are rotated by 0°, 90°, 180° and 270° with respect to a laboratory coordinate system. However, as the rhombohedral distortion is small and close to the resolution limit of EBSD, the domain assignment using MAD is complicated by various microstructure phenomena and defects. This leads to an apparent switching between individual orientations of the polarisation axis within a domain. Nevertheless, the domain structure pattern revealed by the EBSD measurement agrees well with the domain structure arrangement obtained from the polarisation microscopy image and from the Raman mapping, where the projected polarisation axes of the neighbouring and opposing domains were approximately perpendicular and parallel, respectively, cf. Fig. 5a). This finding is consistent with the domain structure, which is typically reported in the BFO domains having the surface orientation $\{001\}_{pc}$[33]. A good agreement between the EBSD map and polarisation microscopy image was achieved even in the interface regions with a complex domain structure. A small tail penetrating into the upper domain that was detected by the polarisation microscopy (Fig. 5a)) was also very well reproduced by the EBSD mapping (Fig. 5b)).

Conclusions

In summary, we present a general approach based on numerical simulations using the Raman tensor formalism combined with polarisation and azimuthal angle-dependent Raman measurements that is capable to identify the polar modes of mixed symmetries in a $(001)_{pc}$ oriented BFO single crystal unambiguously. This method can easily be extended to any crystal orientation. The intensities of some modes are sensitive to the arrangement (in-plane orientation) of the ferroelastic domains. The anisotropic 180° periodicity of the azimuthal angular dependence of their intensity in parallel polarisation can be used for quick identification of the domains and for mapping large domains in BFO, even though the spatial resolution and the scan velocity is low. An advantage of Raman mapping/line scans performed at different excitation wavelengths having different light penetration depths in BFO is the depth sensitivity of the information regarding the tilt of the domain walls relative to the surface.

References

1. Ramesh, R. & Spaldin, N. A. Multiferroics: progress and prospects in thin films. *Nat. Mater.* **6**, 21–29 (2007).
2. Catalan, G. & Scott, J. F. Physics and Applications of Bismuth Ferrite. *Adv. Mater.* **21**, 2463–2485 (2009).
3. Choi, T., Lee, S., Choi, Y. J., Kiryukhin, V. & Cheong, S.-W. Switchable Ferroelectric Diode and Photovoltaic Effect in $BiFeO_3$. *Science* **324**, 63–66 (2009).
4. Martin, L. W., Chu, Y. H. & Ramesh, R. Advances in the growth and characterization of magnetic, ferroelectric, and multiferroic oxide thin films. *Mater. Sci. Eng. R* **68**, 89–133 (2010).
5. Kubel, F. & Schmid, H. Structure of a Ferroelectric and Ferroelastic Monodomain Crystal of the Perovskite $BiFeO_3$. *Acta Cryst. B* **46**, 698–702 (1990).
6. Moreau, J. M., Michel, C., Gerson, R. & James, W. J. Ferroelectric $BiFeO_3$ X-Ray and neutron diffraction study. *J. Phys. Chem. Solids* **32**, 1315–1320 (1971).
7. Tomashpolskii, Y. Y., Venevtsev, Y. N. & Zhdanov, G. S. X-ray diffraction study of the atomic structure of ferromagnetic $BiFeO_3$. *Soviet Phys. crystallogr.* **12**, 209 (1967).
8. Zavaliche, F. *et al.* Ferroelectric domain structure in epitaxial $BiFeO_3$ films. *Appl. Phys. Lett.* **87**, 182912 (2005).
9. Zavaliche, F. *et al.* $BiFeO_3$ films: domain structure and polarization dynamics. *Phase Transition* **79**, 991–1017 (2006).
10. Yang, J. C., Huang, Y. L., He, Q. & Chu, Y. H. Multifunctionalities driven by ferroic domains. *J. Appl. Phys.* **116**, 066801 (2014).
11. Baek, S.-H., Choi, S., Kim, T. L. & Jang, H. W. Domain engineering in $BiFeO_3$ thin films. *Current Applied Physics* **17**, 688–703 (2017).
12. Iliev, M. N., Abrashev, N. V., Mazudmar, D., Shelke, V. & Gupta, A. Polarized Raman spectroscopy of nearly tetragonal $BiFeO_3$ thin films. *Phys. Rev. B* **82**, 014107 (2010).
13. Kreisel, J. *et al.* A phase transition close to room temperature in $BiFeO_3$ thin films. *J. Phys.: Condens. Matter* **23**, 342202 (2011).
14. Himcinschi, C. *et al.* Optical properties of epitaxial $BiFeO_3$ thin films grown on $LaAlO_3$. *Appl. Phys. Lett.* **106**, 012908 (2015).
15. Himcinschi, C., Guo, E.-J., Talkenberger, A., Dörr, K. & Kortus, J. Influence of piezoelectric strain on the Raman spectra of $BiFeO_3$ films deposited on PMN-PT substrates. *Appl. Phys. Lett.* **108**, 042902 (2016).
16. Haumont, R., Kreisel, J. & Bouvier, P. Raman scattering of the model multiferroic oxide $BiFeO_3$: effect of temperature, pressure and stress. *Phase Transitions* **79**, 1043–1064 (2006).
17. Singh, M. K., Jang, H. M., Ryu, S. & Jo, M.-H. Polarized Raman scattering of multiferroic $BiFeO_3$ epitaxial films with rhombohedral R3c symmetry. *Appl. Phys. Lett.* **88**, 042907 (2006).
18. Hermet, P., Goffinet, M., Kreisel, J. & Ghosez, P. Raman and infrared spectra of multiferroic bismuth ferrite from first principles. *Phys. Rev. B* **75**, 220102(R) (2007).
19. Claus, R., Merten, L. & Brandmüller, J. Light Scattering by Phonon-Polaritons, Springer, Berlin (1975).
20. Loudon, R. The Raman effect in crystals. *Advances in Physics* **13**, 423–482 (1964).
21. Alonso-Gutierrez, P. & Sanjuan, M.-L. Ordinary and extraordinary phonons and photons: Raman study of anisotropy effects in the polar modes of $MnGa_2Se_4$. *Phys. Rev. B* **78**, 045212 (2008).
22. Borodavka, F., Pokorny, J. & Hlinka, J. Combined piezoresponse force microscopy and Raman scattering investigation of domain boundaries in $BiFeO_3$ ceramics. *Phase Transitions* **89**, 746–751 (2016).
23. Fukumura, H. *et al.* Observation of phonons in multiferroic $BiFeO_3$ single crystals by Raman scattering. *J. Phys.: Condens. Matter* **19**, 365224 (2007).
24. Hlinka, J., Pokorny, J., Karimi, S. & Reaney, I. M. Angular dispersion of oblique phonon modes in BiFeO3 from micro-Raman scattering. *Phys. Rev. B* **83**, 020101(R) (2011).
25. Palai, R., Schmid, H., Scott, J. F. & Katiyar, R. S. Raman spectroscopy of single-domain multiferroic $BiFeO_3$. *Phys. Rev. B* **81**, 064110 (2010).

26. Porporati, A. A., Tsuji, K., Valant, M., Axelsson, A.-K. & Pezzotti, G. Raman tensor elements for multiferroic $BiFeO_3$ with rhombohedral R3c symmetry. *J. Raman Spectrosc.* **41**, 84–87 (2010).
27. Singh, M. K., Ryu, S. & Jang, H. M. Polarized Raman scattering of multiferroic $BiFeO_3$ thin films with pseudo-tetragonal symmetry. *Phys. Rev. B* **72**, 132101 (2005).
28. Beekman, C., Reijnders, A. A., Oh, Y. S., Cheong, S. W. & Burch, K. S. Raman study of the phonon symmetries in BiFeO3 single crystals. *Phys. Rev. B* **86**, 020403(R) (2012).
29. Sando, D. *et al.* Linear electro-optic effect in multiferroic $BiFeO_3$ thin films. *Phys Rev. B* **89**, 195106 (2014).
30. Sander, A., Christl, M., Chiang, C.-T., Alexe, M. & Widra, W. Domain imaging on multiferroic $BiFeO_3$(001) by linear and circular dichroism in threshold photoemission. *J. Appl. Phys.* **118**, 224102 (2015).
31. Kubel, F. & Schmid, H. Growth, twinning and etch figures of ferroelectric/ferroelastic dendritic BiFeO3 single domain crystals. *J. Cryst. Growth* **129**, 515–524 (1993).
32. Nolze, G., Hielscher, R. & Winkelmann, A. Electron backscatter diffraction beyond the mainstream. *Cryst. Res. Technol.* **52**, 1600252 (2017).
33. Streiffer, S. K. *et al.* Domain patterns in epitaxial rhombohedral ferroelectric films. I. Geometry and experiments. *J. Appl. Phys.* **83**, 2743 (1998).
34. Yang, M.-M., Bhatnagar, A., Luo, Z.-D. & Alexe, M. Enhancement of Local Photovoltaic Current at Ferroelectric Domain Walls in $BiFeO_3$. *Scientific Reports* **7**, 43070 (2017).
35. Weber, M. C. *et al.* Temperature evolution of the band gap in $BiFeO_3$ traced by resonant Raman scattering. *Phys. Rev. B* **93**, 125204 (2016).
36. Himcinschi, C. *et al.* Optical characterisation of BiFeO3 epitaxial thin films grown by pulsed-laser deposition. *phys. status solidi c* **7**, 296–299 (2009).
37. Himcinschi, C. *et al.* Substrate influence on the optical and structural properties of pulsed laser deposited $BiFeO_3$ epitaxial films. *J. Appl. Phys.* **107**, 123524 (2010).
38. Talkenberger, A. *et al.* Raman spectroscopic investigations of epitaxial $BiFeO_3$ thin films on rare earth scandate substrates. *J. Raman Spectrosc.* **46**, 1245–1254 (2015).
39. Yang, X., Lan, G., Li, B. & Wang, H. Raman Spectra and Directional Dispersion in $LiNbO_3$ and $LiTaO_3$. *phys. status solidi (b)* **141**, 287–300 (1987).
40. Martin, R. M. & Damen, T. C. Breakdown of Selection Rules in Resonance Raman Scattering. *Phys. Rev. Lett.* **26**, 86 (1971).
41. Martin, R. M. Theory of the One-Phonon Resonance Raman Effect. *Phys. Rev.* **B 4**, 3676 (1971).
42. Williams, P. F. & Porto, S. P. S. Symmetry-Forbidden Resonant Raman Scattering in Cu_2O. *Phys. Rev. B* **8**, 1782 (1973).
43. Domingo, N., Farokhiopoor, S., Santiso, J., Noheda, B. & Catalan, G. Domain wall magnetoresistance in $BiFeO_3$ thin films measured by scanning probe microscopy. *J. Phys.: Condens. Matter* **29**, 334003 (2017).
44. Momma, K. & Izumi, F. VESTA 3 for three-dimensional visualization of crystal, volumetric and morphology data. *J. Appl. Crystallogr.* **44**, 1272–1276 (2011).
45. Doig, K. I. *et al.* Coherent magnon and acoustic phonon dynamics in tetragonal and rare-earth-doped $BiFeO_3$ multiferroic thin films. *Phys. Rev. B* **88**, 094425 (2013).

Acknowledgements

We thank the German Research Foundation (DFG) for supporting these investigations within the Collaborative Research Centre 920 "Multi-Functional Filters for Metal Melt Filtration – A Contribution towards Zero Defect Materials", subprojects A04 and A05. C.R. acknowledges the financial support by European Social Fond (ESF), the Saxonian Government (grant no. 100231954). EPSRC support through grants EP/P0331544/1 and EP/P025803/1 is also acknowledged. M.A. likes to acknowledge the support of Royal Society through Wolfson Research and Theo Murphy "Blue Sky" Awards.

Author Contributions

C.H. proposed the study, performed and analysed the Raman mappings and wrote the manuscript with important contributions from all other authors. J.R. performed and analysed the azimuthal angle dependent Raman measurements and the line scans. C.R. designed the algorithm for the Raman tensor simulations. M.R. and D.R. performed and analysed the EBSD measurements contributing with writing the EBSD part of the paper. M.M. and M.A. provided the samples and characterized them with piezoresponse force microscopy. J.K. reviewed the manuscript. All authors discussed the results and commented on the paper.

Additional Information

Supplementary information accompanies this paper at https://doi.org/10.1038/s41598-018-36462-5.

Competing Interests: The authors declare no competing interests.

Phys. Status Solidi RRL **11**, No. 3, 1600350 (2017) / **DOI** 10.1002/pssr.201600350

pss +++rapid research letters+++
www.pss-rapid.com

Structure and orbital ordering of ultrathin $LaVO_3$ probed by atomic resolution electron microscopy and Raman spectroscopy

Ionela Lindfors-Vrejoiu[*, 1], Lei Jin[2], Cameliu Himcinschi[*, 3], Johannes Engelmayer[1], Felix Hensling[4], Chun-Lin Jia[2], Rainer Waser[4], Regina Dittmann[4], and Paul H. M. van Loosdrecht[1]

[1] II. Physikalisches Institut, Universität zu Köln, Zülpicher Str. 77, 50937 Köln, Germany
[2] Peter Grünberg Institut (PGI-5) and Ernst Ruska-Centre for Microscopy and Spectroscopy with Electrons (ER-C), Forschungszentrum Jülich GmbH, 52425 Jülich, Germany
[3] Institut für Theoretische Physik, TU Bergakademie Freiberg, Leipziger Str. 23, 09596 Freiberg, Germany
[4] Peter Grünberg Institut (PGI-7), Forschungszentrum Jülich GmbH, 52425 Jülich, Germany

Received 14 October 2016, revised 2 January 2017, accepted 9 January 2017

Keywords $LaVO_3$, perovskites, phase transitions, structure, orbital ordering, thin films, Raman spectroscopy, electron microscopy

---

[*] Corresponding authors: e-mail vrejoiu@ph2.uni-koeln.de, Phone: +49 221 470 1710, himcinsc@physik.tu-freiberg.de, Phone: +49 373 139 2862

Orbital ordering has been less investigated in epitaxial thin films, due to the difficulty to evidence directly the occurrence of this phenomenon in thin film samples. Atomic resolution electron microscopy enabled us to observe the structural details of the ultrathin $LaVO_3$ films. The transition to orbital ordering of epitaxial layers as thin as ≈4 nm was probed by temperature-dependent Raman scattering spectroscopy of multilayer samples. From the occurrence and temperature dependence of the 700 cm^{-1} Raman active mode it can be inferred that the structural phase transition associated with orbital ordering takes place in ultrathin $LaVO_3$ films at about 130 K.

1 Introduction Orbital ordering is a fascinating ordering phenomenon, which has been largely studied in bulk single crystals with perovskite structure, such as $LaVO_3$. Mott–Hubbard insulator $LaVO_3$ exhibits almost concomitant spin ordering (C-type antiferromagnetic) and G-type orbital ordering along with a structural change from orthorhombic to monoclinic below ≈140 K [1–3].

More measurement techniques can be readily employed for probing orbital ordering in bulk samples. Investigations of phase transitions and especially of orbital ordering in thin film samples are often rendered very difficult by the hindering and often dominant contributions of the substrates. Temperature-dependent Raman scattering investigations of $LaVO_3$ (and other RVO_3) single crystals were performed in great detail, in order to study the coupling between structure and electronic properties in the spin (SO) and orbital ordered (OO) states [3–6]. Below $T_{OO} \approx 140$ K, the oxygen stretching mode arising from the crystal distortion coupled with the G-type OO contributes to the Raman scattering spectra around 700 cm^{-1} and serves as a very convenient way to probe the occurrence of the OO phase transition. Recently by temperature-dependent Raman scattering spectroscopy we probed and evidenced the transition to orbital ordering in relatively thick (55 nm) epitaxial $LaVO_3$ film samples grown by pulsed-laser deposition (PLD) on various single crystal substrates [7]. Here we address whether the orbital ordering and the structural phase transition occur also in ultrathin epitaxial films, as thin as about 4 nm. Commonly structural phase transitions are inhibited in epitaxial films, especially ultrathin ones, grown on dissimilar substrates, because of strain and structural accommodation effects. For example Raman investigations of epitaxial films of $BaTiO_3$ revealed them to remain in the same ferroelectric tetragonal phase down to 5 K, despite the fact that $BaTiO_3$ has two structural phase transitions to orthorhombic (at

278 K) and rhombohedral (at 183 K) structure [8, 9]. For $La_{0.7}Sr_{0.3}MnO_3/SrTiO_3$ epitaxial multilayers Raman spectroscopy could reveal that a structural change from the expected rhombohedral structure of the bulk to orthorhombic was undergone by the $La_{0.7}Sr_{0.3}MnO_3$ layers [10].

Raman spectroscopy investigations of ultrathin films is however very difficult, due to the very low volume of material interacting and Raman scattering the incident laser light. In order to have a larger total volume of $LaVO_3$, we have fabricated multilayers in which the ultrathin $LaVO_3$ layers were sandwiched between layers that are expected to be Raman inactive and thus do not contribute to the measured Raman scattering signal. We used a material that is chemically compatible and structurally similar to $LaVO_3$, and can be grown under very similar conditions by PLD, namely $La_{0.75}Sr_{0.25}VO_3$. In $La_{1-x}Sr_xVO_3$ single crystals the substitution with Sr for $x > 0.18$ results in an insulator to metal transition and melting of the G-type OO. Furthermore, for $x \geq 0.26$ the material becomes orbital-disordered, paramagnetic metallic at all temperatures, and undergoes a structural change of the orthorhombic distortion towards cubic structure, with a tolerance factor t approaching closely $t = 1$ (i.e., $t \approx 0.97$ for $x = 0.25$) [11, 12]. This structural change makes it inactive for first order Raman scattering. Raman spectroscopy of $Nd_{1-x}Sr_xVO_3$ single crystals, for $x > 0.12$, allowed to infer that the orbital ordering was destroyed, because the characteristic Raman peak (at $\approx 700\ \mathrm{cm}^{-1}$) corresponding to the structural phase transition and to orbital ordering was not observed down to 5 K [12].

The microstructure of epitaxial multilayers similar to what we investigated here, namely superlattices combining orthorhombic $LaVO_3$ with cubic $SrVO_3$, was studied in detail [13, 14]. The evolution of the oxygen octahedral rotations across the $LaVO_3/SrVO_3$ superlattices grown on cubic $SrTiO_3(100)$ was observed by means of synchrotron X-ray diffraction. The $LaVO_3$ layers were 6 unit cells thick and the $SrVO_3$ layer thickness was varied between 1 and 6 unit cells [15]. It was found that the oxygen octahedra rotations in $LaVO_3$ were gradually suppressed when the $SrVO_3$ layer thickness increased to 6 unit cells, ultimately resulting in severe structural changes of the $LaVO_3$ adjacent layers. Therefore, here we chose to study superlattices grown on orthorhombic $LaGaO_3$ substrates. We also used for the multilayer *almost* cubic $La_{0.75}Sr_{0.25}VO_3$ rather than cubic $SrVO_3$, in order to prevent to a larger extent the possible suppression of octahedral tilts of the ultrathin $LaVO_3$ layers.

2 Experimental methods Epitaxial films and multilayers were fabricated by PLD using a KrF excimer laser for laser ablation, as we previously reported [7]. Twinned $LaGaO_3(110)/(001)_O$ single crystal substrates were employed for the epitaxial growth. A multilayer with 20 layers of nominally 10 unit cells thick $LaVO_3$ and 7 unit cells thick $La_{0.75}Sr_{0.25}VO_3$ was made under the same growth conditions as the bare films [7]. $LaGaO_3$ substrates (pseudocubic $a_{pc} = 3.88$ Å) are a good choice because of the very good lattice match with both $LaVO_3$ ($a_{pc} = 3.925$ Å) and $La_{0.75}Sr_{0.25}VO_3$ ($a_{pc} = 3.896$ Å) at room temperature (RT) [7, 11, 16]. Moreover, $LaGaO_3$ is suitable for Raman scattering spectroscopy of $LaVO_3$ films as it has no Raman active modes and has low background in the vicinity of the main Raman bands of $LaVO_3$ [17]. Cross-sectional lamellar samples for (scanning) transmission electron microscopy ((S)TEM) studies were prepared by focused ion beam milling using an FEI Helios Nanolab 400 s dual-beam system [18], followed by an Ar ion milling by a Bal-Tec Res-120 system. High-angle annular dark-field (HAADF) imaging and energy dispersive X-ray spectroscopy (EDS) mapping were performed at 200 kV on an FEI Titan 80–200 ChemiSTEM microscope [19]. Negative spherical aberration imaging (NCSI) was carried out using an FEI Titan 80–300 microscope operated at 300 kV [20].

Raman scattering spectra were recorded in back-scattering configuration using an Horiba–Jobin–Yvon Labram HR 800 spectrometer equipped with an Olympus Microscope, a 600 grooves/mm grating, and a Peltier cooled CCD detector. For excitation the 632.8 nm (1.96 eV) line of a HeNe laser was used. The beam was focused on the sample (spot size ≈2.5 μm) and collected through a 50× magnification long distance microscope objective (numerical aperture NA = 0.55). The laser power at the sample was kept below 1.5 mW. Temperature-dependent Raman measurements from 90 K up to RT were carried out with a Linkam THMS-600 cooling-heating stage placed under the Raman microscope [21]. At each temperature two measurements were made: for the first measurement the laser was focused at the sample surface (film plus substrate signal); during the second, the laser was focused about 30 μm under the sample surface (substrate signal). As-measured Raman spectroscopy data are shown in the supplementary online material (SOM) (Fig. S1). The Raman scattering signal belonging to the epitaxial films or multilayers was obtained by normalizing the two spectra and their subsequent subtraction [7].

3 Results and discussion The microstructure of the $LaVO_3/La_{0.75}Sr_{0.25}VO_3$ multilayer was investigated by HAADF-STEM and EDS. Figure 1(a) shows a low magnification HAADF-STEM micrograph of the multilayer. Figure 1(b) shows a zoom-in of the multilayer in a region where the twinned $LaGaO_3$ substrate was found to be in the $(001)_O$ orientation, as derived from the analysis of the fast Fourier transform (FFT) of a substrate image, shown at the bottom right of Fig. 1(b). The micrograph shown in Fig. 1(b) allows to observe domains of the multilayer with the long c-axis ($[001]_O$) of the $LaVO_3$ oriented in the plane of the substrate, but in two perpendicular directions indicated on the micrograph (see SOM, Fig. S2). These two directions could be assigned from the analysis of the two different FFT patterns (see insets) [7], considering the positions of the extra spots yielded by an orthorhombic Pbnm structure (marked by the white hollow arrows shown on the FFT patterns). Because the $La_{0.75}Sr_{0.25}VO_3$ layers are

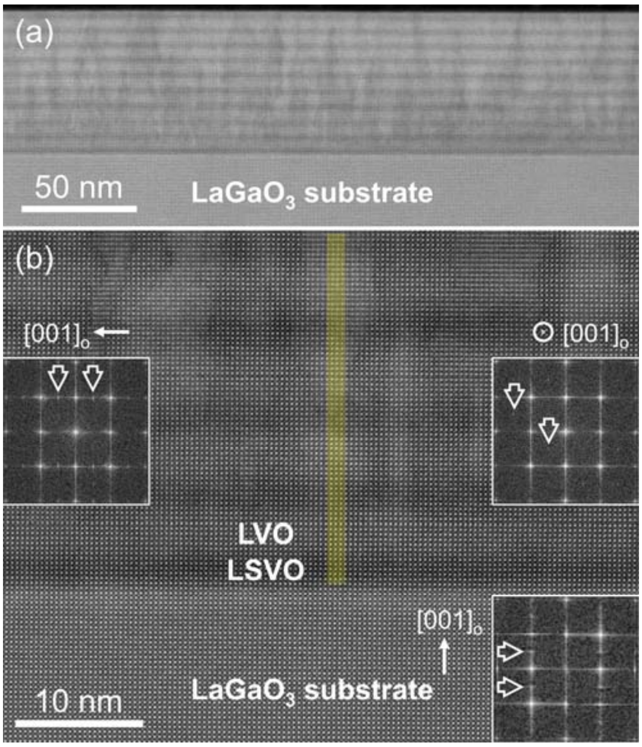

Figure 1 Scanning transmission electron microscopy investigations of the $LaVO_3$ (LVO)/$La_{0.75}Sr_{0.25}VO_3$ (LSVO) multilayer: (a) low magnification HAADF-STEM overview image; (b) high magnification HAADF-STEM image, showing two domains with two different in-plane $[001]_O$ orientations (orthorhombic *c*-axis in the plane of the $LaGaO_3$ substrate, but with two different orientations (90° rotated). The yellow line marks the domains boundary. The FFTs of images taken in the two neighbouring domains and in the substrate area are also included as insets. The arrows in FFTs mark the extra spots yielded by an orthorhombic Pbnm structure.

almost cubic (*vide infra*), they cannot yield these extra spots. Antiphase boundaries are present in the multilayer, starting from the top layer and propagating towards the substrate, as observed for bare $LaVO_3$ films too [7]. Chemical elemental analysis based on EDS of the multilayer is shown in Fig. 2. It allows to ascertain that Sr was incorporated mainly in the nominally $La_{0.75}Sr_{0.25}VO_3$ layers (Fig. 2b), with corresponding less La signal in the $La_{0.75}Sr_{0.25}VO_3$ layers as compared to the nominally $LaVO_3$ layers (Fig. 2c and d). Vanadium signal was uniform across the entire heterostructure (Fig. 2e) and Ga signal was detected only in the $LaGaO_3$ substrate area (Fig. 2f). The interfaces are affected by A-site intermixing: by EDS analysis (Fig. 2b and d) Sr was found also beyond the nominal thickness of the $La_{0.75}Sr_{0.25}VO_3$ layers. Uneven interfaces due to preferential surface diffusion and segregation of Sr were observed in $LaVO_3$/$SrTiO_3$ superlattices as well [22].

The structure of the $LaVO_3$ and $La_{0.75}Sr_{0.25}VO_3$ layers was investigated at atomic scale by NCSI technique. The aim of the analysis was to map the tilt of the LaO and $La_{0.75}Sr_{0.25}O$ planes in the two types of layers at RT. The expectation was that the $LaVO_3$ layers, having orthorhombic [2, 5] or rather slightly monoclinically-distorted structure [23], exhibit tilted LaO planes, whereas the tilts should be much smaller or rather absent in $La_{0.75}Sr_{0.25}VO_3$ layers. In Fig. 3(a) a typical NCSI micrograph taken across a few adjacent layers is shown. The tilt of the LaO/$La_{0.75}Sr_{0.25}O$ planes was analyzed for the entire image and a quantitative map was drawn as shown in Fig. 3(b). The lengths of the arrows scales with α (given in degrees). Inside the $LaVO_3$ layers the LaO planes have sizable values of the tilt angle α (for the definition of α see the magenta solid lines and the schematic at the bottom right in Fig. 3(a)). The sign of α as denoted by the red versus blue colour alternates in adjacent unit cells in the x direction (i.e., || $[001]_O$), yielding a zig-zag structure specific to orthorhombic Pbnm, in agreement also with the FFT patterns shown in Fig. 1(b).

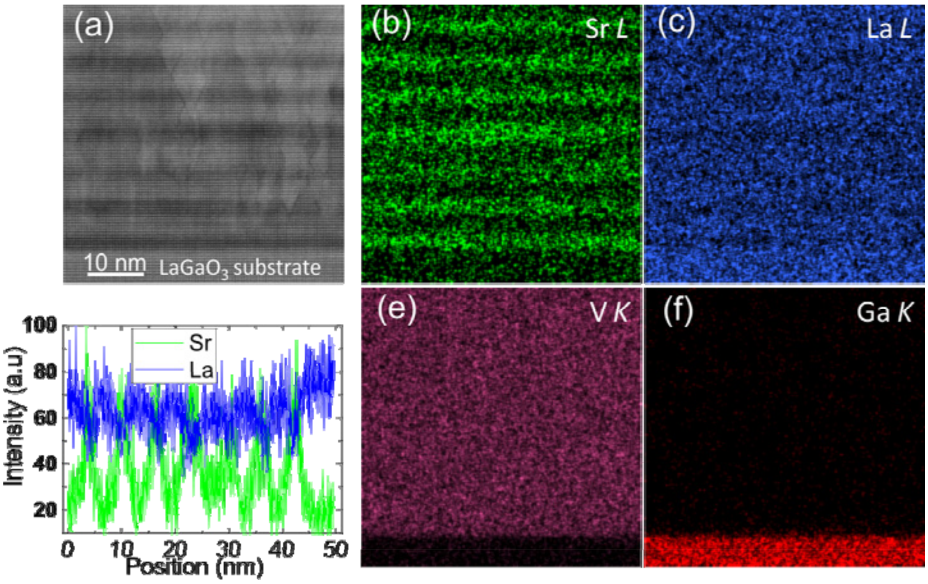

Figure 2 EDS elemental analysis performed during scanning transmission electron microscopy imaging of the $LaVO_3$/$La_{0.75}Sr_{0.25}VO_3$ multilayer: (a) a typical HAADF-STEM image and its corresponding elemental maps for (b) Sr, (c) La, (e) V and (f) Ga. In (d) the intensity profiles for Sr and La across several layers are shown.

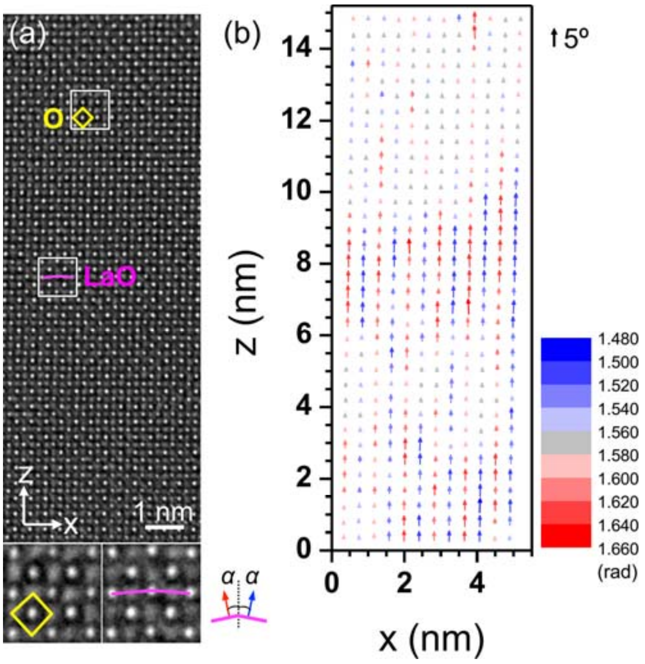

Figure 3 NCSI analysis of the $LaVO_3/La_{0.75}Sr_{0.25}VO_3$ multilayer at RT. (a) A typical NCSI micrograph, comprising about four adjacent $LaVO_3$ and $La_{0.75}Sr_{0.25}VO_3$ layers from the top (z is the growth direction and $x \parallel [001]_O$). (b) Two dimensional map of the LaO plane tilt, corresponding to the NCSI image in (a). The length of the arrows scales with the value of α in degrees (color bar in radians, 1.571 corresponds to $\pi/2$, grey zone). The black arrow at the top right corner of (b) is equivalent to $\alpha = 5°$. The alternate red-blue sizable arrows indicate zig-zag tilts of the LaO plane, specific to the orthorhombic $LaVO_3$ structure (see the magenta solid tilted lines marked on the micrograph and plotted again at bottom right of (a)). $\alpha = 0$ corresponds to a structure with non-tilted LaO planes (see the yellow marked oxygen octahedron fingerprint at bottom left in (a)).

The angle α decreases across the interfaces with the $La_{0.75}Sr_{0.25}VO_3$ layers and it is zero in the middle of the $La_{0.75}Sr_{0.25}VO_3$ layers, as expectable for the *almost* cubic structure, with *almost* straight oxygen octahedra (see the marked yellow oxygen octahedron in Fig. 3(a)). Thus at RT the core of the $LaVO_3$ layers has preserved an orthorhombic structure and the core of the $La_{0.75}Sr_{0.25}VO_3$ layers an *almost* cubic structure, while the interfaces between the two type of layers, which are also affected by Sr intermixing, have an intermediary structure between orthorhombic-like and *almost* cubic.

The subtracted Raman scattering spectra of the multilayer measured at temperatures between RT and 90 K allowed the observation of several Raman bands that can be assigned to the $LaVO_3$ layers. The most important in our study are the bands at $\approx 500\ \mathrm{cm}^{-1}$ and at $\approx 700\ \mathrm{cm}^{-1}$ (marked by the dashed vertical lines) (Fig. 4(a)). In bulk these bands are both related to the structural phase transition and to the orbital ordering in $LaVO_3$, below ≈ 140 K [3–7, 12]. In particular, the band at $700\ \mathrm{cm}^{-1}$ corresponds to an out-of-phase oxygen stretching mode along the orthorhombic c-axis, which has a B_{1g} symmetry in the orthorhombic phase and an A_g symmetry in the monoclinic phase that is G-type OO [3–7, 12, 24]. In the Raman spectra of the $LaVO_3/La_{0.75}Sr_{0.25}VO_3$ multilayer the intensity of this band has a marked increase below ≈ 130 K. This marked increase of the Raman signal is better seen in Fig. 4(b), where the temperature dependence of the Raman intensity for the $700\ \mathrm{cm}^{-1}$ band is plotted. For the integration the Raman signal was fitted with a Lorentzian oscillator at each temperature, and the plotted integrated signal in Fig. 4(b) represents the area under the fitted Lorentzian. The temperature dependence of the Raman intensity is very similar to the temperature dependence we observed for the same Raman mode of epitaxial $LaVO_3$ films (55 nm thick) grown on $DyScO_3$ and $LaGaO_3$ substrates [7], indi-

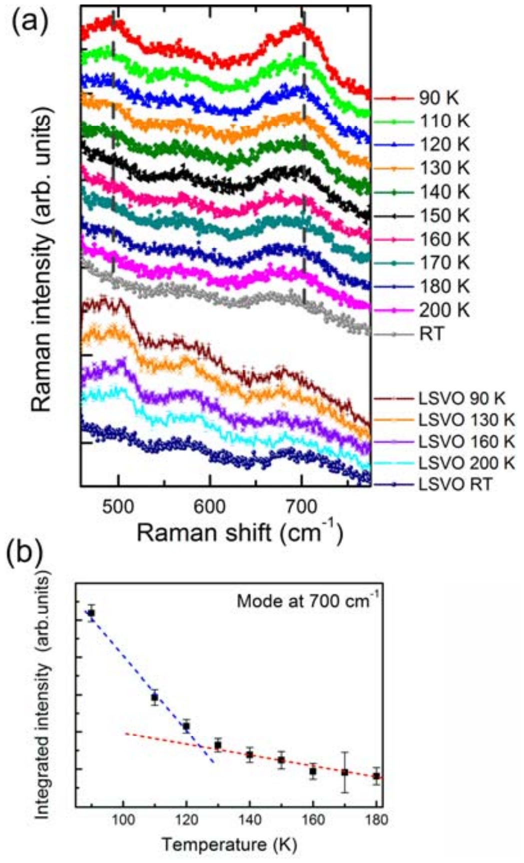

Figure 4 Temperature-dependent Raman spectra of the $LaVO_3/La_{0.75}Sr_{0.25}VO_3$ multilayer, (a) after subtracting the Raman scattering contribution of the $LaGaO_3$ substrate. In (a) for the sake of comparison, the Raman spectra of a 50 nm thick $La_{0.75}Sr_{0.25}VO_3$ (LSVO) film are displayed in the lower part of the graph. The vertical dashed lines mark the position of the two Raman bands that are used for observing the orbital ordering phase transition of $LaVO_3$. The spectra were given a vertical offset for clarity. In (b) the integrated intensity of the mode at $\approx 700\ \mathrm{cm}^{-1}$ is plotted, after subtracting the Raman scattering signal measured at RT and evaluating the data by using Lorentzian fits (the straight red and blue dashed lines are guides for the eye).

cating that OO sets in the $LaVO_3$ layers of the multilayer sample below ≈130 K. In contrast to single crystal samples [3–6] that can be achieved in a single domain state, the phase transition of thin epitaxial $LaVO_3$ films is affected by the influence of the epitaxial growth conditions that lead to strain effects, domain formation and accommodations of the oxygen octahadra rotation patterns (see the SOM). Due to the unavoidable formation of domains of different orientations of the $[001]_O$ axis in epitaxial layers [7, 23] (see Fig. 1 and also Fig. S2), our multilayer has mixed orientations of the *c*-axis of the $LaVO_3$ layers, of undetermined fractions. However, these domains of different orientation preserve epitaxial relationship to the $LaGaO_3$ substrate. Despite all these additional effects present in epitaxial $LaVO_3$, the orbital ordering/structural phase transition is quite robust, being not suppressed in ultrathin layers grown on substrates with Pbnm structure (see also SOM). In Fig. 4(a), for comparison we show also the Raman spectra acquired for a $La_{0.75}Sr_{0.25}VO_3$ epitaxial layer (50 nm thick), grown also on $LaGaO_3$. In the Raman spectra of the $La_{0.75}Sr_{0.25}VO_3$ at RT there are very weak and very broad bands at about 505 cm^{-1} and 685 cm^{-1}, which persist in the spectra down to 90 K, without any detectable increase of intensity or Raman shift changes (Fig. 4(a)). This indicates that no structural phase transition occurs down to 90 K in the 50 nm thick epitaxial $La_{0.75}Sr_{0.25}VO_3$ film, in agreement with the behaviour of bulk $La_{0.75}Sr_{0.25}VO_3$ [1, 11, 12]. This is supported also by resistivity measurements as a function of temperature of the $La_{0.75}Sr_{0.25}VO_3$ film grown on $LaGaO_3$ (not shown here), which showed no indication of a phase transition and had metallic conductivity down to at least 30 K, similar to the bulk [1, 11, 12]. We infer that the temperature-dependent behaviour of the Raman band from 700 cm^{-1} in the spectra of the $LaVO_3/La_{0.75}Sr_{0.25}VO_3$ multilayer can be attributed solely to the structural phase transition accompanied by orbital ordering undergone by the $LaVO_3$ layers. The other Raman band that is related to the orbital ordering of $LaVO_3$ and occurs at ≈500 cm^{-1} also starts developing below ≈140 K in our spectra (Fig. 4(a)). For the measurements of the multilayer sample the band at 500 cm^{-1} has much weaker intensity with respect to the 700 cm^{-1} band. This is likely related to the different symmetries of these two Raman active modes, which result in strong dependence on the light polarization configurations with respect to the *c*-axis orientation of $LaVO_3$, as discussed in [3–5, 7, 12, 24].

4 Conclusion

In summary, by atomic resolution transmission electron microscopy investigations we demonstrated that ultrathin epitaxial $LaVO_3$ layers grown on $LaGaO_3$ substrates preserve an orthorhombic-like structure at room temperature. Furthermore, temperature-dependent Raman scattering spectroscopy enabled us to probe the structural and orbital ordering transition and observe the occurrence of the 700 cm^{-1} Raman active mode at ≈130 K in 4 nm thin $LaVO_3$, which is indicative of the phase transition. This is in contrast to the behaviour of other ultrathin epitaxial perovskite films, which do not undergo the structural phase transitions exhibited by the bulk compounds [9].

Supporting Information Additional supporting information may be found in the online version of this article at the publisher's website.

Acknowledgements We thank Lena Bussmann for assistance with some of the Raman measurements and Doris Meertens for (S)TEM sample preparation.

References

[1] S. Miyasaka, T. Okudo, and Y. Tokura, Phys. Rev. Lett. **85**, 5388 (2000).

[2] P. Horsch, A. M. Oleś, L. F. Feiner, and G. Khaliullin, Phys. Rev. Lett. **100**, 167205 (2008).

[3] S. Miyasaka, Y. Okimoto, M. Ywama, and Y. Tokura, Phys. Rev. B **68**, 100406(R) (2003).

[4] S. Miyasaka, S. Onodo, Y. Okimoto, J. Fujioka, M. Ywama, N. Nagaosa, and Y. Tokura, Phys. Rev. Lett. **94**, 076405 (2005).

[5] S. Miyasaka, J. Fujioka, M. Ywama, Y. Okimoto, and Y. Tokura, Phys. Rev. B **73**, 224436 (2006).

[6] B. Roberge, S. Jandl, A. A. Nugruho, T. T. M. Palstra, L. D. Tung, and G. Balakrishnan, J. Raman Spectrosc. **46**, 1157 (2015).

[7] I. Vrejoiu, C. Himcinschi, L. Jin, C.-L. Jia, N. Raab, J. Engelmayer, R. Waser, R. Dittmann, and P. H. M. van Loosdrecht, APL Materials **4**, 046103 (2016).

[8] D. A. Tenne, X. X. Xi, Y. L. Li, L. Q. Chen, A. Soukiassian, M. H. Zhu, A. R. James, J. Lettieri, D. G. Schlom, W. Tian, and X. Q. Pan, Phys. Rev. B **69**, 174101 (2004).

[9] D. A. Tenne, A. Bruchhausen, N. D. Lanzillotti-Kimura, A. Fainstein, R. S. Katiyar, A. Cantarero, A. Soukiassian, V. Vaithyanathan, J. H. Haeni, W. Tian, D. G. Schlom, K. J. Choi, D. M. Kim, C. B. Eom, H. P. Sun, X. Q. Pan,Y. L. Li, L. Q. Chen, Q. X. Jia, S. M. Nakhmanson, K. M. Rabe, and X. X. Xi , Science **313**, 5793 (2006).

[10] J. Kreisel, G. Lucazeau, C. Dubourdieu, M. Rosina, and F. Weiss, J. Phys.: Condens. Matter **14**, 5201 (2002).

[11] A. V. Mahajan, D. C. Johnston, D. R. Torgeson, and F. Borsa, Phys. Rev. B **46**, 10973 (1992).

[12] J. Fujioka, S. Miyasaka, and Y. Tokura, Phys. Rev. B **72**, 024460 (2005).

[13] P. Boullay, A. David, W. C. Sheets, U. Lüders, W. Prellier, H. Tan, J. Verbeeck, G. Van Tendeloo, C. Gatel, G. Vincze, and Z. Radi, Phys. Rev. B **83**, 125403 (2011).

[14] H. Tan, R. Egoavil, A. Béché, G. T. Martinez, S. Van Aert, J. Verbeeck, G. Van Tendeloo, H. Rotella, P. Boullay, A. Pautrat, and W. Prellier, Phys. Rev. B **88**, 155123 (2013).

[15] U. Lüders, Q.-R. Li, R. Feyerherm, and E. Dudzik, J. Phys. Chem. Solids **75**, 1354 (2014).

[16] L. Hu, X. Luo, K. J. Zhang, X. W. Tang, L. Zu, X. C. Kan, L. Chen, X. B. Zhu, W. H. Song, J. M. Dai, and Y. P. Sun, Appl. Phys. Lett. **105**, 111607 (2014).

[17] L. Gasparov, T. Jegorel, L. Loetgering, S. Middey, and J. Chakhalian, J. Raman Spectrosc. **45**, 465 (2014).

[18] D. Meertens, M. Kruth, and K. Tillmann, J. Large-Scale Res. Facil. **2**, A60 (2016).

[19] A. Thust, J. Barthel, and K. Tillmann, J. Large-Scale Res. Facil. **2**, A41 (2016).
[20] A. Kovács, R. Schierholz, and K. Tillmann, J. Large-Scale Res. Facil. **2**, A43 (2016).
[21] C. Himcinschi, I. Vrejoiu, T. Weissbach, K. Vijayanandhini, A. Talkenberger, C. Röder, S. Bahmann, D. R. T. Zahn, A. A. Belik, D. Rafaja, and J. Kortus, J. Appl. Phys. **110**, 073501 (2011).
[22] L. Fitting Kourkoutis, D. A. Muller, Y. Hotta, and H. Y. Hwang, Appl. Phys. Lett. **91**, 163101 (2007).
[23] H. Rotella, O. Copie, G. Steciuk, H. Ouerdane, P. Boullay, P. Rousse, M. Morales, A. David, A. Pautrat, B. Mercey, L. Lutterotti, D. Chateigner, and W. Prellier, J. Phys.: Condens. Matter **17**, 175001 (2015).
[24] E. Sirandi, D. Lampakis, D. Pallas, E. Liaorokapis, and T. T. M. Palstra, J. Phys.: Conf. Ser. **150**, 042184 (2009).

Influence of piezoelectric strain on the Raman spectra of $BiFeO_3$ films deposited on PMN-PT substrates

Cameliu Himcinschi,[1,a)] Er-Jia Guo,[2,3,4] Andreas Talkenberger,[1] Kathrin Dörr,[2,3] and Jens Kortus[1]

[1]*TU Bergakademie Freiberg, Institute of Theoretical Physics, 09596 Freiberg, Germany*
[2]*Institute of Physics, Martin-Luther-University Halle-Wittenberg, 06099 Halle, Germany*
[3]*Institute for Metallic Materials, IFW Dresden, 01069 Dresden, Germany*
[4]*Quantum Condensed Matter Division, Oak Ridge National Laboratory, Oak Ridge, Tennessee 37830, USA*

(Received 2 November 2015; accepted 15 January 2016; published online 27 January 2016)

$BiFeO_3$ epitaxial thin films were deposited on piezoelectric $0.72Pb(Mg_{1/3}Nb_{2/3})O_3$-$0.28PbTiO_3$ (PMN-PT) substrates with a conductive buffer layer ($La_{0.7}Sr_{0.3}MnO_3$ or $SrRuO_3$) using pulsed laser deposition. The calibration of the strain values induced by the electric field applied on the piezoelectric PMN-PT substrates was realised using X-Ray diffraction measurements. The method of piezoelectrically induced strain allows one to directly obtain a quantitative correlation between the strain and the shift of the Raman-active phonons. This is a prerequisite for making Raman scattering a strong tool to probe the strain coupling in multiferroic nanostructures. Using the Poisson's number for $BiFeO_3$, one can determine the volume change induced by strain, and therefore the Grüneisen parameters for specific phonon modes. © *2016 AIP Publishing LLC*.

[http://dx.doi.org/10.1063/1.4940973]

It has recently been shown that strain engineering is a powerful method to control physical properties of oxide thin films having a perovskite or a spinel structure.[1,2] The usual way to induce different strains in thin films is the growth of films on single crystal substrates with different lattice mismatches. The disadvantage when using this path is that a series of extrinsic factors, for example, different thicknesses, the crystalline quality of the substrates, the growth method, the stoichiometry, or the growth induced disorder can affect the epitaxy and the substrate-film strain transfer. As an alternative way of strain engineering, a piezoelectric component in multiferroic thin film nanostructures is often employed to induce electrically controlled strain in an adjacent magnetostrictive component, thereby causing a large magnetoelectric effect. The structural modification induced by strain is often difficult to assess, especially in the nanostructured films. However, its characterization is vital for understanding the local magnetoelectric coupling. Raman spectroscopy is an established method to detect subtle structural changes, in particular, slight deviations from cubic structure as occurring in the class of oxides with perovskite structure.[3–8]

In order to avoid possible influence of extrinsic factors on the strain and the Raman shifts, piezoelectric single crystal substrates (as, for example, $[Pb(Mg_{1/3}Nb_{2/3})O_3]$-$PbTiO_3$ (PMN-PT)) with large piezoelectric coefficients can be employed to control the in-plane strain of thin films. In this case, the lattice strain can be reversibly modulated using the piezoelectric effect of the substrate and, if the films are epitaxially grown, this strain can be transferred to the epitaxial films. $(1-x)$PMN-xPT with a concentration near to the morphotropic phase boundary at $x \sim 0.3$ possesses excellent piezoelectric activity[9–11] (piezoelectric strain coefficients of thousands of pm/V),[12] having a perovskite structure with lattice constant of 4.02 Å.[13] The PMN-PT substrates used have a monoclinic M_A structure,[14] with the polarization along one of the pseudocubic space diagonals, so that the poled crystals contain a stable domain configuration with four domain variants. For $x = 0.28$, the biaxial strain of the pseudoquadratic surface lattice is rather uniform as shown by X-ray diffraction (XRD), enabling meaningful quantification of strain effects.[14]

The large piezo-strain of the PMN-PT substrates and the elastic coupling at the film-substrate interface was used to tune the magnetisation, the Curie temperature,[15–17] and the transport properties of rare-earth manganates.[18]

In this work, we used piezoelectric PMN-PT substrates. By means of an external electric field, the strain in epitaxial $BiFeO_3$ (BFO) films was accurately calibrated using XRD. Subsequently, the Raman spectra were monitored as a function of applied electric field. This method delivers a quantitative correlation between strain and the shift of the Raman-active phonons, allowing for determination of Grüneisen parameters in the BFO films. Establishing the strain-dependent Raman response provides a powerful tool to characterize strain coupling in multiferroic composite nanostructures.

BFO epitaxial thin films were deposited on piezoelectric $0.72Pb(Mg_{1/3}Nb_{2/3})O_3$-$0.28PbTiO_3$ substrates using pulsed laser deposition. The details of the deposition process can be found elsewhere.[19,20] Conductive buffer layers of $La_{0.7}Sr_{0.3}MnO_3$ (LSMO) or $SrRuO_3$ (SRO) with the thickness of ~15 nm were deposited between the film and the substrate for realising the top electrical contact. The BFO layer deposited on LSMO/PMN-PT was ~160 nm thick, while that deposited on SRO/PMN-PT was ~200 nm thick. The effects of strain were investigated by applying an external dc electric field across the PMN-PT substrate through the buffer conductive upper electrode (SRO or LSMO) and the bottom electrode on the backside of the substrate as is schematically

---

[a)] E-mail: himcinsc@physik.tu-freiberg.de

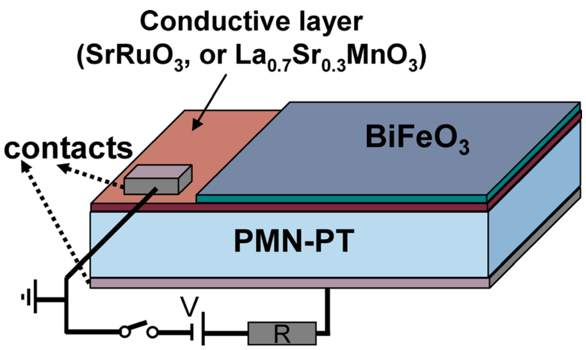

FIG. 1. Sketch of the BFO/buffer/PMN-PT structures used for the XRD and Raman measurements.

shown in Figure 1. This configuration was used for both XRD and Raman measurements, and voltages of 200 V, 300 V, and 400 V which correspond to electric fields values of 6.7 kV/cm, 10 kV/cm, and 13.3 kV/cm, respectively, were applied. Before the Raman measurements, the samples were annealed at 250 °C for 30 min in order to eliminate the electric polarisation history of the substrate, and subsequently poled at 300 V (corresponding to an electric field of 10 kV/cm). At the beginning, the poling is necessary for the reorientation of the domains so that a maximum of piezoelectric effect is expected. Raman spectroscopic measurements were performed using a LabRam spectrometer (Horiba Jobin Yvon) equipped with a 2400 grooves/mm grating and a Peltier cooled CCD detector. The measurements were realised in backscattering geometry with the incident/scattered light being focused/collected through a 50× magnification microscope objective (numerical aperture 0.55). For excitation, the 442 nm line of an HeCd laser was used, which implies pre-resonant conditions for the Raman measurements.

The calibration of the strain induced in the BFO films and PMN-PT substrates by the applied voltage (electric field) was realised using XRD measurements. The θ-2θ scans for both samples exhibit (00*l*) pseudo-cubic reflections of the BFO films and PMN-PT substrates indicating epitaxial growth. Figure 2(a) shows the reciprocal space mapping (RSM) around the (103) asymmetric pseudo-cubic reflection of BFO (200 nm)/SRO/PMN-PT indicating epitaxial growth. Figure 2(b) shows the θ-2θ XRD scans measured for the BFO/LSMO/PMN-PT sample, for the different electric fields applied, in the region of the (002) pseudo-cubic reflections. As it can be seen, the increase of the electric field induces an in-plane shrinkage of the substrate accompanied by an increase in the out-of-plane lattice parameters, due to the piezoelectric nature of PMN-PT. This compressively induced strain is further transmitted via the buffer layer to the BFO film whose out-of-plane parameter also increases. Figures 2(c) and 2(d) show the nearly linear dependence of the out-of-plane strain of BFO films and PMN-PT with increasing electric field for the samples grown with LSMO and SRO buffer layers, respectively. The BFO lattice parameter is larger than the lattice parameters of both SRO and LSMO buffer layers, but closer to that of the SRO. This provides a better accommodation of the BFO film on the SRO buffer layer and consequently a lower compressive strain in this BFO film.

In Figure 3(a), the measured Raman spectra of the 160 nm BFO films deposited on the PMN-PT substrates with the LSMO buffer layer for different applied voltages are shown. It can be observed that the increase in the electric field induces an increase in the Raman scattering signal. For an applied electric field of 13.3 kV/cm, the enhancement of the intensity is about 10% in respect to the spectra measured without voltage. A similar enhancement of the Raman scattering intensity was also measured for the BFO films deposited using an SRO buffer layer. An electric field-induced light scattering was recently observed in the PMN-PT and PMN-PZT ceramics.[21] The behaviour was attributed to the growth of polar

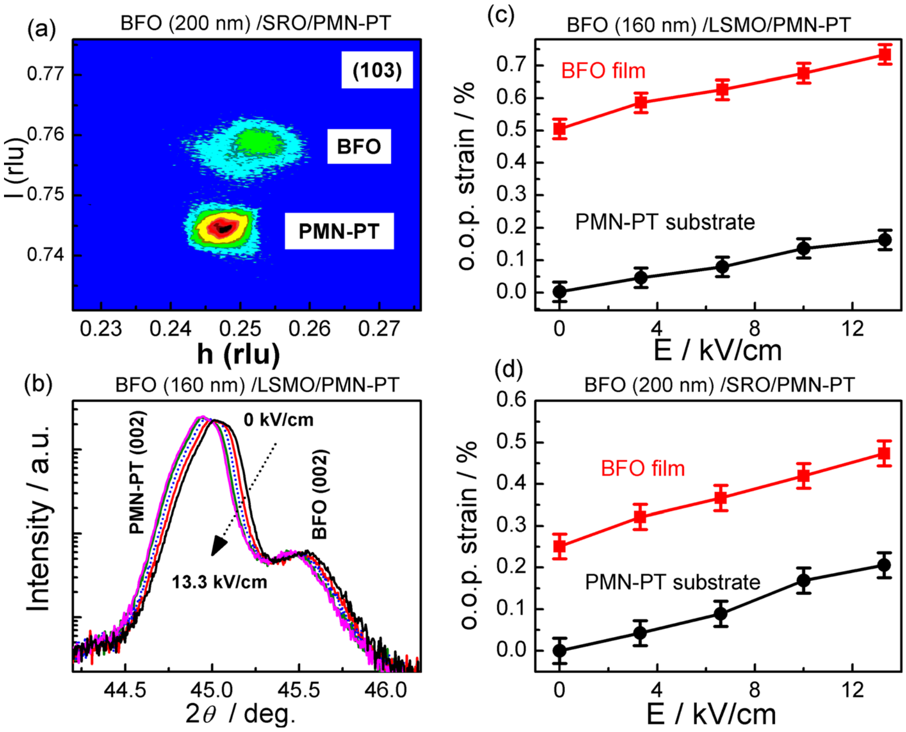

FIG. 2. RSM around the (103) pseudo-cubic reflection of BFO (200 nm)/SRO/PMN-PT sample (a). θ-2θ XRD scans measured for the BFO (160 nm)/LSMO/PMN-PT sample for different electric fields applied (b). The relative changes of the out-of-plane (o.o.p.) lattice parameters of the BFO films and PMN-PT substrates as a function of the field applied for the samples having LSMO buffer layer (c) and SRO buffer layer (d).

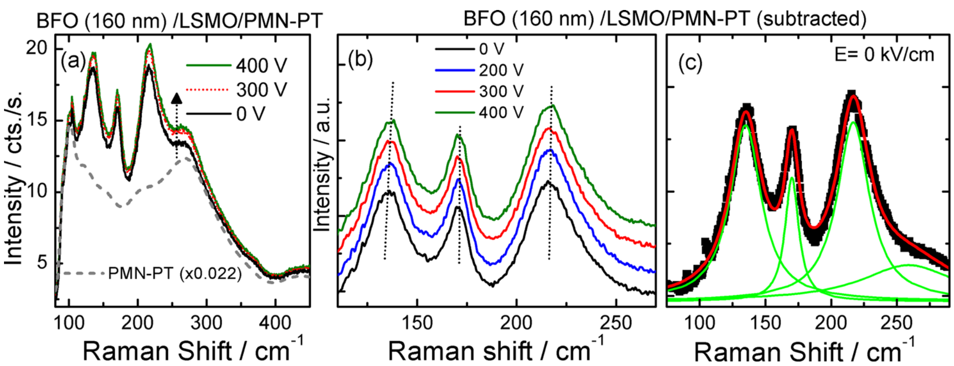

FIG. 3. The Raman spectra of the BFO/LSMO/PMN-PT sample measured for different applied voltages. The grey dashed line shows the spectrum of the PMN-PT substrate scaled for the same intensity at 100 cm^{-1} (a). The subtracted Raman spectra of the BFO film for different applied voltages (b). Example of fitting the Raman data using Lorentzian oscillators (c).

nanoregions, where larger domains and larger domain walls induce an increase in the overall light scattering.[22]

In Figure 3(a), the Raman spectrum of the PMN-PT substrate at 0 V normalised for the same intensity at 100 cm^{-1} is shown for comparison. LSMO and SRO buffer materials have low Raman signal at room temperature. Their contribution to the overall Raman spectrum for thicknesses of 15 nm can be neglected. The spectra corresponding to the BFO films are obtained by subtracting from the film/substrate spectra, the corresponding intensity normalised substrate spectrum. For example, the spectra of the BFO film for the sample grown using an LSMO buffer layer are shown in Figure 3(b) for different applied voltages.

For an epitaxial orientation of (001) pseudo-cubic planes of BFO parallel to the (001) planes of the PMN-PT substrate and for backscattering geometry, the angle between the transferred phonon vector and the c-axis of the rhombohedral BFO structure is 54.7°. For this orientation, the three most intensive peaks in the Raman spectra are polar and have a mixed character, namely, 136 cm^{-1} $E_{TO} \rightarrow A_{1TO}$, 170 cm^{-1} $A_{1LO} \rightarrow E_{LO}$, and 218 cm^{-1} $A_{1LO} \rightarrow A_{1TO}$.[23,24] These peaks shift to higher wavenumbers with increasing applied voltage. This blue shift in the position of the Raman phonon modes indicates an increase in the compressive strain,[25,26] also in agreement with the XRD data.

To determine the position of the BFO phonon modes, the subtracted spectra were evaluated in the spectral range from 80 to 300 cm^{-1}. In this region, the spectra were fitted using 4 Lorentzian oscillators. Figure 3(c) displays the Lorentzian fit to the Raman data for the sample with the LSMO buffer layer without electric field, as an example. The positions of the first three most intensive phonons determined by using this fitting procedure for both BFO films are plotted in Figures 4(a) and 4(b). For both samples and all three peaks, the shift of the position of the phonons to higher energies with the increasing applied electric field can be followed. The Raman-active phonons shift by a different amount depending on the phonon symmetry and on the atoms involved in the vibration, which will be discussed later. The magnitude of the shifts was used for the determination of the Grüneisen parameters of BFO as it is explained in the following.

The Poisson's ratio ν_P is defined as the ratio between the in-plane strain to the strain along the deformation direction in case of a uniaxial stress. In case of biaxial in-plane deformation, considering an elastic isotropic medium and using Hooke's law, one can determine the relationship between the Poisson's ratio ν_P, out-of-plane (ε_c), and in-plane strain ($\varepsilon_a, \varepsilon_b$) values as

$$\nu_p = \frac{\varepsilon_c}{\varepsilon_c - (\varepsilon_a + \varepsilon_b)}. \tag{1}$$

For the in-plane equal deformation, one obtains equal in-plane strain values: $\varepsilon_{ip} = \varepsilon_a = \varepsilon_b$, which relates to the out-of-plane $\varepsilon_{oop} = \varepsilon_c$ strain value by the equation

$$\varepsilon_{ip} = 1/2 \times (1 - 1/\nu_P) \times \varepsilon_{oop}. \tag{2}$$

Using Equation (2), one can determine the relative volume change between two different states which correspond to an initial (ε_{c1}) and a final (ε_{c2}) out-of-plane strain value as follows:

$$\frac{\Delta \mathrm{V}}{\mathrm{V}} = \frac{[1 + 1/2 \times (1 - 1/\nu_P) \times \varepsilon_{c2}]^2 \times (1 + \varepsilon_{c2}) - [1 + 1/2 \times (1 - 1/\nu_P) \times \varepsilon_{c1}]^2 \times (1 + \varepsilon_{c1})}{[1 + 1/2 \times (1 - 1/\nu_P) \times \varepsilon_{c1}]^2 \times (1 + \varepsilon_{c1})}. \tag{3}$$

For similar BFO films as the films investigated in this work, Biegalski *et al.*[14] determined a value of 0.34 for the Poisson's ratio for BFO, measuring both in-plane and out-of-plane film lattice parameters.

The Grüneisen parameter γ describes the change of vibrational frequency induced by a change of the crystal lattice. The isothermal Grüneisen parameter γ_T relates the relative frequency change ($\Delta\omega/\omega$) of a vibrational mode caused by a change in the lattice parameter to the relative volume change ($\Delta V/V$) at a constant temperature[27]

$$\gamma_T = -\frac{\partial(\ln \omega)}{\partial(\ln V)} = -\frac{\Delta\omega/\omega}{\Delta V/V}. \tag{4}$$

Please note that Equation (4) used for the calculation of the Grüneisen parameter represents the simple case of cubic

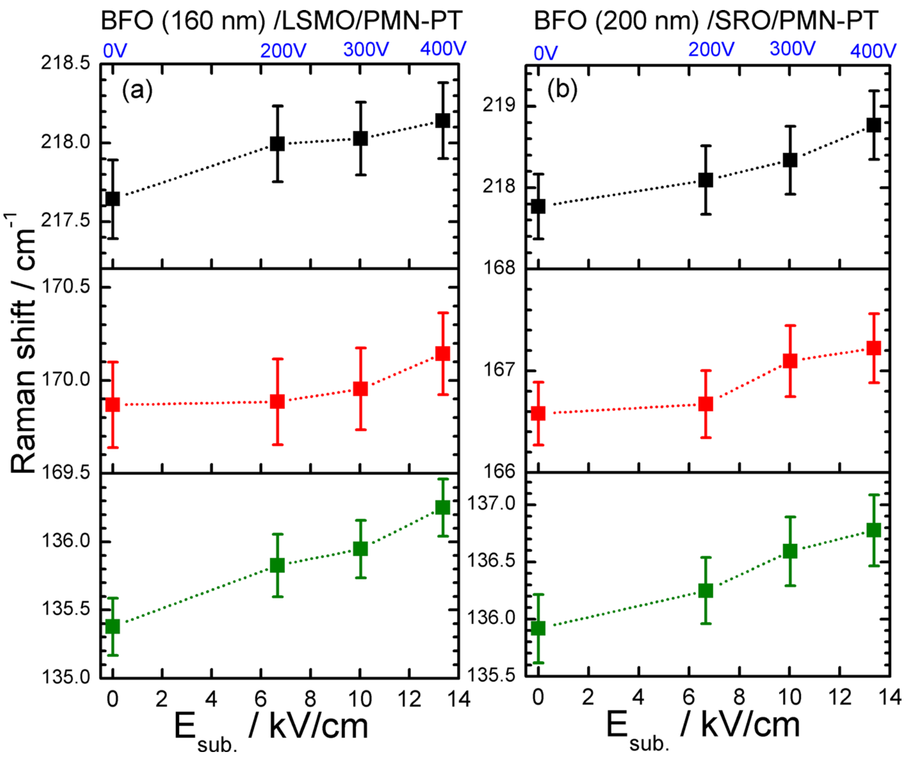

FIG. 4. The position of the Raman phonons obtained from the fits of the data as a function of the applied electric field (voltage) for the samples having a LSMO buffer layer (a) and SRO buffer layer (b).

lattice symmetry and isotropic change in volume in the quasiharmonic approximation.[28] In our case, an in-plane equal deformation is applied to the thin film BFO material so that the use of Equation (4) gives only an approximation of the Grüneisen parameters, in the absence of the knowledge of the anisotropic elastic coefficients of BFO.

Using the out-of-plane parameters of the BFO films as obtained from XRD measurements and using Equation (3), one can determine the volume change $\Delta V/V$ between two different strain states in the film. Volume changes of 0.21% and 0.22% between the initial and final states were obtained for the samples BFO/SRO/PMNPT and BFO/LSMO/PMNPT, respectively. The calculated values of volume change, the levels of the strain induced in the BFO films, and the values of the out-of-plane lattice parameters (see Figure 2) correspond to the rhombohedral phase of BFO.[29–31] On the other hand, the relative frequency change has been determined from Raman spectroscopy.

The values of the Grüneisen parameters determined for BFO films using the method described above and Equation (4) are listed in Table I. The highest values of the Grüneisen coefficients are obtained in both samples for the lowest measured Raman-active mode at ca. 135 cm^{-1}. Such a high value (nearly 3) can be correlated to a higher degree of anharmonicity of this vibration, which, according to Hermet *et al.*,[5] involves the movement of the heavier Bi-atoms. The high anharmonicity can be attributed to the large amplitudes of the Bi-O vibrations. Similar values for the Grüneisen parameters have been determined for bulk BFO using inelastic neutron scattering by Delaire *et al.* for lower frequency Bi-dominated modes.[32]

TABLE I. The Grüneisen parameters for the three most intensive measured phonon modes determined from the XRD and Raman data for both BFO/LSMO/PMN-PT and BFO/SRO/PMN-PT samples.

Sample/Mode	136 cm^{-1}	170 cm^{-1}	218 cm^{-1}
BFO/LSMO/PMN-PT (160 nm)	2.94	0.74	1.05
BFO/SRO/PMN-PT (200 nm)	2.98	1.82	2.15

For the modes occurring at 167 cm^{-1} and 218 cm^{-1} in the sample deposited on the SRO buffer layer, the values of the Grüneisen parameters in Table I are similar to those predicted by first-principle calculations[33] and those determined for BFO powder under high-pressure.[31,34] These two phonon modes involve the movement of the Fe and O ions in the FeO_6 octahedra and their change in frequency can be influenced by the spin-phonon interaction.[35] For the sample deposited on the LSMO buffer layer, the values of the Grüneisen parameter of these two phonon modes are lower; however, these calculated Grüneisen parameters have values close to those determined for Sm-doped BFO powder under high-pressure.[36]

In summary, piezoelectric strain in the PMN-PT substrates induced by electric field was effectively transferred to the BFO films using LSMO or SRO conductive buffer layers. The lattice parameters change as determined by XRD, and the Poisson's ratio for BFO, were used to determine the relative volume change induced by strain in the BFO films. Using the shifts of the phonons measured by Raman and the relative volume change, the Grüneisen parameters of specific Raman phonons modes of $BiFeO_3$ were calculated. Since BFO is an often applied component of strain-coupled multiferroic composite films, this study provides a foundation to characterize the actually acting strain in such films using Raman scattering and, thus, will improve the understanding and utilization of magnetoelectric coupling.

This work was supported by the German Research Foundation, Project No. DFG HI 1534/1-2. The technical support from A. Schmid from Institute of Applied Physics TU Bergakademie Freiberg is acknowledged.

[1] M. Opel, S. Geprägs, E. P. Menzel, A. Nielsen, D. Reisinger, K.-W. Nielsen, A. Brandlmaier, F. D. Czeschka, M. Althammer, M. Weiler, S. T. B. Goennenwein, J. Simon, M. Svete, W. Yu, S.-M. Hühne, W. Mader, and R. Gross, Phys. Status Solidi A **208**, 232 (2011).

[2] L. W. Martin and D. G. Scholm, Curr. Opin. Solid State Mater. Sci. **16**, 199 (2012).

[3] J. Kreisel and P. Bouvier, J. Raman Spectrosc. **34**, 524 (2003).

[4] H. Bea, M. Bibes, S. Petit, J. Kreisel, and A. Barthelemy, Philos. Mag. Lett. **87**, 165 (2007).

[5] P. Hermet, M. Goffinet, J. Kreisel, and Ph. Ghosez, Phys. Rev. B **75**, 220102(R) (2007).

[6] D. A. Tenne and X. X. Xi, J. Am. Ceram. Soc. **91**, 1820 (2008).

[7] R. Palai, R. S. Katiyar, H. Schmid, P. Tissot, S. J. Clark, J. Robertson, S. A. T. Redfern, G. Catalan, and J. F. Scott, Phys. Rev. B **77**, 014110 (2008).

[8] S. Issing, F. Fuchs, C. Ziereis, E. Batke, A. Pimenov, Y. Vu. Ivanov, A. A. Mukhin, and J. Geurts, Eur. Phys. J. B **73**, 353 (2010).

[9] D. Viehland, A. Amin, and J. F. Li, Appl. Phys. Lett. **79**, 1006 (2001).

[10] S.-E. Park and T. R. Shrout, J. Appl. Phys. **82**, 1804 (1997).

[11] X. Huo, S. Zhang, G. Liu, R. Zhang, J. Luo, R. Sahul, W. Cao, and T. R. Shrout, J. Appl. Phys. **113**, 074106 (2013).

[12] K. C. Cheng, H. L. W. Chan, C. L. Choy, Q. R. Yin, H. S. Luo, and Z. W. Yin, *Proceedings of the 2000 12th IEEE International Symposium on Applications of Ferroelectrics* (IEEE, 2000), Vol. 2, pp. 533–536.

[13] B. Noheda, D. E. Cox, G. Shirane, J. Gao, and Z.-G. Ye, Phys. Rev. B **66**, 054104 (2002).

[14] M. D. Biegalski, K. Dörr, D. H. Kim, and H. M. Christen, Appl. Phys. Lett. **96**, 151905 (2010).

[15] C. Thiele, K. Dörr, O. Bilani, J. Rödel, and L. Schultz, Phys. Rev. B **75**, 054408 (2007).

[16] A. Herklotz, M. Kataja, K. Nenkov, M. D. Biegalski, H.-M. Christen, C. Deneke, L. Schultz, and K. Dörr, Phys. Rev. B **88**, 144412 (2013).

[17] M. C. Dekker, A. Herklotz, L. Schultz, M. Reibold, K. Vogel, M. D. Biegalski, H. M. Christen, and K. Dörr, Phys. Rev. B **84**, 054463 (2011).

[18] R. K. Zheng, Y. Wang, H.-U. Habermeier, H. L. W. Chan, X. M. Li, and H. S. Lua, J. Alloys Compd. **519**, 77 (2012).

[19] E. J. Guo, K. Dörr, and A. Herklotz, Appl. Phys. Lett. **101**, 242908 (2012).

[20] E. J. Guo, A. Herklotz, R. Roth, M. Christl, S. Das, W. Widra, and K. Dörr, Appl. Phys. Lett. **103**, 022905 (2013).

[21] W. Zhao, W. Ruan, J. Zeng, L. Huang, K. Zhao, L. Zheng, H. Zeng, Y. Zhou, H. Yang, X. Ruan, and G. Li, Appl. Phys. Lett. **104**, 062907 (2014).

[22] Y. Zhou, W. Zhao, W. Ruan, J. Zheng, L. Zheng, J. Cheng, and G. Li, Appl. Phys. Lett. **106**, 122904 (2015).

[23] J. Hlinka, J. Pokorny, S. Karimi, and I. M. Reaney, Phys. Rev. B **83**, 020101(R) (2011).

[24] A. Talkenberger, I. Vrejoiu, F. Johann, C. Röder, G. Irmer, D. Rafaja, G. Schreiber, J. Kortus, and C. Himcinschi, J. Raman Spectrosc. **46**, 1245 (2015).

[25] C. Himcinschi, I. Vrejoiu, M. Friedrich, E. Nikulina, L. Ding, C. Cobet, N. Esser, M. Alexe, D. Rafaja, and D. R. T. Zahn, J. Appl. Phys. **107**, 123524 (2010).

[26] C. Himcinschi, A. Bhatnagar, A. Talkenberger, M. Barchuk, D. R. T. Zahn, D. Rafaja, J. Kortus, and M. Alexe, Appl. Phys. Lett. **106**, 012908 (2015).

[27] E. Grüneisen, Ann. Phys. **344**, 257 (1912).

[28] G. Grimvall, *Thermophysical Properties of Materials* (Elsevier, Amsterdam, 1999).

[29] M. Guennou, P. Bouvier, R. Haumont, G. Garbariono, and J. Kreisel, Phase Transitions **84**, 474 (2011).

[30] R. Haumont, P. Bouvier, A. Pashkin, K. Rabia, S. Frank, B. Dkhil, W. A. Crichton, C. A. Kuntscher, and J. Kreisel, Phys. Rev. B **79**, 184110 (2009).

[31] S. Gomez-Salces, F. Aguado, F. Rodriguez, R. Valiente, J. Gonzalez, R. Haumont, and J. Kreisel, Phys. Rev. B **85**, 144109 (2012).

[32] O. Delaire, M. B. Stone, J. Ma, A. Huq, D. Gout, C. Brown, K. F. Wang, and Z. F. Ren, Phys. Rev. B **85**, 064405 (2012).

[33] Q. Li, D. H. Huang, Q. L. Cao, and F. H. Wang, Chin. Phys. B **22**, 037101 (2013).

[34] Y. Yang, L. G. Bai, K. Zhu, Y. L. Liu, S. Jiang, J. Liu, J. Chen, and X. R. Xing, J. Phys.: Condens. Matter **21**, 385901 (2009).

[35] M. K. Singh and R. S. Katiyar, J. Appl. Phys. **109**, 07D916 (2011).

[36] Y. J. Wu, X. K. Chen, J. Zhang, W. S. Xiao, Z. Wu, and X. J. Chen, J. Appl. Phys. **114**, 154110 (2013).

APL MATERIALS **4**, 046103 (2016)

Probing orbital ordering in $LaVO_3$ epitaxial films by Raman scattering

I. Vrejoiu,[1,a] C. Himcinschi,[2,a] L. Jin,[3] C.-L. Jia,[3] N. Raab,[4] J. Engelmayer,[1]
R. Waser,[4] R. Dittmann,[4] and P. H. M. van Loosdrecht[1]
[1]*Physikalisches Institut, University of Cologne, D-50937 Cologne, Germany*
[2]*TU Bergakademie Freiberg, Institute of Theoretical Physics, D-09596 Freiberg, Germany*
[3]*Peter Grünberg Institut (PGI-5), Forschungszentrum Jülich GmbH,*
D-52425 Jülich, Germany
[4]*Peter Grünberg Institut (PGI-7), Forschungszentrum Jülich GmbH,*
D-52425 Jülich, Germany

(Received 16 February 2016; accepted 22 March 2016; published online 8 April 2016)

Single crystals of Mott-Hubbard insulator $LaVO_3$ exhibit spin and orbital ordering along with a structural change below ≈140 K. The occurrence of orbital ordering in epitaxial $LaVO_3$ films has, however, been little investigated. By temperature-dependent Raman scattering spectroscopy, we probed and evidenced the transition to orbital ordering in epitaxial $LaVO_3$ film samples fabricated by pulsed-laser deposition. This opens up the possibility to explore the influence of different epitaxial strain (compressive *vs*. tensile) and of epitaxy-induced distortions of oxygen octahedra on the orbital ordering, in epitaxial perovskite vanadate films.
[http://dx.doi.org/10.1063/1.4945658]

Transition-metal oxides, for which strong electron correlations play an important role, exhibit a wide spectrum of intriguing physical properties, such as Mott transitions, colossal magnetoresistance, and high T_C-superconductivity. $LaVO_3$ is a prototypical Mott-Hubbard insulator with a $3d^2$ electronic configuration of V^{3+}. At 143 K, $LaVO_3$ single crystals undergo a magnetic transition from a paramagnetic state to an antiferromagnetic state and a first order structural phase transition from orthorhombic *Pbnm* to monoclinic $P2_1/b$ following right below the magnetic ordering temperature, at 141 K.[1,2] The antiferromagnetic state is a C-type spin-ordered (C-type SO) state with ferromagnetically arranged $V^{3+}(S = 1)$ spins along the *c*-axis and the antiferromagnetic alignment in the *ab* plane. Along with the structural transition, a G-type orbital order (G-type OO) sets in below 141 K as well, with commonly occupied t_{2g} d_{xy} orbitals and d_{yz} or d_{zx} orbitals that are alternately occupied in all directions.

Concerning the motivation for thin films of Mott insulators, an exciting application is their use as the active material in resistive random access memories.[3] Particular interest in epitaxial $LaVO_3$ films has been driven by the "polar discontinuity" at the interface $LaVO_3/SrTiO_3$, analogues to the $LaAlO_3/SrTiO_3$ case.[4,5] The fabrication of phase pure $LaVO_3$ films, however, requires oxygen pressures lower than about 10^{-5} mbar, so that the competing $LaVO_4$ phase does not form. The fabrication of the $LaVO_x$ films under high vacuum conditions affects the stoichiometry of the film and oxygen content of the $SrTiO_3$ substrates. The surface of $SrTiO_3$ substrates may become reduced,[6] and this affects the transport properties of the $LaVO_x/SrTiO_3$ samples dramatically.[7] Temperature-dependent transport properties of $LaVO_x$ films grown on $SrTiO_3$, showing either metallic[4,8] or an overlapping two-component metallic and semiconducting behavior,[7–9] are influenced by contributions from the oxygen-deficient substrate. Similar issues have been encountered

---

[a] Authors to whom correspondence should be addressed. Electronic mail: vrejoiu@ph2.uni-koeln.de and himcinsc@physik.tu-freiberg.de.

for the assessment of the properties of epitaxial $LaTiO_3$ thin films, whose growth also requires high vacuum conditions.[10] The role played in epitaxial film properties by $SrTiO_3$ substrates, which are prone to change readily the oxygen content and the transport properties under reducing conditions, was brought into focus, e.g., by Schneider *et al.*[11]

In contrast, the transport properties of $LaVO_x$ films grown on $DyScO_3$(110) (DSO) substrates, under the same conditions as films grown on $SrTiO_3$ (100) (STO), indicate semiconducting behavior of the vanadate films.[8] The resistance of the $LaVO_x$ films on DSO substrates increased with decreasing temperature and only the resistivity data down to about 180 K were shown by He *et al.*[8] Although the transport properties of the $LaVO_3$ films grown on DSO exhibit the semiconducting behavior expected for a Mott insulating material, $DyScO_3$ crystals are paramagnetic[12] and hinder strongly the magnetic measurements of $LaVO_3$ films. Temperature-dependent magnetic susceptibility and magnetization measurements of $LaVO_3$ single crystals yielded direct information about the antiferromagnetic order and the corresponding transition temperatures.[13,14] However, so far no systematic measurements have been published for $LaVO_3$ epitaxial films. There exists a report on the magnetic properties of $PrVO_3$ epitaxial films grown on STO(100), for which a surprisingly reduced SO temperature of 80 K (in bulk, the antiferromagnetic SO temperature is 140 K) and a hard-ferromagnetic behavior at 10 K were observed.[15]

Probably due to these experimental difficulties, so far the ordering phenomena in epitaxial perovskite vanadate film samples have not been properly addressed. Optical spectroscopy investigations provide alternative methods for studying orbital ordering transitions in $LaVO_3$ films. Though also these techniques may suffer from hindering contributions from the substrates, they are potentially easier methods to separate the substrate and film contributions by making use of the specific spectral film/substrate features. Temperature-dependent Raman scattering and optical conductivity investigations of $LaVO_3$ single crystals were performed in great detail, in order to study the coupling between structure and electronic properties in the SO and OO states.[2,16–20]

Here we investigate the structural phase transitions and the onset of the orbital ordering in $LaVO_3$ epitaxial films fabricated by pulsed-laser deposition (PLD). Temperature-dependent Raman scattering spectroscopy was employed to monitor the occurrence of orbital ordering and its associated structural phase transition in $LaVO_3$ epitaxial films. To the best of our knowledge, neither Raman spectroscopy studies nor experimental evidence of orbital ordering occurring in $LaVO_3$ film samples has been reported so far.

Epitaxial growth of $LaVO_3$ films has been achieved by a variety of techniques, predominantly by PLD[4,5,7–9,21] or by molecular beam epitaxy.[22] The stabilization of the perovskite $LaVO_3$ phase in thin films was successful by performing the growth in either high vacuum[4,5,7–9,22] or in pure Ar or Ar/H_2 atmosphere.[9,21] We fabricated the films by PLD using a KrF excimer laser. The chamber was evacuated down to less than 10^{-7} mbar. STO(100), DSO(110), and twinned $LaGaO_3$(110)/(001) (LGO) single crystal substrates were employed. The substrates were heated to temperatures of about 450 °C in high vacuum conditions. Then Ar/4% H_2 gas mixture was let in the PLD chamber to pressures of $\approx 10^{-3}$ mbar and the substrates were further heated to 700 °C and the films were grown under these conditions. In the same PLD system, using moderate pressures of 4×10^{-4} mbar, Ar/H_2 was successful for the growth of films of other materials that require reducing conditions, such as $EuTiO_3$ films.[23]

A laser fluence of 1.2 J/cm^2 was employed for the ablation of the $LaVO_4$ ceramic target and the laser repetition rate was 3 Hz. After growth, the samples were cooled to room temperature (RT) in the same Ar/H_2 atmosphere. Reflective high energy electron diffraction (RHEED) was used to monitor the growth and estimate the growth rate of the $LaVO_3$ films.

Raman scattering spectra were recorded in back-scattering configuration using a Horiba-Jobin-Yvon Labram HR 800 spectrometer equipped with an Olympus Microscope, a 600 grooves/mm grating, and a Peltier cooled CCD detector. For excitation, the 632.8 nm (1.96 eV) line of a HeNe laser was used. The beam was focused on the sample (spot size of ≈ 2.5 μm) and collected through a 50× magnification long distance microscope objective (numerical aperture NA = 0.55). To avoid sample heating, the laser power at the sample was kept below 1.5 mW. Temperature-dependent Raman measurements from 87 K up to room temperature were carried out with a Linkam THMS-600 cooling-heating stage placed under the Raman microscope. For each temperature, two measurements were done: for the first measurement, the laser was focused at the sample surface (film/substrate signal); during the second, the laser was focused about 20 μm under the sample surface (substrate signal).[24] The Raman scattering signal belonging to the LaVO$_3$ films was obtained by normalizing the two spectra and subsequent subtraction.

Atomic force microscopy (AFM) scans of the samples confirmed the layer-by-layer growth mode (see the topography images in Fig. 1) of the films on all substrates, which was also indicated by RHEED patterns observed during the film growth (Fig. 1, left). The layer-by-layer growth was readily achieved on all the substrates, especially if the crystals had been annealed prior to being used for PLD. The only substrates that were not annealed were the LGO crystals, in order to avoid

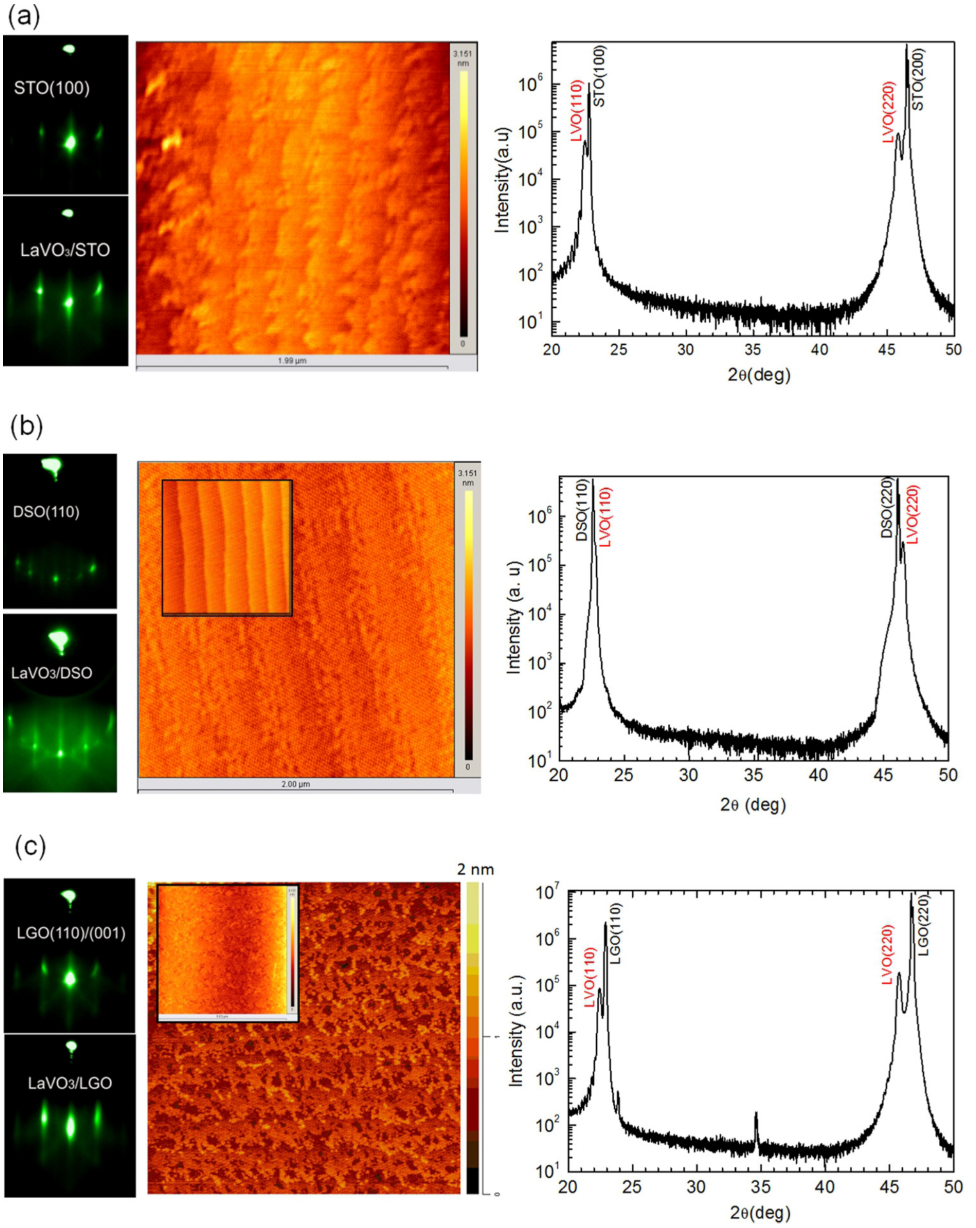

FIG. 1. Morphological and structural characterization of (a) LaVO$_3$ films grown on SrTiO$_3$(100), (b) on DyScO$_3$(110), and (c) on twinned LaGaO$_3$(110)/(001): RHEED patterns of the substrates and films (on the left), atomic force microscopy images (middle), and $2\theta-\omega$ XRD scans (right). The inset in the AFM image from panel (b) shows also the surface morphology of the annealed DyScO$_3$(110) crystal and in (c) of the as-received LaGaO$_3$(110) crystal, prior to being used for film growth. AFM images in (a) and (b) show scans over 2 μm$\times$2 μm areas and in (c) over 5 μm$\times$5 μm areas.

possible mechanical damage occurring during the structural phase transition at 423 K, but also in this case, layer-by-layer growth was achieved.

$LaVO_3$ crystallizes at RT in an orthorhombic structure (*Pbnm*), with lattice parameters a = 5.555 Å, b = 5.553 Å, and c = 7.849 Å and thus $a \approx b \approx c/\sqrt{2}$.[1,13,14,25–27] The low temperature phase is monoclinic $P2_1/b$, with a rather larger change of the c-axis. The structure of $LaVO_3$ exhibits tilted VO_6 octahedra and displaced La ions (with respect to a pure perovskite structure), which in case of the bulk are relatively small and the lattice parameters can be related to a pseudocubic (PC) structure according to the relation: $a_{PC,LaVO_3} \approx a/\sqrt{2} \approx b/\sqrt{2} \approx c/2 = 3.926$ Å. The lattice match of $LaVO_3$ is fairly good with the cubic STO(100) or pseudocubic LGO(110) and DSO(110) substrates ($a_{PC,LGO110} = 3.89$ Å; $a_{STO} = 3.905$ Å; $a_{PC,DSO110} = 3.95$ Å).

$2\theta - \omega$ X-ray diffraction (XRD) scans demonstrate that the $LaVO_3$ films on both substrates are epitaxial and phase pure (Fig. 1, right). For the film grown under compressive stress on STO(100), the average out-of-plane lattice parameter of our $LaVO_3$ films is about 3.955 Å and thus larger than $a_{PC,LaVO_3} \approx 3.926$ Å. The value is in good agreement with the out-of-plane lattice parameter reported for stoichiometric $LaVO_3$ films grown on STO(100) by molecular beam epitaxy.[22] Zhang *et al.*[22] commented that, unlike in the well-studied case of epitaxial $SrTiO_3$ films,[28] for which the out-of-plane lattice parameter expands with increasing amounts of cation non-stoichiometry, the opposite trend was found for $LaVO_3$ films. For the film grown under even higher levels of compressive stress on LGO(110), the average out-of-plane lattice parameter of our $LaVO_3$ films is about 3.96 Å. On the other hand, the average out-of-plane lattice parameter for $LaVO_3$ grown on DSO(110) is about 3.905 Å, which is slightly smaller than the $a_{PC,LaVO_3} \approx 3.926$ Å, due to the tensile epitaxial strain conditions. $2\theta - \omega$ XRD scans do not allow us to distinguish between (110)-oriented and (001) oriented growths of $LaVO_3$. It has been recently theoretically argued that there is no clear energetic preference toward one of these orientations for epitaxially strained $LaVO_3$, both under compressive and tensile strain.[27] Experimentally, so far only the structure and orientation of $PrVO_3$ and $LaVO_3$ films grown under compressive strain on $SrTiO_3$(100) have been studied, and only domains with the c-axis lying in the plane of the $SrTiO_3$ substrate were found.[15,26,29]

The orientation of the c-axis is very important for making the right choice of the polarization of the incident light in optical spectroscopy investigations.[19,20,30] To obtain more information on the epitaxial relationships between the films and the substrates and on the domain structure of the films, we performed transmission electron microscopy of cross sectional specimens. Scanning transmission electron microscopy (STEM) investigations of $LaVO_3$ films grown on cubic STO(100) crystals revealed that the films grow with the long orthorhombic c-axis of the $LaVO_3$ oriented in-plane of the substrate. Figure 2 shows a summary of the investigations of a 33 nm thick $LaVO_3$ film grown on STO(100). Two types of domains, both with the c-axis lying in the plane of the STO substrate but rotated 90° with respect to each other, were identified.[26] High angle annular dark field (HAADF)-STEM images taken in two such domains are shown in Figs. 2(b) and 2(c). The orientation of the orthorhombic unit cell in the two domains was determined by performing Fourier transform of the images, as shown in Figs. 2(d) and 2(e), where also structural models for the two domains are schematically proposed. Structural defects, most likely anti-phase boundaries, present in the $LaVO_3$ films can be better seen at higher magnification, as marked by the box in Fig. 2(f) and zoomed-in in Fig. 2(g).

Figure 3 summarizes the STEM of a 52 nm thick $LaVO_3$ film deposited on DSO. Most of the layer has a (110) orientation, i.e., the long c-axis lies in the plane of the DSO(110) substrate. However, there are also domains with the c-axis oriented perpendicular to the substrate surface. Figure 3(b) shows two neighboring domains for which the c-axis is oriented in-plane, pointing towards the viewer (on the left side of the image), and out-of-plane with respect to the DSO(110) substrate. Analysis of the Fourier transforms of the images in the two regions allowed us to determine the orientation of the orthorhombic c-axis of the $LaVO_3$. Antiphase boundaries are present at the intersection of the domains, similar to what was observed for the $LaVO_3$ grown on STO. In Fig. 3(c), an annular bright field (ABF)-STEM image taken in a domain with in-plane c-axis orientation is shown and the oxygen column position can be thus viewed, allowing the visualisation of the zigzag VO_6 tilts corresponding to the slightly distorted orthorhombic structure of the $LaVO_3$ film.[29]

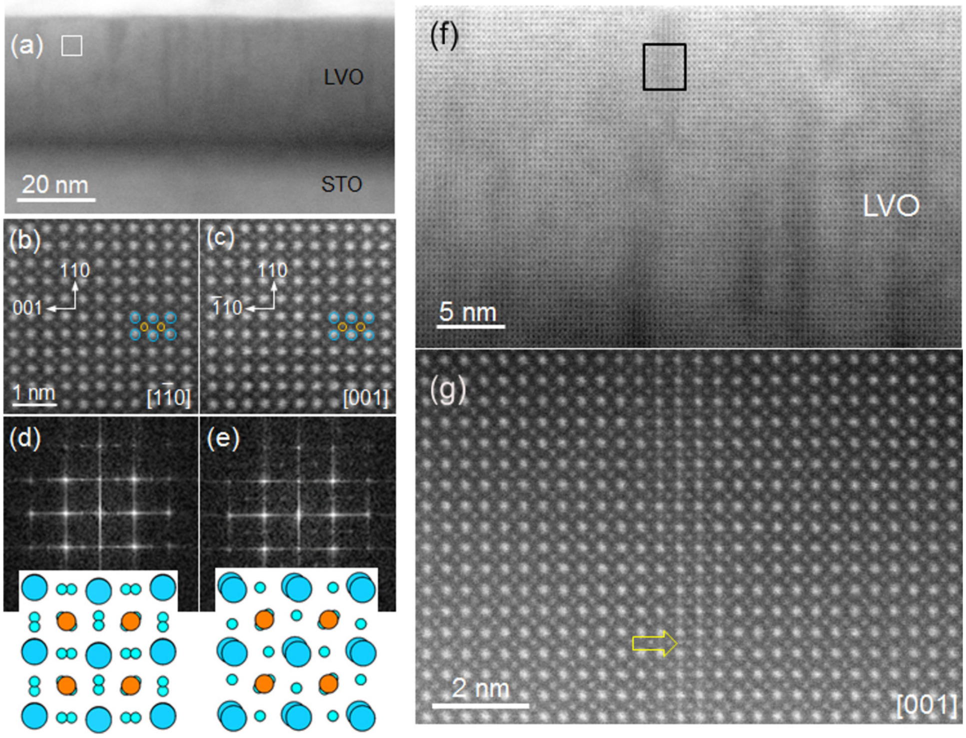

FIG. 2. Cross section HAADF-STEM investigations of a 33 nm thick $LaVO_3$ film grown on $SrTiO_3(100)$: (a) low magnification overview image with a white box indicating where the high magnification images from (b) and (c) were taken; ((b) and (d)) high magnification image of a domain with the $[001]_o$ c-axis pointing to the left and its corresponding fast Fourier transform (FFT) with structure model below; ((c) and (e)) high magnification image of a domain with the $[001]_o$ c-axis pointing to the viewer and the corresponding FFT of the image with proposed structure model below; ((f) and (g)) anti-phase boundaries defects are present in the film, as marked by the black box in (g) and by the yellow arrow at higher magnification view in (f).

For the $LaVO_3$ film deposited on twinned (110)/(001)LGO substrate, we expect that both domains with the c-axis in-plane (on top of (110)LGO) and out-of-plane (on top of (001)LGO) form as well, as confirmed by the Raman data (*vide infra*).

We performed temperature-dependent in plane *dc* resistivity measurements on a 40 nm thick $LaVO_3$ film grown on DSO(110) substrate (not shown). The resistance of the $LaVO_3$ film increased rapidly with decreasing temperature, so that the measurements could not be performed below 200 K, due to the too high resistance.[8,15] The temperature dependence of the resistance of $LaVO_3$ on DSO(110)[8] is in stark contrast to the behavior of the resistance of $LaVO_3$ films on STO(100) substrates, for which metallic-like behavior was measured by several groups.[4,7,8] DSO, which is a better insulator and is less prone to become oxygen deficient or get reduced,[11,31] preserves an insulating surface during and after the $LaVO_3$ deposition. Temperature-dependent *dc* resistivity measurements of $LaVO_3$ single crystals show the onset of the G-type OO by the kinks in the curve, occurring at 141 K.[1] However, no similar kinks have been observed or reported for resistivity data on thin film $LaVO_3$ samples on various substrates.[4,7–9,21]

A convenient method to study the OO transition in bulk $LaVO_3$ is Raman spectroscopy. The Raman spectra of $LaVO_3$ show the activation of a characteristic band at 719 cm^{-1} (89 meV) below the OO transition.[2,16–18,20] This band is readily observed using excitation resonant to the Mott-Hubbard gap near 2 eV, such as the light of a HeNe laser (1.96 eV).[16,17,19] It originates from an out-of-phase oxygen stretching mode along the c-axis and has a B_{1g} symmetry in the orthorhombic *Pbnm* phase and a *Ag* symmetry in the monoclinic OO phase.[2,16–18,32] This Raman mode was observed for $LaVO_3$ crystals for xx-polarized light and not for zz-polarized light (the relations of the optical axes, x, y, and z, to the orthorhombic axes a, b, c are $x = a + b$, $y = a - b$, and

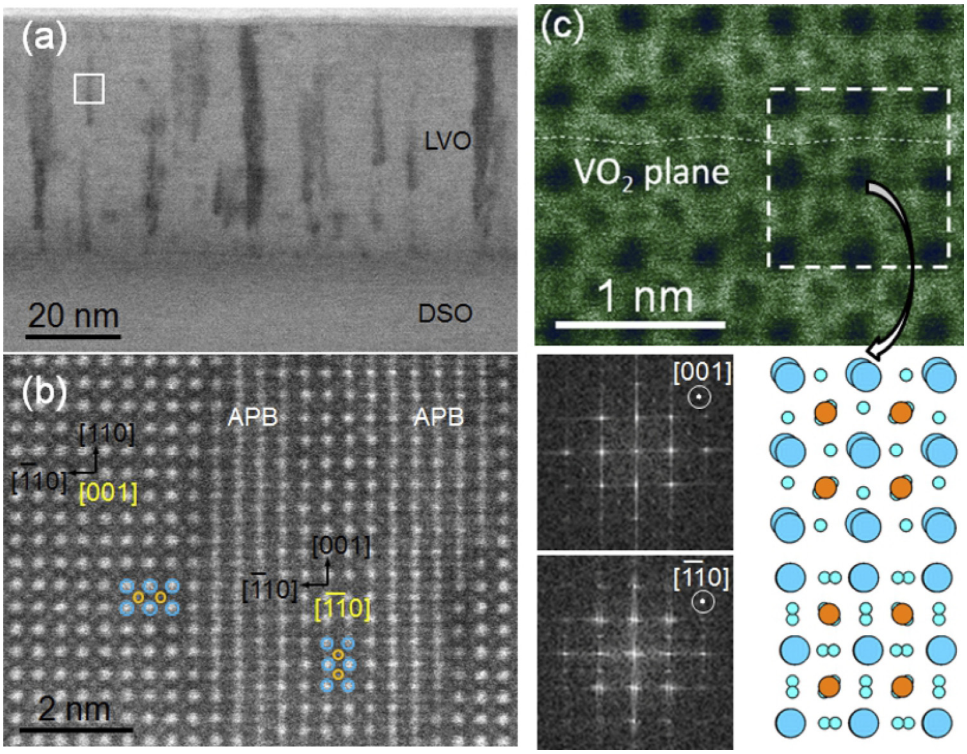

FIG. 3. Cross section HAADF- and ABF-STEM investigations of a 52 nm thick $LaVO_3$ film grown on $DyScO_3(110)$: (a) low magnification overview image with a white box indicating where the high magnification images from (b) were taken; (b) high magnification image of a region where two domains, separated by anti-phase boundaries (APB), are visible: a domain with the in-plane $[001]_o$ c-axis pointing to the viewer, a domain with the out-of-plane $[001]_o$ c-axis pointing to the top surface, and their corresponding fast Fourier transforms (FFT) with structure models at the right; (c) high magnification ABF-STEM image taken in a domain with the $[001]_o$ c-axis pointing to the viewer where the oxygen atomic columns are also imaged and the tilts of the VO_6 octahedra are visible.

$z = c$).[2,16,17,19] We monitored this particular Raman peak in the spectra of a 55 nm thick $LaVO_3$ film grown on DSO(110) substrate. This $LaVO_3$ film was capped with ≈1.5 nm thick amorphous $SrTiO_3$ layer to protect it against oxidation.[33] Figure 4 shows the spectra acquired while heating the sample from 87 K to RT. Three peaks clearly observed at about 182 cm^{-1} (23 meV), 427 cm^{-1} (53 meV), and 717 cm^{-1} (89 meV) at 88 K (as marked by black arrows) can be assigned to the $LaVO_3$ film (Fig. 4(a)). The first two peaks persist in the Raman spectra up to RT: the one at 182 cm^{-1} (23 meV) is related to the rotation of VO_6 octahedra and the one at 427 cm^{-1} (53 meV) corresponds to the Jahn-Teller mode.[16,17] The *Ag* out-of-phase oxygen stretching mode at 717 cm^{-1} (89 meV) disappears at about 160 K (Fig. 4(b)), indicating that OO transition temperature in the $LaVO_3$ film is ≈160 K (Fig. 4(c)). This transition temperature to the G-type OO phase is slightly higher than for bulk crystals. Such a shift is not uncommon in epitaxial strained films and may be due to epitaxy induced structural modifications. It was recently found that in single crystals of $Y_{1-x}La_xVO_3$, G-type OO is present locally above the T_{OO} temperature, but it is short range.[34]

We also measured Raman scattering spectra of $LaVO_3$ films grown on STO(100) substrate down to 87 K (not shown). $SrTiO_3$ is not a good substrate for Raman investigations of thin films samples because it exhibits multiple phonon modes and a strong Raman background that substantially hinder Raman-based thin film experiments.[35] This is in particular true for probing the OO in $LaVO_3$ films since STO has a dominant spectral feature at 716 cm^{-1} (88.7 meV), preventing the unambiguous observation of the 719 cm^{-1} (89 meV) G-type OO-related phonon of $LaVO_3$.

More insight into the OO of the $LaVO_3$ films under compressive strain could be, however, obtained by Raman spectroscopy of (110)/(001)-oriented $LaVO_3$ films grown on LGO(110)/(001) substrates (Fig. 5). LGO crystals allow the observation of the $LaVO_3$ phonons at 270 cm^{-1} (33 meV,

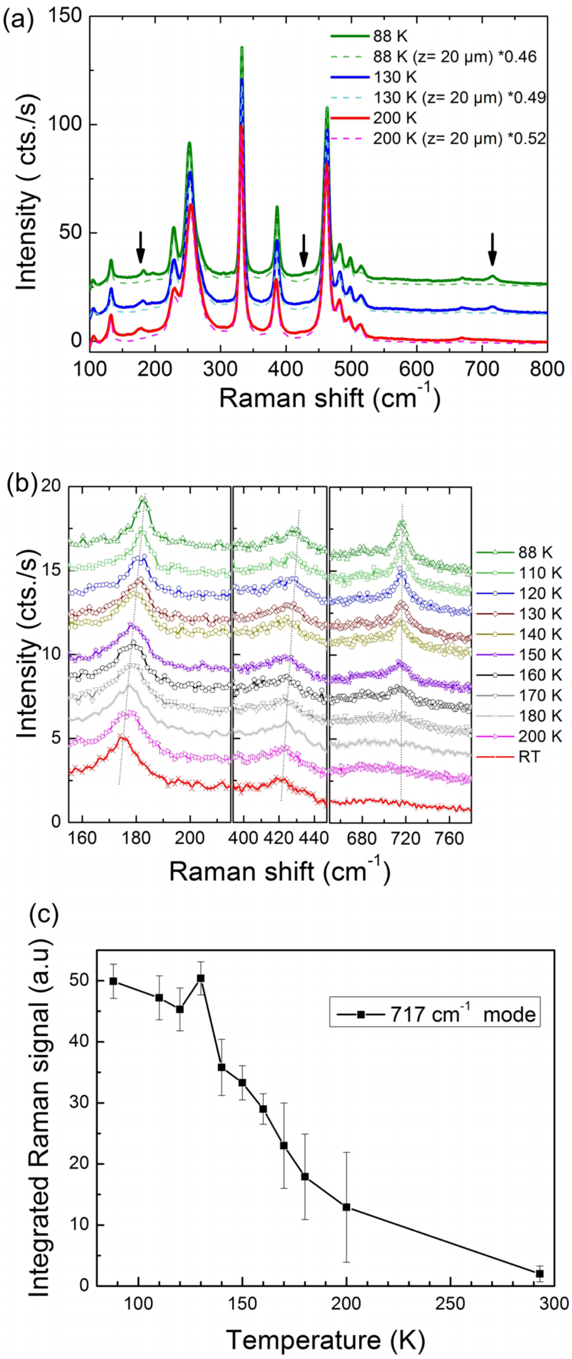

FIG. 4. Temperature-dependent Raman scattering spectroscopy of a 55 nm thick $LaVO_3$ film grown on $DyScO_3(110)$, capped with amorphous $SrTiO_3$: (a) Raman spectra at temperatures above and below the OO-transition, focusing at the sample surface (i.e., film/substrate signal, thick lines) and 20 μm below the surface (substrate signal only, thin dashed lines); the black arrows point at Raman peaks corresponding to the $LaVO_3$ film. (b) Detailed temperature dependence of the three observed Raman scattering peaks belonging to the $LaVO_3$ film was obtained by normalizing the two spectra at the same intensity and their subsequent subtraction. (c) Temperature dependence of the integrated intensity for the Raman peak occurring at about 717 cm^{-1}, evidencing the transition toward orbital ordering ($T_{OO} \approx 160$ K) in $LaVO_3$ films grown under tensile strain.

an oxygen bending mode that is active already at RT, see Ref. 17), 348 cm^{-1} (43 meV) and 513 cm^{-1} (63 meV), and at about 700-725 cm^{-1} (86-90 meV) (Fig. 5(a)). Around 700 cm^{-1} (86 meV), a broad peak is visible already at RT which it splits into two peaks at 90 K, one at 701 cm^{-1} (86 meV) and one at 725 cm^{-1} (90 meV). The former was attributed to the phonon density of states[18] and the

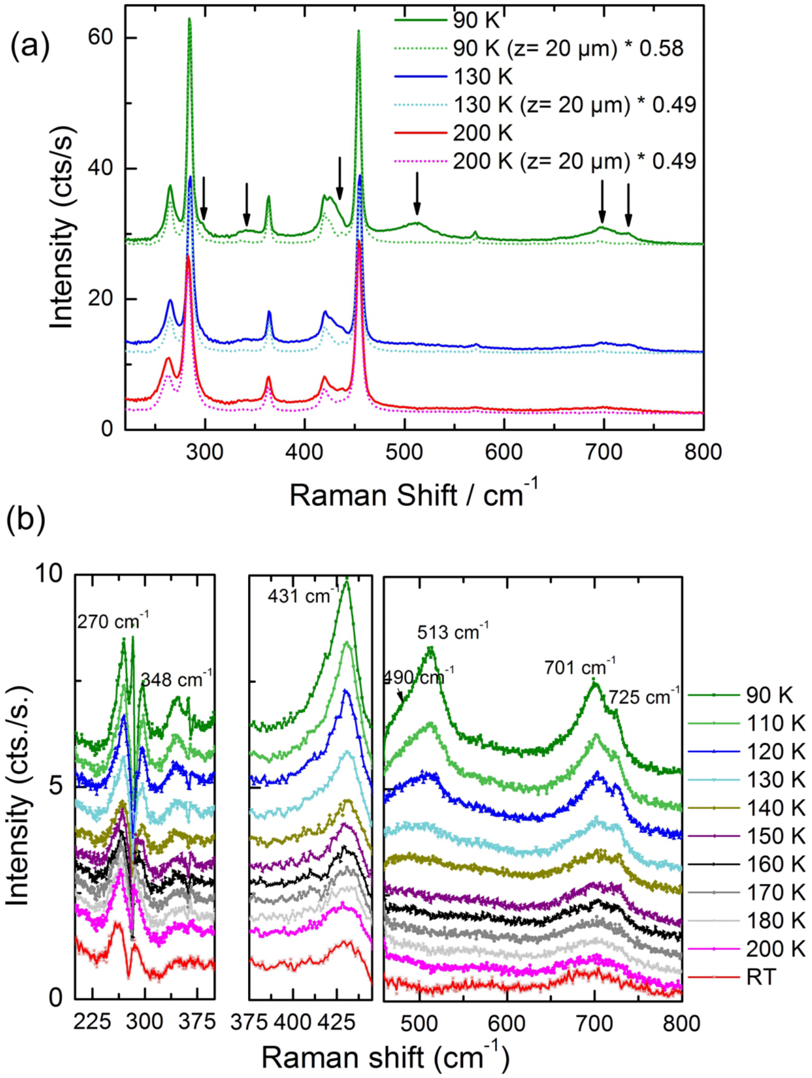

FIG. 5. Temperature-dependent Raman scattering spectroscopy of a 55 nm thick $LaVO_3$ film grown on a twinned $LaGaO_3(110)/(001)$ crystal: (a) Raman spectra at temperatures above and below the OO-transition, focusing at the sample surface (i.e., film/substrate signal, thick lines) and 20 μm below the surface (substrate signal only, thin dashed lines); the black arrows point at Raman peaks corresponding to the $LaVO_3$ film. (b) Detailed temperature dependence of the observed Raman scattering peaks belonging to the $LaVO_3$ film was obtained by normalizing the two spectra at the same intensity and their subsequent subtraction. The Raman band at about 270 cm^{-1} was affected by the subtraction procedure, because of the close proximity of a strong Raman mode of the $LaGaO_3$ crystal.

latter has been assigned to the A_g out-of-phase oxygen stretching mode. For LaVO3/LGO(110), the mode is shifted to higher energy as compared to the mode in $LaVO_3$/DSO(110) samples, in which it occurs at 717 cm^{-1} (89 meV) at 88 K. This energy difference indicates that compressive and tensile epitaxial strain influences the structure of $LaVO_3$ epitaxial films.

In addition to the characteristic phonon peak around 720 cm^{-1} (89 meV) clearly evidencing the structural phase transition and the onset of G-type OO in $LaVO_3$, the spectra of the $LaVO_3$/LGO sample (Fig. 5(b)) also show the appearance of two broad Raman bands at 348 cm^{-1} (43 meV) and 513 cm^{-1} (63 meV) below 160 K. These modes, which are also characteristic for the OO phase,[36] have been reported by Miyasaka *et al.*, who showed them to be resonantly enhanced when exciting at the Mott-Hubbard gap energy.[16,17] Even though it is generally agreed that these modes are associated with the OO phase, the precise origin of these modes is currently not clear. Miyasaka *et al.* assigned them to collective electronic excitations (two-orbiton excitations). Sugai and Hirota[37] argued that this assignment might be incorrect and that, for instance, the 513 cm^{-1} (63 meV) band is more likely due to a Jahn-Teller phonon, in analogy to similar modes in other orthorhombic perovskites.[32] It may be that these modes originate even from multi-phonon processes, as it was debated in the case of similar modes observed in OO phase of $LaMnO_3$.[38]

Summarizing, we fabricated epitaxial films of $LaVO_3$ on various crystals by PLD under reducing Ar/H_2 atmosphere and characterized their domain structure by high resolution scanning transmission electron microscopy. By Raman scattering spectroscopy, for the first time, we evidenced that the transition to orbital ordering occurs in $LaVO_3$ films, both under compressive and tensile strain. This enables the study of further aspects of orbital ordering, such as the influence of compressive *vs*. tensile strain and epitaxy-induced deformations of oxygen octahedra on the orbital-ordering and electronic structure of film samples. Raman scattering spectroscopy in conjunction with future temperature-dependent optical conductivity[19,30] and X-ray spectroscopy[39] measurements corroborated with VO_6 octahedra observations by electron microscopy can provide a comprehensive insight into the structure-electronic property relations of epitaxially modified $LaVO_3$.

I.V. thanks Chencheng Xu, Felix Hensling, Christoph Bäumer, and Dr. Paul Meuffels for kind assistance at PGI-7, Forschungszentrum Jülich. I.V. is also thankful to Professor Markus Grüninger and Professor Thomas Lorenz from II. Physics Institute of University of Cologne and to Dr. Eva Benckiser from MPI-FKF, Stuttgart for helpful discussions.

[1] S. Miyasaka, T. Okuda, and Y. Tokura, Phys. Rev. Lett. **85**, 5388 (2000).
[2] S. Miyasaka, Y. Okimoto, M. Ywama, and Y. Tokura, Phys. Rev. B **68**, 100406(R) (2003).
[3] E. Janod, J. Tranchant, B. Corraze, M. Querré, P. Stoliar, M. Rozenberg, T. Cren, D. Roditchev, V. T. Phuoc, M.-P. Besland, and L. Cario, Adv. Funct. Mater. **25**, 6287 (2015).
[4] Y. Hotta, T. Susaki, and H. Y. Hwang, Phys. Rev. Lett. **99**, 236805 (2007).
[5] Y. Hotta, Y. Mukunoki, T. Susaki, H. Y. Hwang, L. Fitting, and D. A. Muller, Appl. Phys. Lett. **89**, 031918 (2006).
[6] M. L. Scullin, J. Ravichandran, C. Yu, M. Huijben, J. Seidel, A. Majumdar, and R. Ramesh, Acta Mater. **58**, 457 (2010).
[7] H. Rotella, O. Copie, A. Pautraut, P. Boullay, A. David, D. Pellouquin, C. Labbe, C. Frilay, and W. Prellier, J. Phys.: Condens. Matter **27**, 095603 (2015).
[8] C. He, T. D. Sanders, M. T. Gray, F. J. Wong, V. V. Mehta, and Y. Suzuki, Phys. Rev. B **86**, 081401(R) (2012).
[9] F. S. Razavi, S. Jamali Gharetape, D. A. Crandles, G. Christiani, R. K. Kremer, and H.-U. Habermeier, Appl. Phys. Lett. **96**, 042110 (2010).
[10] F. J. Wong, S.-H. Baek, R. V. Chopdekar, V. V. Mehta, H.-W. Jang, C.-B. Eom, and Y. Suzuki, Phys. Rev. B **81**, 161101 (2010).
[11] C. W. Schneider, M. Esposito, I. Marozau, K. Conder, M. Doebeli, Y. Hu, M. Mallepell, A. Wokaun, and T. Lippert, Appl. Phys. Lett. **97**, 192107 (2010).
[12] X. Ke, C. Adamo, D. G. Schlom, M. Bernhagen, R. Uecker, and P. Schiffer, Appl. Phys. Lett. **94**, 152503 (2009).
[13] A. V. Mahajan, D. C. Johnston, D. R. Torgeson, and F. Borsa, Phys. Rev. B **46**, 10966 (1992).
[14] N. H. Hur, S. H. Kim, K. S. Yu, Y. K. Park, and J. C. Park, Solid State Commun. **92**, 541 (1994).
[15] O. Copie, H. Rotella, P. Boullay, M. Morales, A. Pautrat, P.-E. Janolin, I. C. Infante, D. Pravathana, U. Lüders, and W. Prellier, J. Phys.: Condens. Matter **25**, 492201 (2013).
[16] S. Miyasaka, S. Onodo, Y. Okimoto, J. Fujioka, M. Ywama, N. Nagaosa, and Y. Tokura, Phys. Rev. Lett. **94**, 076405 (2005).
[17] S. Miyasaka, J. Fujioka, M. Ywama, Y. Okimoto, and Y. Tokura, Phys. Rev. B **73**, 224436 (2006).
[18] B. Roberge, S. Jandl, A. A. Nugroho, T. T. M. Palstra, L. D. Tung, and G. Balakrishnan, J. Raman Spectrosc. **46**, 1157 (2015).
[19] S. Miyasaka, Y. Okimoto, and Y. Tokura, J. Phys. Soc. Jpn. **71**, 2086 (2002).
[20] J. Fujioka, S. Miyasaka, and Y. Tokura, Phys. Rev. Lett. **97**, 196401 (2006).
[21] I. Chaitanya Lekshami, A. Gayen, and M. S. Hegde, J. Phys. Chem. Solids **66**, 1647 (2005).
[22] H.-T. Zhang, L. R. Dedon, L. W. Martin, and R. Engel-Herbert, Appl. Phys. Lett. **106**, 233102 (2015).
[23] A. Shkabko, C. Xu, P. Meuffels, F. Gunkel, R. Dittmann, A. Weidenkaff, and R. Waser, APL Mater. **1**, 052111 (2013).
[24] M. Hepting, M. Minola, A. Frano, G. Cristiani, G. Logvenov, E. Schierle, M. Wu, M. Bluschke, E. Weschke, H. U. Habermeier, E. Benckiser, M. Le Tacon, and B. Keimer, Phys. Rev. Lett. **113**, 227206 (2014).
[25] P. Bordet, C. Chaillout, M. Marezio, Q. Huang, A. Santoro, S.-W. Cheong, H. Takagi, C. S. Oglesby, and B. Batlogg, J. Solid State Chem. **106**, 253 (1993).
[26] H. Rotella, O. Copie, G. Steciuk, H. Ouerdana, P. Boullay, P. Roussel, M. Morales, A. David, A. Pautraut, B. Mercey, L. Lutterotti, D. Chateigner, and W. Prellier, J. Phys.: Condens. Matter **27**, 175001 (2015).
[27] G. Sclauzero and C. Ederer, Phys. Rev. B **92**, 235112 (2015).
[28] T. Ohnishi, K. Shibuya, T. Yamamoto, and M. Lippmaa, J. Appl. Phys. **103**, 103703 (2008).
[29] H. Rotella, U. Lüders, P.-E. Janolin, V. H. Dao, D. Chateigner, R. Feyerherm, E. Dudzik, and W. Prellier, Phys. Rev. B **85**, 184101 (2012).
[30] J. Reul, A. A. Nugroho, T. T. M. Palstra, and M. Grüninger, Phys. Rev. B **86**, 125128 (2012).
[31] G. Yuan, K. Nishino, M. Lippmaa, and A. Uedono, J. Phys. D: Appl. Phys. **43**, 025301 (2010).

[32] M. N. Iliev, M. V. Abrashev, H.-G. Lee, V. N. Popov, Y. Y. Sun, C. Thomsen, R. L. Meng, and C. W. Chu, Phys. Rev. B **57**, 2872 (1998).

[33] H. Wadati, Y. Hotta, M. Takizawa, A. Fujimori, T. Susaki, and H. Y. Hwang, J. Appl. Phys. **102**, 053707 (2007).

[34] S. Yano, D. Louca, J. C. Neuefeind, J.-Q. Yan, J.-S. Zhou, and J. B. Goodenough, Phys. Rev. B **90**, 214111 (2014).

[35] L. Gasparov, T. Jegorel, L. Loetgering, S. Middey, and J. Chakhalian, J. Raman Spectrosc. **45**, 465 (2014).

[36] S. Ishihara, Phys. Rev. B **69**, 075118 (2004).

[37] S. Sugai and K. Hirota, Phys. Rev. B **73**, 020409(R) (2006).

[38] M. Grüninger, R. Rückamp, M. Windt, P. Reutler, C. Zobel, T. Lorenz, A. Freimuth, and A. Revcolevschi, Nature **418**, 39 (2002).

[39] B. Chen, J. Laverock, D. Newby, Jr., J. F. McNulty, K. E. Smith, P.-A. Glans, J.-H. Guo, R.-M. Qiao, W.-L. Yang, M. R. Lees, L. D. Tung, R. P. Singh, and G. Balakrishnan, J. Phys.: Condens. Matter **27**, 105503 (2015).

APPLIED PHYSICS LETTERS **106**, 012908 (2015)

Optical properties of epitaxial BiFeO$_3$ thin films grown on LaAlO$_3$

Cameliu Himcinschi,[1,a)] Akash Bhatnagar,[2,3] Andreas Talkenberger,[1] Mykhailo Barchuk,[4] Dietrich R. T. Zahn,[5] David Rafaja,[4] Jens Kortus,[1] and Marin Alexe[3]
[1]*Institute of Theoretical Physics, TU Bergakademie Freiberg, D-09596 Freiberg, Germany*
[2]*Max Planck Institute of Microstructure Physics, Weinberg 2, D-06120 Halle, Germany*
[3]*Department of Physics, University of Warwick, Coventry CV4 7AL, United Kingdom*
[4]*Institute of Materials Science, TU Bergakademie Freiberg, D-09596 Freiberg, Germany*
[5]*Semiconductor Physics, Technische Universität Chemnitz, D-09107 Chemnitz, Germany*

(Received 7 October 2014; accepted 20 December 2014; published online 7 January 2015)

Highly strained and nearly pseudomorphic BiFeO$_3$ epitaxial films were deposited on LaAlO$_3$ and TbScO$_3$ substrates, respectively. The symmetry of the tetragonal-like BiFeO$_3$ films is discussed based on polarisation dependent Raman measurements and on the comparison with Raman spectra measured for rhombohedral films deposited on TbScO$_3$. The evaluation of ellipsometric spectra reveals that the films deposited on LaAlO$_3$ are optically less dense and the features in complex dielectric function are blue-shifted by 0.3 eV as compared to the rhombohedral films. Optical bandgaps of 3.10 eV and 2.80 eV were determined for the films deposited on LaAlO$_3$ and TbScO$_3$, respectively. The shift in the optical bandgap and dielectric function is nearly preserved also for thicker films, which indicates that the compressive strain is retained even in films with thicknesses above 100 nm as was confirmed also by XRD investigations. © *2015 AIP Publishing LLC*.
[http://dx.doi.org/10.1063/1.4905443]

BiFeO$_3$ (BFO) is one of the multifunctional materials that was intensively studied in the last decade due to its multiferroic properties at room temperature (RT).[1,2] Bulk BFO shows a distorted perovskite structure with rhombohedral symmetry (R3c) and the polarisation along a $\langle 111 \rangle$ pseudocubic (*pc*) direction. Considering the eight *pc* equivalent directions, one can get eight degenerate states for the polarisation. In thin films, the polarisation can be increased by strain engineering of the domains.[3] This has been achieved by depositing BFO films on substrates with reduced symmetry (such as rare earth scandates),[4] or using substrates with off-cut, and/or with a large lattice mismatch with respect to BFO, for example, LaAlO$_3$ (LAO). BFO thin films grown on LAO substrate showed interesting properties, such as an enhanced electromechanically response,[5] giant polarization,[6] multiferroic phase transition at RT,[7] and a persistent photoconductivity.[8] These properties open doors to applications in many fields.[9]

Such tetragonal-like (T-like) highly strained BFO thin films are experimentally stabilised by epitaxial and pseudomorphic growth on LAO substrates.[10,11] A highly strained structure with c/a ratio of 1.3 and five-fold-coordinated Fe atoms has also been predicted using DFT calculations when the compressive strain is larger than 4%.[12] Subsequent studies revealed the structure of such highly strained films to be monoclinic (M$_c$), which is different from the M$_A$ structure observed in BFO films grown on SrTiO$_3$ substrates.[13]

Despite intensive research, the structure and microstructure of such T-like BFO films are still under debate.[14–16] Raman spectroscopy, which is a very sensitive local probe of the lattice dynamics, can contribute to solve part of the structure-related open questions.[17–19] In this work we use Raman spectroscopy for the characterisation of strain stabilised T-like films of BFO with different thicknesses that are grown on LAO. Henceforth we compare the results with those obtained for the relaxed and rhombohedral BFO films deposited on TbScO$_3$ (TSO) substrates. Considering the photovoltaic[20] and linear electro-optical effects[21] reported for BFO films, and their possible integration in oxide-based solar cells, the knowledge of the dielectric function and optical bandgap of the T-like BFO is crucial. The complex dielectric function and the optical bandgap of these films are derived from spectroscopic ellipsometry measurements.

BFO films were deposited on (001)$_{\mathrm{pc}}$ LAO and (110) TSO substrates using pulsed laser deposition. An excimer laser with a fluency of 0.35 J/cm^2, focused on BFO stoichiometric ceramic target was employed and the substrates were kept at 650 °C during deposition. High resolution X-ray diffraction (HRXRD) experiments were performed on an URD6 diffractometer at 0.154056 nm (CuKα1 radiation), with a monochromator (perfect (111)-oriented dislocation-free Si single-crystal) in the primary beam, and with a 0.13° wide slit in front of the point detector. The ellipsometry measurements were performed at several angles of incidence using an M-2000 Woollam ellipsometer. Raman spectroscopy was performed at RT using a Horiba Jobin Yvon HR 800 spectrometer. The 442 nm line of a HeCd laser was used for excitation, the light being focused and collected through a 100× magnification objective (ca. 1 μm focus size). The laser power was kept below 1 mW in order to avoid changes in the Raman spectra induced by the laser heating.

In Figure 1, atomic force microscopy (AFM) images of a thin (ca. 29 nm) and a thick (ca. 118 nm) film deposited on LAO substrate are shown. The thin film exhibits a smooth topography (Fig. 1(a)) with lattice planes high terraces of ca. 300 nm width, as can be seen in the line profile in the lower panel. The terraces are the fingerprint of the 0.1° off-cut substrate and are preserved after deposition of ca. 29 nm BFO,

---

[a)]E-mail: himcinsc@physik.tu-freiberg.de

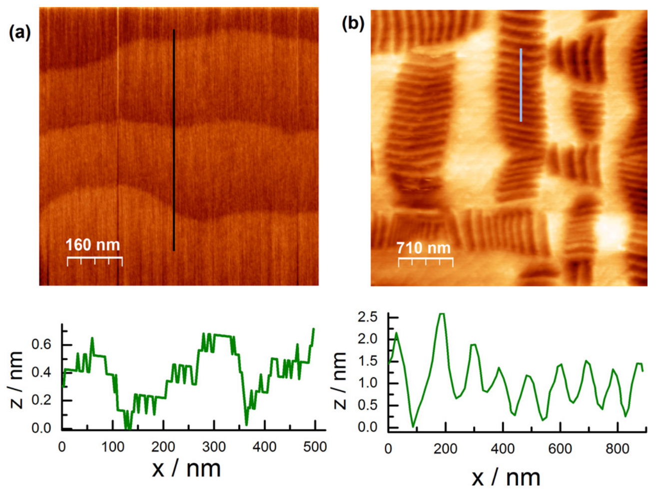

FIG. 1. AFM topography images of the surface of (a) thin (29 nm) and (b) thick (118 nm) T-like BFO films on LAO substrates. The lower panels show the corresponding depth profiles along the trace lines.

indicating a high quality layer-by-layer growth. In the thick film (Fig. 1(b)), the morphology shows stripe-like features, which can be attributed to a partial relaxation of the strain and consists of a mixture of monoclinic phases.[5] The corresponding height profile along the trace line is shown in the lower part of Fig. 1(b).

In Figure 2(a), the cross section HRTEM micrographs of the interface region of a 118 nm BFO film grown on LAO substrate are displayed. The image shows a sharp interface indicating an epitaxial growth of the BFO film on LAO substrate. The θ-2θ XRD pattern of a 118 nm thick BFO film grown on LAO substrate (Fig. 2(b)) exhibit the $(002)_{pc}$ reflections of the BFO film and the (002) LAO substrates. For reference, the XRD pattern from a 43 nm thick BFO film deposited on TSO substrate is also plotted. The peak from the BFO film deposited on TSO appears as a shoulder at $2\theta \sim 45.3°$ close to the TSO substrate peak at $2\theta \sim 45.9°$. This is due to the similar *pc* lattice parameters of bulk BFO and TSO. On the other hand for the BFO film deposited on LAO substrate, the peak of the film is down shifted to $2\theta \sim 38.5°$ in comparison with the substrate peak $2\theta \sim 48°$. This reflects the presence of a large compressive strain in the film and yields to an out-of-plane lattice parameter of $c = 4.67$ Å for the BFO/LAO film and a lattice parameter for LAO of 3.80 Å. Previous investigations of the reciprocal space mapping (RSM) on similar films[8] showed that the in-plane lattice parameters of the BFO films on LAO are nearly equal to that one of the LAO substrate. This allows to determine an equivalent tetragonality ratio of ∼1.23 for the highly strained BFO films. Additionally, the RSM demonstrates a three-fold splitting of the $(103)_{pc}$ peak of the BFO films,[8] which is characteristic for the M_c structure.[13,22]

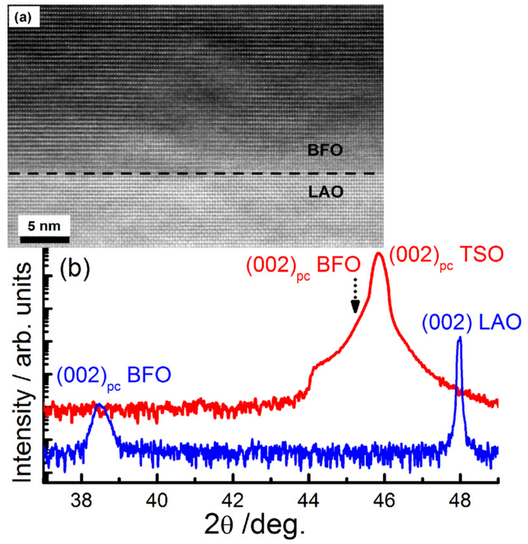

FIG. 2. (a) HRTEM cross section of the interface region of a 118 nm BFO film grown on LAO substrate. (b) *θ-2θ* XRD pattern of a 43 nm thick BFO film deposited on TSO substrate and *θ-2θ* HRXRD of a 118 nm thick BFO film grown on LAO substrate.

The tilting or rotation of the oxygen octahedra has been proposed as a possible mechanism, which allows the accommodation of large strain.[12,23] As a result, the strain can persist in films over larger values of thickness.[13] This mechanism also seems to be dominant in the case of our 118 nm thick BFO film deposited on the LAO substrate. Henceforth, in this work, the BFO films deposited on TSO substrates will be referred as R-like films, because of the good match of the lattice parameter with those of bulk rhombohedral BFO (*pc* lattice parameter: 3.965 Å).[24] The films deposited on LAO will be referred to as T-like, because of the large c/a ratio, although, and as discussed previously, they demonstrate an M_c structure. In order to probe the lattice dynamics in the T-like BFO phase, we employed Raman spectroscopy.

The Raman spectra of the samples were measured in backscattering configuration for parallel $(z(y,y)\bar{z})$ and cross polarisation $(z(y,x)\bar{z})$. z indicates the direction of the laser which was parallel to the $[001]_{pc}$ LAO direction or to the [110] orthorhombic direction of TSO. y was the direction of the incident polarisation (parallel to $[100]_{pc}$ LAO or [-110] TSO), while the scattered radiation was detected either parallel on the y direction, or perpendicular along the x direction (parallel to $[010]_{pc}$ LAO or [001] TSO) for the cross polarisation. The Raman spectra of the LAO and TSO substrates were measured separately, using the same scattering configuration, scaled at the same intensity with the spectra of film/substrate, and subsequently subtracted from these spectra.

In Figure 3, the subtracted Raman spectra of BFO in BFO/LAO and BFO/TSO samples are shown for both parallel and cross polarisation configurations. In the region below $250\,\mathrm{cm}^{-1}$, the stronger peaks of the *R3c* BFO phase appear[25,26] at $137\,\mathrm{cm}^{-1}$, $173\,\mathrm{cm}^{-1}$, and $219\,\mathrm{cm}^{-1}$, which are attributed to vibrations that involve Bi and Fe atoms.[27] These peaks change their relative intensities and are clearly blue shifted by 6–$8\,\mathrm{cm}^{-1}$ in the case of T-like BFO, which can indicate a larger compressive strain. Moreover, new modes, from which the strongest are at $263\,\mathrm{cm}^{-1}$, $367\,\mathrm{cm}^{-1}$, $481\,\mathrm{cm}^{-1}$, $511\,\mathrm{cm}^{-1}$, and $691\,\mathrm{cm}^{-1}$ are identified in the spectra of the T-like BFO films. It should be mentioned that around $367\,\mathrm{cm}^{-1}$ a very weak feature appears also in the spectrum of R-like film but only when recorded in cross polarisation, indicating different symmetry. Overall, the Raman spectra of T-like BFO show a larger number of phonons as compared with spectra of BFO/TSO film. The larger number of phonons and their polarisation dependence was

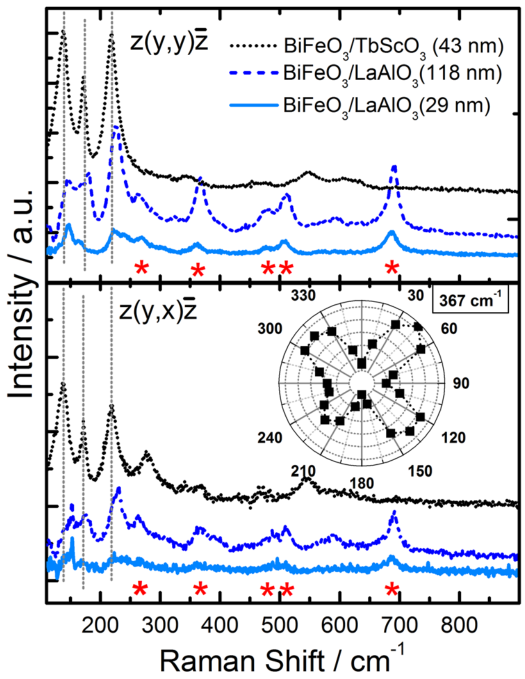

FIG. 3. Subtracted Raman spectra of BFO in BFO/LAO (T-like) and BFO/TSO (R-like) samples for parallel $(z(y,y)\bar{z})$ and cross polarisation $(z(y,x)\bar{z})$.The peaks marked by "*" indicate the most intensive new peaks belonging to the T-like phase. The polar plot of the intensity of the 367 cm^{-1} mode measured in cross polarisation $(z(y,x)\bar{z})$ is shown in the inset.

used by Iliev *et al.*[17,22] to demonstrate monoclinic (Cc) symmetry. Tetragonal symmetries could be excluded because in that case a smaller number of phonons would be expected.

The Raman spectra of the T-like BFO show a strong polarisation dependence. In order to follow this polarisation dependence in detail, we performed measurements for the thicker T-like BFO film, by azimuthally rotating the samples in 15° steps around the z direction (laser) for both parallel and cross polarisation configurations. The spectra obtained were fitted using Gauss functions for each phonon mode. Some of the modes (at 179 cm^{-1}, 225 cm^{-1}, 263 cm^{-1}, 367 cm^{-1}, and 511 cm^{-1}) show a remarkable dependence of their intensity on the azimuthal angle for both parallel and cross polarisation configurations. In particular, we show in the inset of Fig. 3, the strong angular dependence of the intensity of the 367 cm^{-1} mode for the cross polarisation, which indicates a very good in plane orientation of the T-like BFO films.

Because of the lack of T-like BFO single crystals, and therefore lack of measurements done on different scattering surfaces, the complete assignment of all modes cannot be resolved solely from the measurements discussed here. However, based on the Raman tensor of the Cc monoclinic structure and on the symmetry considerations of Iliev *et al.*,[17] the angular intensity dependence of the modes at 367 cm^{-1}, 263 cm^{-1}, and 225 cm^{-1} indicate an A'' symmetry for these modes. Special attention should be paid to the mode at 691 cm^{-1}, which has the highest frequency reported for modes of BFO and is absent in rhombohedral BFO films. This mode was proposed to be a hallmark of high tetragonality (c/a ratio).[28] It should relate to a vibration involving O-atoms[27] and could be a signature of the five-oxygen coordination of Fe (as FeO$_5$ pyramids, and not FeO$_6$ octahedras).[12] Such a change in oxygen coordination in the T-like phase should modify the electronic structure which implies also changes in the dielectric function. We used ellipsometry to measure the complex dielectric function of the T-like BFO phase.

Ellipsometry measures the changes of the polarisation of light after reflection on the investigated sample in form of Ψ and Δ ellipsometric parameters. Analytic expressions for calculating Ψ and Δ as functions of dielectric function and layer thickness can be found in standard textbooks, e.g., Azzam *et al.*[29] In Figure 4(a), the ellipsometric spectra measured at different angles for a BFO thin film deposited on LAO substrate are shown by symbols. The in-plane rotation of the sample brought the same spectra. Considering that the light spot on the sample (ca. 1 mm) is much larger than the ferroelectric domains, we used an isotropic model for evaluation of the optical response of the film.

The measured Ψ and Δ spectra depend on the thickness of the films, and on the dielectric function of both film and substrate. The complex dielectric functions of the TSO and LAO were *a priori* determined from measurements performed on bare substrates. Using the predetermined dielectric functions of the substrates, the ellipsometric spectra of the BFO films/substrate were evaluated. The absorption free range below 2.2 eV was used first for an initial estimation of the film thicknesses using a Cauchy dispersion relation for the refractive index. In order to extract the dielectric response of the BFO films from the ellipsometric data, a three-layer optical model consisting of ambient air/film/substrate was used. A sum of three Gauss oscillators was used to simulate the optical response of the BFO films. Gauss oscillators[30] of the form

$$\varepsilon_{2Gauss} = \sum_n A_n \cdot \left[e^{-4\cdot\ln 2\cdot\left(\frac{E-E_n}{B_n}\right)^2} + e^{-4\cdot\ln 2\cdot\left(\frac{E+E_n}{B_n}\right)^2}\right] \qquad (1)$$

produce a line shape in the imaginary part of the complex dielectric function ε_2, with a Kramers-Kronig consistent line shape for ε_1, where A_n, E_n, and B_n, are the amplitude, energy, and broadening, respectively. The unknown parameters in the model were adjusted in order to get the best match between the model and the experimental data by a fitting procedure, which minimizes the mean square error. The results of the fit: thickness, energy, amplitude, and broadening of the Gauss oscillators for the three BFO films are summarised in Table I. The error bars in determination of thickness are given in Table I, while for all other fit parameters the error bars are lower than 0.03. The fits obtained for the 118 nm thick BFO film on LAO substrate are shown by continuous lines in Fig. 4(a) together with the experimental data (symbols).

The calculated real and imaginary parts of the complex dielectric function for all three investigated films are shown in Fig. 4(b). The imaginary part of the BFO complex dielectric function of the BFO/TSO film is dominated by two absorption peaks at ~3.1 eV and ~4.3 eV assigned to charge transfer excitation.[31] These peaks are blue-shifted in the case of both BFO/LAO films, which induce an overall shift of the complex dielectric function by ca. 0.3 eV to higher energies. Such a large shift cannot be explained only as a strain

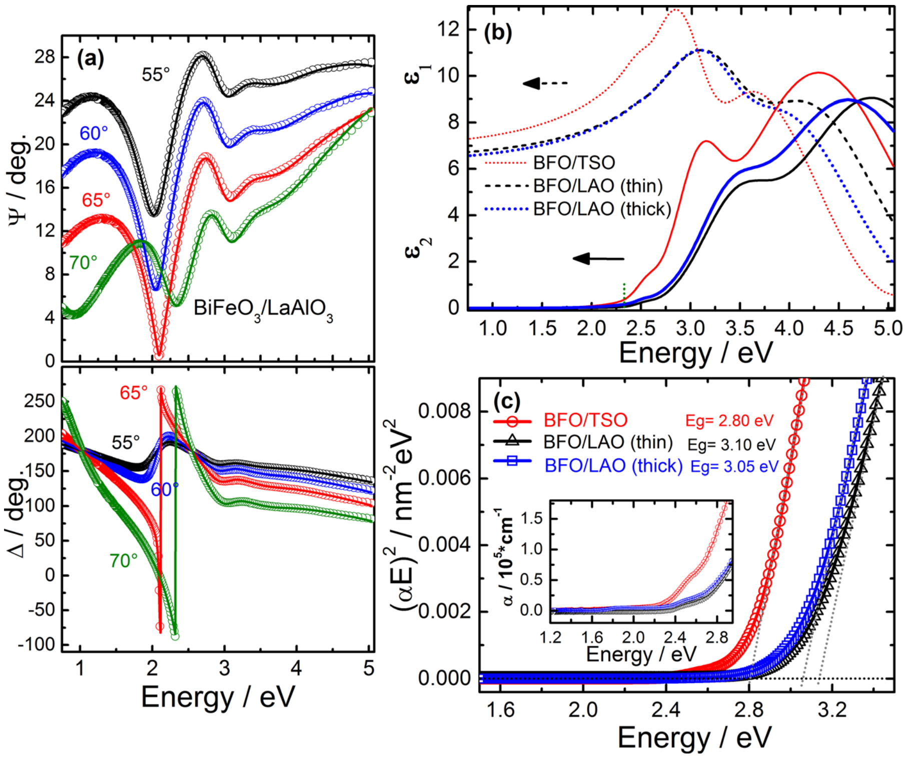

FIG. 4. (a) Ψ and Δ ellipsometric parameters as measured (symbols) and fitted (continuous lines) for a 118 nm BFO film grown on LAO substrate. (b) The calculated real (ε_1) and imaginary part (ε_2) of the complex dielectric function of R-like BFO (films on TSO) and T-like BFO (films on LAO). (c) $(\alpha{\cdot}E)^2$ plot as function of photon energy. The linear extrapolations to zero give the values for direct optical band gaps. The inset shows the absorption coefficients determined by direct numerical inversion.

(elastic) effect and indicates that the T-like BFO phase has a different electronic structure reflected in the different complex dielectric function as compared to R-like BFO films. A similar effect was reported in the case of T-like BFO films deposited on $YAlO_3$ and on LAO for films with thickness below 30 nm.[32,33] In our case the blue-shift of the complex dielectric function is nearly completely preserved also for the 118 nm thick film on LAO, which means that this thick film is still highly strained, as confirmed by XRD measurements. In the absorption free region below 2 eV, the real part of the complex dielectric function for the R-like BFO is larger than of the T-like BFO, which implies that the T-like phase is optically less dense than the R-like phase. Our results are in line with second harmonic generation studies on T-like BFO films.[34] The weak absorption band at 2.5 eV present in all investigated films was previously attributed to defect states.[35] Our T-like films exhibited sub-band gap levels around 2.5 eV in the photoelectrical measurements. Interestingly, these levels were found to be active at RT and thus are apparently capable of affecting the conduction mechanism.[8] The dotted line at 2.33 eV indicates the position of the 532 nm laser line used as excitation for Raman measurements.

TABLE I. Thickness and the BFO complex dielectric function Gaussian oscillator parameters: energy (E_n), amplitude (A_n), and broadening (B_n) obtained after the optical modelling fit of the ellipsometric data for the BFO/TSO and BFO/LAO samples.

		Oscillator parameters		
Sample	Thickness/nm	E_n / eV	A_n	B_n / eV
R-like: BFO/TSO	43 ± 0.5	2.54	0.50	0.24
		3.07	4.25	0.50
		4.28	10.14	1.76
T-like BFO/LAO (thin)	29 ± 0.5	2.52	0.10	0.20
		3.42	3.39	0.79
		4.81	9.05	1.79
T-like BFO/LAO (thick)	118 ± 0.5	2.51	0.07	0.15
		3.36	2.58	0.67
		4.58	8.97	1.89

The onset of absorption region was analysed in order to determine the energy of the direct optical bandgap using the proportionality $\alpha \cdot E \sim (E - E_g)^{1/2}$, where $\alpha = (4\pi k/\lambda)$ is the absorption coefficient and E_g is the energy of the direct optical bandgap.[36] In Figure 4(c), $(\alpha \cdot E)^2$ is plotted versus photon energy. The linear extrapolation to zero absorption leads for R-like BFO to an optical bandgap value of 2.80 eV and for the thin and thick T-like films to values of 3.10 eV and 3.05 eV, respectively. The 0.3 eV blue shift observed in the dielectric function is also evident for the optical bandgap. Previous ellipsometric investigations show the invariance of the bandgap for R-like BFO films deposited on $SrTiO_3$ or LSAT substrates.[37] However, a moderate compressive strain, as in the case of BFO films deposited on $SrTiO_3$, was found to blue shift the optical bandgap and the complex dielectric function by 0.05 eV in comparison with BFO films deposited on $DyScO_3$.[38] In this paper, the shift in the complex dielectric function and optical bandgap of the T-like BFO is much larger as compared with R-like BFO films. This shift is slightly reduced in the 118 nm film to about 0.25 eV, which suggests that the thick film is probably containing a small fraction of R-like phase or other monoclinic phases, but still highly strained (predominantly T-like). A larger blue shift of the optical bandgap of about 0.4 eV, for T-like BFO films deposited on $YAlO_3$ (where the compressive strain is larger than in the case of LAO) was determined by Chen *et al.*[32] and was attributed to structural strain and local symmetry breaking. In the inset of Fig. 4(c) the absorption coefficient determined by direct numerical inversion (point-by-point fit) of the ellipsometric data, keeping the thickness fixed, is shown. Although this method does not insure the Kramers-Kronig consistency of the complex optical constants, it confirms the blue shift of 0.3 eV.

In summary, Raman studies confirmed very good epitaxy of the T-like BFO films grown on LAO substrates, reflected by the remarkable azimuthal/polarisation dependence of the Raman spectra. The larger numbers of phonons observed in the spectra of T-like BFO films as compared with that of R-like BFO films is consistent with a Cc monoclinic structure, with a large tetragonal c/a ratio. The complex dielectric function of T-like and R-like BFO films was determined using spectroscopic ellipsometry. An overall blue shift by ca. 0.3 eV of the complex dielectric function of the T-like BFO films was determined, these films being also optically less dense than R-like BFO films. The direct optical bandgap of T-like BFO was determined to be 3.10 eV, which is blue-shifted by 0.25–0.3 eV as compared with R-like BFO, slightly depending of the film thickness.

This work was supported by the German Research Foundation DFG HI 1534/1-2. M.A. acknowledges the support of Royal Society via Wolfson Award.

[1] G. Catalan and J. F. Scott, Adv. Mater. **21**, 2463 (2009).
[2] R. Ramesh and N. A. Spaldin, Nat. Mater. **6**, 21 (2007).
[3] L. W. Martin, Y. H. Chu, and R. Ramesh, Mater. Sci. Eng. R **68**, 89 (2010).
[4] F. Johan, A. Morelli, D. Biggemann, M. Aredondo, and I. Vrejoiu, Phys. Rev. B **84**, 094105 (2011).
[5] A. R. Damodaran, C.-W. Liang, Q. He, C.-Y. Peng, L. Chang, Y.-H. Chu, and L. W. Martin, Adv. Matter. **23**, 3170 (2011).
[6] D. Ricinschi, K. Y. Yun, and M. Okuyama, J. Phys.: Condens. Matter. **18**, L97 (2006).
[7] I. C. Infante, J. Juraszek, S. Fusil, B. Dupe, P. Gemeiner, O. Dieguez, F. Pailloux, S. Jouen, E. Jacquet, G. Geneste *et al.*, Phys. Rev. Lett. **107**, 237601 (2011).
[8] A. Bhatnagar, Y. H. Kim, D. Hesse, and M. Alexe, Nano Lett. **14**, 5224 (2014).
[9] H. Yamada, V. Garcia, S. Fusil, S. Boyn, M. Marinova, A. Gloter, S. Xavier, J. Grollier, E. Jacquet, C. Carretero *et al.*, ACS Nano **7**, 5385 (2013).
[10] H. Bea, B. Dupe, S. Fusil, R. Mattana, E. Jaquet, B. Warot-Fonrose, F. Wilhelm, A. Rogalev, S. Petit, V. Cros *et al.*, Phys. Rev. Lett. **102**, 217603 (2009).
[11] R. J. Zeches, M. D. Rossell, J. X. Zhang, A. J. Hatt, Q. He, C.-H. Yang, A. Kumar, C. H. Wang, A. Melville, C. Adamo *et al.*, Science **326**, 977 (2009).
[12] A. J. Hatt, N. A. Spaldin, and C. Ederer, Phys. Rev. B **81**, 054109 (2010).
[13] Z. Chen, Z. Luo, C. Huang, Y. Qi, P. Yang, L. You, C. Hu, T. Wu, J. Wang, C. Gao, T. Sritharan, and L. Chen, Adv. Funct. Mater. **21**, 133 (2011).
[14] F. Pailloux, M. Coouillard, S. Fusil, F. Bruno, W. Saidi, V. Gacia, C. Carretero, E. Jacquet, M. Bibes, A. Barthelemy *et al.*, Phys. Rev. B **89**, 104106 (2014).
[15] Y. H. Kim, A. Bhatnagar, E. Pippel, M. Alexe, and D. Hesse, J. Appl. Phys. **115**, 043526 (2014).
[16] H. M. Christen, J. H. Nam, H. S. Kim, A. J. Hatt, and N. A. Spaldin, Phys. Rev. B **83**, 144107 (2011).
[17] M. N. Iliev, M. V. Abrashev, D. Mazumdar, V. Shelke, and A. Gupta, Phys. Rev. B **82**, 014107 (2010).
[18] C. Beekman, W. Siemons, T. Z. Ward, M. Chi, J. Howe, M. D. Biegalski, N. Balke, P. Maksymovych, A. K. Farrar, J. B. Romero *et al.*, Adv. Matter. **25**, 5561 (2013).
[19] P. Hermet, M. Goffinet, J. Kreisel, and Ph. Ghosez, Phys. Rev. B **75**, 220102 (2007).
[20] T. Choi, S. Lee, Y. J. Choi, V. Kiryukhin, and S.-W. Cheong, Science **324**, 63 (2009).
[21] D. Sando, P. Hermet, J. Allibe, J. Bourderionnet, S. Fusil, C. Carretero, E. Jacquet, J.-C. Mage, D. Dolfi, A. Barthelemy *et al.*, Phys. Rev. B **89**, 195106 (2014).
[22] D. Mazumdar, V. Shelke, M. Iliev, S. Jesse, A. Kumar, S. V. Kalinin, A. P. Baddorf, and A. Gupta, Nano Lett. **10**, 2555 (2010).
[23] J. C. Wojdel and J. Iniguez, Phys. Rev. Lett. **105**, 037208 (2010).
[24] F. Kubel and H. Schmid, Acta Crystallogr., Sect. B: Struct. Sci. **46**, 698 (1990).
[25] H. Fukumura, S. Matsui, H. Harima, T. Takahashi, T. Itoh, K. Kisoda, M. Tamada, Y. Noguchi, and M. Miyayama, J. Phys.: Condens. Matter **19**, 365224 (2007).
[26] J. Hlinka, J. Pokorny, S. Karimi, and I. M. Reaney, Phys. Rev. B **83**, 020101 (2011).
[27] J. Bielecki, P. Svedlindh, D. T. Tibebu, S. Cai, S. G. Eriksson, L. Börjesson, and C. S. Knee, Phys. Rev. B **86**, 184422 (2012).
[28] J. Kreisel, P. Jadhav, O. Chaix-Pluchery, M. Varela, N. Dix, F. Sanchez, and J. Fontcuberta, J. Phys.: Condens. Matter **23**, 342202 (2011).
[29] R. M. A. Azzam and N. M. Bashara, *Ellipsometry and Polarized Light* (Elsevier, Amsterdam, 1992).
[30] K. E. Peiponen and E. M. Vartiainen, Phys. Rev. B **44**, 8301 (1991).
[31] S. R. Basu, L. W. Martin, Y. H. Chu, M. Gajek, R. Ramesh, R. C. Rai, X. Xu, and J. L. Musfeldt, Appl. Phys. Lett. **92**, 091905 (2008).
[32] P. Chen, N. J. Podraza, X. S. Su, A. Melville, E. Vlahos, V. Gopalan, R. Ramesh, D. G. Schlom, and J. L. Musfeldt, Appl. Phys. Lett. **96**, 131907 (2010).
[33] H. L. Liu, M. K. Lin, Y. R. Cai, C. K. Tung, and Y. H. Chu, Appl. Phys. Lett. **103**, 181907 (2013).
[34] R. C. Haislmaier, N. J. Podraza, S. Denev, A. Melville, D. G. Scholm, and V. Gopalan, Appl. Phys. Lett. **103**, 031906 (2013).
[35] A. J. Hauser, J. Zhang, L. Mier, R. A. Ricciardo, P. M. Woodward, T. L. Gustafson, L. J. Brillson, and F. Y. Yang, Appl. Phys. Lett. **92**, 222901 (2008).
[36] J. Tauc, R. Grigorovici, and A. Vancu, Phys. Status Solidi B **15**, 627 (1966).
[37] J. F. Ihlefeld, N. J. Podraza, Z. K. Liu, R. C. Rai, X. Xu, T. Heeg, Y. B. Chen, J. Li, R. W. Collins, J. L. Musfeldt *et al.*, Appl. Phys. Lett. **92**, 142908 (2008).
[38] C. Himcinschi, I. Vrejoiu, M. Friedrich, E. Nikulina, L. Ding, C. Cobet, N. Esser, M. Alexe, D. Rafaja, and D. R. T. Zahn, J. Appl. Phys. **107**, 123524 (2010).

Received: 29 April 2015 Revised: 6 July 2015 Accepted: 10 July 2015

(wileyonlinelibrary.com) DOI 10.1002/jrs.4762

Raman spectroscopic investigations of epitaxial $BiFeO_3$ thin films on rare earth scandate substrates

Andreas Talkenberger,[a]* Ionela Vrejoiu,[b] Florian Johann,[b] Christian Röder,[a] Gert Irmer,[a] David Rafaja,[c] Gerhard Schreiber,[c] Jens Kortus[a] and Cameliu Himcinschi[a]*

$BiFeO_3$ epitaxial thin films fabricated by pulsed laser deposition on different scandate substrates were investigated by means of Raman spectroscopy. We observed periodic changes in Raman position, full width at half maximum and intensity for some phonon modes as a function of the azimuthal angle ϕ. Further analysis revealed the possibility to assign the so far controversial discussed Raman modes at low wavenumbers ($<250\,cm^{-1}$) through rotational Raman measurements at different azimuthal angles, which show high sensitivity to the aforementioned parameters. Furthermore, the ferroelectric/ferroelastic domain structure shown by piezo-response force microscopy investigations of the samples was confirmed. Our results are supported by symmetry-based calculations including the analysis of Raman scattering geometry as well as the dielectric function of $BiFeO_3$ in the infrared range. Copyright © 2015 John Wiley & Sons, Ltd.

Keywords: Raman tensor; multiferroic; thin film; bismuth ferrite; azimuthal rotation

Introduction

As one of the most promising single-phase multiferroic materials due to its ferroelectricity and antiferromagnetism at room temperature,[1] the list of publications on $BiFeO_3$ (BFO) in literature is exceptionally long.[2,3] In particular, many results regarding Raman spectroscopic investigations and optical properties of BFO were published; however, some works contain still a few inconsistencies. With a rhombohedrally distorted perovskite structure along the pseudo-cubic $(111)_{pc}$ direction, BFO is described within the hexagonal space group R3c.[4] Group theory predicts 30 phonon normal modes at the Γ-point of the Brillouin zone; three of them are acoustic. Its point group C_{3v} classifies 27 optical phonon modes in the zone centre:

$$\Gamma_{\mathrm{opt,R3c}} = 4A1 + 5A2 + 9E \qquad (1)$$

All phonon modes except the five $A2$ modes are both Raman and infrared (IR) active; the E modes are doubly degenerated.[5,6] The polar modes of $A1$-symmetry and E-symmetry split into transverse optical (TO) and longitudinal optical (LO) phonon modes with different wavenumbers because of the macroscopic electric field associated with the longitudinal modes. For the lattice vibrations with $A1$-symmetry and E-symmetry, the atomic displacement is parallel and perpendicular to the hexagonal z-axis (also referred to as the optical c-axis), respectively. The crystallographic orientation between hexagonal and pseudo-cubic system is $\langle 111\rangle_c \,||\, [001]_{hex}$, as depicted in Fig. 1. In uniaxial crystals, phonon wavenumbers of extraordinary modes show dispersion depending on the angle θ between the transferred phonon wave vector and the hexagonal z-axis (c-axis). In contrast, the wavenumber of the ordinary TO phonons with polarisation in the x,y-plane is independent of θ. In backscattering geometry along the $(100)_{pc}$ direction, the angle $\theta \approx 54.7\,°$ is realised (cf. Fig. 1), resulting in spectra of ordinary E_{TO} phonons and extraordinary phonons with mixed $A1$–E-symmetry or TO–LO-character.[7] Measurements with the phonon wave vector parallel to the hexagonal z-axis ($\theta = 0\,°$) allow the observation of the extraordinary TO phonons of E-symmetry and LO modes of $A1$-symmetry. In case of measurements with the phonon wave vector in the x,y-plane ($\theta = 90\,°$), the extraordinary E_{LO} and $A1_{TO}$ modes can be detected.

From a theoretical point of view, Hermet *et al.*[8] calculated the entire zone-centre phonon spectrum of BFO by means of density functional theory. They conclude a contribution of bismuth atoms to low-wavenumber modes up to $167\,cm^{-1}$, of iron atoms to modes between 152 and $261\,cm^{-1}$ but also to modes at higher wavenumbers and of oxygen atoms above $262\,cm^{-1}$.[8] When comparing the symmetry assignment to the particular phonon modes, several discrepancies appear in literature. Singh *et al.*[6] assigned $A1_{LO}$-symmetry to the prominent BFO phonon modes at

---

* *Correspondence to: Andreas Talkenberger and Cameliu Himcinschi, TU Bergakademie Freiberg, Institute of Theoretical Physics, Leipziger Str. 23, Freiberg D-09596, Germany.*
E-mail: andreas.talkenberger@physik.tu-freiberg.de; himcinsc@physik.tu-freiberg.de

a *TU Bergakademie Freiberg, Institute of Theoretical Physics, Leipziger Str. 23, Freiberg D-09596, Germany*

b *Max Planck Institute of Microstructure Physics, Weinberg 2, Halle D-06120, Germany*

c *TU Bergakademie Freiberg, Institute of Materials Science, Gustav-Zeuner-Str. 5, Freiberg D-09596, Germany*

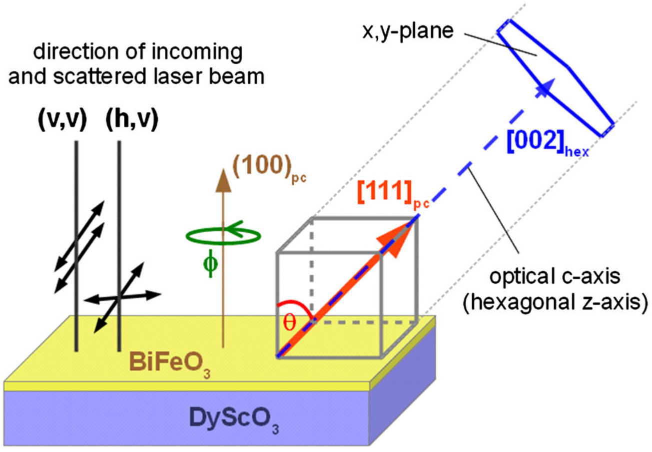

Figure 1. Crystallographic orientation between the pseudo-cubic and hexagonal crystal system. The optical *c*-axis $[111]_{pc}$ corresponds to the hexagonal *z*-axis $[002]_{hex}$. For Raman experiments, the direction of the incoming and scattered laser light is parallel to the surface normal $(100)_{pc}$, shown for parallel and crossed polarisation configuration by the black lines at the left.

136, 168 and 212 cm^{-1} by investigating a "cube on cube" epitaxially grown rhombohedral thin film on $SrTiO_3$ (111) substrate. Also, Fukumura *et al.*[9] as well as Cazayous *et al.*[10] found the *A*1-symmetry for these three modes on BFO single crystals by measuring (111) and (001) pseudo-cubic planes. Porporati *et al.*[11] investigated a coarse-grained BFO polycrystal assigning corresponding modes to E_{TO}-symmetry (136 cm^{-1}) and $A1_{LO}$-symmetry (176 and 219 cm^{-1}). BFO single crystals with pseudo-cubic (100) facets as well as epitaxially grown BFO thin films on $SrTiO_3$ (100) with a $SrRuO_3$ buffer layer were studied by Palai *et al.*,[12] who attest a pseudo-orthorhombic monoclinic crystal structure to the thin film in comparison to the rhombohedral single crystal. Regarding the symmetry assignment, E_{TO}-symmetry is here proposed for all three mentioned phonon modes.[13,14] Hlinka *et al.*[15] determined phonon symmetry by investigating the angular dependence of the phonon mode wavenumbers in sintered BFO ceramic samples as function of the orientation of the phonon propagation vector. They concluded an E_{TO} mode at 132 cm^{-1}, $A1_{LO}$ modes at 178 and 229 cm^{-1}, $A1_{TO}$ modes at 149 and 223 cm^{-1} and an E_{LO} mode at 175 cm^{-1}. The group of Beekman *et al.*[16] gave a symmetry assignment based on rotating the polarisation direction of the exciting laser on (100) pseudo-cubic single crystals. They suggested *E*-symmetry for the intense transverse (TO) modes at 135, 172 and 218 cm^{-1}.

In comparison to single crystals of BFO, epitaxially grown thin films often possess a substrate-induced strain that might lead to the formation of domain patterns in the film and changes of the crystalline symmetry, in order to adapt to the symmetry of the underlying substrate.[17] The influence of the strain and thereby the formation of domain variants in the BFO samples, which we study here by Raman spectroscopy, are investigated in the work of Johann *et al.*.[18] Raman intensity rotational measurements allow to draw conclusions on the distribution of domains, as shown by Rafiq *et al.*,[19] who ascertain a contribution of neighbouring domains to the Raman signal of certain modes in $(K_{0.5}Na_{0.5})NbO_3$ single crystals. A crystallographic domain texture can also affect the wavenumber of the phonon modes because of its different mechanical strains causing wavenumber shifts of the phonon modes in the spectra, as presented in the works of Sakashika *et al.*[20] and Deluca *et al.*[21] for polycrystalline barium titanate and lead zirconate titanate, respectively.

An approach similar to Beekman's[16] experiments is the basis of our investigation on BFO thin films on $DyScO_3$ (DSO), $GdScO_3$ (GSO) and $SmScO_3$ (SSO) substrates by means of highly sensitive Raman spectroscopic experiments. By rotating the thin film samples around the laser and keeping the point of measurement, we detected a periodic variation of Raman intensity, full width at half maximum (FWHM) and position with respect to the azimuthal angle ϕ. No data about the relation between Raman position, FWHM and ϕ for BFO thin films is to be found in literature: Only the intensity variations were reported. In this contribution, a detailed analysis of the phonon mode near 135 cm^{-1} is presented including the impact of another mode near 119 cm^{-1}, which was not detected in Raman spectra of thin film material before. Furthermore, Beekman *et al.*[16] determined Raman tensor elements for the different phonon modes by means of asymmetric Raman tensors, obtaining different tensor elements for different BFO crystals. For our symmetry calculations, we used the symmetric Raman tensors as specified in the tables of Claus *et al.*[22] and successfully simulated the azimuthal behaviour of Raman intensity and position of these two modes offering a symmetry assignment for both. Symmetric tensors are in agreement with the work of Loudon and Pezzotti *et al.*.[23,24] In addition, our experimental Raman data prove the domain character of the BFO/DSO thin film by showing the mentioned variation in Raman position, which is only possible with the existence of two types of ferroelastic domains. These results are confirmed by piezoresponse force microscopy (PFM) measurements.

Experimental

The BFO epitaxial thin films were grown by pulsed laser deposition on (110)-oriented orthorhombic DSO, GSO and SSO single crystal substrates after annealing them for 2 h at 975, 1100 and 1200 °C, respectively. The repetition frequency of the employed KrF laser was 5 Hz. During the growth process, a temperature of ~650 °C and an oxygen partial pressure of 14 Pa were established. PFM was performed with a cypher S system in contact mode and offers information about the ferroelectric/ferroelastic domain structure of the deposited film. Both, vertical and lateral (VPFM and LPFM), orientations of the diamond-coated conductive cantilevers were thereby employed to create a spatial conception of the polarisation patterns.

The Raman spectra were measured with a LabRam Horiba Jobin Yvon spectrometer with the 442-nm excitation line of a He–Cd laser in backscattering geometry, where the incident and scattered beam propagate perpendicularly to the surface of the sample. The measurements were carried out at room temperature by rotating the sample azimuthally around the surface normal in two polarisation configurations: (hv) where the electric field vector of the incoming laser light is perpendicular to the electric field vector of the scattered light and (vv) where these vectors are parallel to each other (Fig. 1). The scattered light was collected with an objective of x100 magnification. To avoid a laser-induced thermal effect on the sample, the laser power was reduced to ~0.8 mW. Furthermore, a Jobin Yvon T64000 micro-Raman spectrometer with an Ar^+ ion laser ($\lambda = 488$ nm) was involved to confirm the Raman data gathered with 442 nm. Due to a triple monochromator in this system, the laser power was increased to ~2 mW to enhance the signal-to-noise ratio. No thermal effects were observed.

High-resolution x-ray diffraction measurements were carried out on an URD6 diffractometer at the wavelength of 0.154056 nm ($CuK_{\alpha1}$ radiation). The diffractometer was equipped with a perfect

(111)-oriented dislocation-free silicon single crystal, used as monochromator in the primary beam.

Results and discussion

In order to calculate the dispersion curves, it is necessary to measure the phonon wavenumbers at $\theta = 0°$ as well as at $\theta = 90°$, that is, with the wave vector parallel and perpendicular to the *z*-axis. As mentioned before, numerous Raman and IR measurements of phonons in BFO exist, which were however measured in backscattering geometry on pseudo-cubic faces in most cases. We use the values for Raman position obtained by the measurements of Hlinka *et al.*[15] for grain orientations near $\theta = 0$ and 90° (Table 1). Their values for the E_{TO} modes agree very well with the results of IR measurements presented by Lobo *et al.*[25] and measured at 5 K on the *x*,*y*-plane of a single crystal ($\theta = 0°$). As shown in the succeeding texts, by means of the fit parameter of the reflectivity measurements reported by Lobo *et al.*,[25] the E_{LO} phonon wavenumbers ($\theta = 90°$) can be calculated using the dielectric function. Excellent agreement with the measured values of E_{LO} phonon wavenumbers of Hlinka *et al.*[15] is achieved, too. Knowing the phonon wavenumbers for $\theta = 0$ and 90°, the phonon wavenumbers for arbitrary angles θ can be thus calculated. The uniaxial BFO crystal with C_{3v} symmetry is characterised by a dielectric function, which is identical for two principal directions. The optically isotropic *x*,*y*-plane is described by $\varepsilon_{\perp}(\omega)$. With $\varepsilon_{||}(\omega)$, we denote the dielectric function in the third principal direction *z*, also referred to as the optical axis *c*, which is perpendicular to the *x*,*y*-plane (cf. Fig. 1). For arbitrary directions with angle θ between the phonon wave vector and the *z*-axis, we obtain[22,26]

$$\varepsilon(\omega,\theta) = \frac{\varepsilon_{\perp}(\omega)\cdot\varepsilon_{||}(\omega)}{\varepsilon_{\perp}(\omega)\sin^2(\theta) + \varepsilon_{||}(\omega)\cos^2(\theta)} \tag{2}$$

$$\text{with } \varepsilon_{\perp}(\omega) = \varepsilon_{\perp\infty} + \sum_{i=1}^{9} \frac{S_{E\perp i}\cdot\omega_{ETO_i}^2}{\omega_{ETO_i}^2 - \omega^2 - i\omega\gamma_{E_i}} \tag{3}$$

$$\text{and } \varepsilon_{||}(\omega) = \varepsilon_{||\infty} + \sum_{i=1}^{4} \frac{S_{A1||i}\cdot\omega_{A1TO_i}^2}{\omega_{A1TO_i}^2 - \omega^2 - i\omega\gamma_{A1_i}} \tag{4}$$

where ω_{ETO_i}, $S_{E\perp i}$ and γ_{E_i} (ω_{A1TO_i}, $S_{A1||i}$ and γ_{A1_i}) are the TO phonon wavenumber, oscillator strength and damping for the *i*th mode of E-symmetry (A1-symmetry). $\varepsilon_{\perp\infty}$ ($\varepsilon_{||\infty}$) denotes the high-frequency dielectric constant perpendicular (parallel) to the optical axis. Lobo *et al.*[25] obtained the wavenumbers of the E_{TO} modes by using Eqn (3). Alternatively, these wavenumbers can be calculated by searching for the wavenumbers of the maxima in the function Im ($\varepsilon_{\perp}(\omega)$). The E_{LO} wavenumbers follow from the locations of the maxima in the function $\mathrm{Im}\left(\frac{-1}{\varepsilon_{\perp}(\omega)}\right)$. With the phonon wavenumbers given in Table 1, we subsequently calculated the angular dependence of the extraordinary phonons. For arbitrary directions with angle θ, their position can be obtained from the zeros of the following equation: (see, for instance, the work of Claus *et al.*[22])

$$\begin{aligned} B(\omega,\theta) &= \varepsilon_{\perp\infty}\cdot\sin^2(\theta)\cdot\sum_{i=1}^{9}\left(\omega_{ELO_i}^2 - \omega^2\right)\sum_{i=1}^{4}\left(\omega_{A1TO_i}^2 - \omega^2\right) \\ &\quad + \varepsilon_{||\infty}\cdot\cos^2(\theta)\cdot\sum_{i=1}^{4}\left(\omega_{A1LO_i}^2 - \omega^2\right)\sum_{i=1}^{9}\left(\omega_{ETO_i}^2 - \omega^2\right) \\ &= 0 \end{aligned} \tag{5}$$

Equation (5) implies that a total number of 9 + 4 = 13 modes is observed for $\theta = 0$ and 90°, respectively. A mode with a certain wavenumber for the wave vector parallel to the *z*-axis continuously changes wavenumber as the wave vector is changed, until it propagates perpendicular to the *z*-axis. The reached wavenumber is that of another phonon mode. The coupling of the extraordinary modes between $\theta = 0$ and 90° can therefore be of four fundamental types: (1) $E_{TO} \leftrightarrow E_{LO}$, (2) $E_{TO} \leftrightarrow A1_{TO}$, (3) $A1_{LO} \leftrightarrow A1_{TO}$ and (4) $A1_{LO} \leftrightarrow E_{LO}$. Figure 2 shows the dispersion branches of the extraordinary phonons and in addition the ordinary phonons $E_{TO} \leftrightarrow E_{TO}$, which have no dispersion. For measurements with backscattering on the pseudo-cubic (100) plane ($\theta \approx 54.7°$), we obtain 13 wavenumbers of the extraordinary phonons, which are listed in Table 1 together with the observable phonons for backscattering, corresponding to 0 and 90°. The alternation of the $A1_{TO}$ and $A1_{LO}$ modes (E_{TO} and E_{LO} modes) with increasing wavenumber is fulfilled. The alternation rule follows from the requirement that the poles and zeros of the dielectric function along a given axis must necessarily alternate.

$A1_{LO}$ phonons with similar wavenumbers were observed in Raman spectra of a small crystallite with $\theta = 90°$ orientation by Bielecki *et al.*.[27] Based on a comparison with the results of Lobo *et al.*[25] and Hlinka *et al.*,[15] a discrepancy in the phonon assignment occurs. The phonons at ~145 and ~174 cm^{-1}, being assigned to an *E*(2) and an *A*1 mode, respectively, should correspond to an $A1_{TO}$(1) and E_{LO}(2) mode, respectively. Backscattering Raman measurements on the polished pseudo-cubic $(111)_{pc}$ plane ($\theta = 0°$) of a single crystal were performed by Fukumura *et al.*.[28] Most of the E_{TO} and $A1_{LO}$ phonon wavenumbers reported there correspond to the values given by Hlinka and Lobo.[15,25] However, the strong $A1_{LO}$ modes were not completely eliminated in crossed polarisation, which is inconsistent with the selection rules and possibly indicates that the polished surface was slightly tilted from the pseudo-cubic (111) plane, that internal reflections contributed to the scattered signal or that other reasons distorted the signal. The $A1_{LO}$(4) phonon above 500 cm^{-1} is not observed, instead the band at 147 cm^{-1} is assigned to an $A1_{LO}$(1) phonon. We assume that this

Table 1. Measured and by using equation (5) calculated extraordinary phonon wavenumbers for θ angles of 0, 54.7 and 90° between phonon wave vector and *z*-axis of the crystal

$\theta = 0°$			$\theta = 90°$			$\theta = 54.7°$
—	Hlinka[15]	Lobo[25]	—	Hlinka[15]	Lobo[25]	Calc.
$E_{TO}(1)$	74	74	$E_{LO}(1)$	81	82.4	79.5
$E_{TO}(2)$	132	134	$E_{LO}(2)$	175	175.1	143.9
$E_{TO}(3)$	240	240	$E_{LO}(3)$	242	242.5	176.1
$E_{TO}(4)$	265	265	$E_{LO}(4)$	276	276.1	224.2
$E_{TO}(5)$	278	276	$E_{LO}(5)$	346	342.3	241.7
$E_{TO}(6)$	351	346	$E_{LO}(6)$	368	366.5	275.6
$E_{TO}(7)$	374	373	$E_{LO}(7)$	430	429	294.5
$E_{TO}(8)$	441	441	$E_{LO}(8)$	468	466.9	349.0
$E_{TO}(9)$	523	522	$E_{LO}(9)$	616	614.6	370.6
$A1_{LO}(1)$	178	—	$A1_{TO}(1)$	149	—	434.5
$A1_{LO}(2)$	229	—	$A1_{TO}(2)$	223	—	473.7
$A1_{LO}(3)$	502	—	$A1_{TO}(3)$	310	—	551.9
$A1_{LO}(4)$	591	—	$A1_{TO}(4)$	557	—	606.3

Calc., calculated.

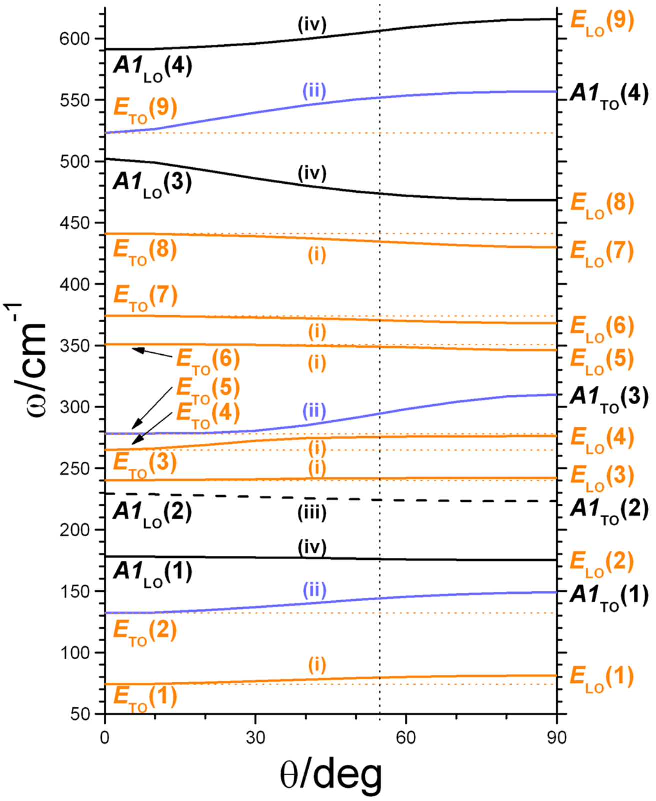

Figure 2. Directional dispersion of the extraordinary phonons (bold lines) and ordinary E_{TO} phonons (dotted lines). Four fundamental types of coupling occur: (1) $E_{TO} \leftrightarrow E_{LO}$ (orange), (2) $E_{TO} \leftrightarrow A1_{TO}$ (blue), (3) $A1_{LO} \leftrightarrow A1_{TO}$ (dashed) and (4) $A1_{LO} \leftrightarrow E_{LO}$ (black).

band stems from the spurious $A1_{TO}(1)$ phonon and the band at 473 cm^{-1} corresponds to a spurious $E_{LO}(8)$ phonon.

Figures 3a and 3b present the experimental Raman spectra of the BFO thin film deposited on DSO, which were recorded in parallel (vv) and crossed (hv) polarisation configuration (cf. Fig. 1). The 442-nm (2.80 eV) laser line used for Raman measurements on thin films was applied because of the pre-resonant conditions. At this energy, the extinction coefficient of BFO has a value of ~0.47 so that the penetration depth of the laser in BFO is approximately 75 nm.[29,30] Thus, the contribution of the substrate to the Raman signal from the BFO/DSO thin film having a thickness of ~175 nm is negligible. By rotating the sample to specified azimuthal angles ϕ, two families of spectra appear, implied through the light blue and dark green lines in Figures 3a and 3b. One family covers the ϕ angles of 0, 90, 180, 270 and 360 °, while the other family contains the Raman spectra at $\phi = 45$, 135, 225 and 315 °. We henceforth refer to these two groups of azimuthal angles by just mentioning Φ_{00} and Φ_{45}, respectively. Both families of spectra show seven strong modes near 135, 172, 218, 277, 350, 465 and 548 cm^{-1}, what is in accordance with other experimental works on BFO (see also Table 2).[6,9,11,13,15] While the intensity for the modes at 135, 172, 218, 465 and 548 cm^{-1} remains steady between the measurements with different azimuthal angles, clear dissimilarities can be detected for the modes at 277 and 350 cm^{-1} with respect to ϕ. These effects seem to be more distinctive for (hv) than for (vv). Therefore, we examine both polarisation data sets separately beginning with (hv).

A deeper view reveals a maximal intensity near 277 cm^{-1} in the Φ_{00}(hv) spectra, which disappears in the Φ_{45}(hv) spectra. Instead, a shoulder occurs near 266 cm^{-1} in Φ_{45}(hv). We suppose that this effect is caused by two different phonon modes, which correspond to different symmetries and appear at the mentioned positions.[11,13,15] This assumption may also explain the behaviour of the apparently single mode at 350 cm^{-1}: Here, the Φ_{45}(hv) spectra exhibit a strong mode at 350 cm^{-1}. This mode is not present in the Φ_{00}(hv) spectra, which show a maximum in intensity around 365 cm^{-1}. Again, the conclusion of two different phonons with unlike symmetry obtrudes. Last but not least, the strong mode at 548 cm^{-1} shows a broadening for Φ_{45}(hv) to lower wavenumbers, most likely originating from an additional phonon mode at 517 cm^{-1} that can be found in literature, too.[13,15] Also, the Raman shift between 100 and 150 cm^{-1} features some inconsistencies that will be considered in the following. In this wavenumber range, the Φ_{45}(hv) spectra show a step-like increase in intensity at 105 and 119 cm^{-1}. The Φ_{00}(hv) spectra reveal a shoulder at 105 cm^{-1} too, but much smaller in intensity. In literature, a mode around 119 cm^{-1} can be found for BFO crystals but was not reported for thin films yet.[11,13] A mode at 105 cm^{-1} is mentioned by Hermet *et al.*,[8] who predicted an E_{TO} mode at 102 cm^{-1} and an E_{LO} mode at 104 cm^{-1}, but given that these two modes are the lowest calculated wavenumbers there, an accordance to the lowest wavenumber modes $E_{TO}(1)$ and $E_{LO}(1)$, listed in Table 1 seems more likely. Komandin *et al.*[31] described an E mode at ~102 cm^{-1} based on reflection IR spectra on BFO ceramic samples and calculated dispersion curves. Borissenko *et al.*[7] found a silent $A2_{LO}$ mode at ~109 cm^{-1} in their experimental studies on BFO single crystals by inelastic x-ray scattering, matching excellently their calculations with density functional theory. In terms of selection rules, all $A2$ modes are Raman forbidden and thus should not occur in Raman spectra. Only if the crystal structure is defective, for example, due

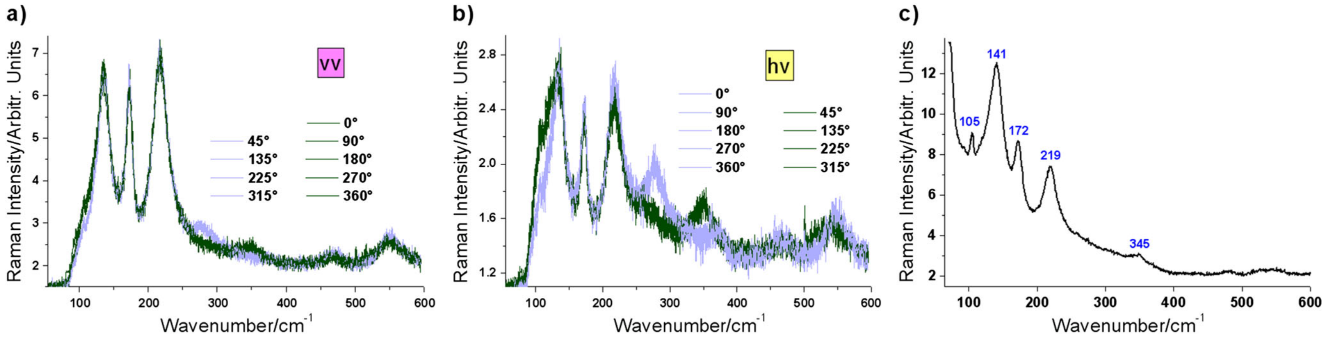

Figure 3. Raman spectra of the $BiFeO_3$ (BFO)/$DyScO_3$ thin film for (a) parallel and (b) crossed polarisation configuration at selected azimuthal angles. Obvious differences in intensity between Φ_{00} and Φ_{45} occur near 105 , 277 and 350 cm^{-1}. The Raman spectrum on a BFO polycrystal, clearly showing a mode at 105 cm^{-1}, is shown in (c).

Table 2. Comparison of Raman wavenumbers for ordinary and extraordinary (eo.) phonon modes from literature and from our calculations as well as experiments on the BiFeO$_3$/DyScO$_3$ thin film

Phonon mode	Calculated and experimental Raman wavenumbers (cm^{-1})						
—	$\theta \approx 54.7^{\circ}$	(100) Pseudo-cubic plane					
—	E_{TO}: Hlinka[15] eo. phonon: Eqn (5)	Fukumura[9]	Cazayous[10]	Palai[14]	Singh[6] room temperature	Beekman[16] room temperature	This work room temperature
—	$T = 5$ K	$T = 4$ K	$T = 10$ K	$T = 81$ K			
$E_{TO}(1)$	74	77	75	74.2	—	—	—
eo. phonon (1)	79.5	—	81	79.6	—	—	—
—	—	—	—	—	—	—	105
$E_{TO}(2)$	132	136	132	127.0	—	—	118
eo. phonon (2)	143.9	147	145	145.0	136	140	135
eo. phonon (3)	176.1	176	175.5	168.0 175.9	168	173	172
eo. phonon (4)	224.2	227	222.7	212.0 224.2	212	220	218
$E_{TO}(3)$	240	—	—	—	—	—	—
eo. phonon (5)	241.7						
$E_{TO}(4)$	265	265	263	265.4	—	265	266
eo. phonon (6)	275.6	279	276	277.7	275	279	277
$E_{TO}(5)$	278						
eo. phonon (7)	294.5	—	295	295.2	—	288	—
eo. phonon (8)	349.0	351	348	350.4	335	350	350
$E_{TO}(6)$	351						
eo. phonon (9)	370.6	375	370	371.5	363	371	365
$E_{TO}(7)$	374						
eo. phonon (10)	434.5	437	—	—	425	—	—
$E_{TO}(8)$	441	—	441	—	—	—	—
eo. phonon (11)	473.7	473	471	473.0	456	—	465
—	—	490	—	—	—	—	—
$E_{TO}(9)$	523	525	523	523.1	—	520	517
eo. phonon (12)	551.9	—	550	553.0	549	550	548
eo. phonon (13)	606.3	—	—	—	597	—	—

to lattice distortions, a break in symmetry is conceivable, softening the Raman selection rules. Not explicitly mentioned but to be seen is this mode also in the Raman spectra of Fukumura's work.[9] To prove the existence of a mode near 105 cm^{-1}, a polycrystalline BFO sample was investigated by means of a Jobin Yvon T64000 Raman spectrometer with an Ar^{+} ion laser ($\lambda = 488$ nm) in backscattering geometry. The spectrum is shown in Fig. 3c. The three prominent modes at 141, 172 and 219 cm^{-1} are a characteristic for BFO, and a fourth mode at 105 cm^{-1} is clearly visible determining our suggestion of a phonon mode at this position. With this experimental set-up, we can prove the existence of this phonon mode at 105 cm^{-1} by excluding a possible influence of the edge filter in the LabRam system. The use of a polycrystal additionally neglects any connection between the film's substrate and this mode.

Now, to come back to the experimental data in parallel polarisation (vv), on closer examination again, a sharp edge in the spectra near 105 cm^{-1} occurs. With respect to Raman intensity *versus* azimuthal angle, a similar behaviour to the findings in the spectra with crossed polarisation can be exposed. At 105, 350 and around 517 cm^{-1} Φ_{00}(vv), spectra possess higher intensities than the Φ_{45}(vv) spectra. At 277 cm^{-1} and similar at wavenumbers around 465 and 548 cm^{-1}, it is just the other way around with Φ_{45}(vv) spectra showing higher intensities than the spectra at Φ_{00} (vv). These observations confirm the existence of further modes in the recorded Raman spectra as suggested in the discussion of the Raman spectra for crossed polarisation (hv). They also show the remarkable sensitivity towards intensity-weak phonons in thin films with respect to the azimutal angle ϕ. Table 2 gives an overview about all Raman positions we found on the BFO/DSO thin film in our experiments compared to the calculated wavenumbers of the extraordinary phonons for $\theta \approx 54.7°$ and the experimental results of Raman backscattering measurements on the pseudo-cubic (100) plane from literature. Other reported Raman measurements were not included in this table because the orientation was not clearly defined, for instance, as the measurements were performed on polycrystalline materials.[11,32,33] Results of IR measurements on polycrystalline material were not included because the dielectric function used for the fits of the reflectivity measurements neglected the directional dispersion.[31,34]

Based on these results, we chose a fitting procedure for the experimental Raman data, which is presented in Fig. 4. All spectra recorded in crossed polarisation (hv) were fitted to ten Lorentzian oscillators near 105, 119, 135, 172, 218, 277, 320, 350, 465 and 548 cm^{-1}. With our main focus on the modes at low wavenumbers (<220 cm^{-1}), we relinquished on fitting the modes at 277 and 548 cm^{-1} with two Lorentzians for each mode and used single modes at 320 and 350 cm^{-1} to simplify the fitting procedure in the wavenumber range of 250–400 cm^{-1}. Figures 4b and 4d show exemplarily the cumulated fitting curves for the spectra at $\phi = 0°$ and $\phi = 45°$ in (hv). The spectra measured in parallel polarisation

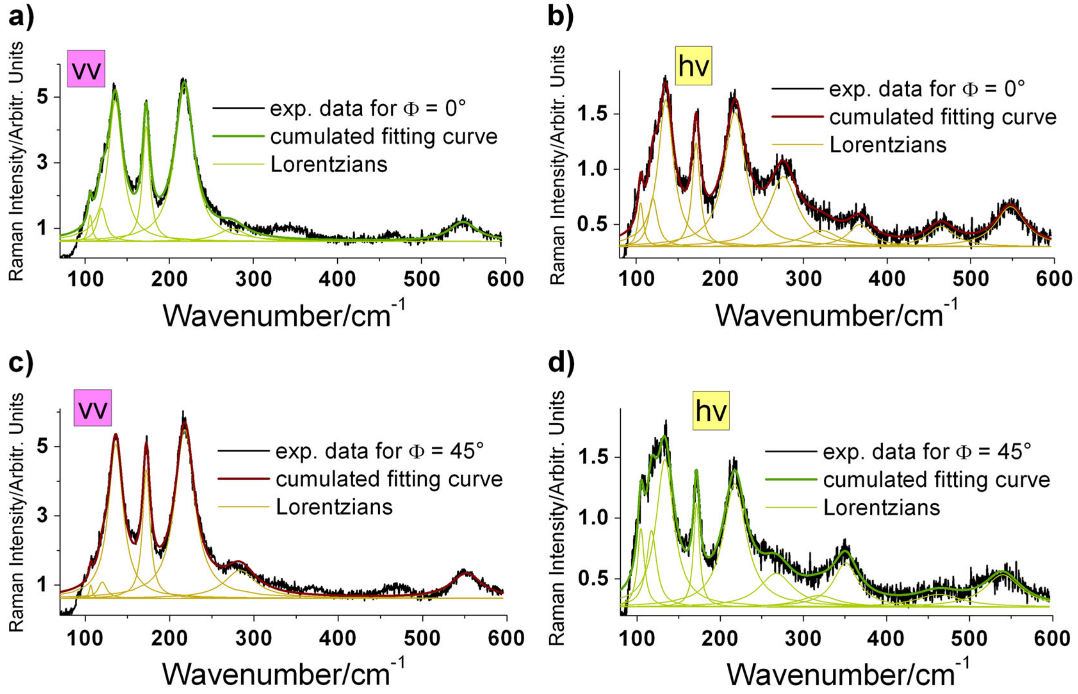

Figure 4. Fit procedure with seven Lorentzian modes in parallel polarisation configuration for $\phi = 0\,°$ (a) and $\phi = 45\,°$ (c). In contrast to this, the spectra taken in crossed polarisation configuration were fitted by ten Lorentzian modes, exemplarily shown for $\phi = 0\,°$ (b) and $\phi = 45\,°$ (d).

(vv) were fitted to seven Lorentzian modes at 105, 119, 135, 172, 218, 277 and 548 cm^{-1}, as depicted for $\phi = 0\,°$ and $\phi = 45\,°$ in Figs 4a and 4c. For simplification, just one Lorentzian function at 277 cm^{-1} was included in the range between 200 and 500 cm^{-1} to generate the cumulating fitting curve. The main purpose of this mode is the minimisation of the influence from this wavenumber range to the fitting parameters of the mode at 218 cm^{-1} in the cumulated fitting curve. Other modes in this range show just a minor contribution to the overall Raman spectrum and thus were neglected.

In Figure 5, the wavenumbers for the phonon modes at 119 and 135 cm^{-1} as function of the azimuthal angle are presented in form of polar plots. Surprisingly, we found a periodic shift of the position of the modes with 90° periodicity. In parallel polarisation configuration (vv), which is depicted in Figs 5a and 5b, a blueshift in wavenumber for Φ_{45} to wavenumbers around 120.5 and 136.2 cm^{-1}, respectively, is observed, compared to lower wavenumbers at 118.5 and 135.4 cm^{-1}, respectively, for Φ_{00} spectra. The amount of these shifts averages out at ~2 cm^{-1} for the mode at 119 and ~0.8 cm^{-1} for the mode at 135 cm^{-1}. In (hv) polarisation (Figs 5c and 5d), the modes show a blueshifted wavenumber for Φ_{00} up to 120 and 135.5 cm^{-1}, respectively, compared to ~116 and 133.5 cm^{-1} for Φ_{45}, respectively. Here, the relative differences are higher than in (vv) configuration comprising about 4 cm^{-1} for the 119 cm^{-1} mode and 2 cm^{-1} for the mode at 135 cm^{-1}.

To explain this behaviour, a comparison to the results from Hlinka *et al.*[15] seems appropriate. In their investigations, an angle ϕ was defined between the phonon propagation vector $\mathbf{q}$ and the optical axis z. Hence, ϕ corresponds to the angle θ defined in this work. By performing experiments on a coarse-grain ceramic BFO sample, they were able to determine the angular dispersion of the phonon modes intensities. In our experiments, by rotating the sample around the direction of the incident laser by the azimuthal angle ϕ (cf. Fig. 1), the angle θ is not altered leading us to another explanation for the observed behaviour of the wavenumber in relation to the azimuthal angle. In the works of Sakashika and Deluca *et al.*[20,21], the experimental set-up matches with our experimental adjustments, although they studied polycrystalline $BaTiO_3$ instead of BFO. The dependence of the peak position on the azimuthal angle is explained by a mechanical and a crystallographic component of the observed wavenumber shift. Thereby, a certain stress, applied to the investigated material, is necessary to generate a local domain ordering, creating an anisotropy at the point of measurement. In our BFO thin film, no external stress is deployed to the sample. However, by means of PFM measurements, we discovered a permanent domain texture that may cause the wavenumber shift with respect to the azimuthal angle. PFM measurements on the investigated BFO/DSO thin film show two families of stripes perpendicular to each other (Fig. 6). VPFM and LPFM signals were captured to obtain information about both out-of-plane and in-plane polarisation orientation. Figure 6a shows the VPFM image of the sample, where stripes belong to the 109° domains.[17] To the right, perpendicular stripes and also more discontinuous to the latter can be seen in Fig. 6b. These stripes belong to the 71° domains.[17] Both angles refer to the orientation of the domain walls.[18] The film seems to consist of only two structural variants, what would be in agreement with the conclusions of Johann *et al.*.[18] The 109° domains are aligned to the (001) orthorhombic axis of the DSO substrate, while the 71° domains are parallel to the $(1\bar{1}0)$ orthorhombic axis of the substrate (see the white arrows in Fig. 6). To confirm the epitaxial growth of the thin film, Fig. 6c presents an x-ray diffraction pattern taken in symmetrical diffraction geometry. Two reflections appear at $2\theta_{XRD} = 45.43$ and 46.02°. With the help of Bragg's law, the interplanar distances were determined to be 3.991 and 3.941 Å, respectively. In the pseudo-cubic crystal system, these values correspond to the lattice parameters for the BFO film and the DSO substrate, respectively. The value for DSO is in excellent agreement with literature, while the out-of-plane lattice parameter of BFO is slightly larger than the lattice parameter of a single crystal

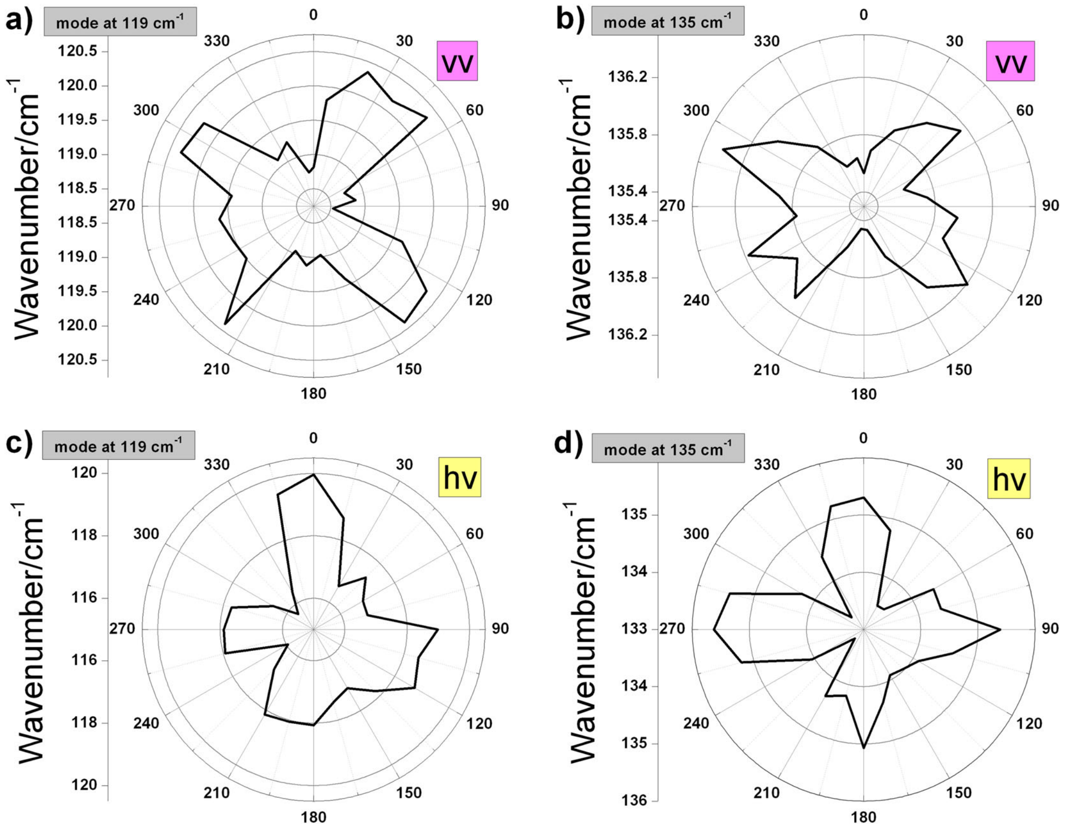

Figure 5. Wavenumbers for the phonon modes at 119 cm^{-1} in parallel (a) and crossed (c) polarisation configuration as well as 135 cm^{-1} in parallel (b) and crossed (d) polarisation configuration. A periodic shift with 90 ° periodicity occurs at both modes in (vv) and (hv), what is only explainable if two types of ferroelastic domains exist in the BiFeO$_3$/DyScO$_3$ thin film.

with 3.96 Å.[35,36] This is due to the compressive strain induced by the orthorhombic crystal system of the DSO substrate. Furthermore, a reciprocal space mapping around the (310)$_{pc}$ reflection of the BFO film was carried out, showing a reflection splitting into two peaks (Fig. 6d). Each peak corresponds to one domain pattern of the BFO thin film and hence confirms the PFM data with its two domain patterns shown before, as well as the epitaxial growth of the film.

When bringing monochromatic light to a sample and detecting the scattered light, as it is performed by Raman spectroscopy, the volume of the material that contributes to the interaction with the incident light and henceforth characterises the Raman signal should not change under azimuthal rotation when using the same point of measurement. This means by rotating the sample and detecting the respective Raman spectra, the ratio between the existing domains in the investigated volume remains equal, and differences in the wavenumber with respect to ϕ should arise from the rotation itself caused by a specific alignment of the observed domains. Hence, only if two domains exist in the thin film, such a periodic behaviour of the wavenumber with respect to ϕ, as it is shown before, is understandable.

To evidence this conclusion, we performed theoretical simulations with two superimposed phonon modes, which originate from the two observed domains. The simulation focuses on the prominent mode near 135 cm^{-1}. Due to the mutual influence of the modes at 105, 119 and 135 cm^{-1} and to the comparatively high values of FWHM for these modes, we decided to fit the experimental data with a single mode that combines all three modes, depicted as hatched area in Fig. 7a. Our simulation calculates the summarised intensity for an ordinary E_{TO} phonon mode near 119 cm^{-1} and an extraordinary phonon mode with mixed $A1_{TO}$ and E_{TO} character near 135 cm^{-1}, what is in accordance to the mentioned symmetry assignments based on phonon dispersion calculations. Referring to group theory and the rhombohedral R3c space group, we used the following symmetric Raman tensors according to Claus *et al.*[22]:

$$R_{ij,z} = \begin{pmatrix} a & 0 & 0 \\ 0 & a & 0 \\ 0 & 0 & b \end{pmatrix} \quad R_{ij,x} = \begin{pmatrix} 0 & c & d \\ c & 0 & 0 \\ d & 0 & 0 \end{pmatrix} \quad R_{ij,y} = \begin{pmatrix} c & 0 & 0 \\ 0 & -c & d \\ 0 & d & 0 \end{pmatrix} \tag{6}$$

With respect to the laboratory coordinate system, the polarisation vectors for incident and scattered light $e_i^{(L)}$ and $e_j^{(S)}$, respectively, are defined as function of the azimuthal angle ϕ:

$$e_i^{(L)} = (\cos\phi, \quad \sin\phi, \quad 0), e_j^{(S)} = (\cos\phi, \quad \sin\phi, \quad 0) \tag{7}$$

By transforming these vectors into the crystal coordinate system, the following rotation matrix M is needed:

$$M = \begin{pmatrix} \frac{1}{\sqrt{2}} & 0 & -\frac{1}{\sqrt{2}} \\ -\frac{1}{\sqrt{6}} & \sqrt{\frac{2}{3}} & -\frac{1}{\sqrt{6}} \\ \frac{1}{\sqrt{3}} & \frac{1}{\sqrt{3}} & \frac{1}{\sqrt{3}} \end{pmatrix} \tag{8}$$

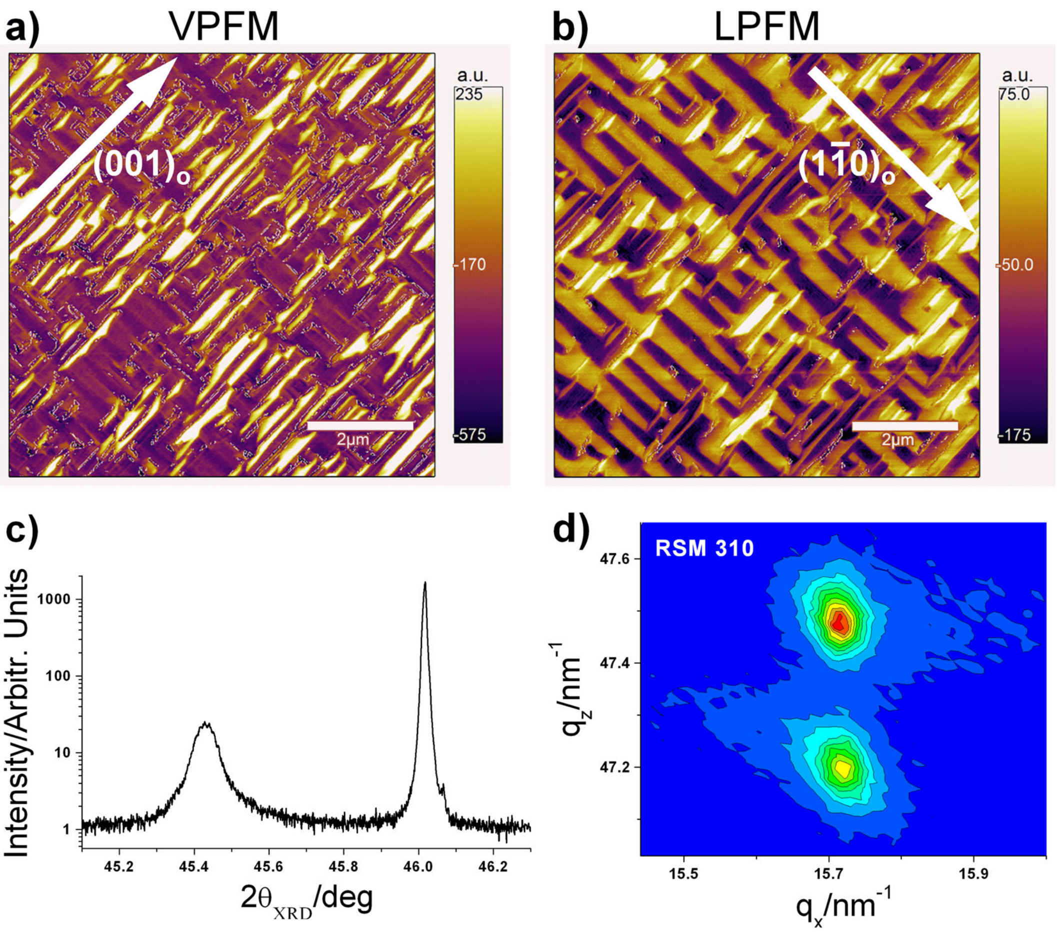

Figure 6. Vertical (a) and lateral (b) piezo-response force microscopy measurements show two families of stripes perpendicular to each other. White arrows indicate the alignment of the two types of ferroelastic domains with respect to the orthorhombic $DyScO_3$ substrate. The epitaxial growth of the $BiFeO_3$ (BFO) thin film is verified by a θ–2θ x-ray diffraction scan (c) as well as a reciprocal space map from the BFO thin film (d), showing a reflection splitting into two peaks, which confirms the domain patterns in the BFO thin film.

Henceforth, the scattered Raman intensity of the single modes can be calculated using the equation:

$$I \sim \left| \tilde{e}_i^{(L)} \left(\sum_k R_{ij,k} \tilde{\xi}_k^{(n)} \right) \tilde{e}_j^{(S)} \right|^2 \tag{9}$$

where $\tilde{e}_i^{(L)}$ and $\tilde{e}_j^{(S)}$ correspond to the polarisation unit vectors for incident and scattered light with respect to the crystal coordinate system and R to the respective Raman tensor in the crystal system. $\tilde{\xi}_k^{(n)}$ refers to the kth component of the $n = 3$ different unit vectors for the mechanical polarisation, which form a right-handed coordinate system. One vector describes the polarisation for extraordinary LO phonons lying in the direction of the phonon wave vector with respect to the crystal system, a second vector describes the polarisation for ordinary TO phonons and a third one corresponds to the polarisation of extraordinary TO phonons.

Knowing from PFM measurements that the two domains of the thin film are aligned orthogonally, both calculated phonon modes consist of two superimposed contributions, one for each domain, which are also shifted 90° to each other. Now, by superimposing the ordinary and extraordinary phonon mode, the observed behaviour of Raman intensity, position and FWHM can be reproduced, as presented by the dashed lines in Figs 7b, 7c and 7d. The simulated mode shows maxima for the wavenumber where minima in FWHM can be detected and vice versa. The results fit very well the experimental data and hence confirm the influence of the orthogonal alignment of the two domains on Raman experiments.

We also detected a similar behaviour for Raman position and FWHM on BFO thin films on GSO and SSO substrates. Like DSO, both substrate materials are orthorhombic, and BFO thin films show maximum values for Raman position where FWHM minimises and vice versa with respect to ϕ under similar experimental conditions. The deviation between minimum and maximum values for Raman position decreases from ~1.5 cm^{-1} at BFO/DSO films to ~0.8 cm^{-1} at BFO/GSO films and ~0.6 cm^{-1} at BFO/SSO films. The same phenomenon can be seen for FWHM with a deviation between minimum and maximum of ~5 cm^{-1} for BFO/DSO films to ~3 cm^{-1} for BFO/GSO films and ~2 cm^{-1} for BFO/SSO thin films. The effects might be connected to the different lattice parameters of the substrates introducing different strains into the BFO thin film. BFO possesses a lattice constant of ~3.96 Å causing a compressive strain in thin films on DSO with a lattice constant around 3.95 Å.[35] For GSO (3.97 Å) and SSO (3.99 Å), thin films become tensile strained.[35]

With respect to the utilised polarisation configurations, we detected a higher displacement of Raman position in (vv) and (hv) for the mode at 119 cm^{-1} than for the mode at 135 cm^{-1}. Also, the displacements are larger in crossed polarisation than in

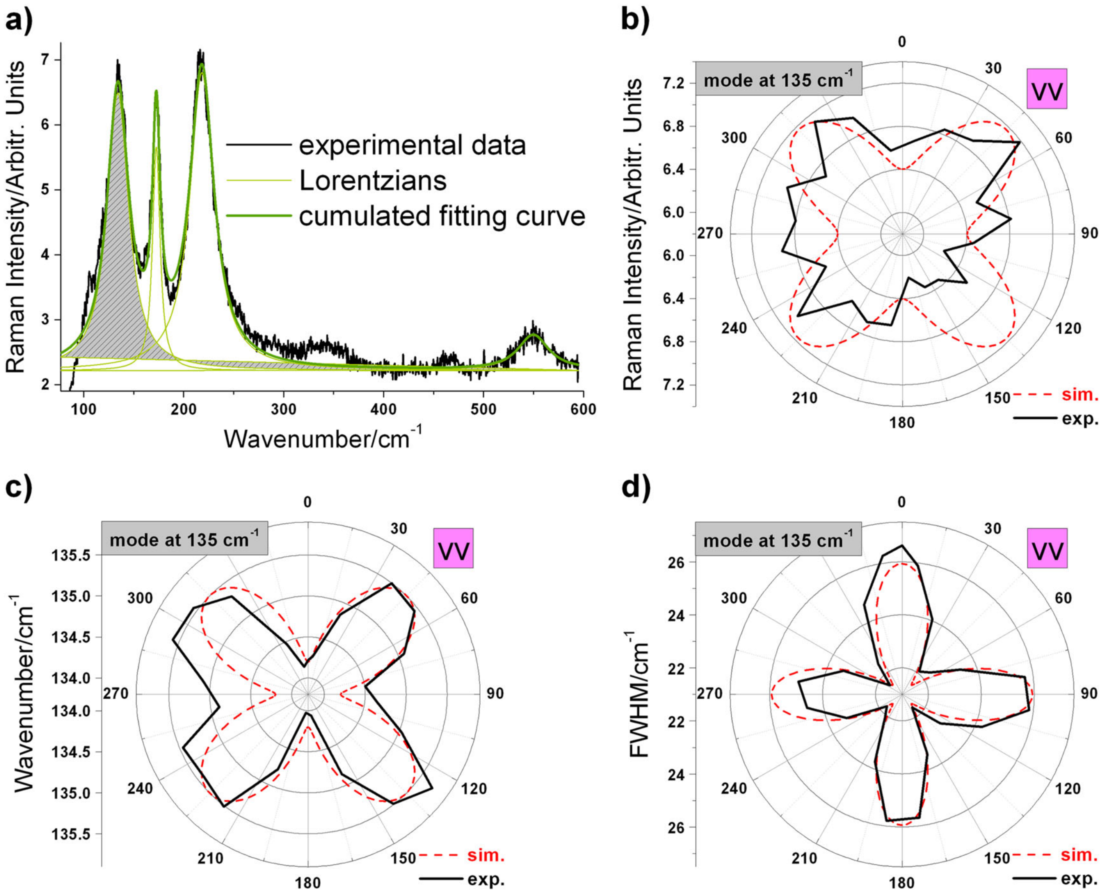

Figure 7. (a) Raman spectra for the $BiFeO_3/DyScO_3$ thin film with one Lorentzian mode in the range of 100–140 cm^{-1}. The experimental behaviour of Raman intensity, wavenumber and FWHM of this mode in relation to the azimuthal angle ϕ as well as the calculated behaviour (red dashed lines) is presented in (b), (c) and (d), respectively. Where the mode shows maxima for the wavenumber, minima in full width at half maximum can be detected and vice versa.

parallel polarisation for both modes. This could originate from an unequal contribution of the particular state of strain to the respective phonon modes because of a different formation of phonon modes in matters of number and variety of atoms or the orientation in the crystal system.

Summary

It was shown that Raman spectroscopy is a powerful tool for the investigation of ferroelastic domain formation in BFO thin films on rare earth scandate substrates, which was cross-checked by PFM and x-ray diffraction measurements. Hereby, we found a 90 ° periodicity of Raman position and FWHM for certain phonon modes of BFO by means of azimuthal rotation of the sample during the Raman measurements, which were performed in parallel and crossed polarisation configurations. Furthermore, we were able to explain the existence of a Raman mode in BFO at 105 cm^{-1}. By means of phonon dispersion calculations based on the dielectric function, we presented a symmetry assignment for the optical phonon modes of BFO that is in accordance with the results of Hlinka *et al.* and Lobo *et al.*.[15,25] Based on these results, we successfully simulated the behaviour of Raman position, intensity and FWHM with respect to the azimuthal angle through symmetry calculations, which support the domain patterns of epitaxial BFO films.

Acknowledgements

This work was supported by the German research foundation in the DFG projects HI 1534 1-1 and HI 1534 1-2.

References

[1] F. Kubel, H. Schmid, *Acta Cryst.* **1990**, *B46*, 698.
[2] D. Sando, A. Barthélémy, M. Bibes, *J. Phys. Condens. Matter* **2014**, *26*, 473201.
[3] J.-G. Park, M. Duc Le, J. Jeong, S. Lee, *J. Phys. Condens. Matter* **2014**, *26*, 433202.
[4] J. M. Moreau, C. Michel, R. Gerson, W. J. James, *J. Phys. Chem. Solids* **1971**, *32*, 1315.
[5] R. Haumont, J. Kreisel, P. Bouvier, *Phase Transitions* **2006**, *79*, 1043.
[6] M. K. Singh, H. M. Jang, S. Ryu, M.-H. Jo, *Appl. Phys. Lett.* **2006**, *88*, 042907.
[7] E. Borissenko, M. Goffinet, A. Bosak, P. Rovillain, M. Cazayous, D. Colson, P. Ghosez, M. Krisch, *J. Phys. Condens. Matter* **2013**, *25*, 102201.
[8] P. Hermet, M. Goffinet, J. Kreisel, P. Ghosez, *Phys. Rev. B* **2007**, 75, 220102(R).
[9] H. Fukumura, S. Matsui, H. Harima, T. Takashashi, T. Itoh, K. Kisoda, M. Tamada, Y. Noguchi, M. Miyayama, *J. Phys. Condens. Matter* **2007**, *19*, 365224.
[10] M. Cazayous, D. Malka, D. Lebeugle, D. Colson, *Appl. Phys. Lett.* **2007**, *91*, 071910.
[11] A. A. Porporati, K. Tsuji, M. Valant, A.-K. Axelsson, G. Pezzotti, *J. Raman Spectrosc.* **2010**, *41*, 84.
[12] R. Palai, J. F. Scott, R. S. Katiyar, *Phys. Rev. B* **2010**, *81*, 024115.
[13] R. Palai, H. Schmid, J. F. Scott, R. S. Katiyar, *Phys. Rev. B* **2010**, *81*, 064110.

[14] R. Palai, H. Schmid, J. F. Scott, R. S. Katiyar, *Phys. Rev. B* **2010**, 81, 139903(E).
[15] J. Hlinka, J. Pokorny, S. Karimi, I. M. Reaney, *Phys. Rev. B* **2011**, 83, 020101(R).
[16] C. Beekman, A. A. Reijnders, Y. S. Oh, S. W. Cheong, K. S. Burch, *Phys. Rev. B* **2012**, 86, 020403(R).
[17] S. K. Streiffer, C. B. Parker, A. E. Romanov, M. J. Lefevre, L. Zhao, J. S. Speck, W. Pompe, C. M. Foster, G. R. Bai, *J. Appl. Phys.* **1998**, *83*, 5.
[18] F. Johann, A. Morelli, D. Biggemann, M. Arredondo, I. Vrejoiu, *Phys. Rev. B* **2011**, *84*, 094105.
[19] M. A. Rafiq, P. Supancic, M. E. Costa, P. M. Vilarinho, M. Deluca, *Appl. Phys. Lett.* **2014**, *104*, 011902.
[20] T. Sakashika, M. Deluca, S. Yamamoto, H. Chazono, G. Pezzotti, *J. Appl. Phys.* **2007**, *101*, 123517.
[21] M. Deluca, G. Pezzotti, *J. Phys. Chem. A* **2008**, *112*, 11165.
[22] R. Claus, L. Merten, J. Brandmüller, *Light Scattering by Phonon-Polaritons*, Springer, Berlin, **1975**.
[23] R. Loudon, *Adv. Phys.* **1964**, *13*, 423.
[24] G. Pezzotti, *J. Appl. Phys.* **2013**, *113*, 211301.
[25] R. P. S. M. Lobo, R. L. Moreira, D. Lebeugle, D. Colson, *Phys. Rev. B* **2007**, *76*, 172105.
[26] T. Kurosawa, *J. Phys. Soc. Jpn.* **1961**, *16*, 1298.
[27] J. Bielecki, P. Svedlindh, D. T. Tibebu, S. Cai, S.-G. Eriksson, L. Börjesson, C. S. Knee, *Phys. Rev. B* **2012**, *86*, 184422.
[28] H. Fukumura, H. Harima, K. Kisoda, M. Tamada, Y. Noguchi, M. Miyayama, *J. Magn. Magn. Mater.* **2007**, *310*, 367.
[29] C. Himcinschi, I. Vrejoiu, M. Friedrich, E. Nikulina, L. Ding, C. Cobet, N. Esser, M. Alexe, D. Rafaja, D. R. T. Zahn, *J. Appl. Phys.* **2010**, *107*, 123524.
[30] C. Himcinschi, A. Bhatnagar, A. Talkenberger, M. Barchuk, D. R. T. Zahn, D. Rafaja, J. Kortus, M. Alexe, *Appl. Phys. Lett.* **2015**, *106*, 012908.
[31] G. A. Komandin, V. I. Torgashev, A. A. Volkov, O. E. Porodinkov, I. E. Spektor, A. A. Bush, *Phys. Solid State* **2010**, *52*, 734.
[32] D. Kothari, V. Raghavendra Reddy, V. G. Sathe, A. Gupta, A. Banerjee, A. M. Awasthi, *J. Magn. Magn. Mater.* **2008**, *320*, 548.
[33] D. Rout, K.-S. Moon, S.- J. L. Kang, *J. Raman Spectrosc.* **2009**, *40*, 618.
[34] S. Kamba, D. Nuzhnyy, M. Savinov, J. Sebek, J. Petzelt, J. Prokleska, R. Haumont, J. Kreisel, *Phys. Rev. B* **2007**, *75*, 024403.
[35] R. Uecker, B. Velickov, D. Klimm, R. Bertram, M. Bernhagen, M. Rabe, M. Albrecht, R. Fornari, D. G. Schlom, *J. Cryst. Growth* **2008**, *310*, 2649.
[36] J. D. Bucci, B. K. Robertson, W. J. James, *Appl. Cryst.* **1972**, *5*, 187.

JOURNAL OF APPLIED PHYSICS **113**, 084101 (2013)

Optical and magneto-optical study of nickel and cobalt ferrite epitaxial thin films and submicron structures

Cameliu Himcinschi,[1,a)] Ionela Vrejoiu,[2,b)] Georgeta Salvan,[3] Michael Fronk,[3]
Andreas Talkenberger,[1] Dietrich R. T. Zahn,[3] David Rafaja,[4] and Jens Kortus[1]
[1]*TU Bergakademie Freiberg, Institute of Theoretical Physics, D-09596 Freiberg, Germany*
[2]*Max Planck Institute of Microstructure Physics, Weinberg 2, D-06120 Halle, Germany*
[3]*TU Chemnitz, Semiconductor Physics, D-09107 Chemnitz, Germany*
[4]*TU Bergakademie Freiberg, Institute of Materials Science, D-09596 Freiberg, Germany*

(Received 6 December 2012; accepted 6 February 2013; published online 22 February 2013)

Epitaxial films and ordered arrays of submicron structures of nickel and cobalt ferrites were deposited on Nb doped $SrTiO_3$ by pulsed laser deposition. X-Ray diffraction and atomic force microscopy showed that the films have a good crystalline quality and smooth surfaces. A larger number of phonon bands was observed in the polarization dependent Raman spectra of the ferrite films than expected for the cubic spinel structures. This is explained by short range ordering of the Ni^{2+} (or Co^{2+}) and Fe^{3+} cations at the octahedral sites inducing a lowering of the symmetry. The same behavior was also observed in the Raman spectra measured for the submicron structures, suggesting the same cation distribution as in the films. The diagonal components of the dielectric function for nickel and cobalt ferrites are determined from ellipsometry in the 0.73–5 eV photon energy range. The absorption edge was analyzed using a bandgap model and the energies for the indirect and direct optical transitions were calculated. It was found that both nickel and cobalt ferrites are indirect bandgap materials with bandgaps of 1.65 eV and 1.42 eV, respectively, while the first direct transitions lie at 2.69 eV and 1.95 eV, respectively. Magneto-optical Kerr effect spectroscopy in combination with spectroscopic ellipsometry allowed the off-diagonal elements of the dielectric tensor to be determined in the energy range from 1.7 eV to 5 eV. © *2013 American Institute of Physics*. [http://dx.doi.org/10.1063/1.4792749]

INTRODUCTION

$CoFe_2O_4$ (CFO) and $NiFe_2O_4$ (NFO) are insulating ferrimagnetic spinel oxides that are attractive for magneto-electric oxide heterostructure devices, as well as various types of high frequency and high power applications.[1,2] MFe_2O_4 ($M = Co$ or Ni) crystallizes in an inverse spinel structure with a general formula for the ion distribution $A^{3+}[B^{2+}B^{3+}]O_4{}^{2-}$ where A denotes tetrahedral cation sites and B denotes octahedral cation sites. The tetrahedral A-sites are occupied by half of the Fe^{3+} cations, while the octahedral B lattice sites are occupied by the rest of the Fe^{3+} cations and the divalent M^{2+} cations. Due to the occurrence of two types of magnetic ions at the octahedral sites, the two magnetic sublattices lead to a volume magnetization of 0.45 MA/m for CFO, and 0.33 MA/m for NFO.[3] A small fraction of the divalent cations can be found at the tetrahedral sites depending on the sample preparation or thermal history of the samples.[4–7]

Raman spectroscopy has been proven to be a sensitive tool to short-range site ordering of the cations in spinel ferrites. Polarized Raman spectra of single crystal NFO indicated a 1:1 ordering of Ni^{2+} and Fe^{3+} at B-sites, inducing a distortion of the structure to a tetragonal symmetry.[8] Pronounced B-sites ordering was also evidenced by Raman spectroscopy by Iliev *et al.*[9] in NFO thin films. Epitaxial strain was found to have an influence on the cation distribution in spinel ferrites.[10] The influence of hydrostatic strain on the spinel structure of polycrystalline CFO,[11] the response of epitaxial CFO thin films to biaxial compressive stress,[12] and the influence of heteroepitaxially induced strain in $BiFeO_3$-CFO nanostructures[13] were also studied using Raman spectroscopy.

While spectroscopic ellipsometry (SE) is commonly used to determine the optical constants and the optical bandgap of various materials, magneto-optical Kerr effect (MOKE) spectroscopy in combination with SE is often applied to obtain the off-diagonal dielectric tensor elements of oxides.[14,15] Numerous MOKE studies in various ferrites are reported in the literature and sometimes the interpretation of the electronic transitions observed in the spectra is contradictory (see, e.g., Fontjin *et al.*[16] for an overview). Only two reports exist on ferrite films, to the best of our knowledge. Kim *et al.*[17] reported MOKE spectra of Fe_3O_4, NFO, and CFO films with thicknesses of about 1 μm fabricated by sol gel. Mistrík *et al.*[18] reported MOKE spectra of a 93 nm thick NFO film deposited by pulsed layer deposition onto fused quartz substrates and found that the experimental spectrum was slightly shifted and broadened compared to the calculated one, probably due to structural defects.

Here the structural, optical, and magneto-optical properties of epitaxial CFO and NFO thin films are investigated by combining XRD, variable angle spectroscopic ellipsometry (VASE), MOKE, and Raman spectroscopy. In addition,

---

[a)] e-mail: himcinsc@physik.tu-freiberg.de.

[b)] Present address: Max Planck Institute for Solid State Research, 70569 Stuttgart, Germany.

arrays of submicron structures are also investigated by Raman spectroscopy.

EXPERIMENTAL

CFO and NFO epitaxial thin films were grown on Nb-doped $SrTiO_3(100)$ (Nb:STO) substrates by pulsed-laser deposition (PLD), using stoichiometric ceramic targets. The films were deposited at a temperature of 575 °C in an oxygen pressure of 6×10^{-3} mbar. For the *in situ* PLD fabrication of ordered arrays of sub-micron CFO and NFO structures SiN stencil masks with rectangular apertures were used, as described elsewhere.[19] The structures were fabricated at the same temperature as the thin films, but in a lower oxygen pressure of 1.2×10^{-3} mbar.

The topography of the epitaxial CFO and NFO films and of the arrays of structures was investigated by atomic force microscopy (AFM) (Veeco, DI5000) working in tapping mode. The ellipsometric measurements were performed in the energy range from 0.73 eV to 5 eV at four angles of incidence using a M-2000 ellipsometer from J. A. Woollam Company. For the Raman scattering experiment, the samples were excited by the 532 nm line of a frequency doubled Nd:YAG laser and the spectra were collected by a LabRam spectrometer (Horiba Jobin Yvon) equipped with a Peltier cooled CCD detector and a 1800 grooves/mm grating. All spectra were obtained at room temperature in a backscattering geometry using an 100× magnification objective which focuses the laser to a spot size of about 1 μm. The laser power was set at 1 mW which was low enough in order to avoid damage of the samples surface and laser heating. The MOKE spectroscopic measurements were performed in polar geometry in the energy range from 1.7 eV to 5.5 eV using a home-built spectrometer based on the design from Herrmann *et al.*[20] The setup measures the rotation $\boldsymbol{\theta_K}$ and the ellipticity $\boldsymbol{\eta_K}$ of the polarization of the light reflected from the sample exposed to a magnetic field (1.7 T) perpendicular to the sample surface. These quantities correspond to the real and imaginary parts, respectively, of the complex Kerr rotation angle of the light polarization: $\Phi_k = \theta_k + i \cdot \eta_k$. The incidence angle is <1.3°. All measurements were carried out *ex situ* under ambient conditions and at room temperature. To exclude the contribution of optical anisotropy, the MOKE spectra were always recorded with the magnetic field pointing out from the sample and a second spectrum with the magnetic field pointing into the sample. The complex Kerr rotation spectra are then calculated as half the difference of the two spectra.

RESULTS AND DISCUSSIONS

In Figure 1(a), the θ-2θ XRD patterns of a ≈ 69 nm thick CFO film and of a ≈ 80 nm thick NFO film grown on Nb:STO substrates are shown. The graphs display the (004) reflection of the CFO and NFO films and the (002) reflection of the Nb:STO substrate. Cubic spinel $NiFe_2O_4$ has a bulk room temperature lattice parameter of a = 8.34 Å and $CoFe_2O_4$ has a = 8.39 Å. Hence a larger compressive lattice mismatch with the cubic perovskite Nb:STO substrate (a = 3.91 Å, which yields 2 a = 7.82 Å and thus a mismatch of 6.6% for bulk NFO and of 7.3% for bulk CFO with respect to the Nb:STO) is expected for the CFO film, leading to a shift of the 004 reflection peak towards lower angles. However, due to the very large mismatch, it is likely that the CFO film relaxes the strain by forming structural defects such as misfit dislocations at a smaller critical thickness than the NFO film. This may explain why the position at which the (004) reflection of the CFO film occurs is at a larger 2θ angle than the same reflection of the NFO film (Fig. 1(a)), indicating that the NFO film is much more strained and has a larger out-of-plane lattice parameter than the CFO film. The formation of other types of extended structural defects and of point defects such as oxygen vacancies may also contribute to the values of the lattice parameters of the films, which deviate from those of the bulk CFO and NFO. Still, the CFO and NFO films grew heteroepitaxially on the Nb:STO substrate. The heteroepitaxial growth was confirmed by the pole figure measurements that were measured on a Bragg-Brentano diffractometer. As a source of the X-rays, the Ni-filtered radiation of a Cu anode (λ = 0.15418 nm) was employed. The pole figures were measured as a sequence of ϕ-scans at different inclinations of the sample from its symmetrical position. Exemplarily, a single ϕ-scan taken at the sample inclination of 35.3° for the NFO film is shown in inset of Fig. 1(a).

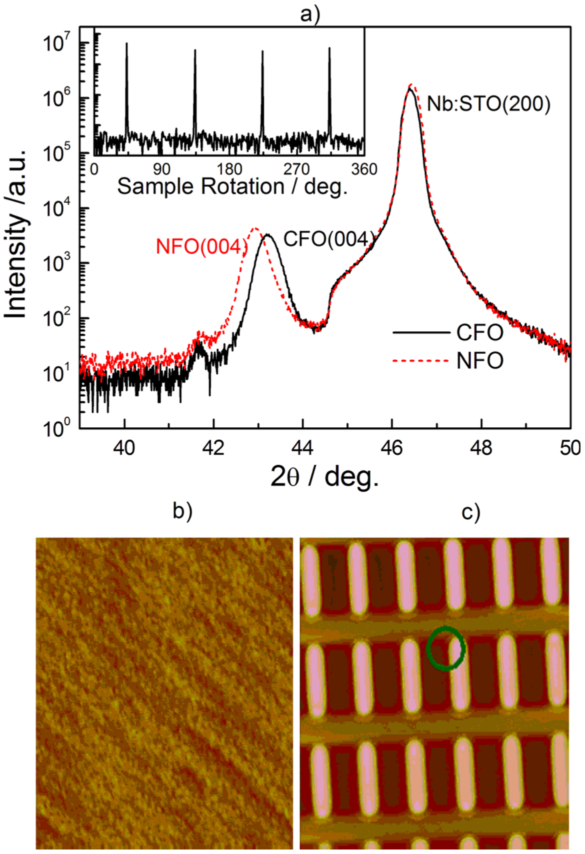

FIG. 1. θ-2θ XRD patterns of NFO and CFO films grown onto Nb:STO substrates. The inset shows a ϕ-scan of the NFO film taken at the sample inclination of 35.3°. (a) Tapping mode AFM image (4 μm × 4 μm, z-range = 1.5 nm) of a 80 nm thick CFO film deposited onto Nb:STO substrate. (b) AFM image (8 μm × 8 μm, z-range = 70 nm) of the CFO structures. The circle gives an estimation of the laser spot size in comparison to the structures dimensions. (c)

The topography of the films and of their submicron-structures was investigated by AFM. Figures 1(b) and 1(c) show two typical AFM micrographs of the 69 nm thick CFO film and of CFO structures, respectively. The CFO and NFO films were relatively smooth, with rms roughness values below 1 nm for CFO/STO for the $4\,\mu m \times 4\,\mu m$ scanned areas. For the CFO submicron structures, an $8\,\mu m \times 8\,\mu m$ area was scanned. Figure 1(c) reveals arrays of ordered structures of uniform shape and size, having dimensions of about $1.8\,\mu m \times 0.5\,\mu m$. The z-range in Figure 1(c) is 70 nm. The circle gives an estimation of the laser spot size used for Raman mapping in comparison to the structure dimensions.

In Figure 2(a), the Raman spectra measured for a Nb:STO(100) substrate and for a 69 nm CFO film grown Nb:STO are shown. The spectra were normalized to the same intensity and the substrate spectrum was subtracted from the film/substrate spectrum. The obtained difference spectrum is shown in the lower part of the figure. The same normalization procedure was applied also for the spectra measured for NFO films and for the measurements performed in different polarization configurations. Removing the substrate contribution from the Raman signal of the ferrite films is important for a clear assignment of the peaks. The direct evaluation of the spectra of the film and substrate[21] can lead to ambiguous peak assignment because the Nb:STO substrate has peaks in the region where the ferrite films also reveal features, as can be see in Figure 2(a).

The spinel structure can be described by the space group $Fd\bar{3}m$ (No. 227) and factor group analysis predicts 5 Raman active internal modes: $A_{1g} + E_g + 3T_{2g}$.[8,22] The comparison of the polarized Raman spectra for NFO and CFO films deposited onto Nb:STO is shown in Figure 2(b). The spectra were measured in backscattering geometry in which the directions of the incident and scattered light are parallel with the normal to the films surface (z). In the parallel polarization configuration (y, y), the polarization directions for the incident and scattered light were both along a [001] direction of the cubic STO substrate, while for the cross polarization (x, y) the detection of the scattered light was realized in a polarization direction perpendicular to that of the incident light. The clear dependence of the Raman spectra on the polarization geometry suggests that the films are epitaxial. As can be seen in Figure 2(b), the number of the observed Raman lines exceeds the expected number of Raman peaks for the spinel structure. The spectra and the polarization dependence in Figure 2(b) for NFO films is very similar to those observed by Ivanov *et al.*[8] for NFO single crystals and by Iliev *et al.*[9] for NFO epitaxial films. This behavior was explained by a short range order of Ni^{2+} and Fe^{3+} cations which induces domain formation with lower symmetry than the cubic inverse spinel one ($Fd\bar{3}m$) and thus new sets of Raman modes. In the spectrum measured in parallel polarization configuration for the NFO films 7 peaks could be clearly identified at ~ 338, 457, 493, 575, 596, 675, and 710 cm^{-1} while for the spinel structure only one A_{1g} and one E_g mode are expected. On the other hand, in the spectrum measured in cross polarization configuration peaks are observed at ~490, 590, 670, and 703 cm^{-1}, instead of two F_{2g} modes which are expected for the spinel structure in our measured range. The positions of the bands and their dependence on polarization resemble those observed for NFO single crystals and NFO films deposited onto $MgAl_2O_4$.[9] Based on these similarities and the symmetry consideration which were discussed in detail by Ivanov *et al.*[8] the additional peaks seen in our spectra could be consistent with the ordering of Ni^{2+} and Fe^{3+} at the octahedral sites, which arises from a structure having tetragonal $P4_122/P44_322$ symmetry coexisting with an orthorhombic structure variant. A direct assignment of each single mode in our spectra cannot be realized because of the tetragonal and orthorhombic phase mixture and mainly because the epitaxial thin films do not allow the measurements in sufficient polarization configurations. A fully inverse octahedral B site arrangement which corresponds to tetragonal symmetry was also found to be

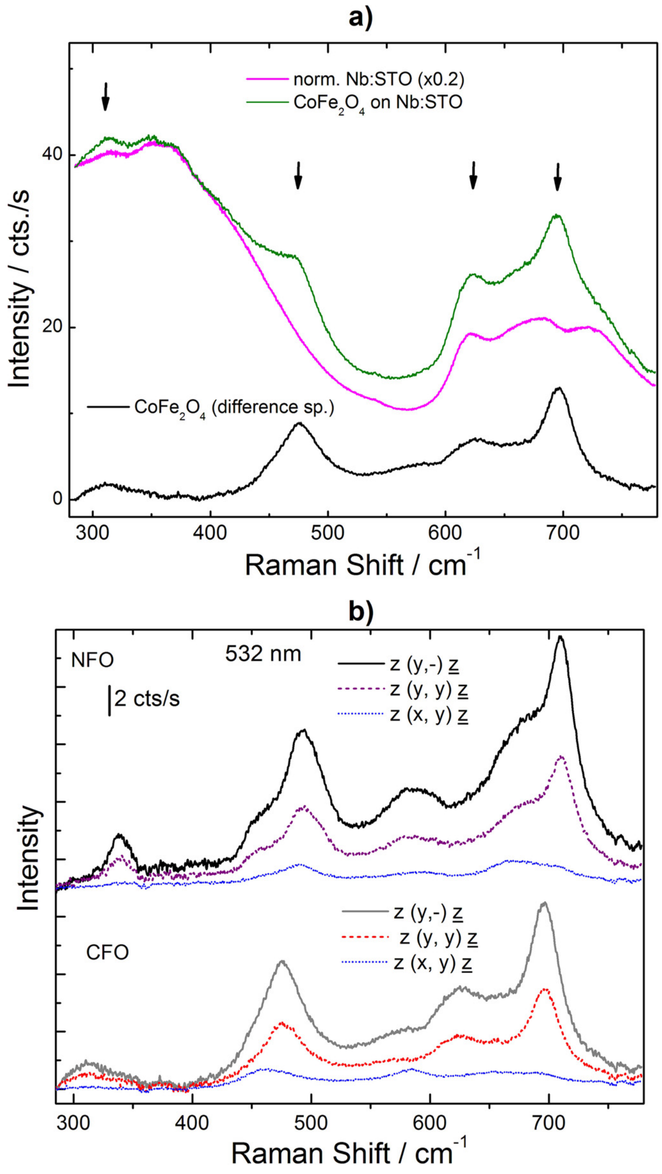

FIG. 2. Normalisation procedure: Raman spectra of Nb:STO substrate (scaled) and of a 80 nm CFO film deposited onto Nb:STO, measured with the 532 nm laser line. The arrows indicate the position of the strongest CFO phonon bands. The difference spectrum is shown in the lower part of the figure. (a) The Raman signal of the NFO (up) and CFO (down) films measured in different polarization configurations. (b)

energetically most favorable by using density functional theory[10] for both NFO and CFO materials. The spectra of the CFO films measured in different polarization configurations shown in the lower part of Figure 2(b) also show a larger number of phonon bands than expected for the ideal spinel structure. This behaviour was again attributed to the local short ordering of Co^{2+} and Fe^{3+} at the octahedral sites which induces the lowering of the symmetry.[12]

Raman measurements were also performed on the structured samples. The circle plotted in Figure 1(c) gives an indication of the laser spot size. Due to the dimension of the laser spot, the lateral resolution is low, thus each single Raman measurement contains contribution from both ferrite structures and the underlying and/or uncovered substrate. The Raman signal of the structures is obtained by performing the same normalization procedure as for the films. In Figures 3(a) and 3(b), typical Raman measured spectra are shown for the CFO and NFO structures, respectively, in comparison with the spectra of the films. As can be seen similar spectra were measured also for the structured arrays suggesting the preservation in the structures of the cation distribution at the tetragonal and octahedral sites as in the epitaxial thin films. This means that the deposition and stoichiometry of the submicron structures are not disturbed by the stencil mask. The small differences in the relative intensities could be explained by a partial relaxation of the epitaxial strain in the structures through the free surfaces of the structure edges.

In order to determine the dielectric function of the NFO and CFO films, the Nb:STO substrate was measured first by ellipsometry. The optical response of the substrate was described using a model consisting of Gaussian oscillators, which ensured the Kramer-Kronig consistency of the real and imaginary parts of the dielectric function. Using the dielectric function of the substrate, the ellipsometric spectra of the ferrite films were evaluated. The absorption free range, below 1.4 eV was used first for an initial estimation of the films thicknesses using a Cauchy dispersion relation for the refractive index. Further, the ellipsometric spectra were evaluated in the whole energy range employing a four-phase model: substrate/film/roughness layer/ambient. A sum of four Gaussian oscillators was used to simulate the optical response of the films, while the roughness layer was considered to be a mixture of 50% film material and 50% voids using Bruggeman effective medium approximation.[23] Thicknesses of 69.3 nm and 80.4 nm were obtained from the ellipsometric evaluation for the NFO and CFO films, respectively, the roughness being below 3 nm in both cases, in good agreement with the AFM results. The real and imaginary parts of the dielectric functions for CFO and NFO are shown in Figure 3(a). These diagonal components of the dielectric function were further used for the evaluation of the MOKE spectra. The dielectric function obtained for the CFO film is in good agreement with the one for a CFO crystal by Martens *et al.* which was determined above 1.5 eV.[15] Converting the dielectric function to optical constants a good agreement was also obtained with the optical constants of CFO and NFO crystals determined above 1.6 eV.[24] Our data extend the range of the dielectric functions down to 0.73 eV, which allows to use the absorption edge for optical gap determination, as described below. It should be pointed out that the imaginary part of the diagonal component of the dielectric function is smaller for NFO than for CFO below 2.4 eV and larger above 3.5 eV. The involvement of possible transitions in this energy range will be discussed later in the evaluation of the magneto-optical data.

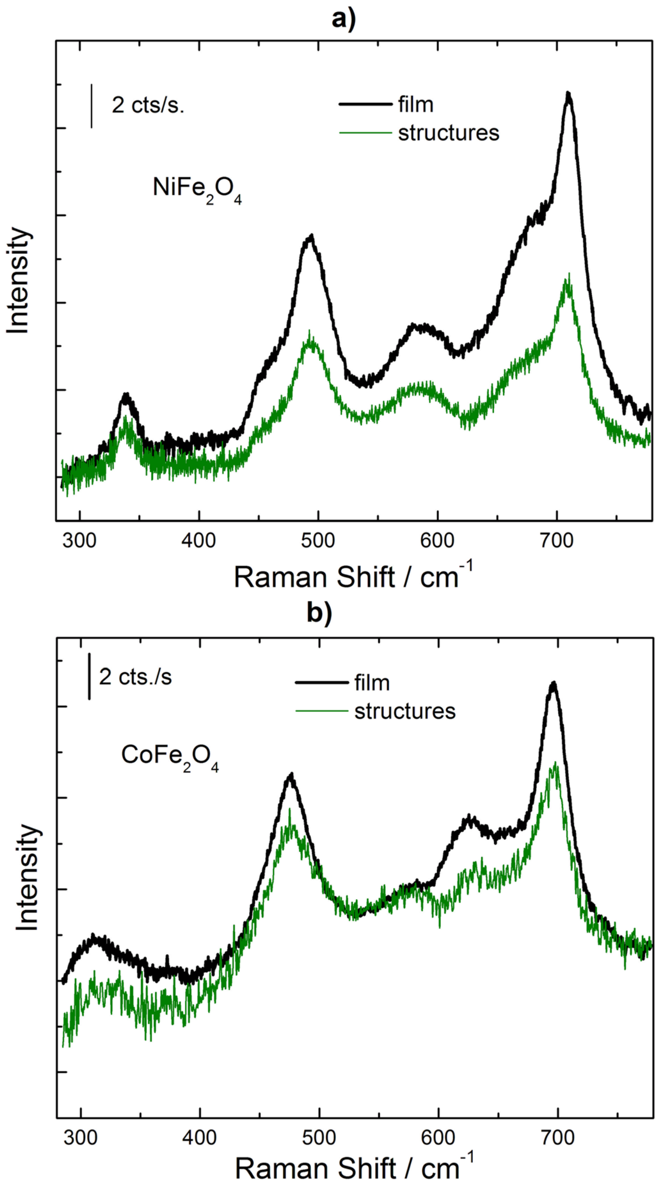

FIG. 3. Raman spectra of NFO (a) and CFO (b) thin films (continuous lines) and structures (dotted lines).

The energy and the type of transition for the optical gap of NFO and CFO films were determined by analyzing the absorption coefficient using the model proposed by Bardeen *et al.*[25] The absorption coefficient $\alpha = (4\pi k/\lambda)$ was calculated from the extinction coefficient k. The product of the absorption coefficient α and photon energy E is proportional to $(E - E_g)^\eta$, E_g is the energy of the optical bandgap, and the exponent η has a value of $^1\!/_2$ for direct transitions and a value of 2 for indirect transitions. In Figures 4(b) and 4(c), $(\alpha \cdot E)^{1/2}$ and $(\alpha \cdot E)^2$ were plotted versus photon energy for NFO and CFO, respectively. The linear extrapolation to zero absorption leads for NFO to values of 2.69 eV and 1.65 eV

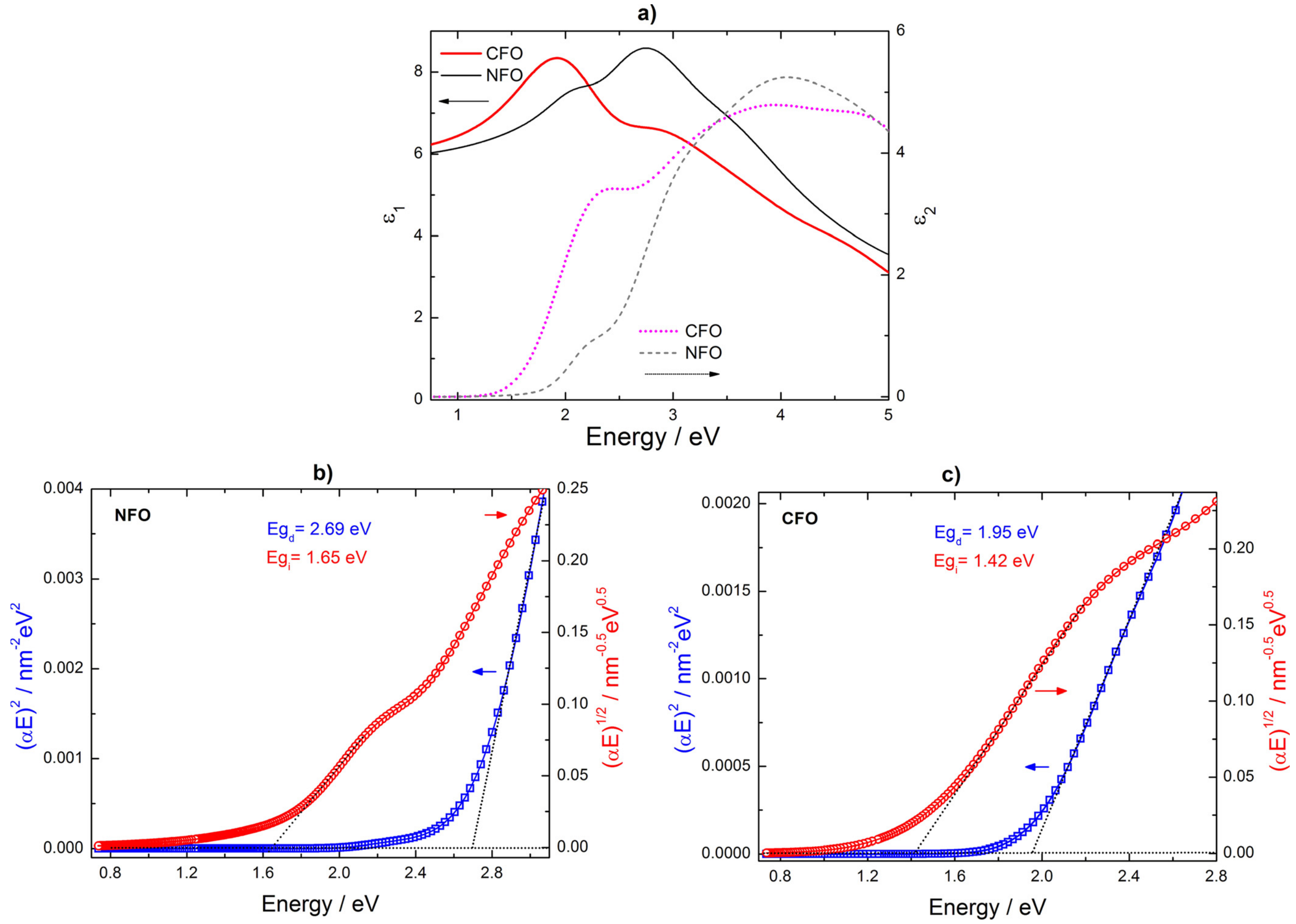

FIG. 4. Real (ε_1) and imaginary parts (ε_2) of the diagonal components of the dielectric function of NFO and CFO films deposited onto Nb:STO substrates as determined by evaluation of the ellipsometric data. (a) $(\alpha \cdot E)^2$ and $(\alpha \cdot E)^{1/2}$ plots as function of photon energy for NFO (b) and CFO (c) films. The linear extrapolations of $(\alpha \cdot E)^2$ and $(\alpha \cdot E)^{1/2}$ to zero give the values for optical band gaps of the direct and indirect transitions, respectively.

for the direct and indirect transitions, respectively. For CFO these values were determined to be 1.95 eV and 1.42 eV. The same method has been employed before for modeling the absorption edge for multiferroic materials.[26,27] The error in the determination of these values was estimated to be ±0.03 eV. The characteristic S-shape of $(\alpha \cdot E)^{1/2}$ which presents two distinct slopes suggests the phonon involvement in the optical absorption process[28,29] indicating that NFO and CFO are indirect bandgap materials. The values for the indirect transitions are larger than the values calculated from first principles for both NFO and CFO.[10,30] On the other hand, the values are smaller than those recently experimentally determined using absorption measurements for NFO[31] and CFO[32] thin films. It should be pointed out that the optical constants obtained from ellipsometry are more reliable than those obtained directly from absorption measurements particularly near to the absorption edge.

The MOKE rotation and ellipticity spectra of the NFO and CFO films are shown in Figure 5. The NFO film exhibits a smaller MOKE signal and therefore the NFO spectra were multiplied by a factor of 3 for a better comparison.

The lineshape of the polar Kerr rotation of the NFO film is similar to that observed for the (111) face of a nickel ferrite single crystal[33] only slight shifts and small differences in the relative intensities of the spectral structures are noticeable. The same observation also holds for the CFO film as compared to the reported MOKE spectra of a $CoFe_2O_4$ (111) single crystal.[15] The similarity between the film and crystal spectra can easily be understood at higher energies considering that the penetration depth, estimated from the optical constants determined in this work, is lower than the film thickness for photon energies above 2.21 eV (CFO) and 2.84 eV (NFO).

However, in order to avoid possible interference effects in the low energy region of the spectra, the off-diagonal component of the dielectric tensor was obtained as described in the following.

The magneto-optical Kerr effect can be described by the occurrence of off-diagonal components of the macroscopic dielectric tensor. In the polar MOKE geometry, as used in this work, the light propagates along the z direction and hence parallel to the magnetic field direction. The dielectric tensor for a tetragonal crystal, such as proposed by Fritsch *et al.*[10] for the investigated systems, exposed to a magnetic field applied along the c direction (along the z-axis) has the following form:

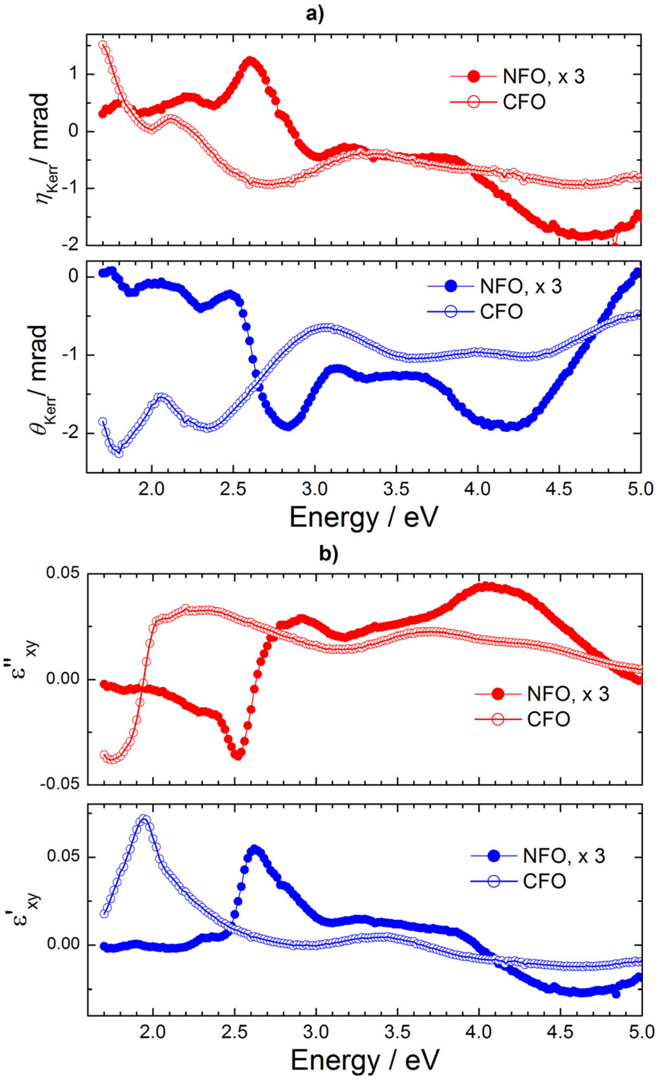

FIG. 5. Complex MOKE spectra of a 69 nm NFO film and of a 80 nm CFO film on STO substrates (a). Real (ε'_{xy}) and imaginary parts (ε''_{xy}) of the off-diagonal component of the dielectric tensor determined from the MOKE spectra and the diagonal components. (b)

$$\hat{\varepsilon} = \begin{bmatrix} \tilde{\varepsilon}_{xx} & \tilde{\varepsilon}_{xy} & 0 \\ \tilde{\varepsilon}_{xy} & \tilde{\varepsilon}_{xx} & 0 \\ 0 & 0 & \tilde{\varepsilon}_{zz} \end{bmatrix}, \tag{1}$$

where all tensor elements are complex quantities, i.e., $\tilde{\varepsilon}_{xx} = \tilde{\varepsilon}'_{xx} + i \cdot \tilde{\varepsilon}''_{xx}$ and $\tilde{\varepsilon}_{xx} = \tilde{\varepsilon}'_{xy} + i \cdot \tilde{\varepsilon}''_{xy}$. The off-diagonal component of the dielectric tensor can be expressed with the help of magneto-optical material constant Q, the so-called Voigt constant: $\tilde{\varepsilon}_{xy} = Q \cdot \tilde{\varepsilon}_{xx}$.[34]

For bulk samples, only the light reflected at the sample surface carries the magneto-optical information and the corresponding change in the light polarization upon reflection can be expressed in the following form:

$$\hat{\Phi}_K = \theta_K + i \cdot \eta_K = i \frac{\sqrt{\varepsilon_{xx}}Q}{1 - \varepsilon_{xx}}. \tag{2}$$

For a film with a thickness smaller than the penetration depth of the light, light can also be reflected at the interface film/substrate and the magneto-optical signal is influenced by interference effects. In this work, we will use the mathematical formalism from Fronk *et al.*[35] to extract the Voigt constant Q by a point-by-point fitting procedure from the MOKE spectra and from the optical constants obtained by spectroscopic ellipsometry. Thus, we calculated the off-diagonal elements of the dielectric tensor for comparison with reported values on ferrites (e.g., in Fontijn *et al.*[16]).

The STO substrate itself exhibits a small MOKE signal in the energy range between 4 eV and 5 eV. This was taken into account in the numerical calculation of the Voigt constant of the NFO and CFO films. The spectral dependence of the real (ε'_{xy}) and imaginary part (ε''_{xy}) of the off-diagonal component of the CFO dielectric tensor is shown in Figure 5(b). The shape and magnitude of the spectra are very similar to that reported for a CFO(111) single crystal.[15] The sign of ε'_{xy} is, however, inversed, due to different sign conventions used in the definition of the complex Kerr rotation angle. Only a few slight differences are noticeable: the transition between the crystal field (CF) splitted *d* orbitals of Co^{2+} is blue shifted in our case (by 0.12 eV); the intervalence charge transfer (IVCT) transition at ∼2.2 eV is stronger in our films compared to the crystal, and the inter-sublattice charge transfer (ISCT) transition at ∼4 eV is smaller in its relative intensity to the other bands compared to the crystal.[32] The observation of the CF band in mixed ferrites is attributed to a distortion of the octahedral site symmetry. Moreover, in ferrites with ions in the high spin state on the tetrahedral lattice sites (such as Co^{2+} in CFO) the CF transitions may have considerable oscillator strength.[16] The blue shift of the CF transition in our CFO film compared to the crystal might be related to the presence of residual strain in the films. The intensity decrease of the ISCT band at ∼4 eV might be explained by a decrease in the net magnetic moment, probably due to structural defects reducing the symmetry of the octahedral and tetrahedral Fe^{3+} sites. A similar observation was reported for the NFO MOKE spectra of films compared to the bulk by Mistrik *et al.*[18]

In case of NFO, the ε'_{xy} and ε''_{xy} spectra calculated in this work exhibit sharper features compared to those reported for a NFO crystal in Ref. 36. This might be due to a better crystalline quality of the films compared to the crystals studied by Fontijn *et al.*[36] Our MOKE spectra are, however, well comparable to those of the 1 μm films studied by Kim *et al.*[17] We therefore refer to the latter reference for the assignment of the spectral features of films in this study.

The crystal field (CF) transition in NFO is much weaker compared to that in CFO, however, still detectable. For Ni^{2+} ions occupying octahedral sites the CF transitions are parity forbidden and should not be observed in NFO. However, if the film has a tetragonal symmetry as indicated by the Raman results, rather than a cubic symmetry, the parity selection rules for the Ni^{2+} ions at the octahedral sites are relaxed and the CF transitions can be observed. In addition, a small fraction (3.5% or less) of Ni^{2+} ions occupying tetrahedral sites could lead detectable MOKE signal[17] while hardly affecting the Raman spectra. The oscillator strength of the CF transition in NFO is lower than in CFO due to the lower spin state of the Ni^{2+} ($3d^8$) ions.

The energy of the transitions determined from the MOKE spectra and from the off-diagonal components of the

TABLE I. The energy of the transitions determined from the MOKE spectra and from the off-diagonal components of the dielectric tensor compared to the values reported for the 1 μm thick films and for the single crystals, respectively, along with the assignment of the spectral features. The ions situated at octahedral positions are denoted by square brackets and the tetrahedral sites are denoted by parentheses.

Sample	MOKE spectra energy/eV, This work	MOKE spectra energy /eV Sol-gel films, Ref. 17	ε'_{xy} spectra energy /eV, This work	ε'_{xy} spectra energy /eV Crystal, Ref. 16	Type	Transition assignment according to Kim *et al.*[17] assuming a cubic inversed spinel structure
CFO	1.78	2.0	1.94	1.82	CF(Co^{2+})	$^4A_2(^4F)\rightarrow{}^4T_1(P)$
	2.05	2.2	2.28	2.21	IVCT	$[Co^{2+}]t_{2g}\rightarrow[Fe^{3+}]t_{2g}$
	2.67	2.6	2.7	2.60	ISCT	$(Fe^{3+})t_2\rightarrow[Fe^{3+}]t_{2g}$
	3.6	3.6	3.68	3.55	IVCT	$[Co^{2+}]t_{2g}\rightarrow[Fe^{3+}]t_{2g}$
	4.3	4.0	4	4	ISCT	$(Fe^{3+})t_2\rightarrow[Fe^{3+}]e_g$
	4.7		4.6			
NFO	1.85	2.2	1.89		CF(Ni^{2+})	$^3T_1(^3F)\rightarrow{}^3A_2(F)$
	2.61	2.6	2.52	2.57	ISCT	$(Fe^{3+})t_2\rightarrow[Fe^{3+}]t_{2g}$
	3.1	3.1	3.15	2.86	IVCT	$[Ni^{2+}]t_{2g}\rightarrow[Fe^{3+}]t_{2g}$
	4.2	4.0	4.15	4.03	ISCT	$(Fe^{3+})t_2\rightarrow[Fe^{3+}]e_g$
	4.65	4.5	4.62		IVCT	$[Ni^{2+}]t_{2g}\rightarrow[Fe^{3+}]t_{2g}$

dielectric tensor (for comparison with Ref. 16) are summarized in Table I and compared to the values reported for the 1 μm thick films and for the single crystals along with the assignment of the spectral features. It should be noted that all band assignments proposed in the literature assume a cubic symmetry of the inverse spinel structure. A small tetragonal distortion should lead to a broadening of the bands compared to the real cubic structure.

From the difference between the energies of the IVCT transitions involving Fe^{3+} ions, the energy splitting between the t$_{2g}$ and the e$_g$ orbitals was calculated to amount to 1.4 eV for CFO and 1.47 eV for NFO. These values are consistent with that reported by Fontijn *et al.*[16]

SUMMARY

The Raman spectra measured on nickel and cobalt ferrite revealed a larger number of phonon bands than expected for the cubic spinel structure. Their polarisation dependence can be explained by a short range ordering of the divalent cations at the octahedral sites which induce a lowering of the symmetry, in agreement with the model proposed by Ivanov *et al.*[8] The Raman investigations performed on the ordered arrays of submicron structures showed the preservation of the cation distribution at the tetragonal and octahedral sites as in the corresponding epitaxial films. The dielectric function of the ferrite films was determined in the 0.73–5 eV energy range. A bandgap model was used to analyze the absorption edges and the energies of the first indirect and direct optical transition were determined for both cobalt and nickel ferrites. It was found that both materials have an indirect bandgap, with values of 1.65 eV and 1.42 eV for nickel ferrite and cobalt ferrite, respectively.

The off-diagonal components of the dielectric tensor determined from the MOKE spectra and ellipsometry spectra compare well with the reported bulk spectra for CFO, except slightly different relative intensities of the IVCT and ISCT bands, which might be related to the presence of structural defects that reduce the symmetry of the octahedral and tetrahedral Fe^{3+} sites in our films. The ε'_{xy} and ε''_{xy} spectra calculated in this work exhibit sharper features as compared to the bulk spectra reported by Fontijn *et al.*,[36] possibly due to a higher crystalline quality of the films.

ACKNOWLEDGMENTS

This work was supported by the German Research Foundation DFG HI 1534/1-1.

[1] N. Li, Y. H. A. Wang, M. N. Iliev, T. M. Klein, and A. Gupta, Chem. Vap. Deposition **17**, 261 (2011).
[2] Z. Chen and V. G. Harris, J. Appl. Phys. **112**, 081101 (2012).
[3] J. M. D. Coey, *Magnetism and Magnetic Materials* (Cambridge University Press, 2009).
[4] G. A. Sawatsky, F. van der Woude, and A. H. Morrish, Phys. Rev. **187**, 747 (1969).
[5] H. L. Yakel, J. Phys. Chem. Solids **41**, 1097 (1980).
[6] D. S. Erickson and T. O. Mason, J. Solid State Chem. **59**, 42 (1985).
[7] P. Chandramohan, M. P. Srinivasan, S. Velmurugan, and S. V. Narasimhan, J. Solid State Chem. **184**, 89 (2011).
[8] V. G. Ivanov, M. V. Abrashev, M. N. Iliev, M. M. Gospodinov, J. Meen, and M. I. Aroyo, Phys. Rev. B **82**, 024104 (2010).
[9] M. N. Iliev, D. Mazumdar, J. X. Ma, A. Gupta, F. Rigato, and J. Fontcuberta, Phys. Rev. B **83**, 014108 (2011).
[10] D. Fritsch and C. Ederer, Appl. Phys. Lett. **99**, 081916 (2011).
[11] Z. Wang, R. T. Downs, V. Pischedda, R. Shetty, S. K. Saxena, C. S. Zha, Y. S. Zhao, D. Schiferl, and A. Waskowska, Phys. Rev. B **68**, 094101 (2003).
[12] M. Foerster, M. Iliev, N. Dix, X. Marti, M. Barchuk, F. Sanchez, and J. Fontcuberta, Adv. Func. Mater. **22**, 4344 (2012).
[13] O. Chaix-Pluchery, C. Cochard, P. Jadhav, J. Kreisel, N. Dix, F. Sanchez, and J. Fontcuberta, Appl. Phys. Lett. **99**, 072901 (2011).
[14] W. F. J. Fontijn, P. J. van der Zaag, M. A. C. Devillers, V. A. M. Brabers, and R. Metselaar, Phys. Rev. B. **56**, 5432 (1997).
[15] J. W. D. Martens, W. L. Peeters, and H. M. Van Noort, J. Phys. Chem. Solids **46**, 411 (1985).
[16] W. F. J. Fontijn, P. J. van der Zaag, L. F. Feiner, R. Metselaar, and M. A. C. Devillers, J. Appl. Phys. **85**, 5100 (1999).
[17] K. J. Kim, H. S. Lee, M. H. Lee, and S. H. Lee, J. Appl. Phys. **91**, 9974 (2002).
[18] J. Mistrík, R. Lopušník, Š. Višňovský, N. Keller, M. Guyot, and R. Krishnan, J. Magn. Magn. Mater. **226–230**, 1820 (2001).
[19] I. Vrejoiu, A. Morelli, D. Biggemann, and E. Pippel, Nanoreviews **2**, 7364 (2011).
[20] T. Herrmann, K. Lüdge, W. Richter, K. G. Georgarakis, P. Poulopoulos, R. Nünthel, J. Lindner, M. Wahl, and N. Esser, Phys. Rev. B **73**, 134408 (2006).

[21] Y. Y. Liao, Y. W. Li, Z. G. Hu, and J. H. Chu, Appl. Phys. Lett. **100**, 071905 (2012).

[22] P. R. Graves, C. Johnston, and J. J. Campaniello, Mater. Res. Bull. **23**, 1651 (1988).

[23] D. E. Aspnes, J. B. Theeten, and F. Hottier, Phys. Rev. B **20**, 3292 (1979).

[24] G. S. Krinchik, K. M. Mukimov, Sh. M. Sharipov, A. P. Khrebtov, and E. M. Speranskaya, Zh. Eksp. Teor. Fiz. **76**, 2126 (1979).

[25] J. Bardeen, F. Blatt, and L. H. Hall, in *Photoconductivity Conference*, edited by R. G. Breckenridge, B. R. Russel, and E. E. Hahn (Wiley-Interscience, New York, 1956).

[26] C. Himcinschi, I. Vrejoiu, M. Friedrich, E. Nikulina, L. Ding, C. Cobet, N. Esser, M. Alexe, D. Rafaja, and D. R. T. Zahn, J. Appl. Phys. **107**, 123524 (2010).

[27] C. Himcinschi, I. Vrejoiu, T. Weißbach, K. Vijayanandhini, A. Talkenberger, C. Röder, S. Bahmann, D. R. T. Zahn, A. A. Belik, D. Rafaja, and J. Kortus, J. Appl. Phys. **110**, 073501 (2011).

[28] S. Guo, H. Arwin, S. N. Jacobsen, K. Järrendhal, and U. Helmersson, J. Appl. Phys. **77**, 5369 (1995).

[29] J. I. Pankove, *Optical Processes in Semiconductors* (Prentice-Hall, Englewood Cliffs, 1971).

[30] Z. Szotek, W. M. Temmerman, D. Ködderitzsch, A. Svane, L. Petit, and H. Winter, Phys. Rev. B **74**, 174431 (2006).

[31] R. C. Rai, S. Wilser, M. Gruminiak, B. Cai, and M. L. Nakarmi, Appl. Phys. A **106**, 207 (2012).

[32] A. V. Ravindra, P. Padhan, and W. Prellier, Appl. Phys. Lett. **101**, 161902 (2012).

[33] F. J. Kahn, S. P. Pershan, and J. P. Remeika, Phys. Rev. **186**, 891 (1969).

[34] J. Zak, E. R. Moog, C. Liu, and S. D. Bader, Phys. Rev. B **43**, 6423 (1991).

[35] M. Fronk, B. Bräuer, J. Kortus, O. G. Schmidt, D. R. T. Zahn, and G. Salvan, Phys. Rev. B **79**, 235305 (2009).

[36] W. F. J. Fontijn, P. J. van der Zaag, and R. Metselaar, J. Appl. Phys. **83**, 6765 (1998).

Thin Solid Films 520 (2012) 4590–4594

Contents lists available at SciVerse ScienceDirect

Thin Solid Films

journal homepage: www.elsevier.com/locate/tsf

Raman spectroscopic and X-ray diffraction investigations of epitaxial $BiCrO_3$ thin films

Andreas Talkenberger [a,*], Cameliu Himcinschi [a], Torsten Weißbach [a], Kannan Vijayanandhini [b], Ionela Vrejoiu [b], Christian Röder [a], David Rafaja [c], Jens Kortus [a]

[a] *Institute of Theoretical Physics, TU Bergakademie Freiberg, Leipziger Str. 23, D-09596 Freiberg, Germany*
[b] *Max Planck Institute of Microstructure Physics, Weinberg 2, D-06120 Halle, Germany*
[c] *Institute of Materials Science, TU Bergakademie Freiberg, Gustav-Zeuner-Str. 5, D-09596 Freiberg, Germany*

ARTICLE INFO

Article history:
Received 31 May 2011
Received in revised form 30 August 2011
Accepted 23 October 2011
Available online 10 November 2011

Keywords:
$BiCrO_3$
Multiferroic thin films
XRD
Raman spectroscopy

ABSTRACT

Epitaxial $BiCrO_3$ thin films were grown onto $NdGaO_3$ (110)- and $(LaAlO_3)_{0.3}$-$(Sr_2AlTaO_6)_{0.7}$ (100)-oriented substrates by pulsed laser deposition. High resolution X-ray diffraction and pole figure measurements were performed in order to obtain information about the crystal structure of the films, about their quality and about the mutual crystallographic orientation between the films and the substrates. The monoclinic (111) plane of $BiCrO_3$ was found out to be parallel to the substrate surface. The epitaxial relation between films and substrates was verified by using polarisation dependent Raman spectroscopic experiments and theoretical calculations based on symmetry.

1. Introduction

Multiferroic epitaxial thin films are of strong research interest due to their potential applications, such as in memory devices [1–3]. For applications the fabrication of high-quality epitaxial thin films and a fundamental understanding of their physical properties are needed.

Among the candidates for multiferroic thin film materials the Bi-based magnetic transition metal perovskites, especially $BiFeO_3$, are on great interest [4,5]. Another interesting potential candidate is $BiCrO_3$ (BCO). BCO was first synthesised by Sugawara and Lida [6] in 1965 and shows a monoclinic crystal structure at room temperature with C2/c symmetry and phase transition to an orthorhombic crystal system above 420 K [7,8]. Recently, a third stable phase in epitaxial strained BCO films similar to a superstructure closely related to the C2/c monoclinic form was observed [9]. Concerning the magnetic and dielectric properties, bulk BCO shows a long-range antiferromagnetic order below $T_N = 109$ K [10] with weak ferromagnetism due to the canting of the Cr spins [11] and possesses an antiferroelectric order up to the structural transition temperature at around 410 K as proposed by Kim [12]. Raman spectroscopy is a non-destructive method which found increasing application in the characterisation of multiferroic thin film materials because of its sensitivity to the film orientation, to the strain and to the phase transitions which are intimately linked to specific phonon modes [13–16].

In this work we present results of the X-ray diffraction (XRD) and Raman spectroscopy studies on epitaxial $BiCrO_3$ (BCO) thin films fabricated by pulsed laser deposition on $(LaAlO_3)_{0.3}$-$(Sr_2AlTaO_6)_{0.7}$ (100)-oriented and $NdGaO_3$ (110)-oriented single crystal substrates.

2. Experimental details

The epitaxial BCO thin films were grown by pulsed laser deposition on (100)-oriented $(LaAlO_3)_{0.3}$-$(Sr_2AlTaO_6)_{0.7}$ (LSAT) and (110)-oriented $NdGaO_3$ (NGO) single crystal substrates. To optimize the epitaxial growth a 40 nm thick $La_{0.7}Sr_{0.3}MnO_3$ (LSMO) buffer layer onto LSAT and a 16 nm thick $SrRuO_3$ (SRO) buffer layer onto NGO has been grown. A KrF laser was used for ablation having a frequency of about 3–5 Hz and an effective energy of 2–3 J/cm². During the growth the substrates were heated up to ~650 °C under an oxygen partial pressure of 0.17–0.70 Pa. The target-to-substrate distance was 6 cm. A commercial $Bi_{1.1}CrO_3$ target (Pi-Kem Ltd.) with bismuth oxide excess, of 2 inch diameter, was employed for ablation.

The Raman spectroscopic measurements were carried out by a LabRam Horiba Jobin Yvon spectrometer using the frequency-doubled 532 nm excitation line of Nd:YAG laser. A backscattering geometry was employed with both incident and scattered light being perpendicular to the sample surface. Measurements were carried out at room temperature by rotating the sample azimuthally around the surface normal using both parallel (vv) and cross (hv) polarisation configurations in order to test the Raman selection rules. The scattered light was collected using a 100× magnification objective. To avoid any

---

[*] Corresponding author at: Leipziger Str. 23, D-09596 Freiberg, Germany. Tel.: +49 3731 39 2591; fax: +49 3731 39 4005.
E-mail address: andreas.talkenberger@tu-freiberg.de (A. Talkenberger).

0040-6090/$ – see front matter
doi:10.1016/j.tsf.2011.10.196

influence of laser heating on the Raman spectra and to prevent damage on the surface of the samples, the laser power was reduced to ~0.6 mW.

The mutual crystallographic orientation between the film and the substrate was determined with the aid of pole figure measurements that were performed on a D8-Discover diffractometer from Bruker/AXS equipped with a general area detector diffraction system. During the pole figure measurement, the intensities diffracted both by the $NdGaO_3$ substrate and by the $BiCrO_3$ thin film were recorded as a function of the diffraction angle (2θ), the sample inclination from its symmetrical position (ψ) and the sample rotation around its (surface) normal direction (ϕ). The measured intensity maxima were plotted in form of the stereographic projection [17]. The 2D detector allowed a simultaneous data acquisition at different diffraction angles, which speeded up the search for the diffraction maxima in possibly strained epitaxially grown films. For the pole figure measurements CoKα radiation was used ($\lambda = 0.178897$ nm). High-resolution XRD (HR-XRD) measurements were carried out on an URD6 diffractometer at 0.154056 nm ($CuK\alpha_1$ radiation). The URD6 diffractometer was equipped with two perfect (111)-oriented dislocation-free silicon single crystals; one used as monochromator in the primary beam, the other as analyser in front of a scintillation detector.

3. Results and discussion

The epitaxial relation between the BCO film and the NGO substrate covered with the SRO buffer was concluded from the pole figure measurements using the procedure described in references [18, 19]. The pole figures measured for the NGO substrate at the detector angles 26.6° and 38.3° were overlaid and are shown in form of the stereographic projection in Fig. 1a. The detector angle is equal to the diffraction angle (2θ) in the middle of the detector area. Because of a large angular acceptance of the 2D detector, the XRD lines (020), (112) and (200) of the orthorhombic NGO, that are located at $2\theta = 37.954°$, 38.295° and 38.514° [20], respectively, were recorded simultaneously.

Likewise, the overlaid pole figures of the monoclinic BCO thin film that were measured at the detector angles 26.6°, 38.0° and 47.0° are displayed in Fig. 1b. The comparison of the pole figures from Fig. 1b with the stereographic projections of BCO having the space group C2/c [8] helped us to assign the individual diffraction maxima. Like for the NGO substrate, diffraction maxima from lattice planes with different interplanar spacings and thus with different diffraction angles were recorded simultaneously because of the large angular acceptance of the 2D detector. For the monoclinic BCO film this concerns the diffraction lines (202) with $2\theta = 37.528°$, (−113) with $2\theta = 37.814°$, (020) with $2\theta = 38.100°$, (31−1) with $2\theta = 38.189°$, (004) with $2\theta = 46.364°$, (400) with $2\theta = 46.998°$ and (−222) with $2\theta = 47.162°$. Because of the proximity of the diffraction angles of $(110)_{NGO}$ (26.780°) and $(111)_{BCO}$ (26.492°), these diffraction lines appear in both pole figures (Fig. 1a and b). The comparison of the stereographic projections of NGO and BCO, which were first oriented according to the measured and overlaid pole figures from Fig. 1, revealed that the lattice planes $(111)_{BCO}$ are nearly parallel to the lattice planes $(110)_{NGO}$. In the plane of the sample the nearly parallel crystallographic directions are $<-110>_{NGO}$ and $<10\text{–}1>_{BCO}$.

The upper part of Fig. 2 shows the monoclinic crystal system of BCO with the (111) and the (−11−1) planes being hatched. The epitaxial orientation relationship between BCO and NGO is displayed in the bottom part of Fig. 2. The pseudo-cubic axes of BCO correspond to the laboratory coordinates used for Raman measurements. It should be mentioned that the thickness of the BCO layer was 160 nm while the SRO buffer layer was only 16 nm thick, thus the SRO reflections were not considered during the pole figure measurement and the interpretation of the measured data.

In order to determine the orientation of the monoclinic BCO thin film grown on the (100)-oriented LSAT substrate coated with the LSMO buffer, symmetrical high resolution XRD measurement was performed. The presence of the XRD lines (111) from BCO and (100) from LSAT and the presence of the thickness oscillations in the HR-XRD pattern (Fig. 3) confirm that the BCO film has grown epitaxially on the LSAT substrate with the orientation $(111)_{BCO} \parallel (100)_{LSAT}$. The periodicity of the thickness oscillations corresponds to the thickness of the BCO layer of 80–90 nm. A high intensity of the thickness oscillations implies a (strained) epitaxial growth without relaxation, which is only possible for coherent epitaxial growth. The presence of the lattice strain and the absence of the lattice strain relaxation were confirmed by the shift of the diffraction line (111) of the monoclinic BCO from $2\theta = 22.76°$ (as calculated for $d_{111} = 0.3904$ nm in non-strained BCO) to $2\theta = 22.63°$. This difference in the diffraction angle corresponds to the out-of-plane lattice deformation ε of 5.65×10^{-3} as calculated using the differential form of the Bragg law,

$$\varepsilon = \frac{\Delta d}{d} = -\cot\theta\Delta\theta. \quad (1)$$

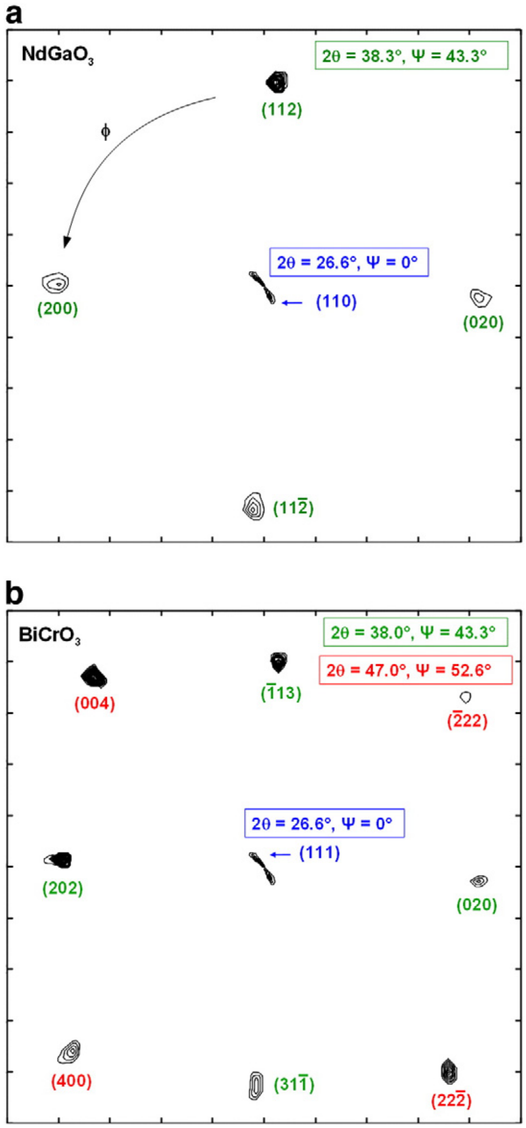

Fig. 1. Overlaid pole figures of the NGO substrate (a) and the epitaxially grown BCO film (b), measured at different detector angles (2θ). Angle ψ denotes the inclination of the diffraction vector from the sample surface perpendicular direction. The split central peak measured at $2\theta = 26.6°$ represents both the $(110)_{NGO}$ reflection and the monoclinic $(111)_{BCO}$ reflection.

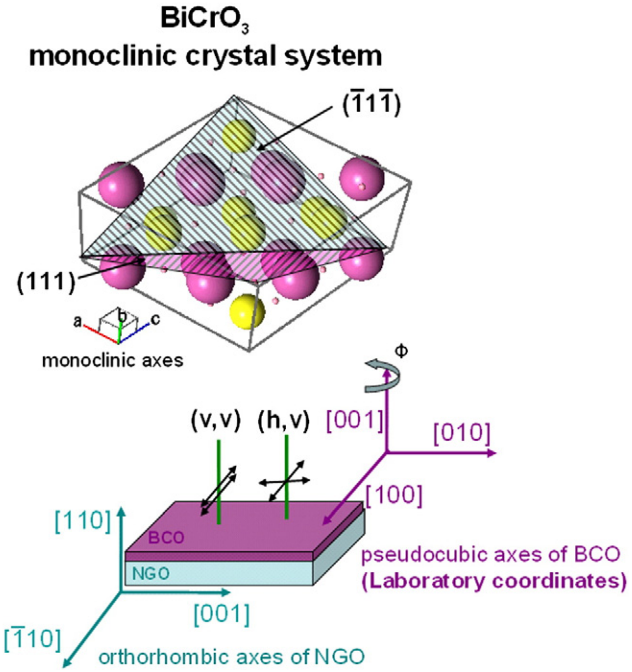

Fig. 2. Crystallographic orientation of monoclinic BCO (upper part) in respect to the crystal axes of orthorhombic NGO substrate (below). The big, middle, and small size balls correspond to the Cr, Bi, and O atoms, respectively. The hatched areas show the (111) and the (−11−1) monoclinic planes of BCO. The pseudocubic axes of BCO correspond to the laboratory coordinates used for the Raman measurements. The direction of the laser (corresponding to the [110] direction of NGO) and of the polarisations for (vv) and (hv) scattering configuration are also schematically shown.

This means that the in-plane lattice parameter of BCO fits to the lattice parameter of the substrate.

The laboratory coordinates used for the Raman measurements are the BCO pseudocubic coordinates as depicted in Fig. 2. The laser direction was parallel to the [110] direction of NGO. The azimuthal rotation of the sample was performed around this direction. The parallel (vv) and cross (hv) polarisation configurations are also schematically shown in Fig. 2. For the film grown on LSAT the situation is similar, the cubic axes of LSAT, being the same as the pseudocubic axes of BCO that represents the laboratory coordinate system.

The epitaxial orientation was also checked by performing polarisation-dependent Raman measurements. For these measurements the electric field vector of the incident laser beam was set either parallel to the field vector of the scattered light (vv) or perpendicular to it (hv). Additionally we rotated the sample azimuthally around its

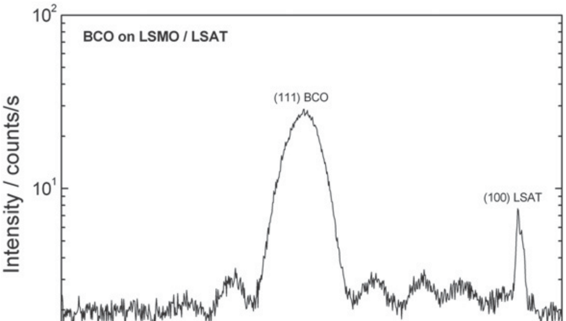

Fig. 3. Theta-2-theta HR-XRD pattern measured for an epitaxially grown BCO film on LSMO/LSAT substrate.

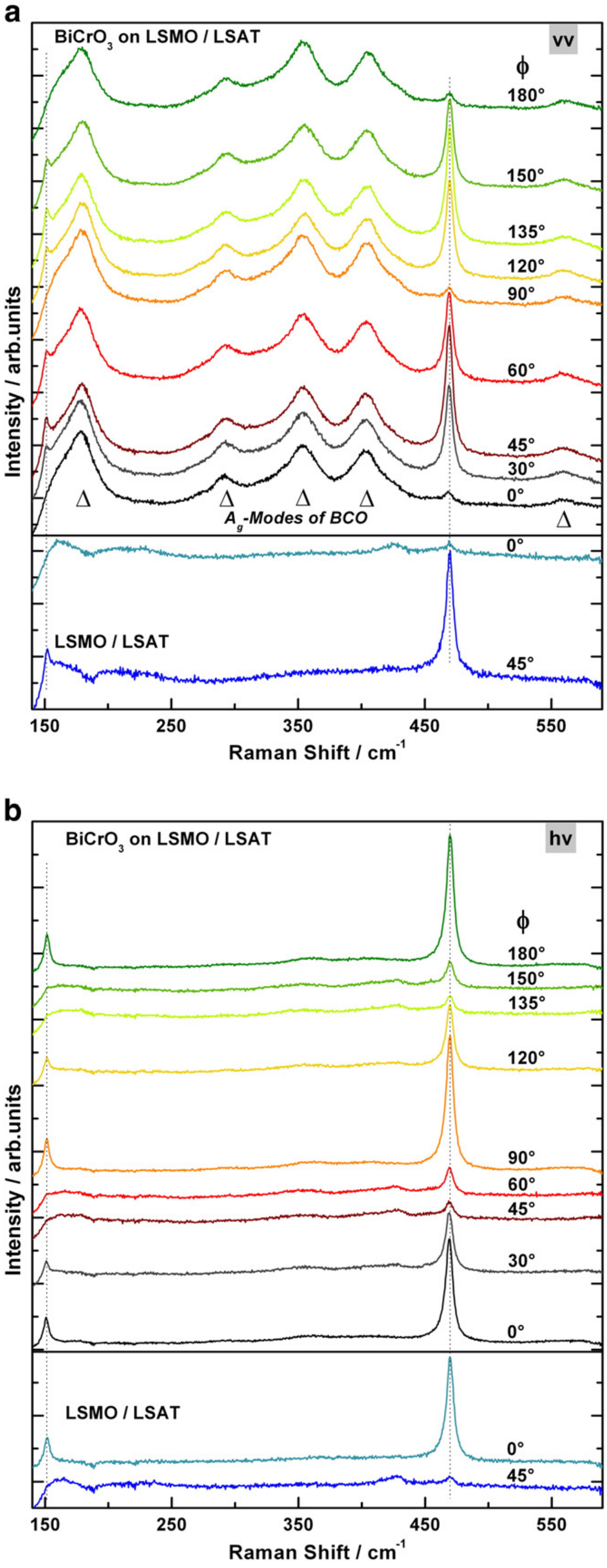

Fig. 4. a) Raman spectra of epitaxially grown BCO film on LSMO/LSAT substrate measured for different azimuthal angles ϕ (0°–180°) using parallel (vv) polarisation. Two representative spectra taken from LSMO/LSAT substrate are shown for comparison. Triangles symbolise the position of the strongest modes of BCO. b) Raman spectra of the same film and same substrate measured at the same azimuthal angles but for cross (hv) polarisation.

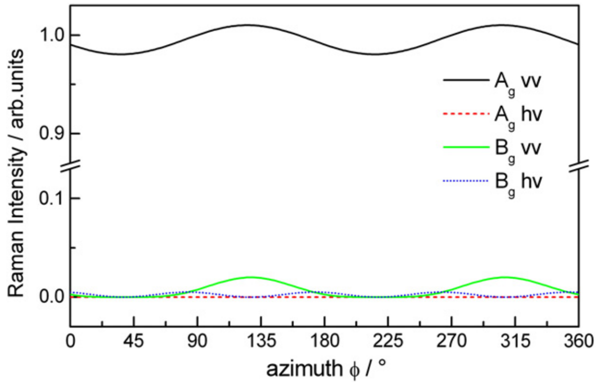

Fig. 5. Simulation of the A_g and B_g modes of BCO considering the C2/c space group for parallel and cross polarisation as function of azimuthal rotation angle with the tensor elements: $a=1$, $b=1$, $c=1$, $d=0.01$, $e=0.1$ and $f=0.1$.

normal (laser) direction. Fig. 4a shows the spectra measured in parallel polarisation configuration for different azimuthal angles for the BCO film deposited on LSMO/LSAT in the upper panel. In the bottom panel of Fig. 4a, we show for simplicity only two of the spectra of LSMO/LSAT measured for azimuthal angles of 0° and 45°. Part (b) of Fig. 4 shows the spectra for the same sample (upper panel), same substrate (down panel) and same rotation angle but measured in cross polarisation. The two peaks at 152 cm^{-1} and 470 cm^{-1} (marked by lines) correspond to the LSAT substrate and obey well the selection rules of a cubic crystal system showing a $\pi/2$ rotational symmetry. The Raman peaks at 179 cm^{-1}, 293 cm^{-1}, 354 cm^{-1}, 403 cm^{-1} and 559 cm^{-1} which belong to BCO [21], only appear in parallel polarisation configuration being completely absent in the spectra recorded in cross polarisation. Moreover the BCO peaks measured in the parallel configuration show nearly the same intensity independent on the azimuth angle. The same behaviour was also observed for the BCO film deposited on NGO. Here we present Raman data for the BCO film on LSAT because the Raman spectrum of LSAT is less complicated in comparison with that of NGO, so that the polarisation behaviour of BCO peaks can be observed more easily.

According to the factor group analysis [22] 60 vibrational modes are expected for BCO considering the monoclinic C2/c space group. 27 of these modes are Raman active (13 A_g + 14 B_g). The Raman tensor of the A_g and B_g modes can be written as [23]:

$$A_g=\begin{pmatrix} a & 0 & d\\ 0 & b & 0\\ d & 0 & c\end{pmatrix}, B_g=\begin{pmatrix} 0 & e & 0\\ e & 0 & f\\ 0 & f & 0\end{pmatrix} \qquad (2)$$

For understanding the behaviour of the BCO Raman modes observed in the polarisation dependent measurements we simulate the behaviour of the A_g and B_g modes for both parallel and cross polarisation as a function of the azimuth angle. The scattered Raman intensity can be written using the following relation [24,25]:

$$\mathrm{I}\sim\left|\mathbf{e}_\mathrm{i}\mathbf{MRM}^{-\mathbf{1}}\mathbf{e}_\mathrm{s}\right|^2, \qquad (3)$$

where $\mathbf{e_i}$ and $\mathbf{e_s}$ are the polarisation vectors for incident and scattered light, respectively. **M** is the Euler rotation matrix and **R** the Raman tensors as given by Eq. (2). In case of monoclinic symmetry, Raman tensors refer to a rectangular coordinate system where the monoclinic axis (in Fig. 3 it is b) coincides with the lattice basis. The other two directions, which are perpendicular to the monoclinic axis, can be chosen arbitrarily. There are several ways of deriving the coordinates of the polarisation vectors in the Raman tensor coordinate system. We have calculated the Euler rotation matrix **M** which rotates the normal to the (111) monoclinic plane into an [100] direction. The transpose of this matrix is then applied to the scattered polarisation direction. To investigate the effect of a rotation on polarisation, another free rotation angle around the [100] axis is included in the polarisation directions representing the azimuthal angle ϕ in the experiments. After these transformations the rotation matrix **M** has the following form:

$$\mathbf{M}=\begin{pmatrix} \cos[\phi]\ \cos[\psi]-\cos[\theta]\ \sin[\phi]\ \sin[\psi] & -\cos[\psi]\ \cos[\theta]\ \sin[\phi]-\cos[\phi]\ \sin[\psi] & \sin[\phi]\ \sin[\theta]\\ \cos[\psi]\ \sin[\phi]+\cos[\phi]\ \cos[\theta]\ \sin[\psi] & \cos[\phi]\ \cos[\psi]\ \cos[\theta]-\sin[\phi]\ \sin[\psi] & -\cos[\phi]\ \sin[\theta]\\ \sin[\psi]\ \sin[\theta] & \cos[\psi]\ \sin[\theta] & \cos[\theta] \end{pmatrix} \qquad (4)$$

Thereby, ψ, θ and ϕ correspond to the Euler angles with ϕ representing the azimuthal angle.

For particular values of the tensor elements ($a=1$, $b=1$, $c=1$, $d=0.01$, $e=0.1$, $f=0.1$) the simulation of the A_g and B_g modes reproduce very well the experimentally observed behaviour. For a perfect cubic structure the off-diagonal elements of the Raman tensor are zero. In the simulations, the off-diagonal elements were set to be one order or two order of magnitudes smaller as the diagonal elements to account for the structural properties of the investigated perovskite. The monoclinic structure of BCO is in fact a slightly distorted cubic structure and can be indexed as pseudo-cubic. The slight distortion from the cubic symmetry is expected to induce off-diagonal elements that are significantly smaller than the diagonal elements.

The results of these calculations are shown in Fig. 5, where it can be seen that the A_g modes are appearing only in parallel polarisation, their intensity being nearly independent on the rotation angle, while the intensity in cross polarisation is very low. The B_g modes have a very low intensity in both cross and parallel configurations. These simulations clearly confirm the obtained experimental data indicating that the most intense Raman modes of BCO are the A_g ones while the B_g modes should have a weak intensity. For a complete determination of the tensor elements high quality single crystals of BCO are needed, which will allow Raman measurements scattered from different crystal planes.

4. Conclusions

High-resolution X-ray diffraction and XRD pole figure measurements have been performed in order to determine the epitaxial relationship between BCO thin films and NGO as well as LSAT substrates. It was found that the BCO films grow with the (111) monoclinic plane parallel to the substrate surface. Parallel and cross polarised Raman spectra for different azimuthal angles show that the BCO modes appear only in parallel configuration. These data were confirmed using symmetry based calculations, which indicate that the A_g modes appear only for parallel polarisation being independent of the azimuthal rotation angle.

Acknowledgements

This work is supported by the German Research Foundation (DFG) HI 1534/1-1. Kannan Vijayanandhini thanks the MPG-CNRS Program for Nanomaterials for supporting her work at MPI-Halle. Christian Röder thanks the Cluster of Excellence “Structure Design of Novel High-Performance Materials via Atomic Design and Defect Engineering (ADDE)” that is financially supported by the European Union (European regional development fund) and by the Ministry of Science and Art of Saxony (SMWK).

References

[1] Y.-H. Chu, L.W. Martin, M.B. Holcomb, M. Gajek, S.-J. Han, Q. He, N. Balke, C.-H. Yang, D. Lee, W. Hu, Q. Zhan, P.-L. Yang, A. Fraile-Rodríguez, A. Scholl, S.X. Wang, R. Ramesh, Nat. Mater. 7 (2008) 478.
[2] G. Catalan, J.F. Scott, Adv. Mater. 21 (2009) 2463.
[3] R. Ramesh, N.A. Spaldin, Nat. Mater. 6 (2007) 21.

[4] J. Wang, J.B. Neaton, H. Zheng, V. Nagarajan, S.B. Ogale, B. Liu, D. Viehland, V. Vaithyanathan, D.G. Schlom, U.V. Waghmare, N.A. Spaldin, K.M. Rabe, M. Wuttig, R. Ramesh, Science 299 (2003) 1719.
[5] H.W. Jang, D. Ortiz, S.-H. Baek, C.M. Folkman, R.R. Das, P. Shafer, Y. Chen, C.T. Nelson, X. Pan, R. Ramesh, C.-B. Eom, Adv. Mater. 21 (2009) 817.
[6] F. Sugawara, S. Iida, J. Phys. Soc. Jpn. 20 (1965) 1529.
[7] C. Darie, C. Goujon, M. Bacia, H. Klein, P. Toulemonde, P. Bordet, E. Suard, Solid State Sci. 12 (2010) 660.
[8] A.A. Belik, S. Iikubo, K. Kodama, N. Igawa, S. Shamoto, E. Takayama-Muromachi, Chem. Mater. 20 (2008) 11.
[9] A. David, P. Boullay, R.V.K. Mangalam, N. Barrier, W. Prellier, Appl. Phys. Lett. 96 (2010) 221904.
[10] M. Opel, S. Geprägs, E.P. Menzel, A. Nielsen, D. Reisinger, K.-W. Nielsen, A. Brandlmaier, F.D. Czeschka, M. Althammer, M. Weiler, S.T.B. Goennenwein, J. Simon, M. Svete, W. Yu, S.-M. Hühne, W. Mader, R. Gross, Phys. Status Solidi A 208 (2011) 2.
[11] N.A. Hill, P. Bättig, C. Daul, J. Phys. Chem. B 106 (2002) 13.
[12] D.H. Kim, Appl. Phys. Lett. 89 (2006) 162904.
[13] D.A. Tenne, X. Xi, J. Am. Ceram. Soc. 91 (2008) 1820.
[14] J. Kreisel, P. Bouvier, J. Raman Spectrosc. 34 (2003) 524.
[15] R. Palai, R.S. Katiyar, H. Schmid, P. Tissot, S.J. Clark, J. Robertson, S.A.T. Redfern, G. Catalan, J.F. Scott, Phys. Rev. B 77 (2008) 0140110.
[16] C. Himcinschi, I. Vrejoiu, M. Friedrich, E. Nikulina, L. Ding, C. Cobet, N. Esser, M. Alexe, D. Rafaja, D.R.T. Zahn, J. Appl. Phys. 107 (2010) 123524.
[17] L.V. Azároff, Elements of X-ray Crystallography, McGraw-Hill Book Company, New York, San Francisco, London, 1968, p. 28.
[18] D. Rafaja, J. Kub, D. Šimek, J. Lindner, J. Petzelt, Thin Solid Films 422 (2002) 8.
[19] P. Kuppusami, G. Vollweiler, D. Rafaja, K. Ellmer, Appl. Phys. A 80 (2005) 183.
[20] PDF2 database on CD-ROM, ICDD Newtown Square, PA, USA, 2003.
[21] C. Himcinschi, I. Vrejoiu, T. Weißbach, K. Vijayanandhini, A. Talkenberger, C. Röder, S. Bahmann, D.R.T. Zahn, A.A. Belik, D. Rafaja, J. Kortus, J. Appl. Phys. 110 (2011) 073501.
[22] D.L. Rousseau, R.P. Bauman, S.P.S. Porto, J. Raman Spectrosc. 10 (1981) 253.
[23] R. Loudon, Adv. Phys. 50 (2001) 813.
[24] G. Turell, J. Raman Spectrosc. 15 (1984) 103.
[25] V. Pajcini, S.A. Asher, J. Am. Chem. Soc. 121 (1999) 10942.

JOURNAL OF APPLIED PHYSICS **110**, 073501 (2011)

Raman spectra and dielectric function of $BiCrO_3$: Experimental and first-principles studies

Cameliu Himcinschi,[1,a)] Ionela Vrejoiu,[2] Torsten Weißbach,[1] Kannan Vijayanandhini,[2] Andreas Talkenberger,[1] Christian Röder,[1] Silvia Bahmann,[1] Dietrich R. T. Zahn,[3] Alexei A. Belik,[4] David Rafaja,[5] and Jens Kortus[1]
[1]*TU Bergakademie Freiberg, Institute of Theoretical Physics, D-09596 Freiberg, Germany*
[2]*Max Planck Institute of Microstructure Physics, Weinberg 2, D-06120 Halle, Germany*
[3]*TU Chemnitz, Semiconductor Physics, D-09107 Chemnitz, Germany*
[4]*International Center for Materials Nanoarchitectonics, National Institute for Materials Science, 1-1 Namiki, Tsukuba, Ibaraki 305-0044, Japan*
[5]*TU Bergakademie Freiberg, Institute of Materials Science, Gustav-Zeuner-Strasse 5, D-09596 Freiberg, Germany*

(Received 9 August 2011; accepted 25 August 2011; published online 3 October 2011)

We present the complex dielectric function of $BiCrO_3$ thin films in the energy range of 0.73–9.8 eV determined using spectroscopic ellipsometry. By analyzing the absorption onset region, it is shown that the optical bandgap of $BiCrO_3$ is indirect, with a value of 2.27 eV. The imaginary part of the $BiCrO_3$ dielectric function, ε_2, calculated using density functional theory in the generalized gradient approximation with an Hubbard potential of 3 eV agrees well with the experimentally determined one. Raman spectra of both polycrystalline and epitaxial thin films of $BiCrO_3$ are reported. The temperature dependent Raman measurements indicate a structural phase transition at ~400 K which was confirmed also by x-ray diffraction investigations. *© 2011 American Institute of Physics.* [doi:10.1063/1.3642985]

INTRODUCTION

Multiferroic materials that simultaneously show electric polarization and magnetization are envisaged to play a significant role in devices if a large magnetoelectric coupling, i.e., in which the polarization and the magnetization can be controlled by applying a magnetic or electric field respectively, could be achieved.[1] Multiferroic epitaxial films may find potential applications in non-volatile ferroelectric memories or novel multiple state memories as well as in devices based on magnetoelectric effects.[2,3] The growth of high-quality single crystalline thin films of multiferroics is essential for their incorporation into practical devices as well as for the study of their intrinsic physical properties, undisturbed by extrinsic contributions from parasitic phases and extended structural defects.[4] Materials showing occurrence of intrinsic multiferroism are, however, rather rare. In multiferroic compounds with perovskite ABO_3-structure this is due to the competition between ferromagnetism and ferroelectricity (the former requires partially filled *d* orbitals whereas the latter needs empty *d* orbitals).[5] One exception is the case of bismuth perovskites, such as bismuth ferrite $BiFeO_3$ which is a single phase multiferroic, with ferroelectric and antiferromagnetic order at room temperature (RT).[6]

Another interesting candidate for intrinsic multiferroism is $BiCrO_3$. The magnetism and ferroelectricity of $BiCrO_3$ are still debated[7–10] due to the lack of high quality single crystals of $BiCrO_3$, preventing reliable investigations for understanding its physical properties. Hill *et al.*[11] have predicted that $BiCrO_3$ has a G-type antiferromagnetic ground state and antiferroelectric structural distortion considering an ideal cubic crystal structure, which leads to structural instability. Recently, Belik *et al.* revealed that $BiCrO_3$ synthesized at high pressure (~6 GPa) shows a first order structural transition from a centrosymmetric $C2/c$ monoclinic structure to a $Pnma$ orthorhombic structure at 420 K.[12] However, the same authors showed later using x-ray diffraction and dynamic ac-magnetic susceptibility studies[13] that the polycrystalline $BiCrO_3$ ceramics contain 10 to 15 vol. % of the orthorhombic phase in addition to the prevailing monoclinic phase. Similar structures were confirmed by Darie *et al.*[14] who showed the appearance of a G-type antiferromagnetic order below 114 K. David *et al.*[15] observed a third monoclinic phase in $BiCrO_3$ films grown on (100) oriented $SrTiO_3$ substrates, and attributed it to inhomogeneous distributions of local strain and to oxygen vacancies. In combination with $BiFeO_3$, $BiCrO_3$ possesses interesting properties: $BiFeO_3$/$BiCrO_3$ heterostructures showed good ferroelectricity and enhanced magnetism due to ferrimagnetic coupling between Fe and Cr ions.[16] Further, multiferroism at room temperature was proved in artificial $BiFeO_3$/$BiCrO_3$ superlattices by Ichikawa *et al.*[17]

Regarding $BiCrO_3$, to our knowledge no reports concerning optical characterization can be found in literature, even though Raman spectroscopy can, based on symmetry considerations, definitely aid to solve the controversy associated with the lack of definite crystal structural information. Raman spectroscopy has found increasing applications for the characterization of ferroelectric and multiferroic materials because the phase transitions are intimately linked to specific phonon modes.[18–21] Additionally, spectroscopic ellipsometry is a non-destructive and very sensitive surface and thin film measurement technique, which can determine

---

[a)] Author to whom correspondence should be addressed. Electronic mail: cameliu.himcinschi@physik.tu-freiberg.de.

the layer thicknesses and the dielectric function of such thin film materials.

In the present work the optical properties of polycrystalline $BiCrO_3$ ceramics and epitaxial $BiCrO_3$ thin films deposited on (110) oriented $NdGaO_3$ single crystalline substrates are investigated by Raman spectroscopy and spectroscopic ellipsometry. To the best of our knowledge this is the first experimental report on the optical properties of $BiCrO_3$.

EXPERIMENTAL

The synthesis of polycrystalline $BiCrO_3$ ceramics was realized by a sintering process which was described in detail elsewhere.[12] Epitaxial thin films of $BiCrO_3$ were grown on (110) oriented $NdGaO_3$ single crystal substrates by pulsed laser deposition technique under the following growth conditions: (i) substrate temperature $(T_s) \sim 650\,^{\circ}C$, (ii) oxygen partial pressure $(pO_2) \sim 0.017$–0.07 mbar (iii) laser fluence $(F_L) \sim 2$–3 J/cm^2 and laser frequency of 3–5 Hz.

The micro-Raman measurements were performed with a LabRam Horiba Jobin Yvon spectrometer (using 532 nm and 785 nm excitation lines of diode lasers), with a UV LabRam spectrometer (using the 325 nm emission line of a HeCd laser), and with a T64000 spectrometer (using the 647 nm emission line of a Kr^+ laser). The laser power was set low enough in order to avoid damage of the samples surface and any influence of laser heating on the Raman spectra. The spectra were recorded in backscattering geometry. Because of the polycrystalline structure of the bulk sample, no changes in the relative intensity of the Raman spectra were observed when using parallel or cross polarization configurations. Temperature-dependent Raman measurements from 87 K up to 500 K were carried out by means of a Linkam THMS-600 cooling-heating stage placed under the Raman microscope. Vacuum Ultraviolet (VUV) spectroscopic ellipsometry was performed in the 4.5–9.5 eV photon energy range using the 3 m-NIM1 monochromator at BESSY II synchrotron at Helmholtz Zentrum Berlin. Variable angle spectroscopic ellipsometry (VASE) measurements were performed in the 0.73 up to 4.5 eV range at four angles of incidence using a VASE ellipsometer (J.A. Woollam Company). Phase composition of the polycrystalline $BiCrO_3$ ceramics was proven both at room temperature and at elevated temperatures up 500 K by using powder x-ray diffraction (PXRD). These PXRD experiments were performed on a D8 Discover diffractometer (Bruker AXS), which was equipped by an x-ray tube with copper anode, by a high-temperature chamber (MRI) and by a two-dimensional position sensitive detector (GADDS). The results of room temperature PXRD were verified by a measurement performed on a conventional Bragg-Brentano diffractometer URD6 (Freiberger Praezisionsmechanik), which was equipped by an x-ray tube with copper anode and by a focusing graphite monochromator located in the front of a scintillation detector.

DFT calculations

Density functional theory (DFT) band structure calculations for bulk crystalline $BiCrO_3$ were carried out using the WIEN2K code, which implements a full potential linear augmented plane wave method.[22] Experimental crystal structure data for the monoclinic antiferromagnetic ground state of $BiCrO_3$ were taken from Ref. 12. Because of the magnetic polarization, the spin density formalism was used. For the exchange and correlation potential, the generalized gradient approximation as given by Perdew, Burke, and Ernzerhof was applied.[23]

The dielectric function was calculated within the random phase approximation using the optic code.[24] This method uses the DFT Kohn-Sham eigenstates for the calculation of the transition matrix elements in a perturbation expansion. For the integration over the Fermi surface, the eigenstates must be known in detail to achieve good precision. Therefore, a dense **k**-grid with 544 **k**-points in the irreducible part of the Brillouin zone is used. This **k** grid is displaced with respect to the origin to omit high-symmetry **k** points. In order to describe the localized, atomic-like Cr *3d* orbitals, a local, orbital dependent U potential is applied for these states. We use this potential in the fully localized limit,[25] with a moderate value for the effective parameter of $U\text{-}J = 3$ eV. In order to compare the electronic structure to the excitations in the dielectric function, we show the density of states (DOS) projected on atomic muffin-tin spheres. The electron density projected onto an atom therefore depends on the muffin-tin radius of the attached sphere. These radii are chosen in a way that the spheres touch each other, but do not overlay.

RESULTS AND DISCUSSION

Spectroscopic ellipsometry measures the changes of the polarization state of light after reflection from the sample under study.[26] These changes are measured in form of the ellipsometric parameters, Ψ and Δ, which are related to the ratio $\boldsymbol{\rho}$ of the effective reflection coefficients $\langle r_p\rangle$ and $\langle r_s\rangle$ for p-and s-polarized light as follows: $\rho = \frac{\langle r_p\rangle}{\langle r_s\rangle} = \tan\Psi \cdot e^{i\Delta}$.

The effective dielectric function $\langle\varepsilon(\omega)\rangle = \langle\varepsilon_1(\omega)\rangle + i\langle\varepsilon_2(\omega)\rangle$ of the materials penetrated by light can be determined from ρ using the expression[27] $\langle\varepsilon\rangle = \sin^2\varphi_0 + \sin^2\varphi_0\tan^2\varphi_0\left[\frac{1-\rho}{1+\rho}\right]^2$, where φ_0 is the incidence angle.

The ellipsometric spectra measured for a 55 nm $BiCrO_3$ film deposited onto $NdGaO_3$ are shown in Fig. 1(a) by symbols. The data measured using VASE in the range of $0.73-4.5$ eV were appended to the data measured using VUV ellipsometry using synchrotron radiation up to 9.8 eV. Ψ and Δ spectra depend on the thickness and the roughness of the films, and on the dielectric function of both film and substrate. In order to extract the information contained in the ellipsometric spectra a four-layer optical model consisting of ambient air/surface roughness/film/substrate was used. The dielectric function of the $NdGaO_3$ was *a priori* determined from measurements performed on the bare substrate in the same energy range. The surface rough layer was assumed to consist of 50% voids and 50% $BiCrO_3$ and was modeled using the Bruggeman effective-medium approximation.[28] The imaginary part, ε_2, of the dielectric function of $BiCrO_3$ was parameterized using one Tauc-Lorentz[29,30] and three Gaussian oscillators. The unknown parameters in the model

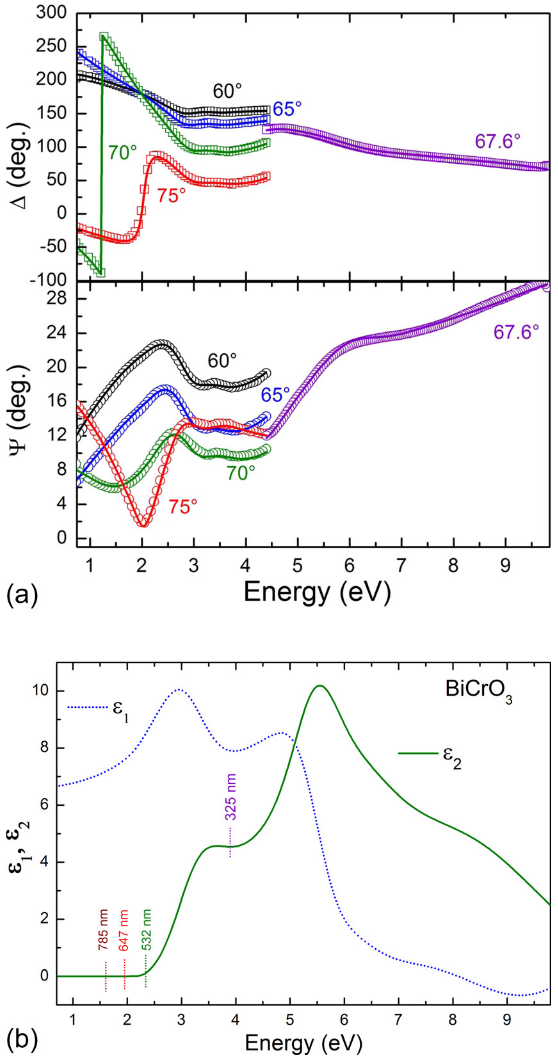

FIG. 1. (Color online) (a) Ellipsometry spectra for a 55 nm thick $BiCrO_3$ film deposited onto $NdGaO_3(110)$ substrate. The symbols denote the experimental data, while the lines show the fits. (b) Real (ε_1) and imaginary part (ε_2) of the dielectric function of the same $BiCrO_3$ film deposited onto $NdGaO_3$ substrate as determined by evaluation of the ellipsometric data. The vertical dotted lines mark the energies of the excitation lines used for the Raman measurements.

were adjusted in order to get the best match between the model and the experimental data by a fitting procedure which minimizes the mean square error. A similar procedure was also used for the characterization of the $BiFeO_3$ epitaxial thin films.[31,32] The fits are shown in Fig. 1(a) by continuous lines. A thickness of 55.5 nm was obtained for the $BiCrO_3$ films, and a roughness of 2.7 nm which is in good agreement with the roughness determined by atomic force microscopy. The imaginary part ε_2 of the dielectric function of the $BiCrO_3$ film as determined from the evaluation is shown in Fig. 1(b). The real part of the dielectric function, ε_1, was determined from ε_2 using the Kramers-Kronig relation. The vertical dotted lines mark the excitation energies of the lasers used for the Raman measurements. This means that for the first two wavelengths (785 and 647 nm) the $BiCrO_3$ material is transparent, the 532 nm line gives pre-resonant conditions for the Raman measurements, while 325 nm lies in the absorption band of $BiCrO_3$ near to the first electronic transitions.

In order to determine the energy of the optical bandgap and the type of optical transition, the absorption edge can be examined using the proportionality relation proposed by Bardeen *et al.*:[33] $\alpha \cdot E \propto (E - E_g)^\eta$, where α is the absorption coefficient, E is the photon energy, E_g is the energy of the optical bandgap, and η is a constant with the value 1/2 for direct transitions and 2 for indirect transitions. The absorption coefficient α, can be calculated from the extinction coefficient k, determined from ellipsometry as $\alpha = (4\pi k/\lambda)$. Figure 2 shows the plots of $(\alpha \cdot E)^{1/2}$ and $(\alpha \cdot E)^2$ versus photon energy. By linear extrapolations toward zero absorption,[34] values of 2.27 ± 0.03 eV for the indirect transition (from the $(\alpha \cdot E)^{1/2}$ plot) and 2.95 ± 0.03 eV for the direct transition (from the $(\alpha \cdot E)^2$ plot) are obtained. The characteristic shape of $(\alpha \cdot E)^{1/2}$ showing two distinct slopes[34,35] indicates phonon contributions to the optical absorption processes suggesting that $BiCrO_3$ is an indirect bandgap material. The band structure calculations also indicate that the optical bandgap of $BiCrO_3$ is indirect. In comparison to $BiFeO_3$, material which was proved by ellipsometry to have a direct optical bandgap,[36–38] we found out that $BiCrO_3$ is an indirect bandgap material. Moreover the first direct optical transition in $BiCrO_3$ is by ~200 meV larger than that in $BiFeO_3$.

In the imaginary part of the dielectric function, ε_2, critical points at ~3.5, 5.5, and 8 eV can be identified. The dielectric function calculated using density functional theory is shown in Fig. 3(a) and compared with the experimental determined dielectric function. Good agreement of the shape and of the absorption edge was obtained for a Hubbard potential U of 3 eV. The critical points seen in ε_2 are due to the transitions from occupied to unoccupied states. In order to assign the bands seen in ε_2 the density of states was computed. Figure 3(b) shows the total DOS for $BiCrO_3$ and the relevant atomic projection of DOS. The allowed optical transitions should have energies matching the energy difference of the bands involved in the transition. The first peak at 3.5 eV is caused by transitions from the upper valence band to the lower conduction band. These correspond either to

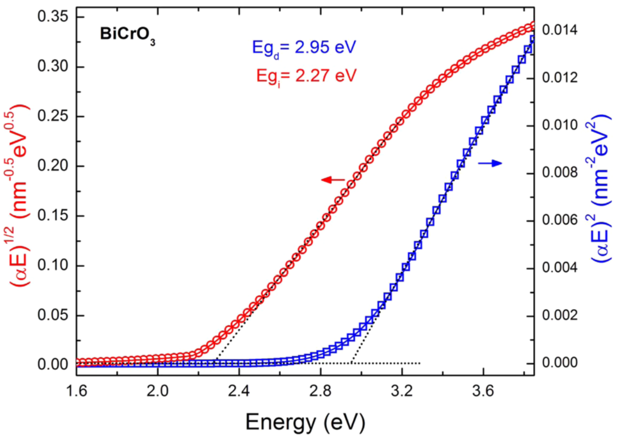

FIG. 2. (Color online) $(\alpha \cdot E)^2$ and $(\alpha \cdot E)^{1/2}$ plotted as function of photon energy, E, for a 55 nm $BiCrO_3$ film deposited on $NdGaO_3(110)$ substrate. The linear extrapolations of $(\alpha \cdot E)^2$ and $(\alpha \cdot E)^{1/2}$ to zero yield values of 2.95 eV and 2.27 eV for optical band gaps of the direct and indirect transitions for $BiCrO_3$.

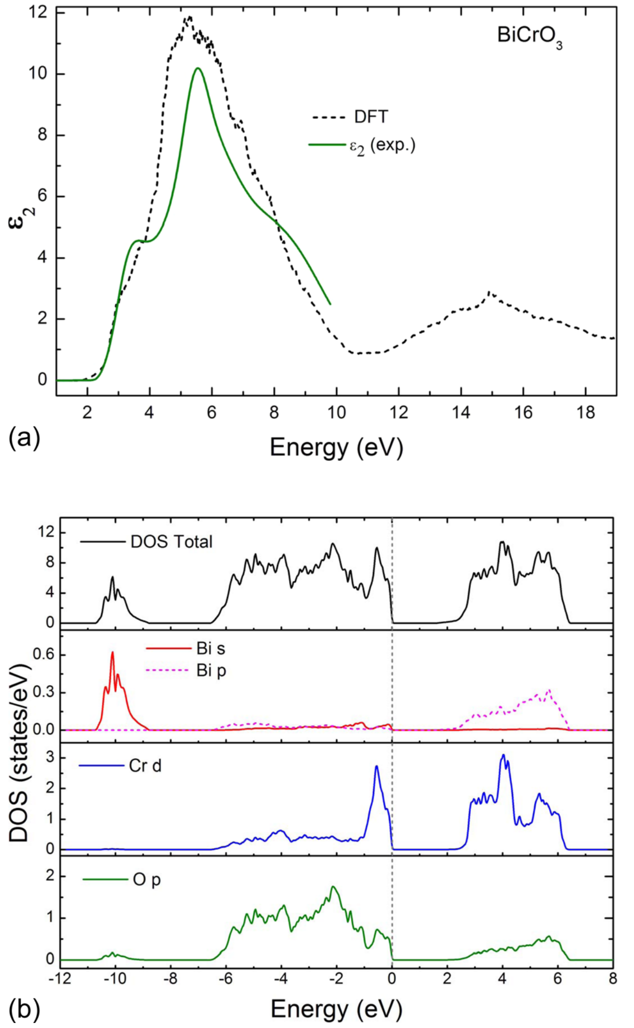

FIG. 3. (Color online) (a) Comparison between the imaginary part of the BiCrO$_3$ dielectric function as determined by ellipsometry (continuous line), and calculated using DFT (dashed line) (U−J = 3 eV); (b) Total DOS and DOS projected on atomic muffin-tin spheres (U−J = 3 eV).

transitions from Cr *3d* valence states to conduction band, or from occupied O *2p* to unoccupied Cr *3d*, or *d*-*d* transitions between Cr *3d* states of different Cr atoms. For the next two features, the peak at 5.5 eV and the shoulder at ∼ 8 eV, several transitions are responsible. Because of the energy differences involved, initial states as well as final states are mainly O *2p* and Cr *3d*, with small contributions from Bi *6p* states. The higher energy peak at 15 eV involves mainly transitions from the Bi *6s* electrons to the conduction band.

In Fig. 4 the Raman spectra of polycrystalline BiCrO$_3$, measured at room temperature using 325, 532, 647, and 785 nm excitation lines with the incident light being linearly polarized and unpolarized scattered light, are shown. Due to the cut-off filters corresponding to the above mentioned wavelengths the spectra could only be measured starting from 171, 125, 45, and 75 cm^{-1} Raman shift, respectively. The phonon modes observed in these spectra are similar in terms of frequency and relative intensity for all four excitation lines, however, for the epitaxial BiCrO$_3$ films, the best results have been obtained by using the 532 nm excitation line. The triangles in Fig. 4 indicate the phonon modes observed also in the Raman spectra of BiCrO$_3$ thin films as will be shown later. The spectrum measured using the 325 nm excitation line gives resonant Raman conditions because this excitation line is energetically larger than the optical bandgap as determined from spectroscopic ellipsometry. In this case the spectrum was multiplied by a factor 5, the low intensity being explained by the very low penetration depth of only 33 nm of the 325 nm laser line (as calculated from the ellipsometry data). The phonons of BiCrO$_3$ detected for the excitation at 325 nm occur at similar frequency positions as those measured using the other excitation lines. The small differences in position and relative intensities can be explained by the resonant measurement conditions due to the enhancement of Raman cross section near an electronic resonance.[39] The first peak at 185 cm^{-1} is very weak because the cutoff filter for 325 nm laser line has a very weak transmission below 220 cm^{-1}.

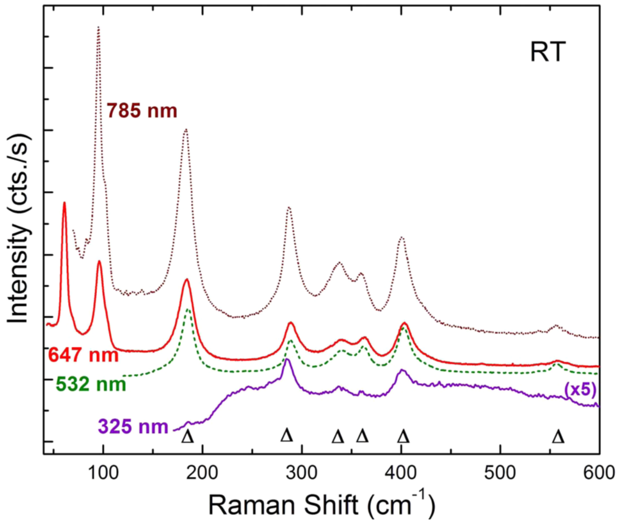

FIG. 4. (Color online) Raman spectra of polycrystalline BiCrO$_3$, measured at room temperature with the 325, 532, 647, and 785 nm excitation lines, respectively.

Figure 5(a) shows the temperature dependence of the Raman spectra of polycrystalline BiCrO$_3$ ceramics measured using the 785 nm excitation line. The sample was first cooled to 87 K and then sequentially heated up to 500 K, with the Raman spectra recorded at the temperatures indicated in the figure. Finally, the sample was cooled back to 300 K. The phonon bands broaden, shift to lower frequencies, decrease in intensity with increasing temperature, and nearly disappear in the spectra measured above 403 K. On the other hand, starting with 398 K, new peaks appear which then dominate the 500 K spectrum. The stronger peaks are indicated by arrows at 130, 210, 302, and 535 cm^{-1}. These spectral changes correlate well to a structural phase transition from a monoclinic structure (space group: *C*2/*c*) to an orthorhombic structure above 420 K (space group: *Pnma*) which was previously revealed by neutron powder diffraction studies on a similar polycrystalline BiCrO$_3$ sample.[12] For the monoclinic structure (C2/c) the Wyckoff positions are given in the Table I.[12] According to factor group analysis one can expect 60 normal modes, of which 27 are Raman active (13 A_g + 14 B_g).[40] The Raman tensors of A_g and B_g modes for the *C2*/*c* space group can be written as[41]

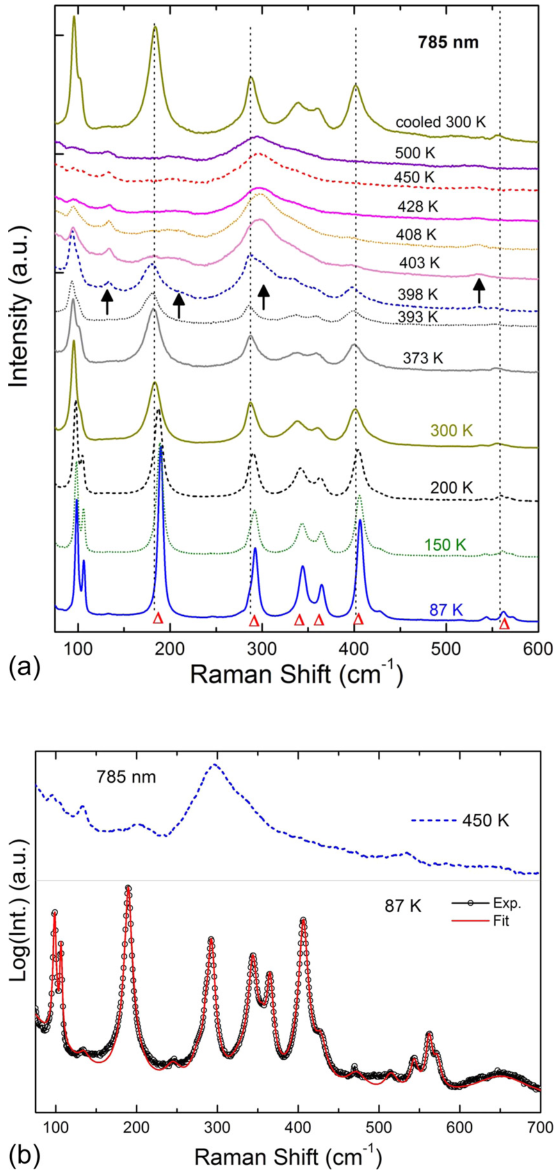

FIG. 5. (Color online) (a) Temperature dependence of the Raman spectra of polycrystalline $BiCrO_3$ from 87 K up to 500 K, and subsequently cooling to 300 K, measured with a 785 nm laser line. (b) The Raman spectrum measured at 87 K and the fit using Lorentzian peaks at a logarithmic scale. The spectrum measured at 450 K is shown at a similar scale for comparison.

$$A_g = \begin{pmatrix} a & 0 & d \\ 0 & b & 0 \\ d & 0 & c \end{pmatrix}, \quad B_g = \begin{pmatrix} 0 & e & 0 \\ e & 0 & f \\ 0 & f & 0 \end{pmatrix}.$$

TABLE I. Wyckoff notations, atomic site symmetries, and the irreducible representations for the atoms in monoclinic $BiCrO_3$ (c2/c symmetry).

Atom	Wyckoff Position	Site Symmetry	Modes (Irreducible Representation)
Bi	8 f	C_1	$3A_g + 3A_u + 3B_g + 3B_u$
Cr1	4 e	C_2	$A_g + A_u + 2B_g + 2B_u$
Cr2	4 d	C_i	$3A_u + 3B_u$
O1	8 f	C_1	$3A_g + 3A_u + 3B_g + 3B_u$
O2	8 f	C_1	$3A_g + 3A_u + 3B_g + 3B_u$
O3	8 f	C_1	$3A_g + 3A_u + 3B_g + 3B_u$
			$\Gamma_{\text{total}} = 13A_g + 16A_u + 14B_g + 17B_u$
			$\Gamma_{\text{Raman}} = 13A_g + 14B_g$

For the orthorhombic *Pnma* space group, the factor group analysis predicts 60 normal modes, 24 of them being Raman active ($7\ A_g + 5\ B_g + 7\ B_{2g} + 5\ B_{3g}$). Thus, a larger number of phonon modes is expected in the Raman spectra of the monoclinic crystal structure as compared to the number of modes observable for the orthorhombic structure due to the higher symmetry of the latter. The presence of fewer modes in the spectra recorded above 428 K as compared to the spectra recorded at lower temperatures, see Figure 5(a), is thus a clear indication of a structural phase transition. After cooling the sample from 500 K back to 300 K, the Raman spectrum is similar to the one initially measured at 300 K, clearly indicating that this structural transition is reversible. The dotted vertical lines are guide for the eyes showing that the positions of the peaks at 183, 287, and 402 cm^{-1} in the spectrum measured at 300 K are the same after annealing at 500 K and cooling back to 300 K.

The Rietveld analysis[42,43] of the room temperature PXRD pattern performed using the FULLPROF suite[44,45] revealed that the $BiCrO_3$ ceramic contains monoclinic $BiCrO_3$ as the predominant phase. Based on the structure model from Ref. 12, the following lattice parameters were refined: $a = 9.4724(4)$ Å, $b = 5.4813(2)$ Å, $c = 9.5752(4)$ Å, $\beta = 108.595(4)$. The addition of orthorhombic $BiCrO_3$ as a second phase did not improve significantly the agreement between the measured and calculated PXRD patterns. The refined amount of orthorhombic $BiCrO_3$ in the $BiCrO_3$ ceramics was below 1 vol. %, which is beyond the limit of the quantitative phase analysis using PXRD.

PXRD carried out at elevated temperatures (Fig. 6) confirmed the reversible phase transition in the $BiCrO_3$ ceramics that was expected from the temperature induced changes in the Raman spectra [Fig. 5(a)]. Above 423 K, the sample contained the orthorhombic $BiCrO_3$ crystallizing in the space group[12] *Pnma* as a single phase. The Rietveld analysis[44,45] of the PXRD patterns taken at 423 K revealed the following lattice parameters: $a = 5.5480(7)$ Å, $b = 7.7575(10)$ Å, $c = 5.4260(7)$ Å.

In Fig. 5(b) the Raman spectrum of polycrystalline $BiCrO_3$ measured at 87 K, using the 785 nm excitation line and the corresponding fitted spectrum using Lorentz oscillators are shown at a logarithmic scale. We could identify 20 peaks in the spectrum, the most intense ones being at 99, 106, 190, 292, 344, 365, 406, and 562 cm^{-1}. As shown in Fig. 4 there are 2 other peaks below the measured range at 60 and 67 cm^{-1} which could be detected at room temperature when measuring with the 647 nm excitation line. Because of the polycrystalline character of the sample all Raman modes should be detectable using backscattering geometry. From the 27 expected modes for the *C2/c* space group, only 22 modes could be detected. The other 5 modes probably exhibit either too weak intensities or have frequencies outside the measured spectral range. Polarization dependent Raman measurements at room temperature on $BiCrO_3$ epitaxial films[46] show that the most intense Raman

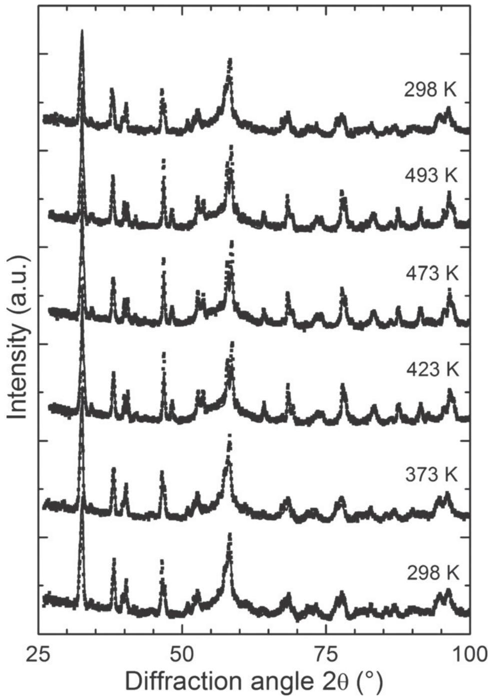

FIG. 6. Parts of the powder x-ray diffraction patterns taken at 298, 373, 423, 473, and 493 K, and after cooling the sample to 298 K. The measured data are plotted by dots/small boxes, the Rietveld fits by solid lines. The strong diffraction line that appears at the diffraction angle of 38° stems from the tantalum heating band.

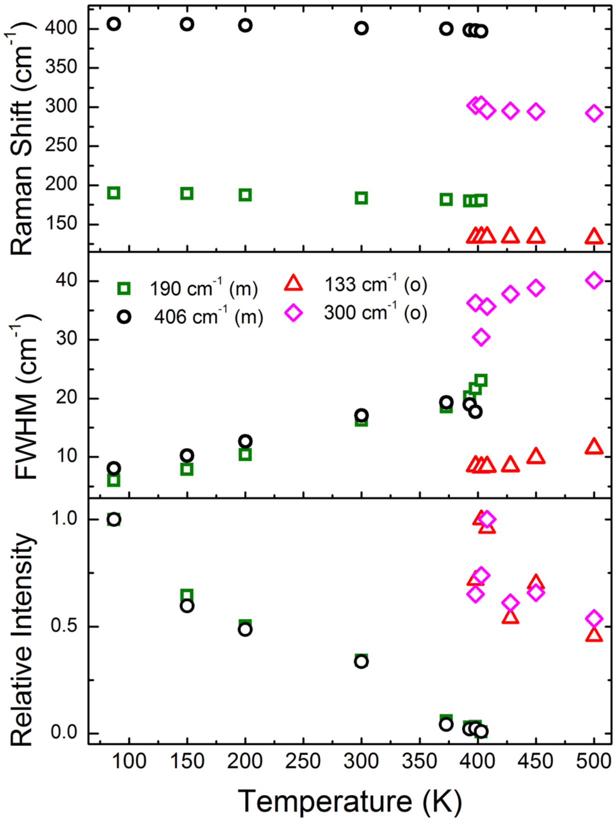

FIG. 7. (Color online) Temperature dependence of frequency, full width at half maximum, and relative intensity of selected Raman bands of the monoclinic (m) and of the orthorhombic (o) phases.

modes of the monoclinic phase are the A_g ones, while the B_g modes should have a weak intensity.

The spectrum of the $BiCrO_3$ ceramic acquired at 450 K is also shown in the upper part of the Fig. 5(b) normalized at a similar intensity scale for comparison. For the *Pnma* space group, the factor group analysis predicts 24 Raman active modes, but the spectrum measured at 450 K exhibits only ten modes. It should be noted that also for other perovskite oxides belonging to the *Pnma* space group, e.g. $LaMnO_3$,[47,48] a lower number of modes than theoretically predicted was observed experimentally.

The evolution of the frequency, full width at half maximum (FWHM), and relative intensity for selected Raman bands of the low temperature monoclinic phase and high temperature orthorhombic phase, obtained after spectral deconvolution, are shown in Fig. 7. Only the fitting parameters of the phonons at 190 and 406 cm^{-1} of the monoclinic (m) phase and at 133 and 300 cm^{-1} of the orthorhombic (o) phase are shown, for the clarity of the figure. The intensity of each mode of the monoclinic phase is normalized to its intensity in the spectrum recorded at 87 K. For the modes of the orthorhombic phase the normalization was done with respect to the corresponding mode intensity in the spectrum recorded at 408 K. The intensities of the modes stemming from the monoclinic phase decrease with increasing temperature and completely vanish at 408 K, while the modes corresponding to the orthorhombic phase start developing at 398 K. This indicates that around 400 K there is a small temperature range (about 10 K) were the monoclinic and the orthorhombic phases coexist. The frequencies of all modes are red shifted with increasing temperature. The two bands of the monoclinic phase have similar FWHM values in the whole temperature range below the transition. The phonon at 133 cm^{-1} corresponding to the orthorhombic phase is narrower, while the phonon at 300 cm^{-1} is broader, as compared with the phonons of the monoclinic phase.

In Fig. 8 the polarized and unpolarized Raman spectra measured at 87 K with the 532 nm excitation line for the 55 nm $BiCrO_3$ film grown on $NdGaO_3$ are shown. For comparison, the unpolarized spectrum measured for polycrystalline $BiCrO_3$ is shown in the lower part of the figure. The spectra of the film were obtained by subtracting the intensity normalized $NdGaO_3$ spectra measured under the same polarization conditions. The noise in the spectra is related to the very small Raman signal related to the small scattering volume in the 55 nm film. The most intensive peaks corresponding to $BiCrO_3$ are indicated by triangles, while the features marked by stars are substrate related, resulting from the normalization subtraction procedure. As it is clearly seen in the Fig. 8, the $BiCrO_3$ peaks of the film are detectable in the unpolarized $(z(y,-)\bar{z})$ and in the parallel $(z(y,y)\bar{z})$ polarization configuration, the spectra being similar with that of polycrystalline bulk $BiCrO_3$. This indicates that the films have a similar crystalline structure to the polycrystalline sample at low temperatures. On the other hand, when using cross polarization $(z(y,x)\bar{z})$ no peaks from $BiCrO_3$ could be measured, except for the very weak peak at 183 cm^{-1} which probably stems from the polarization leakages of the most intensive $BiCrO_3$ peak. This strong polarization dependence means that the film has good epitaxial quality. Polarization

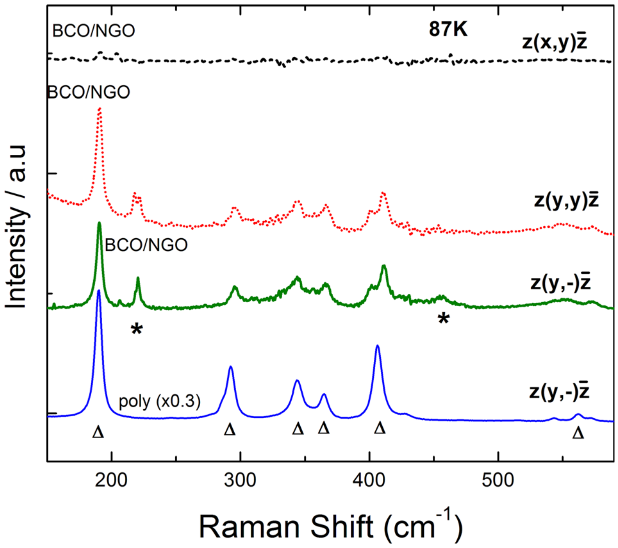

FIG. 8. (Color online) Parallel ($z(y,y)\bar{z}$), cross ($z(y,x)\bar{z}$), and unpolarized ($z(y,-)\bar{z}$) Raman spectra at 87 K for a 55 nm $BiCrO_3$ epitaxial film deposited on $NdGaO_3(110)$ substrate. The peaks marked by asterisks belong to the substrate and occur due to the normalization procedure as described in the text. The unpolarized Raman spectrum of polycrystalline $BiCrO_3$ is shown for comparison.

dependent Raman measurements for different azimuthal angles for $BiCrO_3$ epitaxial films deposited onto (La,Sr)(Al, Ta)O_3 substrates show that the A_g modes appear as the most intense ones only in parallel polarization, while the B_g modes should have a weak intensity in both cross and parallel polarization configuration.[46] For the $BiCrO_3$ film deposited onto $NdGaO_3$, the same polarization behavior is observed indicating that the most intensive peaks, marked in the figures by triangles, stem from modes with A_g symmetry.

CONCLUSIONS

In this work, the dielectric function of $BiCrO_3$ was determined from spectroscopic ellipsometry and compared to that calculated using density functional theory. The assignment of the peaks in the imaginary part of the dielectric function was realized based on the density of states calculations. From the shape of the absorption onset region it is concluded that $BiCrO_3$ is an indirect bandgap material. The number of the Raman modes of polycrystalline $BiCrO_3$ remains constant for measurements performed in the 87–400 K temperature range, and decreases as the temperature increases above 400 K. Raman modes can be correlated to a reversible phase transition from the "low-temperature" monoclinic to the "high-temperature" orthorhombic phase. This phase transition was confirmed by *in situ* powder x-ray diffraction investigations. The Raman spectra of the epitaxial $BiCrO_3$ films indicate the same monoclinic phase as in the polycrystalline material at lower temperatures.

ACKNOWLEDGMENTS

This work was supported by the German Research Foundation DFG HI 1534/1-1. The experimental work in Bessy was supported by the BMBF project 05 ES3XBA/5. The support in Bessy from Dr. C. Cobet is acknowledged. Kannan Vijayanandhini thanks the MPG-CNRS Program for Nanomaterials for supporting her work at MPI Halle. The financial support by the European Union (European regional development fund) and by the Ministry of Science and Art of Saxony (SMWK) through the Cluster of Excellence ADDE is also acknowledged.

[1] R. Ramesh and N. A. Spaldin, Nat. Mater. **6**, 21 (2007).
[2] Y-H. Chu *et al.*, Nat. Mater. **7**, 478 (2008).
[3] G. Catalan and J. F. Scott, Adv. Mater. **21**, 2463 (2009).
[4] J. Lu, K. G. West, and S. A. Wolf, *Novel Magnetic Oxide Thin Films*, edited by S. Ramanathan (Springer, Berlin, 2010), Chap. 3.
[5] N. A. Spaldin and M. Fiebig, Science **309**, 391 (2005).
[6] P. Fischer, M. Polomska, I. Sosnowska, and M. Szymanski, J. Phys. C **13**, 1931 (1980).
[7] F. Sugawara, S. Iiida, Y. Syono, and S. I. Akimoto, J. Phys. Soc. Jpn. **25**, 1553 (1968).
[8] M. Murakami, S. Fujino, S. H. Lim, C. J. Long, L. G. Salamanca-Riba, M. Wuttig, I. Takeuchi, V. Nagarajan, and A. Varatharajan, Appl. Phys. Lett. **88**, 152902 (2006).
[9] D. H. Kim, H. N. Lee, M. Varela, and H. M. Christen, Appl. Phys. Lett. **89**, 162904 (2006).
[10] M. Opel *et al.*, Phys. Status Solidi A **208**, 232 (2011).
[11] N. A. Hill, P. Bättig, and C. Daul, J. Phys. Chem. B **106**, 3383 (2002).
[12] A. A. Belik, S. Iikubo, K. Kodama, N. Igawa, S. Shamoto, and E. Takayama-Muromachi, Chem. Mater. **20**, 3765 (2008).
[13] A. A. Belik and E. Takayama-Muromachi, J. Phys.: Conf. Ser. **165**, 012035 (2009).
[14] C. Darie, C. Goujon, M. Bacia, H. Klein, P. Toulemonde, P. Bordet, and E. Stuard, Solid State Sci. **12**, 660 (2010).
[15] A. David, Ph. Boullay, R.V.K. Mangalam, N. Barrier, and W. Prellier, Appl. Phys. Lett. **96**, 221904 (2010).
[16] R. Nechache, P. Gupta, C. Harnagea, and A. Pignolet, Appl. Phys. Lett. **91**, 222908 (2007).
[17] N. Ichikawa, Appl. Phys. Exp. **1**, 101302 (2008).
[18] J. Kreisel and P. Bouvier, J. Raman Spectrosc. **34**, 524 (2003).
[19] D. A. Tenne and X. X. Xi, J. Am. Ceram. Soc. **91**, 1820 (2008).
[20] R. Palai, R. S. Katiyar, H. Schmid, P. Tissot, S. J. Clark, J. Robertson, S. A. T. Redfern, G. Catalan, and J. F. Scott, Phys. Rev. B **77**, 014011 (2008).
[21] S. Issing, A. Pimenov, V. Yu. Ivanov, A. A. Mukhin, and J. Geurts, Phys. Rev. B **81**, 024304 (2010).
[22] P. Blaha, K. Schwarz, G. K. H. Madsen, D. Kvasnicka, and J. Luitz, WIEN2K, An Augmented Plane Wave + Local Orbitals Program for Calculating Crystal Properties (Karlheinz Schwarz, Technische Universität Wien, Austria, 2001).
[23] J. P. Perdew, K. Burke, and M. Ernzerhof, Phys. Rev. Lett. **77**, 3865 (1996).
[24] C. Ambrosch-Draxl and J. Sofo, Comput. Phys. Commun. **175**, 1 (2006).
[25] V. I. Anisimov, I. V. Solovyev, M. A. Korotin, M. T. Czyzyk, and G. A. Sawatzky, Phys. Rev. B **48**, 16929 (1993).
[26] R. M. A. Azzam and N. M. Bashara, *Ellipsometry and Polarized Light* (Elsevier, Amsterdam, 1987).
[27] *Optical Characterisation of Epitaxial Semiconductor Layers*, edited by G. Bauer and W. Richter (Springer, Berlin, 1996).
[28] D. E. Aspnes, J. B. Theeten, and F. Hottier, Phys. Rev. B **20**, 3292 (1979).
[29] J. Tauc, R. Grigorovici, and A. Vancu, Phys. Status Solidi **15**, 627 (1966).
[30] G. E. Jellison and F. A. Modine, Appl. Phys. Lett. **69**, 371 (1996).
[31] C. Himcinschi, I. Vrejoiu, M. Friedrich, L. Ding, C. Cobet, N. Esser, M. Alexe, and D. R. T. Zahn, Phys. Stat. Solidi C **7**, 296 (2010).
[32] C. Himcinschi, I. Vrejoiu, M. Friedrich, E. Nikulina, L. Ding, C. Cobet, N. Esser, M. Alexe, D. Rafaja, and D. R. T. Zahn, J. Appl. Phys. **107**, 123524 (2010).
[33] J. Bardeen, F. Blatt, and L. H. Hall, in *Photoconductivity Conference*, edited by R. G. Breckenridge, B. R. Russel, and E. E. Hahn (Wiley-Interscience, New York, 1956)
[34] S. Guo, H. Arwin, S. N. Jacobsen, K. Järrendhal, and U Helmersson, J. Appl. Phys. **77**, 5369 (1995).
[35] J. I. Pankove, *Optical Processes in Semiconductors* (Prentice-Hall, Englewood Cliffs, 1971).
[36] J. F. Ihlefeld *et al.*, Appl. Phys. Lett. **92**, 142908 (2008).

[37] A. J. Hauser, J. Zhang, L. Mier, R. A. Ricciardo, P. M. Woodward, T. L. Gustafson, L. J. Brillson, and F. Y. Yang, Appl. Phys. Lett. **92**, 222901 (2008).

[38] A. Kumar *et al*., Appl. Phys. Lett. **92**, 121915 (2008).

[39] P. Y. Yu and M. Cardona, *Fundamentals of Semiconductors* (Springer-Verlag, Berlin, 1999).

[40] D. L. Rousseau *et al*., J. Raman Spectrosc. **10**, 253 (1981).

[41] R. Loudon, Adv. Phys. **13**, 423 (1964).

[42] H. M. Rietveld, Acta Crystallogr. **22**, 151 (1967).

[43] H. M. Rietveld, J. Appl. Crystallogr. **2**, 65 (1969).

[44] J. Rodriguez-Carvajal, Physica B **192**, 55 (1993).

[45] T. Roisnel and J. Rodriguez-Carvajal, Mater. Sci. Forum. **378–383**, 118 (2001).

[46] A. Talkenberger, C. Himcinschi, T. Weiβbach, K. Vijayanandhini, I. Vrejoiu, C. Röder, D. Rafaja, and J. Kortus, "Raman spectroscopic and X-ray diffraction investigations of epitaxial $BiCrO_3$ thin films," Thin Solid Films (accepted).

[47] M. N. Iliev and M. V. Abrashev, J. Raman Spectrosc. **32**, 805 (2001).

[48] M. N. Iliev, M. V. Abrashev, J. Laverdière, S. Jandl, M. M. Gospodinov, Y.-Q. Wang, and Y.-Y. Sun, Phys. Rev. B **73**, 064302 (2006).

JOURNAL OF APPLIED PHYSICS **107**, 123524 (2010)

Substrate influence on the optical and structural properties of pulsed laser deposited $BiFeO_3$ epitaxial films

C. Himcinschi,[1,4,a)] I. Vrejoiu,[2] M. Friedrich,[1] E. Nikulina,[2] L. Ding,[1] C. Cobet,[3] N. Esser,[3]
M. Alexe,[2] D. Rafaja,[5] and D. R. T. Zahn[1]
[1] *Semiconductor Physics, Chemnitz University of Technology, D-09107 Chemnitz, Germany*
[2] *Max Planck Institute of Microstructure Physics, D-06120 Halle, Germany*
[3] *Department Berlin, Institute for Analytical Sciences, D-12489 Berlin, Germany*
[4] *Institute of Theoretical Physics, TU Bergakademie Freiberg, D-09599 Freiberg, Germany*
[5] *Institute of Materials Science, TU Bergakademie Freiberg, D-09599 Freiberg, Germany*

(Received 30 November 2009; accepted 4 May 2010; published online 24 June 2010)

Epitaxial $BiFeO_3$ films pulsed laser deposited on $SrTiO_3$, Nb:doped $SrTiO_3$, and $DyScO_3$ were studied using variable angle spectroscopic ellipsometry, vacuum ultraviolet ellipsometry, micro-Raman spectroscopy, and x-ray diffraction. The energy band gap of the film deposited on $DyScO_3$ is 2.75 eV, while the one for the film deposited on Nb:doped $SrTiO_3$ is larger by 50 meV. The blueshift in the dielectric function of the $BiFeO_3$ films deposited on Nb:doped $SrTiO_3$ compared to the films deposited on $DyScO_3$, indicates a larger compressive strain in the films deposited on Nb:doped $SrTiO_3$. This is confirmed by Raman spectroscopy and by high resolution x-ray diffraction investigations. © *2010 American Institute of Physics*. [doi:10.1063/1.3437059]

I. INTRODUCTION

Multiferroic epitaxial films have received great attention due to their attractive physical properties and the potential applications in nonvolatile ferroelectric memories or novel multiple state memories and devices based on magnetoelectric effects.[1,2] The growth of high-quality single crystalline thin films of multiferroics is essential for the study of their intrinsic fundamental physical properties, undisturbed by extrinsic contributions from parasitic phases and extended structural defects, and for their incorporation into practical devices.[3] Bismuth ferrite $BiFeO_3$ (BFO) is a rare case of a single phase room temperature (RT) multiferroic with the ferroelectric Curie temperature ($T_c = 820\ ^\circ C$) and the antiferromagnetic Néel temperature ($T_N = 370\ ^\circ C$) well above RT.[4]

Despite the great interest in multiferroic thin films, there are only few studies regarding the optical properties of BFO. Most investigations of the dielectric function of these materials are limited to the region below 6.5 eV,[5,6] the energy domain available in commercial ellipsometers, while the vacuum ultraviolet (VUV) range is hardly explored at all. On the other hand, the phonon assignment of the BFO Raman scattering data is still debated.[7–9] Additional complications arise from the fact that the physical properties of the BFO films were found to be influenced by the substrates on which the films were deposited.[10]

Here the optical and structural properties of epitaxial BFO films deposited on different substrates are investigated by combining variable angle spectroscopic ellipsometry (VASE), VUV spectroscopic ellipsometry, Raman spectroscopy, transmission electron microscopy (TEM), and x-ray diffraction (XRD).

II. EXPERIMENTAL PROCEDURE

Epitaxial thin films of BFO were deposited by pulsed laser deposition on $SrTiO_3$ (100) (STO), on Nb-doped $SrTiO_3$ (100) (Nb:STO), and $DyScO_3$ (DSO) (110) substrates at $T_g = 625 - 650\ ^\circ C$ and 0.14 mbar O_2.[11]

The topography of the employed substrates and of the epitaxial BFO films was investigated by atomic force microscopy (AFM) (Veeco, DI5000) working in noncontact mode. Cross section samples for TEM were thinned using mechanical and ion-beam based standard methods. Standard TEM investigation was performed in a Philips CM20T operating at 200 keV.

VUV spectroscopic ellipsometry was performed in the 4.5–9.5 eV photon energy range using the 3m-NIM1 monochromator at "Berliner Elektronenspeicherring-Gesellschaft für Synchrotronstrahlung" (BESSY). The spectra were recorded using a rotating-analyzer type ellipsometer at 67° angle of incidence. A more detailed description of the experimental set-up can be found elsewhere.[12] VASE measurements were performed in the 0.73 eV up to 4.5 eV range at four angles of incidence using a VASE ellipsometer (J.A. Woollam Co.).

The Raman measurements were performed with a Dilor XY spectrometer. The 514.5 nm emission line of an Ar^+ ion laser was used for excitation. The samples were measured under a 100× microscope objective using a laser power of 2 mW.

The VASE and VUV spectra were added and evaluated in the whole energy range (0.73–9.5 eV). First, the dielectric functions of the Nb:STO and DSO substrates were determined from the ellipsometric spectra and they were further used to determine the dielectric function of the BFO films.[13] By describing the optical response of the BFO films using a Cauchy dispersion relation for the refractive index in the absorption free range (up to ~2.2 eV), the following thick-

---

[a)] Author to whom correspondence should be addressed. Electronic mail: c.himcinschi@physik.tu-chemnitz.de. Tel.: +49 371 531 36731. FAX: +49 371 531 21819.

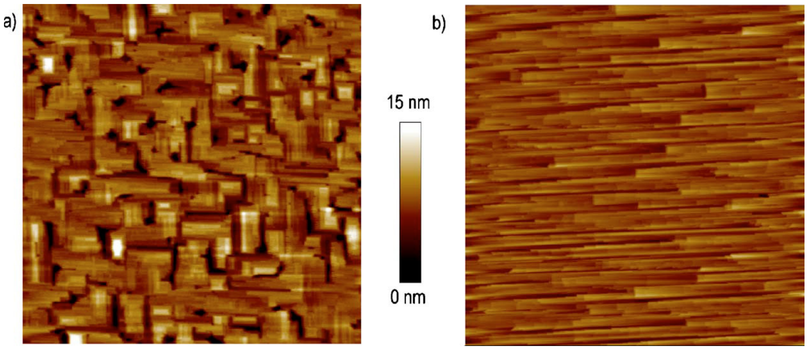

FIG. 1. (Color online) AFM images (4×4 μm^2 scans) of: (a) the 54.3 nm BFO film deposited onto STO (100), and (b) the 34.1 nm BFO films deposited on DSO (110).

ness values were obtained for the films under investigation: 54.3 nm BFO/STO, 106.5 nm BFO/Nb:STO, and 34.1 nm and 135.3 nm for the BFO/DSO films. The error in the determination of thickness was ±0.3 nm. XRD experiments were performed on a triple-crystal diffractometer equipped with a sealed x-ray tube with Cu anode, with a monochromator in the primary beam, and with an analyzer in the front of the scintillation detector. Both, the monochromator and the analyzer were made from a perfect (111)-oriented dislocation-free Si single-crystal. The instrumental broadening as measured on a Si single-crystal employed as a sample was about 7 arc sec.

III. RESULTS AND DISCUSSIONS

The topography of the epitaxial BFO films was investigated by AFM. Figure 1 shows two typical AFM micrographs of the BFO/STO and of the BFO/DSO thinnest films investigated here. The different morphology most probably arises from the differences in the growth processes of $BiFeO_3$ on top of the $SrTiO_3(100)$ and $DyScO_3(110)$ surfaces. Nevertheless, both BFO films are relatively smooth (with rms roughness values of 1.8 nm for BFO/STO and 0.9 nm for BFO/STO, for the 4×4 μm^2 scanned areas shown in Fig. 1), and no impurity phases such as Bi_2O_3 or γ-Fe_2O_3 were observed.[14,15] Bi_2O_3 impurities typically have rectangular shapes and different growth rate, so that they usually appear as protuberances embedded in the smoother $BiFeO_3$ matrix.

Figure 2 shows a cross section TEM bright field micrograph of the same sample imaged by AFM in Fig. 1(a). The TEM investigations confirmed that no parasitic phases are formed[15] in this thin BFO/STO film and from selective area electron diffraction patterns the film was proven to be epitaxially grown on STO(100).

The ellipsometric spectra in the 0.73–9.5 eV energy range were evaluated using an oscillator model which ensures Kramer–Kronig consistency of the optical constants.[13] Figure 3 shows the real (ε_1) and the imaginary part (ε_2) of the dielectric function determined for a BFO film (106.5 nm) deposited on Nb:STO and for a BFO film (135.3 nm) deposited on DSO. These data extend the range of the dielectric function (or optical constants) determination as compared to previous reports,[5,6] to 9.5 eV photon energy. A clear blueshift of the dielectric function of the BFO film deposited on Nb-:STO with respect to that of the BFO film deposited on DSO can be observed in Fig. 3. This indicates a larger compressive strain in the films deposited on Nb:STO as compared to the films deposited on DSO. The strain behavior of the films will be discussed later taking into account the Raman and XRD data.

In the imaginary part of the dielectric function, ε_2, critical points at ~3.2, 4.3, 6.3, and 7.6 eV can clearly be identified. Similar energy positions were calculated using density functional theory for the imaginary part of the dielectric function of BFO.[16] Comparing the experimental data to the theoretical calculations, the peak at 3.2 eV can be attributed to transitions from occupied O 2*p* to unoccupied Fe 3*d* states

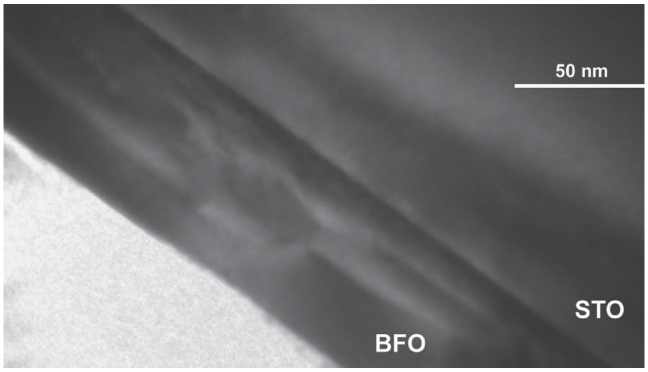

FIG. 2. Cross section TEM micrograph of the thinner BFO film deposited on STO (100).

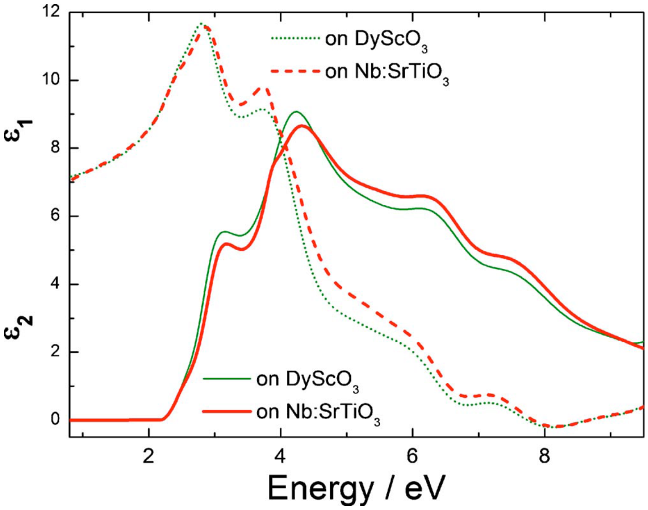

FIG. 3. (Color online) Real (ε_1) and imaginary part (ε_2) of the dielectric function of a 106.5 nm BFO film deposited on Nb:STO (100) and of a 135.3 nm BFO film deposited on DSO (110).

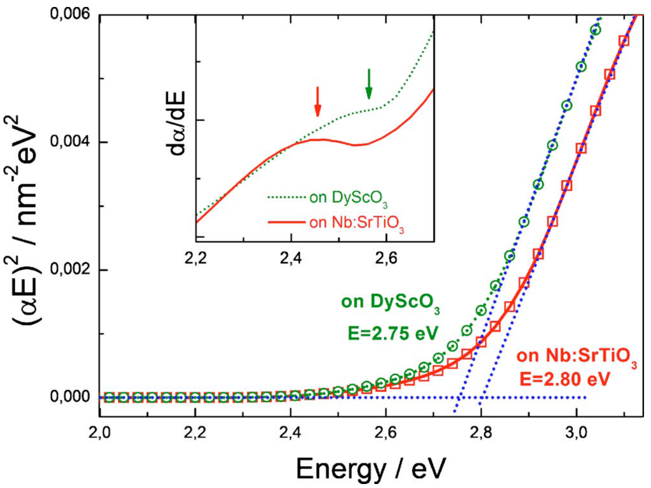

FIG. 4. (Color online) $(\alpha \cdot E)^2$ plotted as function of photon energy, E, for BFO films deposited on DSO and Nb:STO substrates. The linear extrapolation of $(\alpha \cdot E)^2$ to zero indicates a direct band gap. The inset shows $dE/d\alpha$ with some subband gap transitions.

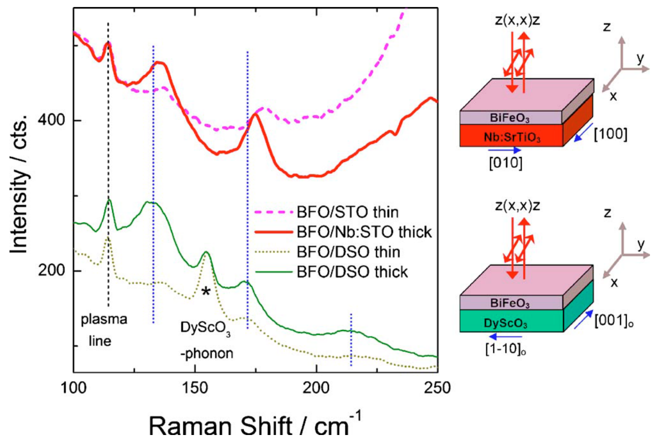

FIG. 5. (Color online) Raman spectra of the BFO films deposited on STO (100), Nb:STO (100), and DSO (110) substrates. The spectra were obtained in normal backscattering using the parallel polarization configuration, as schematically shown on the right.

or d–d transitions between the Fe 3*d* valence and conduction bands.[16] The other three energy positions correspond to transitions from the O 2*p* valence band to Fe 3*d* or to Bi 6*p* high-energy conduction bands.

In order to determine the energy band gap, $(\alpha \cdot E)^2$ versus photon energy E, with α being the absorption coefficient $[\alpha=(4\pi k/\lambda)]$, was plotted in Fig. 4.[17] The linear extrapolation of $(\alpha \cdot E)^2$ to zero indicates a direct band gap and allows the band gap values to be determined: while the band gap of the film deposited on DSO amounts to (2.75 ± 0.01) eV, the band gap for the film deposited on Nb:STO is larger by 50 meV. These values are in good agreement with the band gap calculated by Clark and Robertson using the density-functional based screened exchange method[18] and with other experimental band gap values determined for BFO thin films.[19–21] Considering the inverse dependence of the band gap with respect to the lattice parameter, i.e., the smaller the lattice parameter the larger the band gap,[22] one can conclude that the in-plane lattice parameters for BFO films, when deposited on STO, must be smaller than for the BFO films deposited on DSO. In the inset of Fig. 4, $dE/d\alpha$ is plotted as a function of energy. This representation reveals a feature located at 2.46 and 2.56 eV in the BFO films deposited on Nb:STO and DSO, respectively. Similar subband gap states were detected for epitaxial BFO films deposited on STO and were confirmed by cathodoluminescence measurements.[19] These states are considered to be defect states most likely being due to oxygen vacancies in the BFO films.

Figure 5 shows the Raman spectra of BFO films deposited on STO, Nb:STO, and DSO substrates, respectively, measured using the 514.5 nm (2.41 eV) excitation line. The spectra were measured in normal backscattering geometry in which the directions of the incident and scattered light are parallel with the normal to the films surface. The parallel polarization configuration with the polarization direction along the [100] direction of cubic STO or $[001]_o$ orthorhombic direction of DSO was used (see schematics on the right of Fig. 5). Group theory predicts 13 Raman active phonon modes for single crystal rhombohedral BFO which can be summarized using the following irreducible representation: $\Gamma = 4A_1 + 9E$.[7,8] According to the Raman selection rules both A_1 and E modes are expected to be detected in the parallel polarization configuration used in our measurements. Interpretation of the experimental Raman spectra of BFO is still subject of discussion.[9] In the spectral range investigated in this paper (see Fig. 5) Fukumura *et al.*[7] detected four modes using the parallel polarization configuration, namely three A_1 modes (at 147, 176, and 227 cm^{-1}) and one E mode (at 136 cm^{-1}). Similar peaks were measured on BFO single crystals by Cazayous *et al.*[23] and assigned in the same way. On the other hand, in the Raman spectra of 600 nm BFO films measured by Singh *et al.*[8,24] three peaks were observed at 136, 168, and 212 cm^{-1} and were assigned to longitudinal-optical A_1(LO) modes. DFT calculations leave the 147 cm^{-1} peak as the only unassigned experimental mode and directly question its origin.[9]

In the Raman spectra shown in Fig. 5 there are three peaks that can be attributed to the BFO films at ≈133, 172, and 215 cm^{-1} (the last peak is only appearing in the films deposited on DSO). The line at 114.5 cm^{-1} is a plasma line and the mode at 155 cm^{-1} is a DSO phonon mode. It should be pointed out that the films investigated in this work are much thinner than those measured by Singh *et al.*[8,24] The increasing background in the high-frequency side of the spectra of films grown on STO substrate is due to the Raman spectra of the substrate itself. A closer look at the spectra in the Fig. 5 reveals a clear blue shift of the BFO modes when going from the films deposited on DSO to those deposited on STO or when decreasing the film thickness. For example, the peak at 133 cm^{-1} for the thick BFO/DSO film is shifted by ~4 cm^{-1} to higher wave numbers in the case of the thin BFO/STO film while the peak at 172 cm^{-1} is blueshifted by ~7 cm^{-1}. The blueshift of the Raman peaks indicates an increase in compressive strain in the films. This means that the BFO films deposited on STO have a higher compressive strain than those deposited on DSO. These results confirm the behavior observed in the dielectric function and the band gap for these BFO films. On the other hand, the thin films are

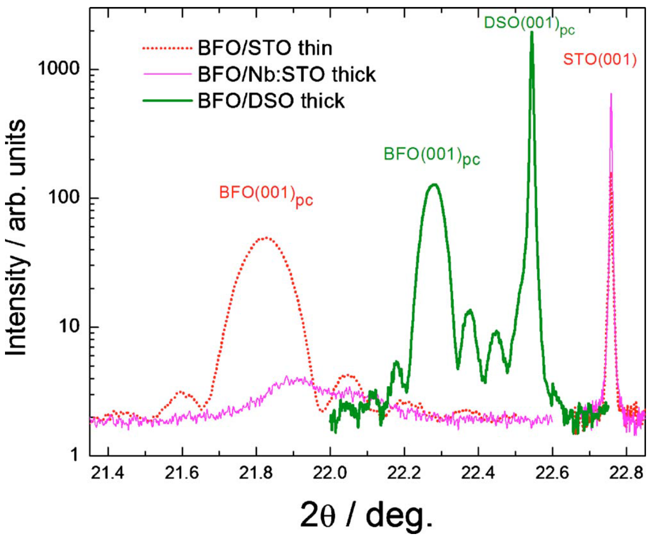

FIG. 6. (Color online) High resolution θ-2θ XRD scan around (001) reflection of BFO films grown on STO (100), Nb:STO (100), and DSO (110) substrates, respectively.

more compressed than the thick ones, a fact which can be well understood considering the lattice mismatch between the BFO films and the STO and DSO substrates. This is further supported by XRD measurements.

The high resolution XRD patterns of the 54.3 nm thin BFO film grown on STO substrate, of the 106.5 nm thin BFO film on Nb:STO, and of the 135.3 nm thin BFO film on DSO measured as θ-2θ scans are shown in Fig. 6. The structure of bulk BFO is described as rhombohedrally distorted cubic perovskite[25] and can be indexed in a pseudocubic lattice with a=3.96 Å.[26] On the other hand, the cubic lattice parameters for STO(100) and the pseudocubic lattice parameters for DSO(110) substrates are 3.905 Å and 3.951 Å, respectively.[27,28] From the XRD patterns, the lattice parameter of the substrates were determined to be 3.904 Å for STO and Nb:STO, and 3.941 Å for DSO using Bragg's law. The out-of-plane pseudocubic lattice parameter was determined to be 4.069 Å for the 54.3 nm thin BFO film deposited on STO and 3.987 Å in the case of the film deposited on DSO. Satellite peaks surrounding the (001) diffraction peak of BFO for the films deposited on STO and DSO can be clearly identified in Fig. 6. As known from high-resolution x-ray scattering from thin films,[29] these interference fringes point to a structure with no relaxation that is only possible for a perfect epitaxial growth, for which the in-plane lattice parameter of BFO must agree with the lattice parameter of the respective substrates. The situation is different for the thick BFO film deposited on Nb:STO. In this case no interference fringes are observed indicating that this film is partially relaxed probably due to appearance of the misfit dislocations and formation of ferroelastic domains. By indexing the two diffractions peaks at 21.90° and 22.08° of this film we obtained out-of-plane pseudocubic lattice parameters of 4.055 Å and 4.023 Å, respectively. The double-peak indicates a "bimodal" distribution of the interplanar spacings, a possible explanation of this phenomenon is an inhomogeneous distribution of microstructure defects, e.g., dislocations. Similar effects were also observed in the case of BFO films deposited on STO, when the strain is relaxed with increasing thickness, the relaxation induces an increase in the in-plane lattice parameter accompanied by the decrease in the out-of plane lattice parameter.[30,31] In comparison with the 106.5 nm BFO film on Nb:STO the thicker BFO film (135.3 nm) deposited on DSO remains epitaxially strained as proved by the high resolution x-ray data. This is due to the lower lattice misfit for the BFO/DSO interface as compared to the BFO/STO interface, as indicated by the different distances between the respective substrate and film peaks in Fig. 6.

The larger out-of-plane lattice parameter of BFO film deposited on STO as compared with the film deposited on DSO and the match of the in-plane parameter to those of the substrates attests the larger in-plane compression in the case of the deposition on STO. The thick film deposited on Nb:STO relaxes in comparison with the thinner film on STO but is still more compressed than the BFO films on DSO as seen in the Raman spectra in Fig. 5. This is also proved by the XRD data as, despite the partial relaxation, the BFO film on Nb:STO shows a higher out-of-plane lattice parameter than the film deposited on DSO. Thus the XRD results confirm the strain behavior suggested by the ellipsometry and Raman results, indicating the presence of higher compressive strain for the BFO films grown on STO or Nb:STO as compared with the films grown on DSO.

IV. CONCLUSIONS

The complex dielectric function of BFO films deposited on Nb:STO and DSO substrates was determined up to 9.5 eV by combining VASE and VUV ellipsometry. The blueshift of the imaginary part of the dielectric function and of the optical band gap for the films deposited on Nb:STO (100) as compared with those grown on DSO (110) is associated with a higher compressive strain in the former films. The shifts of the Raman phonon modes in BFO support this assumption, while the high resolution XRD data confirms the presence of larger compressive strain for the BFO films deposited on STO with respect to the films deposited on DSO. The results of this work demonstrate that the substrate has a strong influence on the optical and structural properties of pulsed laser deposited epitaxial BFO thin films.

ACKNOWLEDGMENTS

The experimental work was supported by the BMBF project 05 ES3XBA/5, the SFB 762 project "Funktionalität Oxidischer Grenzflächen," and the European Community through the "NanoCharM" project under the Seventh Framework Programme (FP7).

[1] Y.-H. Chu, L. W. Martin, M. B. Holocomb, M. Gajek, S.-J. Han, Q. He, N. Balke, C.-H. Yang, D. Lee, W. Hu, Q. Zhan, P.-L. Yang, A. Fraile-Rodriguez, A. Scholl, S. X. Wang, and R. Ramesh, Nature Mater. **7**, 478 (2008).
[2] G. Catalan and J. F. Scott, Adv. Mater. **21**, 2463 (2009).
[3] R. Ramesh and N.-A. Spaldin, Nature Mater. **6**, 21 (2007).
[4] P. Fischer, M. Polomska, I. Sosnowska, and M. Szymanski, J. Phys. C **13**, 1931 (1980).
[5] J. F. Ihlefeld, N. J. Podraza, Z. K. Liu, R. C. Rai, X. Xu, T. Heeg, Y. B. Chen, J. Li, R. W. Collins, J. L. Musfeldt, X. Q. Pan, J. Schubert, R. Ramesh, and D. G. Schlom, Appl. Phys. Lett. **92**, 142908 (2008).

[6] A. Kumar, R. C. Rai, N. J. Podraza, S. Denev, M. Ramirez, Y.-H. Chu, L. W. Martin, J. Ihlefeld, T. Heeg, J. Schubert, D. G. Schlom, J. Orenstein, R. Ramesh, R. W. Collins, J. L. Musfeldt, and V. Gopalan, Appl. Phys. Lett. **92**, 121915 (2008).

[7] H. Fukumura, H. Harima, K. Kisoda, M. Tamada, Y. Noguchi, and M. Miyayama, J. Magn. Magn. Mater. **310**, e367 (2007).

[8] M. K. Singh, H. M. Jang, S. Ryu, and M.-H. Jo, Appl. Phys. Lett. **88**, 042907 (2006).

[9] P. Hermet, M. Goffinet, J. Kreisel, and P. Ghosez, Phys. Rev. B **75**, 220102(R) (2007).

[10] Y. Yang, J. Y. Sun, K. Zhu, Y. L. Liu, and L. Wan, J. Appl. Phys. **103**, 093532 (2008).

[11] I. Vrejoiu, M. Alexe, D. Hesse, and U. Gösele, Adv. Funct. Mater. **18**, 3892 (2008).

[12] T. Wethkamp, K. Wilmers, N. Esser, W. Richter, O. Ambacher, H. Angerer, G. Jungk, R. L. Johnson, and M. Cardona, Thin Solid Films **313–314**, 745 (1998).

[13] C. Himcinschi, I. Vrejoiu, M. Friedrich, L. Ding, C. Cobet, N. Esser, M. Alexe, and D. R. T. Zahn, Phys. Status Solidi C **7**, 296 (2010).

[14] H. Béa, M. Bibes, A. Barthélémy, K. Bouzehouane, E. Jacquet, A. Khodan, J.-P. Contour, S. Fusil, F. Wyczisk, A. Forget, D. Lebeugle, D. Colson, and M. Viret, Appl. Phys. Lett. **87**, 072508 (2005).

[15] S. H. Lim, M. Murakami, W. L. Sarney, S. Q. Ren, A. Varatharajan, V. Nagarajan, S. Fujino, M. Wuttig, I. Takeuchi, and L. G. Salamanca-Riba, Adv. Funct. Mater. **17**, 2594 (2007).

[16] H. Wang, Y. Zheng, M.-Q. Cai, H. Huang, and H. L. W. Chan, Solid State Commun. **149**, 641 (2009).

[17] J. I. Pankove, *Optical Processes in Semiconductors* (Prentice-Hall, New Jersey, 1971).

[18] S. J. Clark and J. Robertson, Appl. Phys. Lett. **90**, 132903 (2007).

[19] A. J. Hauser, J. Zhang, L. Miee, R. A. Ricciardo, P. M. Woodward, T. L. Gustafson, L. J. Brillson, and F. Y. Yang, Appl. Phys. Lett. **92**, 222901 (2008).

[20] S. R. Basu, L. W. Martin, Y. H. Chu, M. Gajek, R. Ramesh, R. C. Rai, X. Xu, and J. L. Musfeldt, Appl. Phys. Lett. **92**, 091905 (2008).

[21] H. Shima, T. Kawae, A. Morimoto, M. Matsuda, M. Suzuki, T. Tadokoro, H. Naganuma, T. Iijima, T. Nakajima, and S. Okamura, Jpn. J. Appl. Phys. **48**, 09KB01 (2009).

[22] M. B. Ortuño-Lopez, M. Sotelo-Lerma, A. Mendoza-Galvan, and R. Ramirez-Bon, Vacuum **76**, 181 (2004).

[23] M. Cazayous, D. Malka, D. Lebeugle, and D. Colson, Appl. Phys. Lett. **91**, 071910 (2007).

[24] M. K. Singh, S. Ryu, and H. M. Jang, Phys. Rev. B **72**, 132101 (2005).

[25] F. Kubel and H. Schmid, Acta Crystallogr., Sect. B: Struct. Sci. **46**, 698 (1990).

[26] J. Li, J. Wang, M. Wuttig, R. Ramesh, N. Wang, B. Ruette, A. P. Pyatakov, A. K. Zvezdin, and D. Viehland, Appl. Phys. Lett. **84**, 5261 (2004).

[27] J. Wang, J. B. Neaton, H. Zheng, V. Nagarajan, S. B. Ogale, B. Liu, D. Viehland, V. Vaithyanathan, D. G. Schlom, U. V. Waghmare, N. A. Spaldin, K. M. Rabe, M. Wuttig, and R. Ramesh, Science **299**, 1719 (2003).

[28] Y.-H. Chu, Q. Zhan, L. W. Martin, M. P. Cruz, P.-L. Yang, G. W. Pabst, F. Zavaliche, S.-Y. Yang, J.-X. Zhang, L.-Q. Chen, D. G. Schlom, N. Lin, T.-B. Wu, and R. Ramesh, Adv. Mater. **18**, 2307 (2006).

[29] U. Pietsch, V. Holy, and T. Baumbach, *High-Resolution X-Ray Scattering From Thin Films To Lateral Nanostructures*, 2nd ed. (Springer, Berlin, 2004), pp. 179–203.

[30] D. H. Kim, H. N. Lee, M. D. Biegalski, and H. M. Christen, Appl. Phys. Lett. **92**, 012911 (2008).

[31] K. Saito, A. Ulyanenkov, V. Grossmann, H. Ress, L. Bruegemann, H. Ohta, T. Kurosawa, S. Ueki, and H. Funakubo, Jpn. J. Appl. Phys., Part 1 **45**, 7311 (2006).

Phys. Status Solidi C **7**, No. 2, 296–299 (2010) / **DOI** 10.1002/pssc.200982414

physica status solidi pss c
www.pss-c.com
current topics in solid state physics

Optical characterisation of $BiFeO_3$ epitaxial thin films grown by pulsed-laser deposition

Cameliu Himcinschi[*, 1], **Ionela Vrejoiu**[2], **Marion Friedrich**[1], **Li Ding**[1], **Christoph Cobet**[3], **Norbert Esser**[3], **Marin Alexe**[2], **and Dietrich R. T. Zahn**[1]

[1] Semiconductor Physics, Chemnitz University of Technology, Reichenhainerstr. 70, 09107 Chemnitz, Germany
[2] Max Planck Institute of Microstructure Physics, Weinberg 2, 06120 Halle, Germany
[3] Institute for Analytical Sciences, Department Berlin, Albert-Einstein-Str. 9, 12489 Berlin

Received 29 June 2009, revised 19 October 2009, accepted 6 November 2009
Published online 5 January 2010

PACS 77.84.Dy, 78.20.Ci, 81.15.Fg

---

[*] Corresponding author: e-mail c.himcinschi@physik.tu-chemnitz.de, Phone: +49 371 531 36731, Fax: +49 371 531 21819

Epitaxial thin films of bismuth ferrite, $BiFeO_3$, were deposited by pulsed laser deposition (PLD) on $SrTiO_3$ (100), Nb-doped $SrTiO_3$ (100) and $DyScO_3$ (110) substrates. Ellipsometric spectra are obtained in the energy range 0.73-9.5 eV by combining Variable Angle Spectroscopic Ellipsometry (VASE) and vacuum ultraviolet (VUV) ellipsometry with synchrotron radiation. The optical constants of $BiFeO_3$ films were determined by analysing the ellipsometric spectra with a model that describes the optical response of a system consisting of air, film and substrate. The shift towards higher energies of the refractive index and extinction coefficient of the film deposited onto Nb-doped $SrTiO_3$ as compared with that deposited onto $DyScO_3$ was attributed to a more compressive in-plane epitaxial strain.

1 Introduction The interest in multiferroic epitaxial films arises from their interesting properties and is stimulated by the potential applications in non-volatile ferroelectric memories or novel multiple state memories and devices based on magnetoelectric effects [1]. The growth of high-quality single crystalline thin films of multiferroics is a prerequisite for the study of their intrinsic fundamental physical properties, undisturbed by the extrinsic contributions from extended structural defects, and for their incorporation into practical devices [2]. Bismuth ferrite $BiFeO_3$ (BFO) is a single phase room temperature (RT) multiferroic with the ferroelectric Curie temperature (T_c=370 °C) and the antiferromagnetic Néel temperature (T_N=820 °C) well above RT [3]. Despite the great interest in multiferroic thin films, there are only few studies regarding the optical properties of BFO. Moreover, most investigations of the dielectric function of these materials are limited to the region below 6 eV [4], the energy domain available in commercial ellipsometers, while the vacuum ultraviolet (VUV) range is hardly explored at all. Ellipsometry is a non-destructive and very sensitive surface and thin film measurement technique which can determine film thickness, surface roughness and dielectric properties of such materials with a very high precision. The VUV ellipsometry was proved to be a powerful method for achieving sub-monolayer sensitivity for organic thin films [5] and was used to determine the dielectric function of thin diffusion barriee layers [6].

In this paper the optical properties of BFO films deposited on different substrates are investigated by combining Variable Angle Spectroscopic Ellipsometry (VASE) and VUV spectroscopic ellipsometry.

2 Experimental Epitaxial thin films of bismuth ferrite were deposited by pulsed laser deposition (PLD) on Nb-doped $SrTiO_3$ (100) (Nb:STO), on STO (100) and $DyScO_3$ (DSO) (110) substrates, at T_g=650 °C and 0.14 mbar O_2 [7].

VUV-spectroscopic ellipsometry measurements were performed in the 4.5-9.5 eV photon energy range using the 3m-NIM1 monochromathor at BESSY. The spectra were recorded using a rotating-analyser type ellipsometer at 67° angle of incidence. As polariser and analyzer MgF_2 Rochon prisms were used. A more detailed description of the experimental set-up can be found elsewhere [8]. VASE measurements were performed in the 0.73 eV up to 4.5 eV range at four angles of incidence using a VASE ellipsometer from J.A. Woollam Company. The VASE and VUV spectra were appended and evaluated in the whole energy range (0.73 eV-9.5 eV).

Spectroscopic ellipsometry is an optical technique which measures the changes of the polarization state of a polarized light beam after reflection from the sample under study. These changes are measured as the ellipsometric parameters ψ and Δ which are related to the ratio of the effective reflection coefficients $<r_p>$ and $<r_s>$ for p- and s-polarised light:

$$\rho = \frac{< r_p >}{< r_s >} = \tan(\Psi)\cdot\exp(i\Delta) \tag{1}$$

where ρ is the complex reflectance ratio. The ψ and Δ values depend on the thickness, roughness, refractive index n, and extinction coefficient k of the layers and the substrate. In order to extract the information contained in the ellipsometric spectra, a multilayer model was applied. One straightforward and very important model for understanding how the values of the thickness or optical constants can be computed is the three-phase model consisting of ambient–film–substrate [9]. In the calculation of Ψ and Δ ellipsometric spectra the propagation of light through the multilayered structures is described by the complex refractive index $\tilde{n} = n+ik$ and the thickness t of each layer This model considers that propagation of light in a layer is governed by linear equations and the continuity of the tangential electric field across an interface between two isotropic media can be written as a 2×2 matrix. Following this approach, the effective reflection coefficients $<r_p>$ and and $<r_s>$ can be determined from the Fresnel coefficients of transmission and reflection at each interface. Analytic algebraic expressions can be written for predicting Ψ and Δ as functions of optical constants and layer thickness. The algebra for calculating Ψ and Δ will not be presented here, but can be found in standard references [9].

In a fitting procedure of the experimental spectra by a variation of the parameters contained in the model, the mean square error (MSE) function expressed by:

$$MSE = \frac{1}{2N-M}\sum_{i=1}^{N}\left[\left(\frac{\Psi_i^{\text{mod}} - \Psi_i^{\text{exp}}}{\sigma_{\Psi,i}^{\text{exp}}}\right)^2 + \left(\frac{\Delta_i^{\text{mod}} - \Delta_i^{\text{exp}}}{\sigma_{\Delta,i}^{\text{exp}}}\right)^2\right] \tag{2}$$

is minimised. Here N is the number of experimental (Ψ,Δ) pairs, M is the number of variable parameters and σ is the standard deviation on the experimental data points.

3 Results and discussion The Nb:STO and DSO substrates were measured using VASE and VUV ellipsometry. The optical response of the substrates was described using a Gaussian oscillator model which implies the Kramer-Kronig consistency of the real and imaginary parts of dielectric function. The dielectric functions of Nb:STO and DSO obtained from the fit of the ellipsometric spectra are shown in Fig. 1. In the case of Nb:STO the data agree well with the results of Zollner *et al.* for STO [10]. In the case of DSO the dielectric function obtained from ellipsometry indicates a wide bandgap material with an onset of absorption above 6 eV and a strong absorption peak centered at ~ 8 eV.

Using the dielectric functions determined for the substrates the ellipsometric spectra of BFO films were evaluated. First, the absorption free energy range (0.73-2 eV) was used in order to determine the thickness of the BFO films. A four-phase model: substrate/film/roughness layer/ambient was employed. The optical response of the film is described by a Cauchy dispersion relation for the refractive index:

$$n = A_n + \frac{B_n}{\lambda^2} \tag{3}$$

while the roughness layer was considered to be a mixture of 50 % film material and 50 % voids by using a Bruggeman Effective Medium Approximation (EMA) [11]. The thickness of the film and the thickness of the rough layer together with A_n and B_n Cauchy constants were the fit parameters.

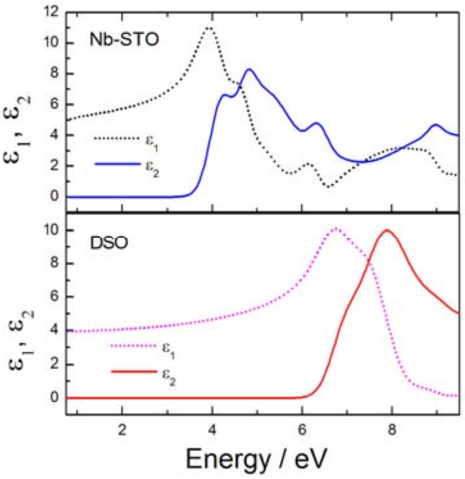

Figure 1 Real and imaginary parts of the dielectric function of Nb:STO(100) (upper panel) and DSO(110) (lower panel) substrates as determined from ellipsometry.

In Fig. 2a the ellipsometric spectra (symbols) and the corresponding fits (lines) are shown for a 106.5 nm BFO film on Nb:STO substrate.

For the same sample a roughness of 3.6 nm was obtained using the EMA model. This value agrees quite well with the 2.5 nm roughness obtained from Atomic Force Microscopy (AFM) measurements. The AFM image for this sample is shown in Fig. 2b. All thicknesses and roughnesses obtained for the investigated samples are summarized in Table I. The error in determination of thickness was ~ ± 0.3 nm while the error of the roughness determined by EMA model was ~ ± 0.5 nm.

Table 1 Layer and roughness thickness as determine from ellipsometry.

Samples	Layer thickness/nm	Roughness thickness/nm
BFO on STO	54.3	2.6
BFO on Nb:STO	106.5	3.6
BFO on DSO	34.1	1.6
	135.3	4.0

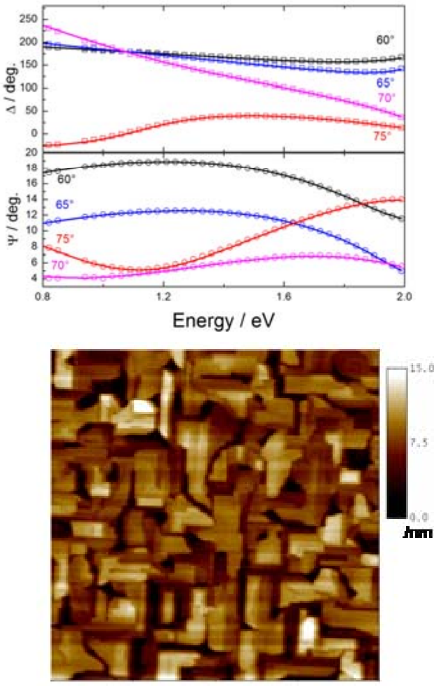

(a)

(b)

Figure 2 (a) Ellipsometry spectra for a 106.5 nm BFO film deposited onto Nb:STO substrate in the transparent range. The symbols denote the experimental data, while the lines show the fits. (b) 4 µm x 4 µm AFM image of the same sample.

Furthermore, having determined the layer and roughness thicknesses, the ellipsometric data were evaluated in the whole energy range. Initially a point-by-point fit, in which the data at each wavelength are fitted separately, was used. Subsequently, a sum of Gaussian oscillators was used to simulate the line shape of the imaginary part of the dielectric function, while the real part of the dielectric function is generated according to the Kramers-Kronig relation. Figure 3 shows the ellipsometric experimental data (symbols) and the fits (lines) obtained by using the procedure described above for the 106.5 nm BFO film on Nb:STO substrate. As a result of the fits the optical constants of the BFO films were determined in the 0.73-9.5 eV energy range.

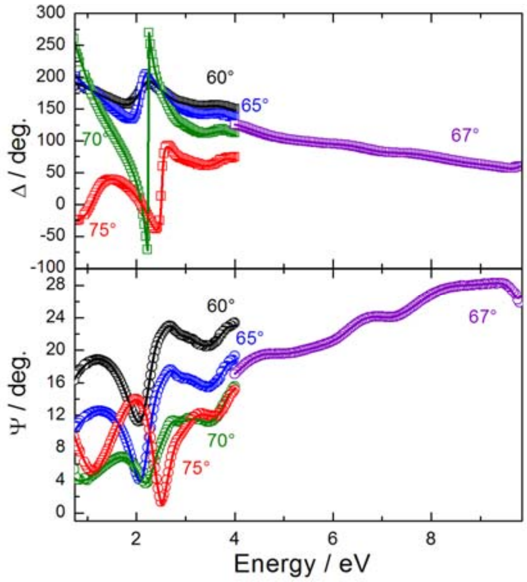

Figure 3 Ellipsometry spectra for a 106.5 nm BFO film deposited onto Nb:STO substrate in the 0.73 - 9.5 eV range. The symbols denote the experimental data, while the lines show the fits.

Figure 4 shows the refractive index and extinction coefficient for the BFO films deposited onto Nb:STO and DSO substrates respectively. The data agree well with those published by Kumar *et al.* [12] for BFO films deposited onto STO substrates in the photon energy range up to 6.5 eV. Our data extend the range of optical constant determination up to 9.5 eV. It can be clearly seen that the data for the films deposited onto Nb:STO are blue shifted with respect to the data for the films deposited onto DSO. This kind of behaviour suggests a more compressive strain in the films deposited onto Nb:STO. Indeed the BFO films grown on STO have an in-plane compressive strain [13] as compared with the films deposited onto DSO [14]. This behaviour is due to the lattice mismatch between BFO and the two different substrates, the room temperature pseudocubic lattice parameter being 3.965 Å for BFO while it is 3.905 Å and 3.951 Å for STO(100) and DSO(110) respectively [13, 14]. Consequently a more compressive strain is expected in the BFO films when deposited onto STO as compared to the deposition on DSO. The compressive strain explains the blue shift of the optical constants for the films deposited onto Nb:STO.

Moreover by plotting $(\alpha \cdot E)^2$ *vs.* E where α is the absorption coefficient ($\alpha = (4\pi k / \lambda)$) and E is the photon energy [15] we obtain a bandgap of (2.75 ± 0.01) eV for the films deposited onto DSO while the bandgap for the films deposited onto Nb:STO is blue-shifted by 50 meV. Such a behaviour (the smaller the lattice parameter the higher the bandgap) [16] support assumption of a smaller in-plane lattice parameters for BFO films when deposited onto STO.

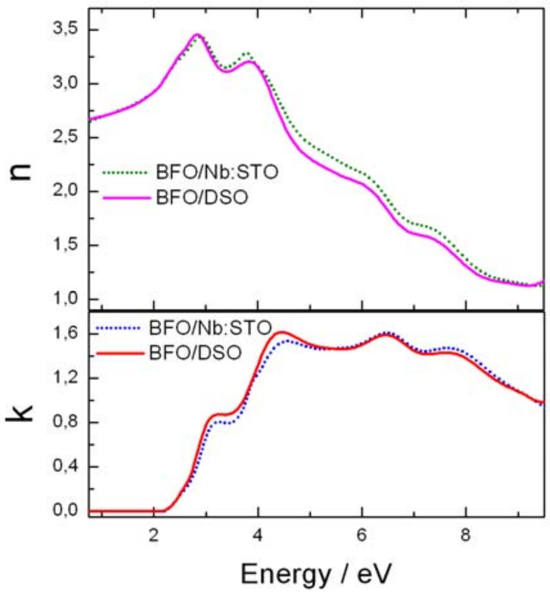

Figure 4 Refractive index and extinction coefficient for the BFO films deposited onto DSO and Nb:STO substrates, respectively.

These results were also confirmed by Raman spectroscopy [17] In the case of the films deposited onto Nb:STO the $\mathbf{A_1}$ phonon bands of BFO at ~ 135 cm^{-1} and ~175 cm^{-1} are shifted by ~ 3 cm^{-1} to higher wavenumbers as compared to the BFO films on DSO. This blue-shift of the Raman modes indicates again the presence of higher compressive strain for BFO films on Nb:STO.

4 Conclusions The optical constants of BFO films deposited onto Nb:STO and DSO substrates were determined up to 9.5 eV by evaluating the ellipsometric spectra in a multilayer model which describes the optical response of the sample. The difference in optical constants was attributed to a more compressive strain in the case of the films deposited onto Nb:STO.

It was found that the optical gap for the films deposited onto Nb:STO are blue-shifted by ~50 meV as compared to the films deposited onto DSO.

Acknowledgements The experimental work was supported by the BMBF project 05 ES3XBA/5, the SFB 762 project “Funktionalität Oxidischer Grenzflächen”, and the European Community through the "NanoCharM" project under the Seventh Framework Programme (FP7).

References

[1] Y.-H. Chu, L. W. Martin, M. B. Holocomb, M. Gajek, S.-J. Han, Q. HE, N. Balke, C.-H. Yang, D. Lee, W. Hu, Q. Zhan, P.-L. Yang, A. Fraile-Rodriguez, A. Scholl, S. X. Wang, and R. Ramesh, Nature Mater. **7**, 478 (2008).

[2] R. Ramesh, and N.-A. Spaldin, Nature Mater. **6**, 21 (2007).

[3] J. F. Ihlefeld, N. J. Podraza, Z. K. Liu, R. C. Rai, X. Xu, T. Heeg, Y. B. Chen, J. Li, R. W. Collins, J. L. Musfeldt, X. Q. Pan, J. Schubert, R. Ramesh, and D. G. Schlom, Appl. Phys. Lett. **92**, 142908 (2008).

[4] P. Fischer, M. Polomska, I. Sosnowska, and M. Szymanski, J. Phys. C **13**, 1931(1980).

[5] O. D. Gordan, C. Himcinschi, D. R. T. Zahn, C. Cobet, N. Esser, and W. Braun, Appl. Phys Lett. **88**, 141913 (2006).

[6] S. Rudra, T. Wächtler, M. Friedrich, S. J. Louis, C. Himcinschi, S. Zimmermann, S. E. Schulz, S. Silaghi, C. Cobet, N. Esser, T. Gessner, and D. R. T. Zahn, Phys. Status Solidi A **205**, 922 (2008).

[7] I. Vrejoiu, M. Alexe, D. Hesse, and U. Gösele, Adv. Funct. Mater. **18**, 3892 (2008).

[8] T. Wethkamp, K. Wilmers, N. Esser, W. Richter, O. Ambacher, H. Angerer, G. Jungk, R. L. Johnson, and M. Cardona, Thin Solid Films **313/314**, 745 (1998).

[9] R. M. A. Azzam, N. M. Bashara, Ellipsometry and Polarized Light (Elsevier, Amsterdam 1987).

[10] S. Zollner, A. A. Demkov, R. Liu, P. L. Feijes, R.B. Gregory, P. Alluri, J. A. Curless, Z. Yu, J. Ramdani, R. Droopad, T. E. Tiwald, J. N. Hilfiker, and J. A. Woollam, J. Vac. Sci. Tehnol. B **18**, 2242 (2000).

[11] D. Bruggeman, Ann. Phys. Leipzig **24**, 636 (1935).

[12] A. Kumar, R. C. Rai, N. J. Podraza, S. Denev, M. Ramirez, Y.-H. Chu, L. W. Martin, J. Ihlefeld, T. Heeg, J. Schubert, D. G. Schlom, J. Orenstein, R. Ramesh, R. W. Collins, J. L. Musfeldt, and V. Gopalan, Appl. Phys. Lett. **92**, 121915 (2008).

[13] J. Wang, J. B. Neaton, H. Zheng,V. Nagarajan, S. B. Ogale, B. Liu, D. Viehland, V. Vaithyanathan, D. G. Schlom, U. V. Waghmare, N. A. Spaldin, K. M. Rabe, M. Wuttig, and R. Ramesh, Science **299**, 1719 (2003).

[14] Y.-H. Chu, Q. Zhan, L. W. Martin, M. P. Cruz, P.-L. Yang, G. W. Pabst, F. Zavaliche, S.-Y. Yang, J.-X. Zhang, L.-Q. Chen, D. G. Schlom, N. Lin, T.-B. Wu, and R. Ramesh, Adv. Mater. **18**, 2307 (2006).

[15] J. I. Pankove, Optical Processes in Semiconductors (Prentice-Hall, New Jersey, 1971).

[16] M. B. Ortuno-Lopez, M. Sotelo-Lerma, A. Mendoza-Galvan, and R. Ramirez-Bon, Vacuum **76**, 181 (2004).

[17] C. Himcinschi, I. Vrejoiu, L. Ding, M. Friedrich, C. Cobet, N. Esser, M. Alexe, and D. R. T. Zahn, Appl. Phys. Lett. (submitted).

phys. stat. sol. (a) **205**, No. 4, 841–844 (2008) / **DOI** 10.1002/pssa.200777753

physica status solidi a
www.pss-a.com
applications and materials science

Etching-back of uniaxially strained silicon on insulator investigated by spectroscopic ellipsometry

C. Himcinschi*, [1, 2], R. Singh[2], O. Moutanabbir[2], R. Scholz[2], M. Reiche[2], S. H. Christiansen[2], U. Gösele[2], and D. R. T. Zahn[1]

[1] Chemnitz University of Technology, Semiconductor Physics, 09107 Chemnitz, Germany
[2] Max Planck Institute of Microstructure Physics, Weinberg 2, 06120 Halle, Germany

Received 7 June 2007, revised 24 November 2007, accepted 28 November 2007

PACS 68.35.Gy, 68.37.–d, 78.20.Ci, 78.66.Db, 81.65.Cf, 81.70.Fy

---

* Corresponding author: e-mail c.himcinschi@physik.tu-chemnitz.de, Phone: +49 371 531 36731, Fax: +49 371 531 21819

Spectroscopic Ellipsometry was employed to study the etching process of uniaxially strained Si (sSi) layers obtained by direct wafer bonding of Si wafers in a mechanically bent state followed by thinning one of the Si wafers, the donor wafer, by the smart-cut process, keeping the other, the handle wafer intact. The smart-cut process requires a high dose hydrogen implantation into the donor wafer prior to bonding. As a result of the implantation conditions a ~600 nm uniaxially sSi layer could be transferred onto the handle wafer. In order to thin down and smooth the surface damage of the transferred layer induced by the implantation and splitting process, the samples were dipped in a solution of tetra-methyl ammonium hydroxide (TMAH). The thicknesses of the transferred sSi layers determined from ellipsometry were in good agreement with those obtained from Transmission Electron Microscopy (TEM), while the roughness values were matching those obtained from Atomic Force Microscopy (AFM). The etching rate has also been determined.

1 Introduction To slow down the urge of down scaling in silicon technology novel materials and structure developments are considered as alternatives for performance enhancement. Among those, silicon-on-insulator (SOI) and strained silicon (sSi) are promising approaches [1]. Recently, mobility increase for electrons and holes were obtained for very low values of uniaxial strain [2] induced by processing at the transistor level [3]. Even though the performance enhancement by this local, i.e., device level straining, is high, it is also worth looking into global straining on the wafer level. An approach to strain globally, on wafer level, uniaxially in tension and compression based on the concept of direct wafer bonding of prestrained wafers and smart-cut [4] was recently demonstrated [5].

One important step in the sSi manufacturing is the etching process. Tetra-methyl ammonium hydroxide (TMAH) has become one of the highly preferred silicon etchants due to its non-toxicity, selectivity and compatibility with semiconductor processing [6–8].

A non-destructive way to check the etching rate and the roughness induced by etching is provided by Spectroscopic Ellipsometry (SE) which is a very surface sensitive method.

In this paper we present an ellipsometric study of the etching of uniaxially sSi by TMAH. The results from ellipsometry are compared with those from cross sectional Transmission Electron Microscopy (TEM) and Atomic Force Microscopy (AFM).

2 Experiment Uniaxial strain on wafer level was created by exploiting mechanical straining of the material upon bending. Two wafers were bent over a cylinder, following the concept introduced by Belford et al. [9]. The curved wafers are brought into contact via direct wafer bonding and covalent bonds across the bonded interface form upon annealing in the bent state. After releasing from the bonding machine, the thinning of one of the wafers was realized by the smart-cut process [4]. Three different radii

Table 1 Labelling of the investigated samples.

sample label	interface oxides deposited on 4 inch wafer	initial protective oxide on the 3 inch donor wafer*
S200	200 nm	100 nm
S300	300 nm	50 nm

* The protective oxide was removed after implantation prior to bonding.

of curvature for the bending cylinder were used: 0.5 m, 0.75 m and 1 m. Experimental details on the bonding set-up can be found elsewhere [5].

50 nm or 100 nm thick oxide films were thermally grown on the 3 inch donor wafer prior to implantation and bonding as a protective layer. The 3 inch wafers were implanted at room temperature with 150 keV H_2^+ at a fluence of 4×10^{16} cm^{-2}. After implantation the protective oxide was removed by hydrofluoric acid. Thermally grown oxide films (200 nm and 300 nm) were deposited onto the 4 inch handle wafers prior to bonding. Standard chemical RCA cleaning of the Si wafers was performed prior to bonding. The 3 inch donor wafers were bonded to 4 inch handle wafers according to the description in Table 1.

The ellipsometric measurements were performed using a VASE Woollam Co. ellipsometer in the spectral range from 250 nm to 1000 nm with a step width of 10 nm. The ellipsometer is equipped with an autoretarder, which allows the measurements of the ellipsometric parameter Δ in a 360° interval.

3 Results and discussion After splitting the 3 inch donor wafers by the smart-cut process ~600 nm uniaxially sSi layers are transferred onto the 4 inch handle wafers. Cross sectional TEM images revealed that ~585 nm sSi was transferred in the case of S200 samples (Fig. 1a) while ~630 nm sSi was transferred in the case of S300 samples (Fig. 1c). The difference of ~50 nm in the thickness of the transferred layers is simply attributed to the difference in H_2^+ implantation depth affected by the thickness of the protective oxide used, in agreement with simulations using Stopping and Range of Ions in Matter (SRIM) program [10].

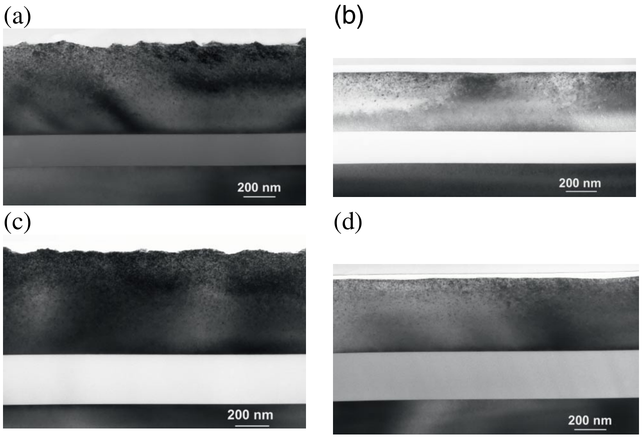

Figure 1 Cross sectional TEM images for the S200 sample before (a), and after 60 s TMAH etching (b); and for the S300 sample before (c), and after 60 s TMAH etching (d).

The TEM images show rough surfaces of the transferred layers caused by the implantation damage and splitting (Fig. 1a and c). To characterise the surface roughness AFM was employed. In Fig. 2a, the AFM image shows a root mean square (RMS) roughness of ~11.5 nm for the transferred layer measured on 10 µm × 10 µm large area.

In order to thin down and smooth the surface damage induced by implantation, the samples were dipped in a solution of tetra-methyl ammonium hydroxide (TMAH) 40%, at 55 °C for different durations ranging from 0 s to 180 s, after splitting and before the spectroscopic ellipsometry measurements. Before TMAH etching the samples were dipped in HF (5%) solution for 20 s in order to remove the native oxide.

The cross sectional TEM images of the samples S200 and S300 after 60 s etching are shown in Fig. 1b and d, respectively. About 150 nm of the sSi layer was etched away after 60 s. The surface looks also smoother as confirmed by AFM measurements (Fig. 2b) indicating that RMS roughness decreases to ~3.1 nm after 60 s etching for measurements on equal area.

Spectroscopic ellipsometry was used to investigate the etching process as a function of etching time. Spectroscopic ellipsometry is an optical technique which measures the changes of the polarization state of a polarized light beam after reflection from the sample under study [11].

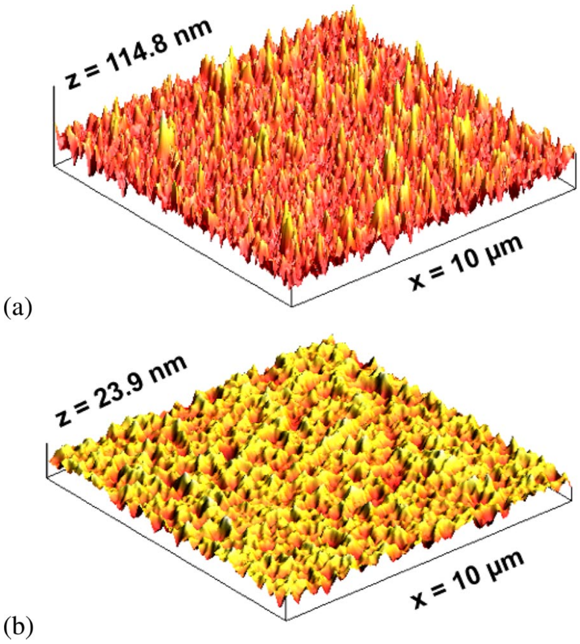

Figure 2 (online colour at: www.pss-a.com) AFM images for the S200 sample before (a), and after 60 s TMAH etching. The RMS values are 11.5 nm and 3.1 nm for the scanned areas of 10 µm × 10 µm in figure (a) and (b) respectively.

These changes are measured as the ellipsometric parameters Ψ and Δ which are related to the ratio of the effective reflection coefficients $\langle r_p \rangle$ and $\langle r_s \rangle$ for p- and s-polarised light:

$$\rho = \frac{\langle r_p \rangle}{\langle r_s \rangle} = \tan(\Psi) \exp(i\Delta), \quad (1)$$

where ρ is the complex reflectance ratio. $\langle r_p \rangle$ and $\langle r_s \rangle$ are functions of the complex refractive indices of the films and the substrate and of their thicknesses. In order to extract useful information about layer thicknesses or roughness the experimental data are compared with simulated data generated using a model which describes the structure of the sample and its optical response. The unknown parameters in the model are adjusted in order to get the best match between the model and the experimental data.

In Fig. 3 typical Ψ and Δ ellipsometric spectra are plotted using the sample S200 after 60 s TMAH etching, as an example. The spectra are measured at angles of incidence near the Brewster angle of Si, namely 65°, 70° and 75°, and are dominated by a number of oscillation peaks which are due to the interference of the light in the sSi and silicon oxide layers.

The structure of the model used to describe the optical response of the samples is shown in the inset of Fig. 3. The thicknesses of the thermally grown oxides (200 nm or 300 nm) were determined by ellipsometry measurements on a reference 4 inch wafer before bonding. Literature data for optical constants of Si and SiO_2 were used [12, 13]. Using the known optical constants of Si and SiO_2, the thickness of the sSi layer and the thickness of the roughened layer were allowed to vary during the fitting procedure of the ellipsometric spectra. The roughness was modeled using the Bruggeman Effective Medium Approximation (EMA) considering a voids density of 50% [14]. A good agreement between fit lines of the model data and the experimental data (symbols) was obtained. For the particular case of the S200 sample after 60 s TMAH etching (Fig. 3), the thickness of the sSi layer was determined to be ~380 nm while the surface roughness was 2.6 nm.

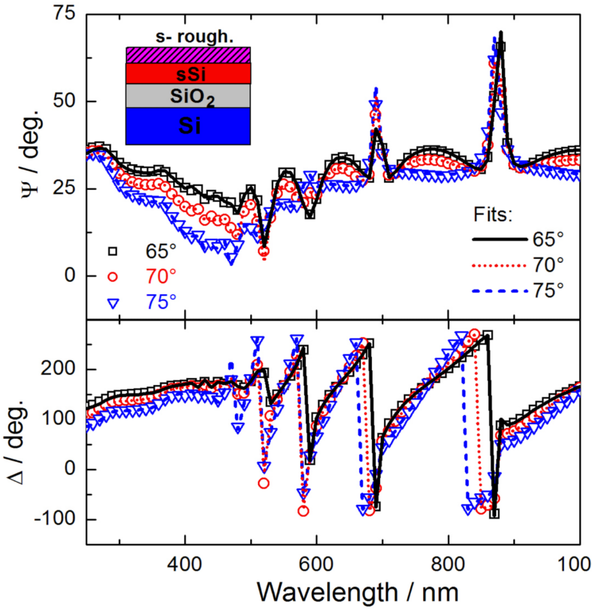

Figure 3 (online colour at: www.pss-a.com) Ellipsometry spectra for an sSOI sample after 60 s TMAH etching, consisting of 380 nm sSi on 200 nm SiO_2 on the Si handle wafer. The symbols denote the experimental data, while the lines show the fits.

It should be mentioned that the optical response of the sSi layer was modelled with the optical constants of unstrained Si. This approximation is justified since we found no difference in the ellipsometric spectra of the sSi samples obtained by smart-cut after wafer bonding over cylinders and unstrained Si, reference samples obtained by an identical smart-cut process without bending. On the other hand the highest strain values for these samples are below 0.1%, as was measured by ultraviolet Raman spectroscopy [15] which represents low strain as compared to sSi obtained by SiGe technology.

Figure 4 summarizes the results obtained after evaluating the ellipsometric spectra. The thicknesses of the sSi transferred layer are in good agreement with those obtained from TEM. The TMAH etching rate was calculated to be ~2.2 nm/s and ~1.9 nm/s for the samples S200 and

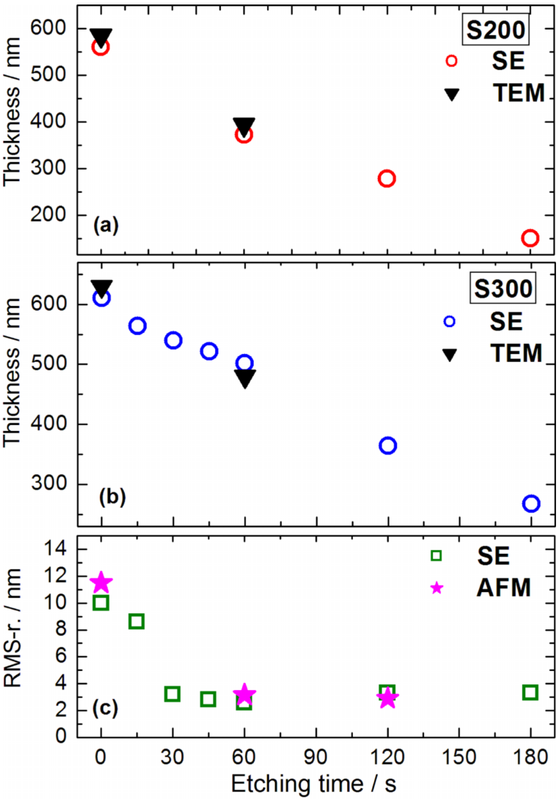

Figure 4 (online colour at: www.pss-a.com) Thickness values of the transferred layer as function of etching time, measured by ellipsometry and TEM for the sample S200 (a) and S300 (b). The roughness values determined from ellipsometry and AFM are also shown for the sample S300 (c).

S300 respectively. The slightly higher etching rate for the S200 sample could be explained by the higher initial roughness of this sample, as can be seen in Fig. 1a. The smart cut process, i.e. splitting induced by implantation and annealing is responsible for the initial roughness prior to etching. TMAH etching decreases the roughness with increasing etching time. The smoothening of the surface with increasing etching time is confirmed by the roughness values obtained by ellipsometry modelling as shown in the Fig. 4c for the sample S300. The ellipsometry results are confirmed also by the roughness values obtained by AFM investigations.

4 Conclusion The TMAH etching process of uniaxially strained silicon on insulator, obtained by direct wafer bonding of Si wafers in the bent state followed by thinning one of the Si wafers by the smart-cut process was investigated by spectroscopic ellipsometry. The thickness and the roughness values determined by ellipsometry modelling were compared with those obtained by cross sectional TEM and AFM respectively and a very good agreement was observed. Ellipsometry is shown to be an appropriate tool for calibrating the etching back processes related to the use of smart cut in the production of SOI and sSOI wafers.

Acknowledgements The experiments were financially supported by the German Federal Ministry of Education and Research (BMBF) in the framework of the TeSiN/TESIN+ project (contract no. V03110).

References

[1] G. K. Celler and S. Cristoloveanu, J. Appl. Phys. **93**, 4955 (2003).
[2] B. M. Haugerud, L. A. Bosworth, and R. E. Belford, J. Appl. Phys. **94**, 4102 (2003).
[3] S. E. Thompson, M. Armstrong, C. Auth, S. Cea, R. Chau, G. Glass et al., IEEE Electron Device Lett. **25**, 191 (2004).
[4] M. Bruel, Electron. Lett. **31**, 1201 (1995).
[5] C. Himcinschi, I. Radu, F. Muster, R. Singh, M. Reiche, M. Petzold, U. Gösele, and S. H. Christiansen, Solid-State Electron. **51**, 226 (2007).
[6] O. Tabata, R. Asahi, H. Funabashi, K. Shimaoka, and S. Sugiyama, Sens. Actuators A **34**, 51 (1992).
[7] K. Sakaino and S. Adachi, Sens. Actuators A **88**, 71 (2001).
[8] K. Biswas and S. Kal, Microelectron. J. **37**, 519 (2001).
[9] R. E. Belford, U.S. Patent, No. 6,455,397 B1 (2002).
[10] www.srim.org
[11] R. M. A. Azzam and N. M. Bashara, Ellipsometry and Polarized Light (Elsevier, Amsterdam, 1987).
[12] B. Johs and C. Herzinger, Guide to using WVASE32 (J. A. Woollam Co., Inc., Lincoln, NE, 1995).
[13] E. D. Palik (ed.), Handbook of optical constants of solids (Academic Press, New York, 1985), p. 759.
[14] D. A. G. Bruggeman, Ann. Phys. **24**, 636 (1935).
[15] C. Himcinschi, M. Reiche, R. Scholz, S. H. Christiansen, and U. Gösele, Appl. Phys. Lett. **90**, 231909 (2007).

APPLIED PHYSICS LETTERS **90**, 231909 (2007)

Compressive uniaxially strained silicon on insulator by prestrained wafer bonding and layer transfer

C. Himcinschi,[a] M. Reiche, R. Scholz, S. H. Christiansen, and U. Gösele
Max Planck Institute of Microstructure Physics, Weinberg 2, 06120 Halle, Germany

(Received 7 April 2007; accepted 15 May 2007; published online 7 June 2007)

Wafer level compressive uniaxially strained silicon on insulator is obtained by direct wafer bonding of silicon wafers in cylindrically curved state, followed by thinning one of the wafers using the smart-cut process. The mapping of the wafer bow demonstrates the uniaxial character of the strain induced by the cylindrical bending. The interfacial properties are investigated by infrared transmission imaging, scanning acoustic microscopy, and transmission electron microscopy. UV-Raman spectroscopy is employed to determine the strain in the thin transferred layer as a function of radius of curvature of the initial bending. © *2007 American Institute of Physics*. [DOI: 10.1063/1.2747182]

Strain in silicon provides for enhanced carrier mobilities compared to the unstrained counterparts. Combining the straining of silicon with silicon on insulator technology combine mobility enhancement and reduced parasitics.[1] Biaxially strained Si (sSi) has been widely explored in the past few years due to the enhancement of carrier mobility in metal-oxide-semiconductor field-effect transistors (MOSFETs).[2,3] Unfortunately, the hole mobility improvement induced by the biaxial strain is minor in the *p*-type MOSFETs at large vertical electric fields.[3] However, processing-induced uniaxial channel straining at the transistor level has been shown to solve this performance problem.[4] It was found that uniaxial compressive strain on (001) wafers along the ⟨110⟩ directions provides for the optimized enhancement for holes.[5] For mechanically induced ultralow strain levels (below 0.05%), *p*-MOSFETs showed an increase in effective mobility of more than 15%.[6] It might be an advantage in the long run to induce strain globally using a wafer-bonding-based approach to uniaxial straining and possibly combining this with additional straining at the transistor level.[7] An approach on how to strain globally, i.e., on wafer level, uniaxially in tension was recently demonstrated[8] based on the concept of direct wafer bonding[9] of prestrained wafers, which was first introduced by Belford *et al.*[10]

A highly sensitive method to study the local strain is the UV micro-Raman spectroscopy.[11] With the continuing miniaturization of the microelectronic devices, the use of short wavelength UV lasers for Raman spectroscopy has been proven to have significant advantages over the conventional visible lasers due to the short penetration depth and therefore surface-near probing of the material.[12]

In this letter we report on the realization of compressive uniaxial strained silicon on insulator (sSOI) wafers by mechanically curving and direct wafer bonding of the prestrained Si wafers, followed by thinning one of the wafers by the smart-cut process.[13] The sSOI wafers were characterized by profilometry and transmission electron microscopy, while the strain in the transferred sSi layer was derived from Raman spectroscopy.

3 and 4 in. double side polished Si(100) wafers were used for the experiments. The 3 in. wafers were implanted at room temperature with 150 keV H_2^+ at a dose of 4×10^{16} cm^{-2}. On the 4 in. wafers a 300 nm thick thermal oxide was grown. Thus, a bonding of the thin and thick oxides on silicon was realized that is known to provide for a good bonding energy.[14]

The concept of realizing uniaxial strain on wafer level is shown schematically in Fig. 1. The two wafers were bent over a cylinder thereby creating a curved or bowed wafer with a strained state induced. The bending direction was parallel to the [110] direction of the wafer. The curved wafers are brought into contact via direct wafer bonding and covalent bonds across the bonded interface form upon annealing in the bent state. After releasing from the bonding machine, the implanted 3 in. wafer was thinned down by the smart-cut process to a layer thickness of ~600 nm. After splitting, the bonded wafer stack assumes an almost flat surface and substantial strain is transferred to the thinned Si layer. For the 3 in. wafer being the top wafer, as shown in Fig. 1, compressive uniaxial strain is obtained. Three different radii of curvature for the bending cylinder were used: 0.5, 0.75, and 1 m. Experimental details on the bonding setup can be found elsewhere.[8]

The measurements of the wafer bow were carried out using a Veeco Dektak 8 profilometer. The Raman measurements were performed by means of a LabRam HR800 UV spectrometer (from Horiba Jobin Yvon). The 325 nm emission line of a He–Cd laser was used for excitation.

The quality of the bonded interfaces was assessed by infrared (IR) transmission imaging after annealing and releasing the bonded wafers from the bonding setup. Figure 2(a) shows the IR image of a typical interface for a bonded wafer pair in the bent state after annealing at 200 °C for 12 h. The bonded interface was found to be void- and bubble-free over most of the wafer area, except of a few

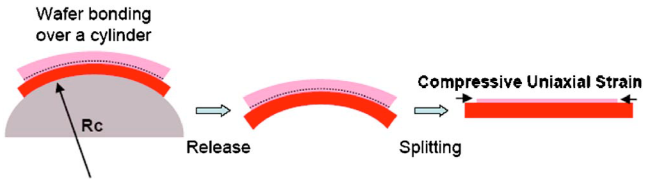

FIG. 1. (Color online) Schematic drawing of the concept to realize uniaxial compressive strain on wafer level.

---

[a] Electronic mail: c.himcinschi@physik.tu-chemnitz.de

0003-6951/2007/90(23)/231909/3/$23.00

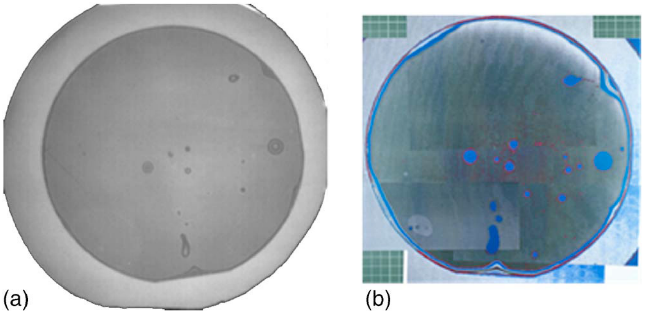

FIG. 2. (Color online) Infrared transmission (a) and scanning acoustic microscopy (b) images of a bonded wafer pair after annealing at 200 °C for 12 h and release from the bonding setup.

TABLE I. Predicted and experimental bow values for the bonded wafer pairs, uniaxially bent over cylinders with different radii of curvature.

Radius of curvature (m)	Bow predicted by radius of curvature on 1 in. length (μm)	Bow measured on 1 in. length (μm) (on [110] direction)
1	78.1	56.2 2.4[a] After splitting: 1.1
0.75	104.2	75.9
0.5	156.2	90.2

[a] Perpendicular to [110].

voids that were detected. These voids might be related to some particles at the wafer surfaces which could not be completely removed during the RCA cleaning process. The IR transmission imaging can detect only the macroscopic voids or bubbles (having a diameter of ~1 mm or more). Therefore, acoustic microscopy measurements on the bonded wafer pair were performed to detect microscopic voids (having diameters of a few tens of micrometers) at the bonded interface. An acoustic microscopy image of the bonded wafer pair [the same as in Fig. 2(a)] after annealing at 200 °C for 12 h is shown in Fig. 2(b). This image shows some microscopic voids concentrated in the middle of the samples in the vicinity of the macroscopic bubbles observed in the IR transmission image. The rest of the bonded interface is free of microscopic voids.

After release from the bonding setup the bow of the bent wafers was measured by profilometry. In Fig. 3 a map of the bow on a 1×1 in.^{2} area for bending with 1 m radius of curvature is shown. The horizontal direction in Fig. 3 is parallel to the bending direction ([1 1 0] wafer direction). It is obvious that the bow is much larger in the bending direction (56.2 μm) compared to the bow in the direction perpendicular to it (2.4 μm), indicating the uniaxial prestrain distribution. Similar measurements were performed after release from the bonding setup on the wafers for bending with radii of curvature of 0.75 and 0.5 m. The results are summarized in Table I. When comparing to the bow values (column 2 in Table I) which correspond to the cylinder curvature it becomes obvious that the bonded wafers keep most of the bow induced by the bending even after release from the bonding setup.

For the layer transfer using the wafer bonding and smart cut, a second annealing step was carried out at 500 °C for 1 h. Upon splitting off a thin layer (from the 3 in. wafer) the bent wafer pair turns flat and a large fraction of the strain energy stored in the bent wafer pair turns into uniaxial strain in the thin split off layer. Indeed, after layer transfer by splitting, the bow measurements showed the almost complete loss of bow (1.5 μm below remain) being measured on a scan of 1 in. length for the case of 1 m of radius of curvature of the cylinder.

In Fig. 4 a cross-sectional transmission electron microscopy (TEM) image of a wafer pair after splitting is shown. The bonded interface between the transferred Si and the oxide is smooth and free of any nanoscopic void. The damage region induced by implantation extends approximately between 500 and 600 nm from the surface of the Si/SiO$_2$ handle wafer. In order to reduce the surface damage induced by implantation mediated splitting, the samples were dipped in a solution of tetramethyl ammonium hydroxide for 120 s after splitting prior to the Raman measurements. A final thickness of ~365 nm (indicated by the arrow in Fig. 4) for the transferred sSi layer was obtained after this etching process.

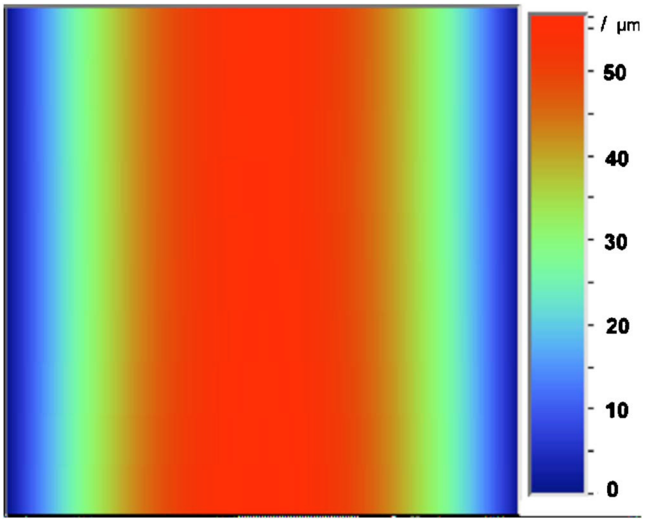

FIG. 3. (Color online) Mapping (1×1 in.^{2}) of the bow of a bonded wafer pair after release from the bending over a cylinder with 1 m radius of curvatures. The horizontal direction was parallel to the bending direction ([110] wafer direction).

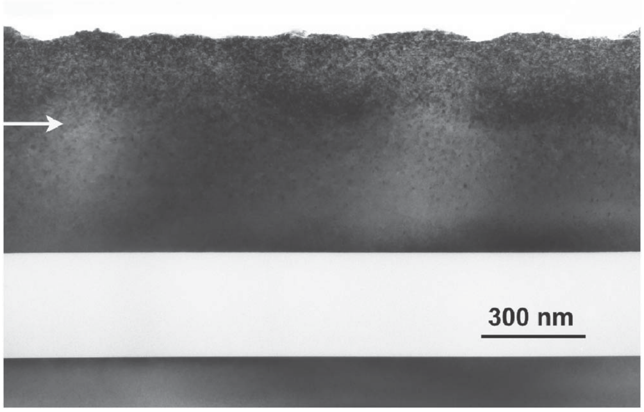

FIG. 4. Cross-sectional TEM image of a uniaxially compressive strained silicon layer on an oxidized Si wafer as realized by wafer bonding and layer transfer processes.

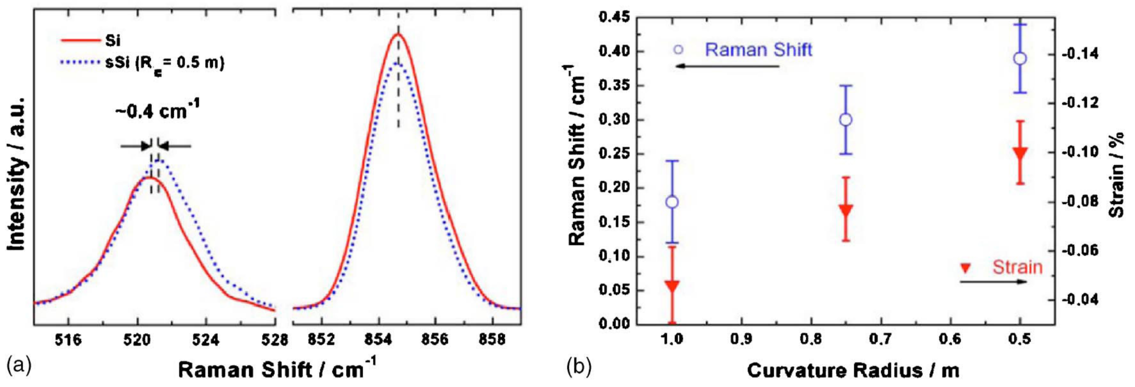

FIG. 5. (Color online) Raman spectra for unstrained Si and uniaxially compressive strained Si layer corresponding to an initial radius of curvature of 0.5 m (a) and dependence of the Raman frequency shifts and strain values on the initial radii of curvature (b).

The strain in the thin transferred Si layers was investigated by UV micro-Raman measurements. The 325 nm UV laser line used for the Raman measurements has a penetration depth of ~9 nm into Si. Thus the Raman spectra show the Si phonon peak coming from the transferred Si layer without any contribution to the signal from the underlying Si substrate. In Fig. 5(a) the Raman spectra for the unstrained and uniaxially strained Si transferred layers are shown by continuous and dotted lines, respectively. The transfer of the unstrained Si layer was accomplished in a similar way as for the strained Si, but in this case the wafers were not bent prior to bonding. The spectrum of the strained Si corresponds to a radius of curvature of the bending cylinder of 0.5 m. For an accurate determination of the Si peak position a plasma line of the HeCd laser (at 854.73 cm^{-1}) was used as a reference. The plasma lines can be used for calibration since they are caused by Rayleigh scattering and thus insensitive to strain and temperature in materials.[11] As obvious from Fig. 5(a), the Si peak of the strained Si layer is shifted by ~0.4 cm^{-1} to a higher frequency compared to the Si peak in the unstrained Si. Shifts towards higher frequencies were found for all investigated uniaxially strained Si samples.

In Fig. 5(b) the dependence of the strain-induced shifts of Raman frequencies on the radii of curvature is shown by round symbols. By measuring several points on each of the wafers, the statistical deviation of the Raman frequency shifts was found to be smaller than 0.06 cm^{-1}. This finding is a proof of homogeneous uniaxial strain throughout the entire wafer. The strain values may be calculated from the Raman frequency peak positions. A compressive strain will result in an upward shift of the strained silicon peak compared to the peak position for unstrained Si. According to De Wolf[15] the uniaxial stress can be calculated from the Raman shift according to

$$\sigma(\mathrm{MPa}) = -434\ \Delta\omega(\mathrm{cm}^{-1}). \tag{1}$$

Considering the relation between stress (σ) and strain (ε) $\varepsilon = \sigma/E$, where E is Young's modulus ($E_{[110]} = 169$ GPa), the strain can be calculated from the Raman shift as follows:

$$\varepsilon(\%) = -0.256\ \Delta\omega(\mathrm{cm}^{-1}), \tag{2}$$

where $\Delta\omega$ represents the frequency shift of the Si peak positions in cm^{-1} for strained Si compared to unstrained Si and ε is the strain in percent. The strain values were calculated from the Raman frequency shifts for the three radii of curvature used. The dependence of the strain values on the radius of curvature is shown in Fig. 5(b) by squared symbols.

Silicon layers atop an oxide layer on Si uniaxially strained in compression were fabricated by wafer bonding of prestrained wafers followed by layer splitting. This method allows straining at the wafer level as proved by three dimensional profilometry. Infrared transmission, scanning acoustic microscopy, and transmission electron microscopy indicate an almost defect-free bonding interface before and after the layer splitting. The strain values, as determined from Raman spectroscopy, can be controlled by varying the curvature radius of the bending cylinder used for bending the wafers before bonding. A maximum compressive uniaxial strain of 0.1% could be obtained for a radius of curvature of 0.5 m.

The experiments were financially supported by the German Federal Ministry of Education and Research (BMBF) in the framework of the TeSiN/TESIN+ project (Contract No. V03110).

[1] G. K. Celler and S. Cristoloveanu, J. Appl. Phys. **93**, 4955 (2003).
[2] E. A. Fitzgerald, Y.-H. Xie, M. L. Green, D. Brasen, A. R. Kortan, J. Michel, Y.-J. Mii, and B. E. Weir, Appl. Phys. Lett. **59**, 811 (1991).
[3] K. Rim, J. Chu, H. Chen, K. A. Jenkins, T. Kanarsky, K. Lee, A. Mocuta, H. Zhu, R. Roy, J. Newbury, J. Ott, K. Petrarca, P. Mooney, D. Lacey, S. Koester, K. Chan, D. Boyd, M. Ieong, and H.-S. Wong, Symp. VLSI Tech. Dig. **2002**, 98.
[4] S. E. Thompson, M. Armstrong, C. Auth, S. Cea, R. Chau, G. Glass, T. Hoffman, J. Klaus, M. Zhiyong, B. Mnintyre, A. Murthy, B. Obradovic, L. Shifren, S. Sivakumar, S. Tyagi, T. Ghani, K. Mistry, M. Bohr, Y. El-Mansy, IEEE Electron Device Lett. **25**, 191 (2004).
[5] S. E. Thompson, G. Sun, Y. S. Choi, and T. Nishida, IEEE Trans. Electron Devices **53**, 1010 (2006).
[6] B. M. Haugerud, L. A. Bosworth, and R. E. Belford, J. Appl. Phys. **94**, 4102 (2003).
[7] R. E. Belford, J. Electron. Mater. **30**, 807 (2001).
[8] C. Himcinschi, I. Radu, F. Muster, R. Singh, M. Reiche, M. Petzold, U. Gösele, and S. H. Christiansen, Solid-State Electron. **51**, 226 (2007).
[9] S. H. Christiansen, R. Singh, and U. Gösele, Proc. IEEE **94**, 2061 (2006).
[10] R. E. Belford, U.S. Patent No. 6,455,397 B1 (September 24, 2002).
[11] I. De Wolf, Semicond. Sci. Technol. **11**, 139 (1996).
[12] K. F. Dombrowski, I. De Wolf, and B. Dietrich, Appl. Phys. Lett. **75**, 2450 (1999).
[13] M. Bruel, Electron. Lett. **31**, 1201 (1995).
[14] C. Himcinschi, M. Friedrich, K. Hiller, T. Gessner, and D. R. T. Zahn, Semicond. Sci. Technol. **19**, 579 (2004).
[15] I. De Wolf, J. Raman Spectrosc. **30**, 877 (1999).

Available online at www.sciencedirect.com
ScienceDirect
Solid-State Electronics 51 (2007) 226–230
SOLID-STATE ELECTRONICS
www.elsevier.com/locate/sse

Uniaxially strained silicon by wafer bonding and layer transfer

C. Himcinschi [a,*], I. Radu [a], F. Muster [b], R. Singh [a], M. Reiche [a], M. Petzold [b],
U. Gösele [a], S.H. Christiansen [a,c]

[a] *Max Planck Institute of Microstructure Physics, Weinberg 2, 06120 Halle, Germany*
[b] *Fraunhofer Institute for Mechanics of Materials, Heideallee 19, 06120 Halle, Germany*
[c] *Martin Luther Universität Halle-Wittenberg, Hoher Weg 8, 06099 Halle, Germany*

The review of this paper was arranged by Raphaël Clerc, Olivier Faynot and Nelly Kernevez

Abstract

Uniaxial strain on wafer-level was realised by mechanically bending and direct wafer bonding of Si wafers in the bent state followed by thinning one of the Si wafers by the smart-cut process. This approach is flexible and allows to obtain different strain values at wafer-level in both tension and compression. UV micro-Raman spectroscopy was used to determine the strain in the thin transferred Si layers. Numerical modelling by 3D finite elements of the strain provided a good description of the experimental results.

Keywords: Wafer bonding; Strained silicon; Uniaxial strain; Raman spectroscopy

1. Introduction

In silicon technology, transistor speed is the key factor for performance and has to be enhanced in each technology generation. Device down scaling increased the transistor speed in the last 30 years and allowed in addition for an increased number of transistors on a given area. Today, silicon technology has reached the nano-era with channel lengths of less than 50 nm [1] and further down scaling becomes increasingly difficult. To slow down the urge of down scaling performance enhancement novel materials and structure developments are considered. Among those, silicon-on-insulator (SOI) and strained silicon (sSi) are promising approaches [2].

Up to now biaxially tensile strained silicon-on wafer-level has been widely explored for performance enhancement since engineering the strain in the silicon channel was successfully carried out by established heteroepitaxial growth processes. For this type of material a silicon layer is epitaxially and pseudomorphically grown on a thick relaxed SiGe layer that itself is epitaxially deposited and plastically relaxed on a Si(100) wafer [3]. With this approach tensile strain around 1% in the Si layer could be realized. This tensile strain leads to a substantial mobility enhancement for electrons [4,5]. Unfortunately, the hole mobility enhancement induced by 1% biaxial tensile strain is minor. It becomes significant only for much higher tensile strain which however cannot easily be achieved by epitaxy [5]. Recently, processing-induced uniaxial channel straining in tension and compression at the transistor level has been shown [6]. From these experiments, it is known that mobility enhancements for electrons and holes can be achieved by uniaxial straining at values smaller than 1%. Even uniaxial strain below 0.05% yields to mobility enhancement of up to 15% [7].

In this paper, we will present an approach that allows to create uniaxial strain flexibly in tension or compression on wafer-level by exploiting mechanical straining of the material upon bending. For mechanical uniaxial straining, two wafers were bent over a cylinder (bending over a sphere

---

[*] Corresponding author. Tel.: +49 345 5582 912; fax: +49 345 5511 223.
E-mail address: cameliu@mpi-halle.de (C. Himcinschi).

0038-1101/$ - see front matter © 2007 Elsevier Ltd. All rights reserved.
doi:10.1016/j.sse.2007.01.018

would lead to biaxial strain), following the concept introduced first by Belford et al. [8]. The bent wafers are brought into contact via direct wafer bonding and covalent bonds across the bonded interface form upon annealing in the bent state. By thinning one of the wafers to less than 1 µm thickness the bonded pair assumes an almost flat surface and substantial strain is transferred to the thinned wafer. This strain is essentially uniaxial and can be exploited in devices. The layer strain is measured by UV micro-Raman spectroscopy and compared with the calculated strain obtained from 3D finite element (FE) modelling.

2. Experimental

Three- and 4-in. double side polished Si(100) wafers were used for the experiments. The 4-in. wafers were implanted at room temperature with 100 keV H_2^+ at a dose of 4×10^{16} cm^{-2}. A 50 nm thick oxide was thermally grown on the 4″ wafer before implantation. Standard chemical cleaning of the Si wafers was performed prior to bonding.

Uniaxial strain in the 4-in. wafer was realized by mechanically bending the wafers over a cylinder in an experimental setup shown in Fig. 1, bonding in the bent state and subsequently thinning down the implanted wafer. The wafers are forced to stay bent by screws (visible in the setup in Fig. 1) and this bent state needs to be kept during an annealing step at elevated temperatures (200 °C for 15 h) which is required to increase the bond energy at the bonded interface. The bending direction is parallel to the [110] direction of the wafer. After annealing and releasing the screws the 3-in. wafer is keeping the bow remaining bonded to the 4-in. wafer in the bent state as can be seen in Fig. 1. The resulting maximum strain depends on the curvature radius of the cylinder and the thicknesses of the two bonded wafers assuming that no glide at the bonding interface takes place during the bonding process. Different curvatures of the cylinder, which induces different initial bows of the wafers, were employed as can be seen in Table 1.

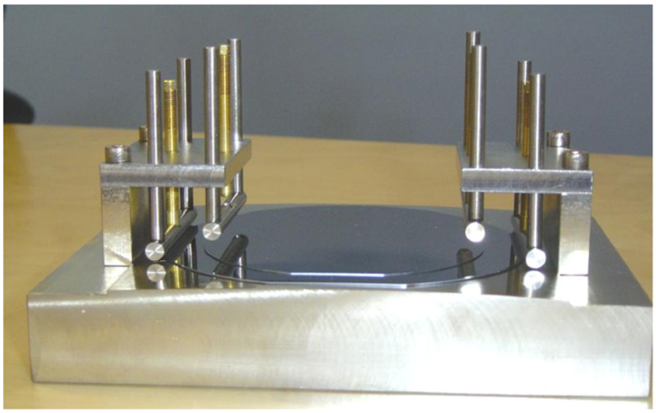

Fig. 1. Bonding setup for the realization of uniaxial strain over the entire wafer area.

Table 1
Design parameters of the bonding setup for realising uniaxially strained Si

Radius of curvature/m	Bow theory		Bow experiment
	On 4″ length/mm	On 1″ length/µm	On 1″ length/µm
1	1.25	78.1	55
0.75	1.67	104.2	70
0.5	2.5	156.2	Not measured

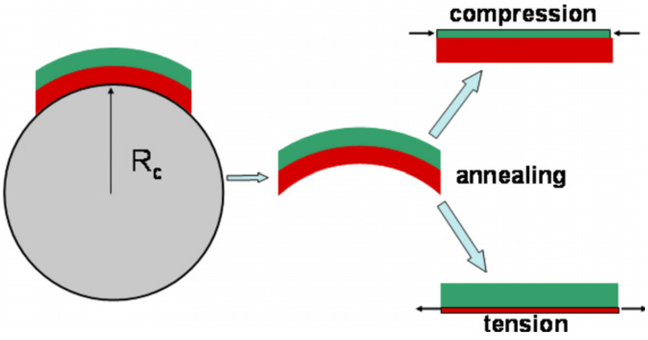

Fig. 2. Sketch of the concept for realising uniaxial strain at wafer-level.

The concept of realising uniaxial strain on wafer-level is shown schematically in Fig. 2. The thinning of one of the wafers is essential to transfer a large fraction of the strain energy that is stored in the both starting wafers and to exploit the resulting strain in devices. The thinning by grinding and etch-back is difficult to be carried out for bent wafers. Thus, thinning by splitting one of the wafers by the smart-cut process [9] was used. The smart-cut process relies on high dose hydrogen implantation induced splitting of a thin slice off a wafer which stays attached to another wafer when bonded. Smart-cut of bent wafers requires implantation of one of the wafers prior to bending and bonding. Annealing is needed to increase the bond strength without initiating the blistering of the implanted wafer. Essentially, smart-cut of bent wafers resembles smart-cut of flat wafers. The experimental conditions used for the experiments shown in this paper, correspond to the realisation of tensile strain. The smart-cut experiments to thin down the implanted 4-in. wafers by splitting were carried out by annealing the bonded wafers after release from the bonding machine for 1 h at 500 °C.

The measurements of the wafer bow in the bent state were carried out using a Tencor line scan profilometer. The Raman measurements were performed by means of a LabRam HR800 UV spectrometer (from Horiba Jobin Yvon) equipped with a liquid nitrogen cooled CCD detector (2048 × 512 pixels) and a 2400 grooves mm^{-1} grating. The 325 nm emission line of a He–Cd laser was used for excitation. In order to smooth the surface damage induced by implantation, the samples were dipped in a solution of tetra-methyl ammonium hydroxide for 60 s after splitting and before the Raman measurements.

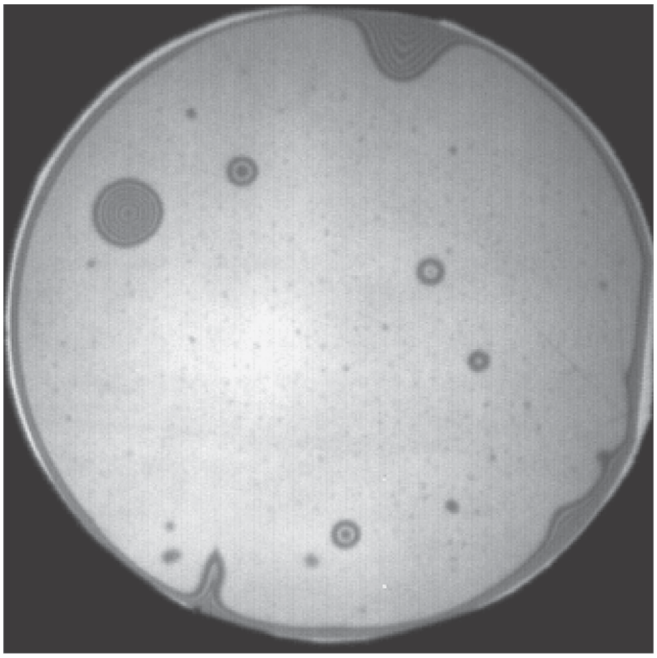

Fig. 3. Infrared transmission image of a bonded pair after annealing and release from the bonding machine. The image shows just the area of the 3-in. wafer.

3. Results and discussion

The bonded interfaces were investigated by infrared (IR) transmission imaging after annealing and releasing the bonded wafers from the bonding setup. A typical interface of a bonded wafer pair in the bent state is shown in Fig. 3. A few voids were detected at the bonded interface. The voids might be caused by the presence of some particles at the Si surfaces (the wafers were cleaned in a cleanroom, but the bonding process was not carried out in cleanroom environment) preventing the bonding to be realised on the whole area.

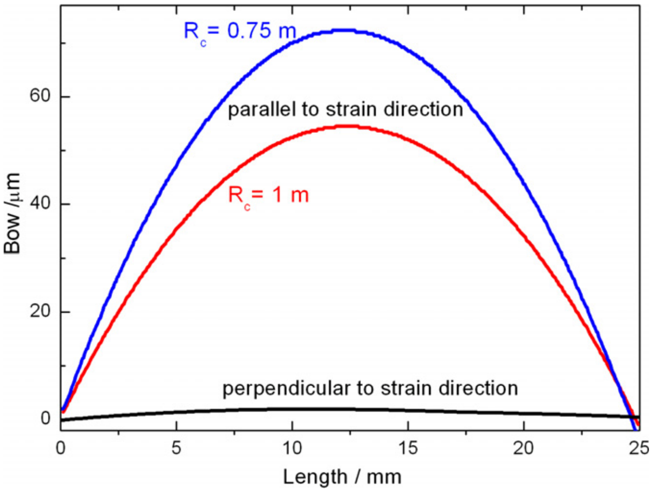

Fig. 4. Bow profiles of uniaxially bent bonding pairs for curvatures of 0.75 m and 1 m. The measurement was performed over a 1-in. lateral scan, parallel and perpendicular to the strain direction.

In Fig. 4 the bow curves of the bent wafers after releasing from the bonding machine are shown. It is obvious that the bow is much larger in the bending direction ([1 1 0] wafer direction) compared with the bow on the direction perpendicular to it, suggesting the expected uniaxial distribution of the strain. Wafer bows of $\sim$55 µm and $\sim$70 µm were obtained on a linear scan length of 1-in. for curvature radius of 0.75 m and 1 m, respectively. When comparing with the theoretical values from Table 1 it is evident that the bonded wafers keep most of the bow induced by the bending even after release from the bonding setup. The smaller bow values found in the experiments can be due to the fact that the edges of the 4-in. wafer are not attached to the smaller 3-in. wafer.

To transfer a large fraction of the strain energy that is stored in the bent handle wafer the splitting was realised by annealing at 500 °C for 1 h. After splitting a thin layer from the 4-in. wafer is transferred to the 3-in. wafer taking over the stored energy and becoming uniaxially strained in tension. The strain in the thin transferred Si layers ($\sim$0.5 µm) was investigated by UV micro-Raman measurements. The 325 nm UV laser line used for the Raman measurements has a penetration depth of $\sim$9 nm into Si. Thus the Raman spectra will show the strained Si phonon peak from the transferred Si layer without any signal from the underlying Si substrate. The FEM simulation discussed later on indicates that the strain gradient in the direction perpendicular to the surface is negligible. In so far, it can be assumed that the results of the surface sensitive Raman investigation is representative for the sSi film in general.

Fig. 5 shows the Raman spectra for unstrained bulk Si and uniaxial strained Si obtained after splitting of the bonded wafers for the samples corresponding to a curvature radius of the bending cylinder of 1 m, 0.75 m, and 0.5 m, respectively. To determine the Si peak position accurately, the plasma line of the He–Cd laser at 854.73 cm^{-1} was used as a reference. The plasma lines can be used for calibration since they are Rayleigh scattered and thus insensitive to stress in materials [10]. The peak positions in the Raman spectra were fitted with a Gauss–Lorentz function using the Labspec software provided by the equipment manufacturer. It can clearly be seen that the Si peak for the strained Si samples are down shifted with respect to the Si peak in bulk Si. The calculated shifts were 0.16 cm^{-1}, 0.23 cm^{-1}, and 0.3 cm^{-1} for the samples corresponding to a curvature radius of the bending cylinder of 1 m, 0.75 m, and 0.5 m, respectively. By measuring five different points on the wafer the statistical error in determining the shifts was found to be $\sim$0.06 cm^{-1}, which suggests homogeneous strain on the wafer.

The strain in the Si layer may be calculated from the Si peak position. A tensile strain will result in a down shift of the strained silicon peak compared to the peak position for bulk Si. According to De Wolf [11] the uniaxial stress can be calculated from the Raman shift from the relation: $\sigma/\mathrm{MPa} = -434 \cdot \Delta\omega/\ \mathrm{cm}^{-1}$. Considering the relation between stress (σ) and strain (ε): $\varepsilon = \sigma/E$, where E is the Young's

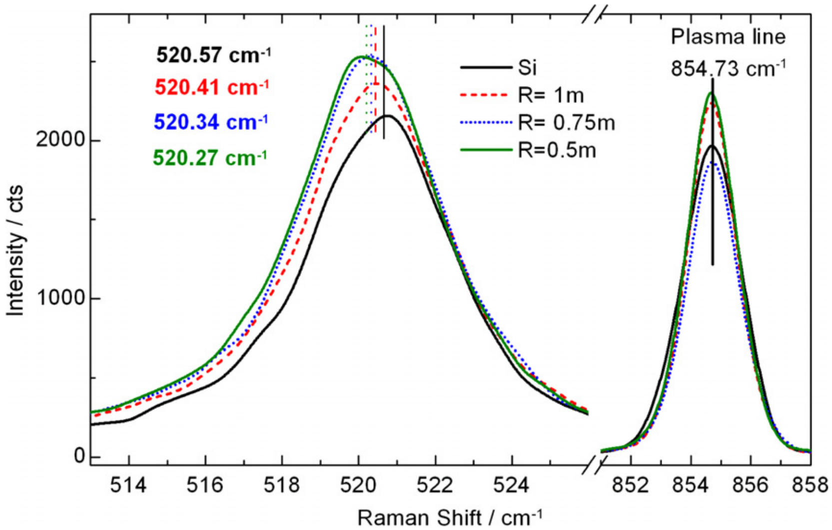

Fig. 5. Raman spectra for Si bulk and uniaxial strained Si samples corresponding to curvature radius of 1 m, 0.75 m, and 0.5 m.

modulus, the strain can be calculated from the Raman shift as follows:

$$\varepsilon/\% = -0.256 \cdot \Delta\omega/\mathrm{cm}^{-1}$$

where $\Delta\omega$ represent the shift of the Si peak positions in cm^{-1} for strained Si compared to unstrained bulk Si and ε is the strain in percents.

Strain values of 0.041%, 0.058%, and 0.077% were calculated from the Raman shift for the uniaxially strained Si samples corresponding to a curvature radius of the bending cylinder of 1 m, 0.75 m, and 0.5 m, respectively. The dependence of the strain values on the curvature radius is plotted in Fig. 6 by squared symbols.

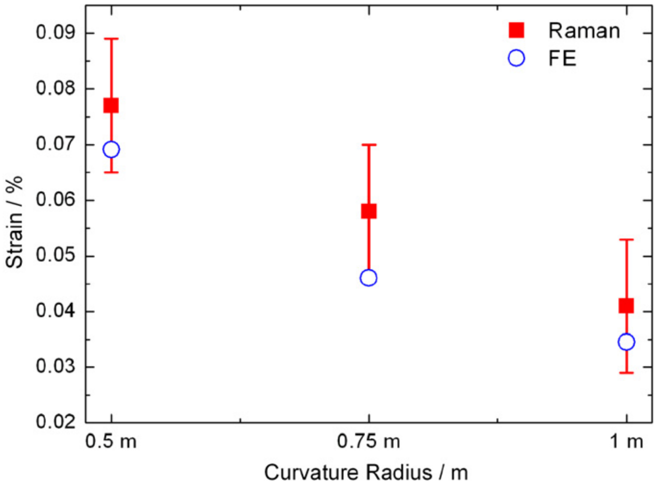

Fig. 6. Comparison of the strain values obtained from Raman measurements (squares) and finite element calculations (circles).

3.1. Finite elements calculations

Numerical simulations of the three-dimensional strained state of the bending, bonding and thinning process were carried out using 3D finite elements with the commercially available program ANSYS. Strain energy is stored in both the bent wafers. After bonding and thinning one of the wafers the strain energy stored in the bent wafer pair is transferred to the thin layer. The final strain distributions

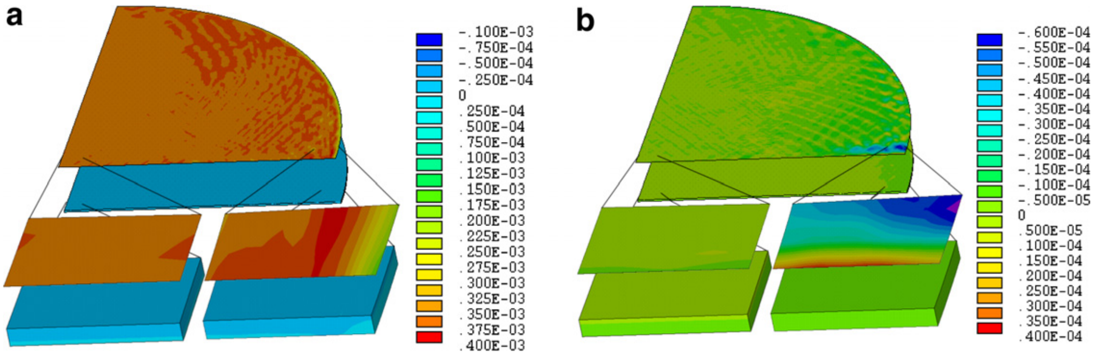

Fig. 7. Strain distributions (absolute values) obtained from FE calculations for a thin Si layer transferred to a Si wafer along the x-direction (parallel to the [1 1 0] wafer direction) (a) and along the y-direction (perpendicular to the [1 1 0] wafer direction) (b). The calculations correspond to an initial radius of curvature of 1 m.

(absolute values) in the thin transferred layer and the handle wafer are shown in Fig. 7a along the *x*-direction and in Fig. 7b along the *y*-direction for a sample corresponding to an initial radius of curvature of a 1 m. The *x*-direction is parallel to the [1 1 0] wafer direction and the *y*-direction is perpendicular to it. The upper layers show the strain distributions in the thin transferred sSi layer, while the lower layers show the strain distributions in the handling wafer. For a better visualisation, the areas indicated at the centre and the edge of the wafers are also shown at a larger magnification. An essentially uniaxial strain distribution is obtained in the thinned wafer, as shown in Fig. 7. The strain is concentrated in the thin transferred layer with the handle wafer being almost strain free. A large area of the thin layer is homogeneously strained with some minor edge effects.

The FE calculations were performed for all three curvature radii used in the experiments. The average strain values (in percentages) obtained in the thin transferred layers from FE calculations are indicated by circles in Fig. 6. There is a good agreement in terms of average strain between the experimental and calculated values, the calculated values lying within the error bars of the experimentally determined strain values.

4. Conclusions

A concept and experimental realisation to obtain wafer-level uniaxial strain was presented in this paper. Uniaxial straining of Si wafers was realised by mechanical bending over a cylinder, wafer bonding and layer splitting. After annealing and releasing from the bonding setup, the bonded wafers kept most of the bow induced by the bending. The layer transfer of uniaxially strained Si was realised using the smart-cut approach. UV micro-Raman spectroscopy was used to determine the uniaxial strain in the transferred layer. The strain values obtained from the Raman measurements are in good agreement with those obtained from 3D finite elements calculations. Further experiments with oxidized silicon handle wafers are needed to optimize the layer transfer process and to create uniaxial strained silicon-on-insulator wafers.

Acknowledgements

The experiments were financially supported by the German Federal Ministry of Education and Research (BMBF) in the framework of the TeSiN/TESIN+ Project (Contract No. V03110).

References

[1] <www.intel.com>.

[2] Celler GK, Cristoloveanu S. J Appl Phys 2003;93:4955–78.

[3] Fitzgerald EA, Xie Y-H, Green ML, Brasen D, Kortan AR, Michel J, et al. Appl Phys Lett 1991;59:811–3.

[4] Welser J, Hoyt JL, Takagi S, Gibbons JF. IEDM 1994;94:373–6.

[5] Rim K, Chu J, Chen H, Jenkins KA, Kanarsky T, Lee K. In: Symp VLSI Tech Dig; 2002. p. 98–9.

[6] Thompson SE, Armstrong M, Auth C, Cea S, Chau R, Glass G, et al. IEEE Electr Dev Lett 2004;25:191–3.

[7] Haugerud BM, Bosworth LA, Belford RE. J Appl Phys 2003;94:4102–4.

[8] Belford RE. US patent, No. 6,455,397 B1; 2002.

[9] Bruel M et al., In: IEEE international SOI conference proceedings, New York, USA; 1995. p. 178–9.

[10] De Wolf I. Semicond Sci Technol 1996;11:139–54.

[11] De Wolf I. J Raman Spectros 1999;30:877–83.

APPLIED PHYSICS LETTERS **90**, 021902 (2007)

Strain relaxation in nanopatterned strained silicon round pillars

C. Himcinschi,[a] R. Singh, I. Radu, A. P. Milenin, W. Erfurth, M. Reiche,
U. Gösele, and S. H. Christiansen
Max Planck Institute of Microstructure Physics, Weinberg 2, 06120 Halle, Germany

F. Muster and M. Petzold
Fraunhofer Institute for Mechanics of Materials, Heideallee 19, 06120 Halle/Saale, Germany

(Received 6 November 2006; accepted 11 December 2006; published online 8 January 2007)

Periodic arrays of strained Si (*s*Si) round nanopillars were fabricated on *s*Si layers deposited on SiGe virtual substrates by electron-beam lithography and subsequent reactive-ion etching. The strain in the patterned *s*Si nanopillars was determined using high-resolution UV micro-Raman spectroscopy. The strain relaxes significantly upon nanostructuring: from 0.9% in the unpatterned *s*Si layer to values between 0.22% and 0.57% in the round *s*Si pillars with diameters from 100 up to 500 nm. The strain distribution in the *s*Si nanopillars was analyzed by finite element (FE) modeling. The FE calculations confirm the strain relaxation after patterning, in agreement with the results obtained from Raman spectroscopy. © *2007 American Institute of Physics*.

[DOI: 10.1063/1.2431476]

Strain-relaxed SiGe virtual substrates offer an attractive platform to utilize tensile strain in epitaxially grown Si overlayers due to the fact that they provide a larger lattice constant than silicon.[1] If thin Si layers are grown on strain-relaxed SiGe, the electron and hole mobilities increase due to the effective mass reduction and the band structure modification induced by strain.[2,3]

The enhanced carrier mobility in strained Si (*s*Si) layers will increasingly be exploited in future complementary metal-oxide-semiconductor technology nodes for which many transistor dimensions lie well in the nanometric range. Since the band structure engineering to improve device performance is based on strain engineering, it is essential to retain the strain in the layers and structures during various processing steps that are required by the technology. Consequently, the behavior of the strain state of *s*Si layers after nanopatterning is of significant technological importance.

UV micro-Raman spectroscopy is a viable, nondestructive, and sensitive method to study the local strain in Si microelectronic devices.[4,5] With the continuing miniaturization of the microelectronic devices, the use of UV lasers for Raman spectroscopy has been proven to have significant advantages over the conventional visible lasers.[6,7] The reduced penetration depth of UV light in Si improves considerably the detection of the strain localized close to Si surface.

In the present work the strain relaxation in round *s*Si nanopillars was examined. The strain values and the strain distribution in the patterned *s*Si pillars with different dimensions were determined by means of UV-Raman spectroscopy and three-dimensional (3D) finite element (FE) modeling.

Biaxially tensile strained Si was epitaxially grown on strain-relaxed $Si_{0.78}Ge_{0.22}$ virtual substrates which consist of an ~2 μm thick compositionally graded buffer layer followed by a relaxed SiGe layer having a comparable thickness of ~2 μm grown on Si (100) wafer. The *s*Si layer is thin enough (~17 nm) not to be relaxed by misfit dislocations to form at the SiGe/*s*Si interface. Round *s*Si pillars with diameters from 100 to 500 nm were patterned by means of electron-beam lithography (EBL) with a periodicity of 500 nm on 250×250 μm^2 fields. After EBL exposure and development of the unexposed negative resist, the samples were etched by means of reactive-ion etching. The space between the *s*Si nanostructures was etched into the SiGe layer to a depth of ~80 nm.

The Raman measurements were performed by means of a LabRam HR800 UV spectrometer (from Horiba Jobin Yvon). A He–Cd laser with a wavelength of 325 nm was used for excitation. The diameter of the incident laser beam on the sample was ~1.5 μm and the power measured under the microscope objective was ~2 mW. By reducing the power ten times we found out that the *s*Si phonon position is shifted up by ~0.35 cm^{-1}, while the phonon position of the bulk Si is not changed. The influence of the laser power on the *s*Si Raman shift is related to the annealing effects being induced by the different expansion coefficients of Si and SiGe. In the results presented in this letter this effect was always taken into consideration and corrected. The peak positions in the Raman spectra were fitted with a Gauss-Lorentz function using the LABSPEC software provided by the equipment manufacturer.

Figures 1(a) and 1(b) show the scanning electron microscopy (SEM) images of round *s*Si pillars with diameters of 100 and 500 nm, respectively. The dotted circle in the same figure shows an estimate of the laser spot size. Since the dimension of the laser spot is larger than that of the patterned

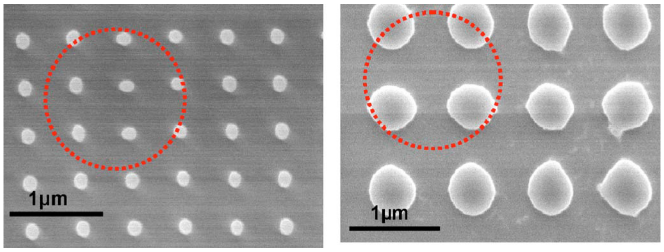

FIG. 1. (Color online) SEM images of patterned round *s*Si pillars with diameters of 100 and 500 nm, respectively. The dotted circles give an estimate of the laser spot size.

---

[a] Electronic mail: cameliu@mpi-halle.de

0003-6951/2007/90(2)/021902/3/$23.00

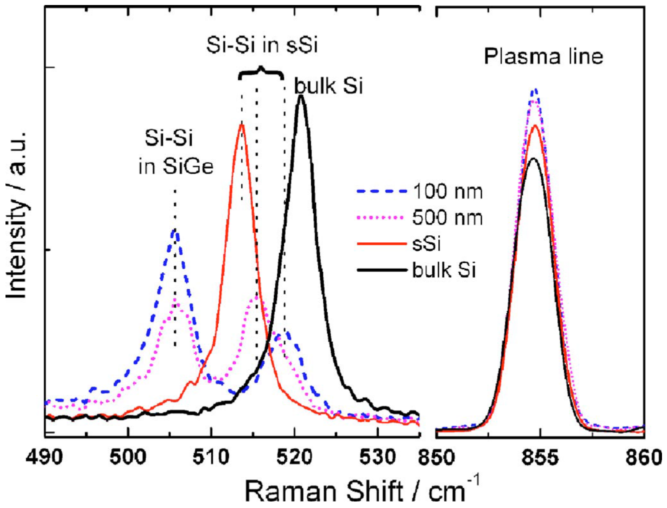

FIG. 2. (Color online) Typical UV-Raman spectra measured for bulk Si (thick line), unpatterned *s*Si (thin line), and for patterned round *s*Si pillars with diameters of 100 nm (dashed line) and 500 nm (dotted line).

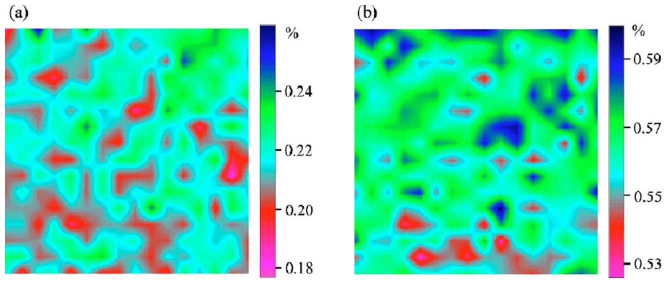

FIG. 3. (Color online) Strain distribution determined by Raman mapping ($3\times 3\ \mu m^2$) for patterned round *s*Si pillars with diameters of 100 nm (a) and 500 nm (b), respectively.

pillars, each single Raman measurement contains contributions from more than one pillar and from the SiGe virtual substrate layer between pillars.

Typical UV-Raman spectra measured for bulk Si, unpatterned *s*Si, and for patterned round *s*Si pillars with diameters of 100 and 500 nm are presented in Fig. 2. To determine the *s*Si peak position accurately, the plasma line of the HeCd laser at 854.7 cm^{-1} was used as a reference because it is independent of temperature and strain. Therefore, the plasma lines can be used for calibration.[4] The Raman spectra of the bulk Si and unpatterned *s*Si show besides the plasma line, the Si phonon in bulk and *s*Si at ~520.8 cm^{-1} and at ~513.5 cm^{-1}, respectively. After calibrating a spectrum with respect to the plasma line position, the strain in the Si layer may be calculated from the *s*Si peak position. The strain in the *s*Si can be calculated from the empirical formula[8,9]

$$\varepsilon = 0.123(\omega_{\text{bulk Si}} - \omega_{\text{strained Si}}), \tag{1}$$

where ω represent the peak positions in cm^{-1} for strained and bulk Si, 0.123 is the inverse strain-phonon coefficient in cm, and ε is the strain in %. Thus, tensile strain will result in a shift of the Si phonon band to lower frequencies. For the unpatterned *s*Si sample the shift of the Si phonon peak position corresponds to a strain of ~0.9%.

The spectra of the samples patterned with round *s*Si nanopillars show two distinctive peaks: one at ~505 cm^{-1} that originates from the Si–Si vibrational mode in SiGe and the other at ~515–519 cm^{-1} that originates from the Si phonon in *s*Si. The shift of the Si phonon in the patterned samples with respect to unpatterned *s*Si samples, as seen in Fig. 2, indicates that the strain in the patterned *s*Si pillars is partially relaxed.

Moving the sample under the microscope by means of a motorized *XY* table, the Si phonon frequency can be determined as a function of position on the samples. For each single point on the sample surface the Raman frequency of the Si was determined after correcting for the plasma line position.[10] The values of the Raman shifts for each single point of the mapped region were converted into strain values using Eq. (1). Figure 3 shows the strain distribution determined from the Raman mapping ($3\times 3\ \mu m^2$) for patterned round *s*Si pillars with diameters of 100 and 500 nm, respectively. Since the laser probes more than one pillar in every single measurement (cf. Fig. 1), the measured strain is averaged for all the probed pillars. Due to the large beam size, the round *s*Si pillars could not be spatially resolved in the strain distribution mapping even though the step of the *XY* table movement was only 0.2 μm.

The average strain in the round *s*Si pillars with diameters from 100 up to 500 nm varies from 0.22% to 0.57%. The strain values measured by Raman mapping for patterned round *s*Si pillars with diameters ranging from 100 to 500 nm are shown in Fig. 4 by triangles and are compared with the strain value in the unpatterned *s*Si sample. The standard deviation determined from the statistical analysis of the few hundred points measured for each mapping was between 0.01% and 0.015%. This results in the error bars to reside within the dimensions of the triangular markers in Fig. 4.

Numerical simulations of the strain states of the round pillars were carried out using 3D finite elements with the commercially available software ANSYS. The strain of the unpatterned *s*Si layer on the virtual SiGe substrate was initialized to the measured value of 0.9%. Further, a model representing the patterned round pillars was build and the strain distribution within the pillars was calculated. In Fig. 5 the strain distribution obtained by FE simulations within a round *s*Si pillar with a diameter of 100 nm along the radial and tangential polar coordinates is shown. The calculated strain distributions show that the strain relaxes nearby the free surfaces and remains concentrated at the interface be-

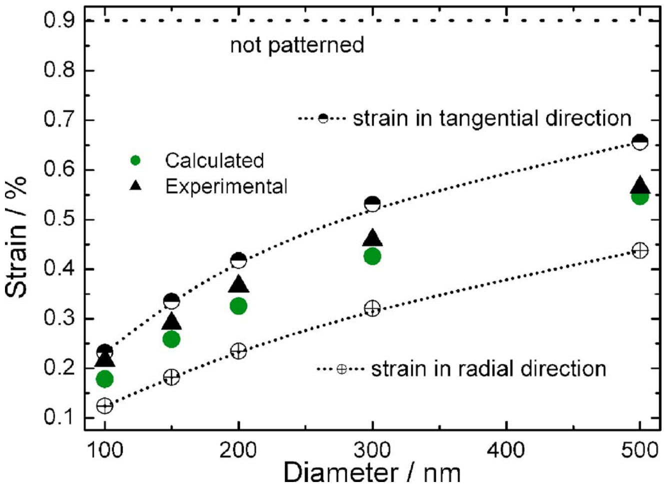

FIG. 4. (Color online) Comparison of the strain values measured by Raman (triangles) and calculated by finite element modeling (circles) for patterned round *s*Si pillars with diameters from 100 to 500 nm.

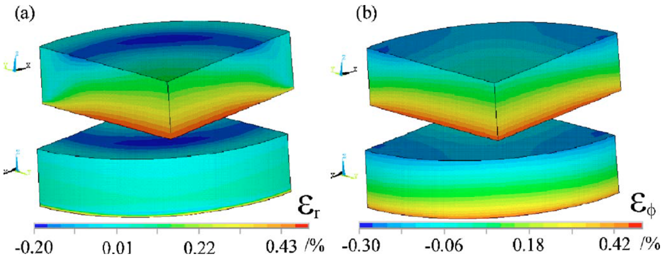

FIG. 5. (Color online) Strain distribution obtained from finite element calculations within a round *s*Si pillar with a diameter of 100 nm on the radial (a) and tangential (b) polar coordinates.

tween the *s*Si layer and SiGe virtual substrate. Similar effects were observed in the case of rectangular *s*Si pillars patterned directly on a silicon dioxide layer.[11]

The FE calculations were performed for pillar diameters ranging from 100 to 500 nm. The calculated average strain values of the *s*Si pillars are shown in Fig. 4 by circular markers. In the same figure the calculated strain values on the tangential and radial directions are shown. The strain measured by Raman mapping represents an average for different spatial orientations and cannot be resolved along the directions on which the FE calculations were done. However, there is a good agreement between the average strain values measured by UV-Raman and calculated by FE, as seen in Fig. 4.

Obviously, a substantial relaxation of the strain upon nanopatterning of *s*Si layers can be observed. The smaller the nanostructure, the larger is the strain relaxation. From the initial strain of ~0.9%, 37% is relaxed in the case of 500 nm diameter pillars and ~75% in the case of 100 nm diameter pillars. The strain relaxation is mediated by the large free surface area of the nanopillars.

In conclusion round nanopillars of *s*Si were fabricated onto fully relaxed $Si_{0.78}Ge_{0.22}$ (SiGe) layers and investigated by means of UV micro-Raman spectroscopy. The strain values measured by Raman spectroscopy are in good agreement with those obtained from 3D FE calculations. The strain distributions obtained by Raman mapping show that the strain in the patterned *s*Si pillars relaxes partially. The relaxation of the strain takes place at the free surfaces and depends on the size of the nanopillars. Since the strain relaxation may critically influence the strain engineering it should be taken into account when designing chips with devices in the nanometer dimensions.

The authors would like to thank D. Webb (International Rectifier Epi Services) for supplying the virtual substrates created by the SiGe grading process. They are thankful to U. Doss for the EBL. The experiments were financially supported by the German Federal Ministry of Education and Research (BMBF) in the framework of the TeSiN project (Contract No. V03110).

[1] E. A. Fitzgerald, Y.-H. Xie, M. L. Green, D. Brasen, A. R. Kortan, J. Michel, Y.-J. Mii, and B. E. Weir, Appl. Phys. Lett. **59**, 811 (1991).
[2] M. T. Currie, C. W. Leitz, T. A. Langdo, G. Taraschi, and E. A. Fitzgerald, J. Vac. Sci. Technol. B **19**, 2268 (2001).
[3] D. K. Nayak and S. K. Chun, Appl. Phys. Lett. **64**, 2514 (1994).
[4] I. De Wolf, Semicond. Sci. Technol. **11**, 139 (1996).
[5] I. De Wolf, Spectroscopy Europe **15**, 6 (2003).
[6] K. F. Dombrowski, I. De Wolf, and B. Dietrich, Appl. Phys. Lett. **75**, 2450 (1999).
[7] K. F. Dombrowski, B. Dietrich, I. De Wolf, R. Rooyackers, and G. Badenes, Microelectron. Reliab. **41**, 511 (2001).
[8] J. C. Tsang, P. M. Mooney, F. Dacol, and J. O. Chu, J. Appl. Phys. **75**, 8098 (1994).
[9] T. A. Langdo, M. T. Currie, A. Lochtefeld, R. Hammond, J. A. Carlin, M. Erdtmann, G. Braithwaite, V. K. Yang, C. J. Vineis, H. Badawi, and M. T. Bulsara, Appl. Phys. Lett. **82**, 4256 (2003).
[10] C. Himcinschi, I. Radu, R. Singh, W. Erfurth, A. P. Milenin, M. Reiche, S. H. Christiansen, and U. Gösele, Mater. Sci. Eng., B **135**, 184 (2006).
[11] R. Z. Lei, W. Tsai, I. Aberg, T. B. O'Reilly, J. L. Hoyt, D. A. Antoniadis, Henry I. Smith, A. J. Paul, M. L. Green, J. Li, and R. Hull, Appl. Phys. Lett. **87**, 251926 (2005).

ELSEVIER

Materials Science and Engineering B 135 (2006) 184–187

MATERIALS SCIENCE & ENGINEERING B

www.elsevier.com/locate/mseb

Relaxation of strain in patterned strained silicon investigated by UV Raman spectroscopy

C. Himcinschi *, I. Radu, R. Singh, W. Erfurth, A.P. Milenin, M. Reiche, S.H. Christiansen, U. Gösele

Max Planck Institute of Microstructure Physics, Weinberg 2, 06120 Halle, Germany

Abstract

Tensile strained Si (sSi) layers were epitaxially deposited onto fully relaxed $Si_{0.78}Ge_{0.22}$ (SiGe) epitaxial layers (4 μm) on silicon substrates. Periodic arrays of 150 nm × 150 nm and 150 nm × 750 nm pillars with a height of 100 nm were fabricated into the sSi and SiGe layers by electron-beam lithography and subsequent reactive ion etching. The strain in the patterned and unpatterned samples was analyzed using high-resolution UV micro-Raman spectroscopy. The 325 nm excitation line used probes strain in Si close to the surface (penetration depth of ~9 nm). The Raman measurements revealed that the nano-patterning yields a relaxation of strain of ~33% in the large pillars and ~53% in the small pillars of the ~0.95% initial strain in the unpatterned sSi layer.

Keywords: Strained silicon; Raman spectroscopy; Strain relaxation; SiGe

1. Introduction

Virtual substrates composed of strain-relaxed graded SiGe-layers on Si(1 0 0) offer an attractive platform for building strained Si-based microelectronic devices [1]. The relaxed SiGe layers have a larger lattice constant than Si, so that the epitaxy of thin pseudomorphic Si layers yields biaxial tensile strain in the epitaxial layer. Biaxial tensile strain of the order of ~1% in silicon increases the electron and hole mobilities due to the effective mass reduction and the band structure modification induced by strain [2–4].

The enhanced carrier mobility in strained Si (sSi) layers will be exploited in future complementary metal-oxide-semiconductor (CMOS) technology nodes for which many transistor dimensions lie well in the nanoscale range. Since the band engineering in such devices is almost exclusively strain induced it is very important to retain the strain in the Si layer during various processing steps. Consequently, the behaviour of the strained state of sSi layers after nanopatterning is of significant technological importance.

UV micro-Raman spectroscopy is a viable, non-destructive, and sensitive tool to study the strain in Si microelectronic devices [5,6]. With the continuing miniaturisation of the microelectronic devices, the use of UV lasers for Raman spectroscopy has been proved to have significant advantages over the conventional visible lasers [7,8]. The reduced penetration depth of UV light in Si improves considerably the detection of the strain localised close to Si surface.

In the present study UV micro-Raman spectroscopy was employed to investigate the strain distribution in Si layers deposited on SiGe strain-relaxed virtual substrates. The evolution of the strain in patterned sSi nanostructures with different dimensions was analyzed.

2. Experimental

Biaxially tensile strained Si was epitaxially grown on strain-relaxed $Si_{0.78}Ge_{0.22}$ virtual substrates. The virtual substrates were grown on Si(1 0 0) wafers using reduced pressure chemical vapour deposition (RPCVD) method and consist of a 2 μm thick compositionally graded buffer layer followed by a relaxed SiGe layer having the same thickness. The strained Si cap layer is thin enough (~17 nm) to be free of dislocations and fully strained.

sSi pillars of 150 nm × 150 nm and 150 nm × 750 nm were patterned by means of electron beam lithography (EBL) with a periodicity of 500 nm on 100 μm × 100 μm fields. EBL was carried out in a JEOL JSM 6400 scanning electron microscope (SEM) equipped with a LaB6 cathode and an EBL equipment

---

[*] Corresponding author. Tel.: +49 345 5582 912; fax: +49 345 5511 223.
E-mail address: cameliu@mpi-halle.de (C. Himcinschi).

0921-5107/$ – see front matter © 2006 Elsevier B.V. All rights reserved.
doi:10.1016/j.mseb.2006.08.023

(ELPHY plus) of the Raith GmbH. A negative resist (AR-N 7500) on the basis of polymethyl methacrylate (PMMA) was used. Marker structures (double cross with micrometer dimensions) were patterned in addition nearby the fields of nanostructures, for an easier detection of the patterned fields. After EBL exposure and development of the unexposed negative resist, the samples were etched by means of reactive ion etching (RIE) using an Oxford Plasma Lab System 100 machine equipped with an ICP 380 source. The octafluorocyclobutane and argon gas mixture was used during plasma etching process. The space between the sSi nanostructures was etched into the SiGe layer to a depth of ~80 nm. Finally the remaining exposed resist on the patterned sSi structures was chemically removed.

The Raman measurements were performed by means of a LabRam HR800 UV spectrometer (from Horiba Jobin Yvon) equipped with a liquid nitrogen cooled CCD detector (2048 × 512 pixels) and a 2400 grooves mm^{-1} grating. The 325 nm emission line of a He–Cd laser was used for excitation in a backscattering geometry with both the incident and the scattered beam passing the microscope's objective. A 40× UV objective was used to focus the laser to a diameter of ~1.5 μm on the sample surface. Each spectrum was obtained at room temperature by averaging two spectra recorded for 30 s each. The peak positions in the Raman spectra were fitted with a Gauss–Lorentz function using the Labspec software provided by the equipment manufacturer.

3. Results and discussions

Fig. 1a shows the atomic force microscopy (AFM) image (40 μm × 40 μm) of the unpatterned sSi layer on the virtual substrate. Periodically alternating structures are observed. This wavy morphology known as crosshatch pattern [9] arises from the misfit dislocations in SiGe when grown on the lattice mismatched Si(1 0 0) substrates [10].

Biaxial tensile strain in Si results in a shift of the Raman peak towards lower frequencies compared to unstrained bulk Si [6]. The 325 nm UV laser line used for the Raman measurements has a penetration depth of ~9 nm into Si. Thus in the case of the unpatterned sample where the thickness of sSi layer is ~17 nm, the Raman spectrum will show just the phonon from the sSi and no signal from the underlying SiGe layer.

To determine the sSi peak position accurately, the plasma line of the He–Cd laser at 854.73 cm^{-1} was used as a reference. The plasma lines can be used for calibration since they are Rayleigh scattered and consequently insensitive to temperature and strain in the material [6].

After calibration of the spectrum with respect to the plasma line position, the strain in the Si layer may be calculated from the sSi peak position. A compressive strain will results in an upward shift of the Raman peak, while tensile stress will result in a down shift [11]. Because of the larger lattice parameter of the SiGe virtual substrate compared to that of Si, the cap Si layer will be tensile strained. Assuming that the SiGe lattice constant changes linearly with the composition, the strain in the Si layer can be calculated from the empirical formula [12,13]:

$$\varepsilon = 0.123(\omega_{\text{bulk Si}} - \omega_{\text{strained Si}}) \tag{1}$$

where ω represents the peak positions (cm^{-1}) for strained and bulk Si, 0.123 is the inverse strain-phonon coefficient (cm), and ε is the strain (%).

Moving the sample under the microscope by means of a motorised *XY* table, the Si phonon position was determined as a function of position on the unpatterned strained Si layer. For each single point the Raman shift of the Si peak was determined after correcting for the plasma line position. The average shift of the strained Si peak with respect to the unstrained bulk Si peak as determined from scanning an area of 40 μm × 40 μm (step width of 1.5 μm) was 7.69 cm^{-1} with a standard deviation of 0.14 cm^{-1}. The values of the shifts for each single point of the mapped region were converted to strain by using Eq. (1).

Fig. 1b shows the strain distribution determined from the Raman mapping on the unpatterned strained Si layer. Crosshatch pattern are clearly observed in the strain distribution similar with those observed in the AFM image. The average strain on the mapped area was determined to be 0.95% with a standard deviation of 0.017%.

Fig. 2 shows the scanning electron microscopy (SEM) images of nanostructured Si pillars with area dimensions of 150 nm × 150 nm (a) and 150 nm × 750 nm (b). The circles in

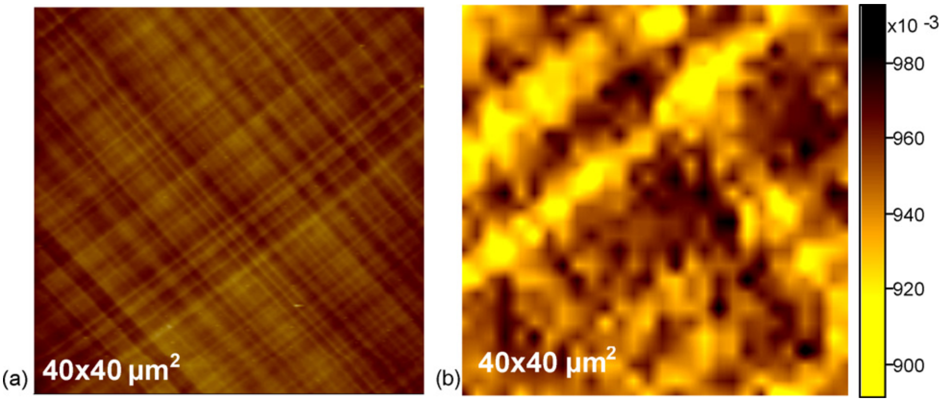

Fig. 1. (a) AFM micrograph (40 μm × 40 μm) of the strained Si layer showing a crosshatch pattern with a RMS roughness of ~2.3 nm. (b) The strain distribution determined by Raman mapping (40 μm × 40 μm) reveals a clear crosshatch pattern in the strain distribution of the strained Si layer. The scale bar represents the strain values in percents.

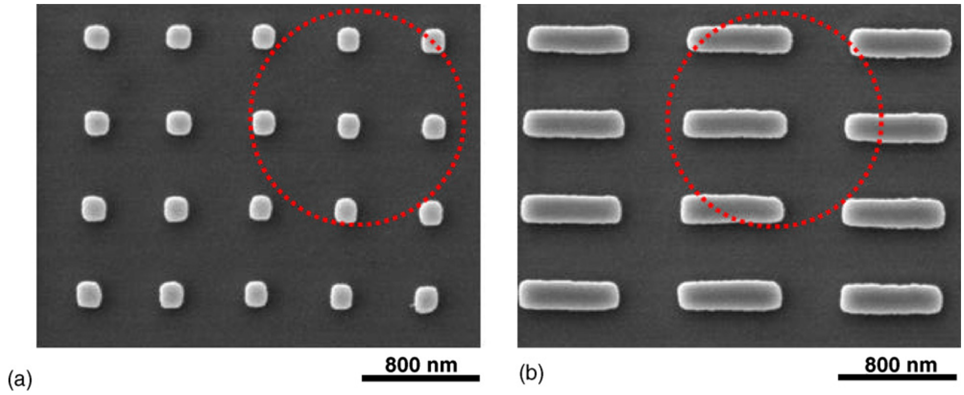

Fig. 2. SEM images of patterned sSi with pillars of 150 nm × 150 nm (a) and 150 nm × 750 nm (b). The circles give an estimation of the laser spot size used for the Raman mapping.

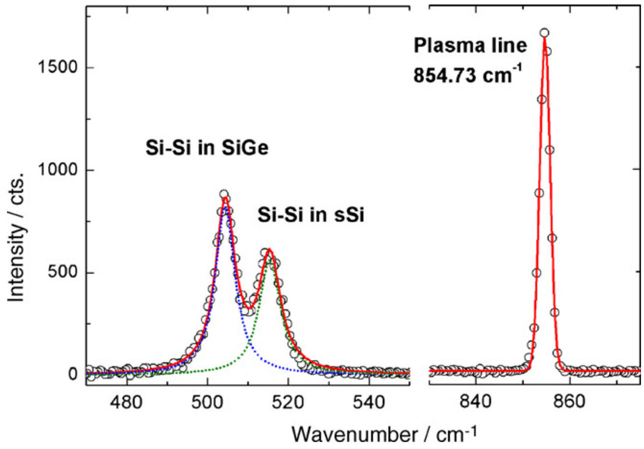

Fig. 3. Typical Raman spectrum obtained from the patterned sSi layer on $Si_{0.78}Ge_{0.22}$ virtual substrate. The peaks at 505 cm^{-1} and 516 cm^{-1} correspond to the Si–Si bands in SiGe and sSi, respectively, while the peak at 854.7 cm^{-1} corresponds to plasma line of the He–Cd laser.

the same figure indicate an estimation of the laser spot size (∼1.5 µm). Since the dimension of the laser spot is larger than the patterned structures, each single Raman measurement contains contributions from the sSi layer that resides close to the surface in the pillars and the relaxed SiGe layer from the virtual substrate in between the pillars.

A typical Raman spectrum measured on the wafer in the area of pillars is presented in Fig. 3. Besides the plasma line, the spectrum shows two distinctive peaks: one at ∼504 cm^{-1} that originates from the Si–Si vibrational mode in SiGe and another at ∼516 cm^{-1} that originates from the Si phonon in sSi.

Raman mappings on the patterned wafer were carried out on areas of 2.5 µm × 2.5 µm with a step between measurements of 0.1 µm. The average shifts of the sSi peaks with respect to the unstrained bulk Si peak were 3.61 cm^{-1} and 5.12 cm^{-1} for the 150 nm × 150 nm and 150 nm × 750 nm sSi pillars, respectively. The strain in the sSi was determined in a similar manner as in the case of unpatterned sSi.

Fig. 4 shows the strain distribution on the patterned sSi layer in the case of 150 nm × 150 nm (a) and 150 nm × 750 nm (b) pillars, respectively. Since the laser beam probes a few pillars within one measurement (cf. Fig. 2) the measured strain is averaged for these pillars. Due to the large beam size, the sSi pillars could not be spatially resolved in the strain distribution mapping even though the step of the *XY* table movement was only 0.1 µm. The average strain in sSi is 0.45% with a standard deviation of 0.015% for the 150 nm × 150 nm pillars and 0.63% with a standard deviation of 0.015% for the 150 nm × 750 nm pillars. Clearly, a relaxation of the strain in the patterned sSi pillars can be observed. The smaller the nanostructures, the larger is the strain relaxation. From the initial strain of ∼0.95%, 33% is relaxed in the case of 150 nm × 750 nm pillars and ∼53% in the

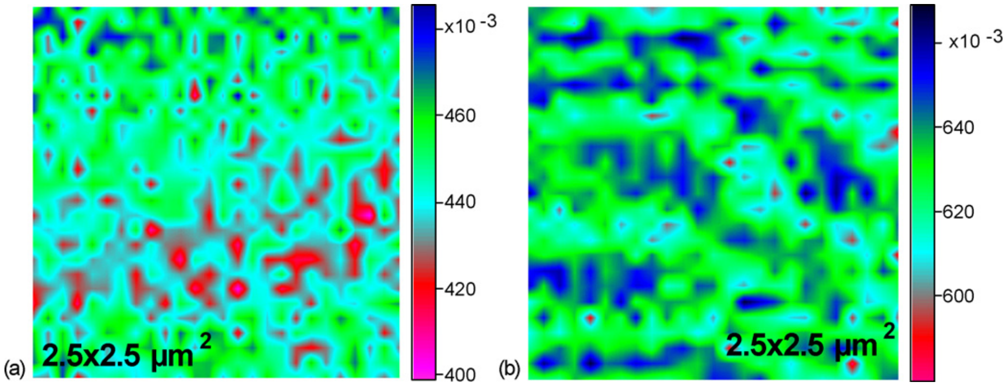

Fig. 4. Strain distribution determined by Raman mapping (2.5 µm × 2.5 µm) for structured sSi with nanopillars of 150 nm × 150 nm (a) and 150 nm × 750 nm (b).

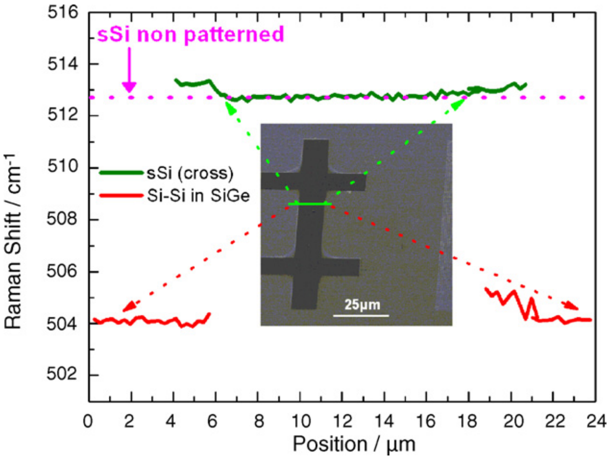

Fig. 5. Results of a Raman line scan across the sSi microstructure marker.

case of 150 nm × 150 nm pillars. The strain relaxation is mediated by the large free surface area at the edges of the pillars.

To easily identify the nanopatterned fields with pillars on the wafer, double-cross markers with micrometer dimensions were patterned close to the fields. Such a marker is shown in the inset of Fig. 5. The Raman line scan across the marker, done as indicated in Fig. 5, shows that the sSi peak is not shifted compared to unpatterned sSi. However, a slight relaxation of the strain can be observed at the free edges of the double-cross structures. These findings indicate that the relaxation of the strain in the case of the pillars is due to the free edges and it is not due to the processing (e-beam lithography, RIE, and resist removal). Outside of the cross-marker the Raman spectra contain only a peak at ∼504 cm^{-1} originating from Si–Si vibrational mode in SiGe.

4. Conclusions

The strain distribution in nanopatterned (pillars with 150 nm × 150 nm and ∼150 nm × 750 nm area dimension) and unpatterned sSi layers epitaxially deposited onto fully relaxed $\mathrm{Si}_{0.78}\mathrm{Ge}_{0.22}$ (SiGe) layers was investigated by means of UV micro-Raman spectroscopy. In the unpatterned layers crosshatch patterns were observed both in the Raman strain distribution and in the AFM images. UV micro-Raman spectroscopy results show that the strain in the patterned sSi pillars partially relaxes. The strain relaxation depends on the nanopattern size and geometry and should be considered in designing the chips since it could critically influence the strain engineering.

Acknowledgements

We would like to thank D. Webb (International Rectifier Epi Services) for supplying the substrates created by the SiGe grading process. We are thankful to U. Doss for EBL. The experiments were financially supported by the German Federal Ministry of Education and Research (BMBF) in the framework of the TeSiN project (contract no. V03110).

References

[1] E.A. Fitzgerald, Y.-H. Xie, M.L. Green, D. Brasen, A.R. Kortan, J. Michel, Y.-J. Mii, B.E. Weir, Appl. Phys. Lett. 59 (1991) 811.
[2] M.T. Currie, C.W. Leitz, T.A. Langdo, G. Taraschi, E.A. Fitzgerald, J. Vac. Sci. Technol. B 19 (2001) 2268.
[3] D.K. Nayak, S.K. Chun, Appl. Phys. Lett. 64 (1994) 2514.
[4] G. Abstreiter, H. Brugger, T. Wolf, H. Jork, H.J. Herzog, Phys. Rev. Lett. 54 (1985) 2441.
[5] I. De Wolf, Spectrosc. Europe 15 (2003) 6.
[6] I. De Wolf, Semicond. Sci. Technol. 11 (1996) 139.
[7] K.F. Dombrowski, B. Dietrich, I. De Wolf, R. Rooyackers, G. Badenes, Microel. Reliability 41 (2001) 511.
[8] B. Dietrich, K.F. Dombrowski, J. Raman Spectrosc. 30 (1999) 893.
[9] S. Kishino, M. Origima, K. Kurata, J. Eletrochem. Soc. 119 (1972) 617.
[10] H. Chen, Y.K. Li, C.S. Peng, H.F. Liu, Y.L. Liu, Q. Huang, J.M. Zhou, Q.K. Xue, Phys. Rev. B 65 (2002) 233303.
[11] I. De Wolf, J. Raman Spectrosc. 30 (1999) 877.
[12] J.C. Tsang, P.M. Mooney, F. Dacol, J.O. Chu, J. Appl. Phys. 75 (1994) 8098.
[13] T.A. Langdo, M.T. Currie, A. Lochtefeld, R. Hammond, J.A. Carlin, M. Erdtmann, G. Braithwaite, V.K. Yang, C.J. Vineis, H. Badawi, M.T. Bulsara, Appl. Phys. Lett. 82 (2003) 4256.

Verzeichnis der wissenschaftlichen Veröffentlichungen (Januar 2020)

Scopus Author Identifier: http://www.scopus.com/authid/detail.uri?authorId=8304651900
(h-index 20, 1243 Citations)

101) H. Zielke, T. Wetzig, **C. Himcinschi**, M. Abendroth, M. Kuna, and C.G. Aneziris
Infuence of carbon content and coking temperature on the biaxial flexural strength of carbon-bonded alumina at elevated temperatures
Carbon 159, 324-332 (2020) **doi: 10.1016/j.carbon.2019.12.042**

100) E. Storti**, C. Himcinschi**, J. Kortus, and C.G. Aneziris
Synthesis and characterization of calcium zirconate nanofibers produced by electrospinning
J. European Ceramic Society 39, 5338-5344 (2019) **doi: 10.1016/j.jeurceramsoc.2019.08.007**

99) E. Zuñiga-Puelles, R. Cardoso-Gil, M. Bobnar, I. Veremchuk, **C. Himcinschi**, C. Hennig, J. Kortus, G. Heide, and R. Gumeniuk
Structural stability and thermoelectric performance of high quality synthetic and natural pyrites
Dalton Trans., 48, 10703-10713 (2019) **doi: 10.1039/c9dt01902b**

98) **C. Himcinschi**, J. Rix, C. Röder, M. Rudolph, M.-M. Yang, D. Rafaja, J. Kortus, and M. Alexe
Ferroelastic domain identification in BiFeO3 crystals using Raman spectroscopy
Scientific Reports 9, 379_1_9 (2019) **doi: 10.1038/s41598-018-36462-5**

97) P. Wyżga, I. Veremchuk, **C. Himcinschi**, U. Burkhardt, W. Carrillo-Cabrera, M. Bobnar, C. Hennig, A. Leithe-Jasper, J. Kortus, and R. Gumeniuk
Indium thiospinel In1−x□xIn2S4 – structural characterization and thermoelectric properties
Dalton Trans., 48, 8350-8360 (2019) **doi: 10.1039/c9dt00890j**

96) U. Kempe, G. Trullenque, R. Thomas, S. Sergeejv, S. Presnyakov, N. Rodionov, **C. Himcinschi**
Substitution-induced internal strain and high disorder in weakly radiation damaged hydrothermal zircon from Mt. Malosa, Malawi
European Journal of Mineralogy 30 (4), 659-679 (2018) **doi: 10.1127/ejm/2018/0030-2739**

95) **C. Himcinschi**, C. Biermann, E. Storti, B. Dietrich, G. Wolf, J. Kortus, C.G. Aneziris
Innovative carbon-bonded filters based on a new environmental-friendly binder system for steel melt filtration
J. European Ceramic Society 38, 5580-5589 (2018) **doi: 10.1016/j.jeurceramsoc.2018.08.029**

94) I. Plesco, J. Strobel, F. Schütt, **C. Himcinschi**, N. B. Sedrine, T. Monteiro, M.R. Correia, L. Gorceac, B. Cinic, V. Ursaki, J. Marx, B. Fiedler, Y.K. Mishra, L. Kienle, R. Adelung and I. Tiginyanu
Hierarchical Aerographite 3D flexible networks hybridized by InP micro/nanostructures for strain sensor applications
Scientific Reports 8, 13880_1_10 (2018) **doi: 10.1038/s41598-018-32005-0**

93) M. Rudolph, A. Salomon, A. Schmidt, M. Motylenko, T. Zienert, H. Stöcker, **C. Himcinschi**, L. Amirkhanyan, J. Kortus, C.G. Aneziris, D. Rafaja
Induced Formation of Transition Aluminas from Boehmite
Advanced Engineering Materials 19, 1700141_1_10 (2017) **doi: 10.1002/adem.201700141**

92) J. Solarek, **C. Himcinschi**, Y. Klemm, C.G. Aneziris, and H. Biermann
Ductile behavior of fine-grained, carbon-bonded materials at elevated temperatures
Carbon 122, 141-149 (2017) **doi: 10.1016/j.carbon.2017.06.041**

91.) I. Lindfors-Vrejoiu, L. Jin, **C. Himcinschi**, J. Engelmayer, F. Hensling, C.-L. Jia, R. Waser, R. Dittmann and P.H.M. van Loosdrecht
Structure and orbital ordering of ultrathin $LaVO_3$ probed by atomic resolution electron microscopy and Raman spectroscopy
physica status solidi (rrl) 11, 1600350 (2017) **doi: 10.1002/pssr.201600350**

90.) U. Kempe, M. Trinkler, A. Pöppl, and **C. Himcinschi**

Coloration of natural zircon
The Canadian Mineralogist 54, 635-660 (2016) **doi: 10.3749/canmin.1500093**

89.) G. Irmer, C. Röder, **C. Himcinschi**, and J. Kortus
Nonlinear optical coefficients of wurtzite-type α-GaN determined by Raman spectroscopy
Phys. Rev. B 94, 195201_1_8 (2016) **doi: 10.1103/PhysRevB.94.195201**

88.) C. Popescu, G. Dorcioman, B. Bita, C. Besleaga, I. Zgura, **C. Himcinschi**, A.C. Popescu
Fabrication of periodical surface structures by picosecond laserirradiation of carbon thin films: transformation of amorphous carbonin nanographite
Applied Surface Science 390, 236–243 (2016) **doi: 10.1016/j.apsusc.2016.08.029**

87.) I. Vrejoiu, **C. Himcinschi**, L. Jin, C.-L. Jia, N. Raab, J. Engelmayer, R. Waser, R. Dittmann and P. H. M. van Loosdrecht
Probing orbital ordering in LaVO3 epitaxial films by Raman scattering
APL Mater. 4, 046103 (2016) **doi: 10.1063/1.4945658**

86.) V. Craciun, D. Craciun, G. Socol, S. Behdad, B. Boesl, **C. Himcinschi**, H. Makino, M. Socol, and D. Simeone
Investigations of Ar ion irradiation effects on nanocrystalline SiC thin films
Applied Surface Science 374, 339–345 (2016). **doi: 10.1016/j.apsusc.2015.12.130**

85.) **C. Himcinschi**, E.J. Guo, A. Talkenberger, K. Dörr, and J. Kortus
Influence of piezoelectric strain on the Raman spectra of $BiFeO_3$ films deposited on PMN-PT substrates
Appl. Phys. Lett. 108, 042902 (2016) **doi: 10.1063/1.4940973**

84.) A.G. Milekhin, L. Sveshnikova, T. Duda, E. Rodyakina, V. Dzhagan, E. Sheremet, O. Gordan, C. Himcinschi, A. Latysheva, D.RT. Zahn
Resonant surface-enhanced Raman scattering by optical phonons in amonolayer of CdSe nanocrystals on Au nanocluster arrays
Appl. Surface Sci. 370, 410 (2016) **doi: 10.1016/j.apsusc.2016.02.185**

83.) A. Talkenberger, I. Vrejoiu, F. Johann, C. Röder, G. Irmer, D. Rafaja, G. Schreiber, J. Kortus and **C. Himcinschi**
Raman spectroscopic investigations of epitaxial $BiFeO_3$ thin films on rare earth scandate substrates
J. Raman Spec. 46, 1245 (2015) **doi: 10.1002/jrs.4762**

82.) A.G. Milekhin, L.L. Sveshnikova, T. A. Duda, E.E. Rodyakina, V. M. Dzhagan, O. D. Gordan, S.L. Veber, **C. Himcinschi**, A.V. Latyshev, and D. R. T. Zahn
Surface-enhanced Raman scattering by colloidal CdSe nanocrystal submonolayers fabricated by the Langmuir–Blodgett technique
Beilstein J. Nanotechnol. 6, 2388 (2015) **doi: 10.3762/bjnano.6.245**

81.) T. Szatkowski, M. Wysokowski, G. Lota, D. Peziak, V.V. Bazhenov, G. Nowaczyk, J. Walter, S.L. Molodstov, H. Stöcker, **C. Himcinschi**, I. Petrenko, A. Stelling, S. Jurga, T. Jesionowski, and H. Ehrlich
Novel Nanostructured Hematite-Spongin Composite Developed using Extreme Biomimetic Approach
RSC Adv. 5, 79031 (2015) **doi: 10.1039/C5RA09379A**

80.) A.C. Popescu, G. E. Stan, L. Duta, C. Nita, C. Popescu, V.A. Surdu, M.A. Husanu, B. Bita, R. Ghisleni, **C. Himcinschi**, and V. Craciun
The Role of Ambient Gas and Pressure on the Structuring of Hard Diamond-Like Carbon Films Synthesized by Pulsed Laser Deposition
Materials 8, 3284-3305 (2015) **doi:10.3390/ma8063284**

79.) **C. Himcinschi**, A. Bhatnagar, A. Talkenberger, M. Barchuk, D.R.T. Zahn, D. Rafaja, J. Kortus, and M. Alexe
Optical properties of epitaxial $BiFeO_3$ thin films grown on $LaAlO_3$
Appl. Phys. Lett. 106, 012908_1-5 (2015) **doi: 10.1063/1.4905443**

78.) T. Deepa Rani, K. Tamilarasan, E. Elangovan, S. Leela, K. Ramamurthi, K. Thangaraj, **C. Himcinschi**, I. Trenkmann, S. Schulze, M. Hietschold, A. Liebig, G. Salvan, D.R.T. Zahn
Structural and optical studies on Nd doped ZnO thin films
Superlattices and Microstructures 77, 325–332, (2015) **doi: 10.1016/j.spmi.2014.10.001**

77.) G. Irmer, C. Röder, **C. Himcinschi**, and J. Kortus
Raman tensor elements and Faust-Henry coefficients of wurtzite-type α-GaN: How to overcome the dilemma of the sign of Faust-Henry coefficients in α-GaN?
J. Appl. Phys. 116, 245702_1-12 (2014) **doi: 10.1063/1.4904841**

76.) M. Wysokowski, M. Motylenko, J. Walter, G. Lota, J. Wojciechowski, H. Stöcker, R. Galli, A.L. Stelling, **C. Himcinschi**, E. Niederschlag, E. Langer, V.V. Bazhenov, T. Szatkowski, J. Zdarta, I. Pertenko, Z. Kljajić, T. Leisegang, S.L. Molodtsov, D.C. Meyer, T. Jesionowski, and H. Ehrlich
Synthesis of nanostructured chitin–hematite composites under extreme biomimetic conditions
RSC Adv. 4, 61743-61752 (2014) **doi: 10.1039/C4RA10017D**

75.) V.M. Dzhagan, M.Ya. Valakh, C. Himcinschi, A.G. Milekhin, D. Solonenko, N.A. Yeryukov, O.E. Raevskaya, O.L. Stroyuk, and D.R.T. Zahn
Raman and Infrared Phonon Spectra of Ultrasmall Colloidal CdS Nanoparticles
J. Phys. Chem. C 118, 19492−19497 (2014) **doi: 10.1021/jp506307q**

74.) B. Mahns, O. Kataeva, D. Islamov, S. Hampel, F. Steckel, C. Hess, M. Knupfer, B. Büchner, **C. Himcinschi**, T. Hahn, R. Renger, and J. Kortus
Crystal Growth, Structure, and Transport Properties of the Charge- Transfer Salt Picene/2,3,5,6-Tetrafluoro-7,7,8,8-tetracyanoquinodimethane
Crystal Growth Design 14, 1338−1346 (2014) **doi: 10.1021/cg401841n**

73.) A. Dorner-Reisel, R. Lieberwirth, S. Svoboda, K. Günther, C. Röder, **C. Himcinschi**, G. Irmer, S. Weißmantel
Wear behaviour of hydrogen free diamond-like carbon thin films in diesel fuel at different temperatures
Diamond & Related Materials 44, 78–87 (2014) **doi: 10.1016/j.diamond.2014.01.013**

72.) V. M. Dzhagan, A. P. Litvinchuk, M. Valakh, M. Kruszynska, J. Kolny-Olesiak, **C. Himcinschi**, and D. R. T. Zahn
Raman scattering in orthorhombic $CuInS_2$ *nanocrystals*
physica status solidi a 211, 195-199 (2014) **doi: 10.1002/pssa.201330229**

71.) C. Röder, T. Weißbach, **C. Himcinschi**, J. Kortus, S. Dudczig, and C.G. Aneziris
Raman spectroscopic characterization of novel carbon-bonded filter compositions for steel melt filtration
J. Raman Spec. 45, 128-132 (2014) **doi: 10.1002/jrs.4426**

70.) G. Irmer, C. Röder, **C. Himcinschi**, and J. Kortus
Phonon polaritons in uniaxial crystals: A Raman scattering study of polaritons in α-GaN
Phys. Rev. B 88, 104303_1-14 (2013) **doi: 10.1103/PhysRevB.88.104303**

69.) C. Röder, F. Lipski, F. Habel, G. Leibiger, M. Abendroth, **C. Himcinschi**, and J. Kortus
Raman spectroscopic characterization of epitaxially grown GaN on sapphire
J. Phys. D: Appl. Phys. 46, 285302_1-7 (2013) **doi:10.1088/0022-3727/46/28/285302**

68.) Alexander G. Milekhin, N.A. Yeryukov, L. Sveshnikova, T.A. Duda, D. Protasov, A.K. Gutakovskii, S.A. Batsanov, N.V. Surovtsev, S.V. Adichtchev, **C. Himcinschi**, V. Dzhagan, F. Haidu, and D.R.T. Zahn
CdZnS quantum dots formed by the Langmuir–Blodgett technique
J. Vac. Sci. Technol. B 31, 04D109_1-7 (2013) **doi: 10.1116/1.4810782**

67.) **C. Himcinschi**, I. Vrejoiu, G. Salvan, M. Fronk, A. Talkenberger, D.R.T. Zahn, D. Rafaja, and J. Kortus

Optical and magneto-optical study of nickel and cobalt ferrite epitaxial thin films and submicron structures
J. Appl. Phys. 113, 084101_1-8 (2013) **doi: 10.1063/1.4792749**

66.) S. Haas, F. Schneider, **C. Himcinschi**, V. Klemm, G. Schreiber, J. von Borany, J. Heitmann
Ge nanoparticle formation by thermal treatment of rf-sputtered $ZrO_2/ZrGe_2O_3$ *superlattices*
J. Appl. Phys. 113, 044303_1-4 (2013) **doi: 10.1063/1.4780033**

65.) A.G. Milekhin, N.A. Yeryukov, L.L. Sveshnikova, T.A. Duda, S.S. Kosolobov, Al.V. Latyshev, N.V. Surovtsev, S.V. Adichtchev, **C. Himcinschi**, E.I. Zenkevich, W.-B. Jian, and D.R.T. Zahn
Raman Scattering for Probing Semiconductor Nanocrystal Arrays with a Low Areal Density
J. Phys. Chem. C 116, 17164−17168 (2012) **doi: 10.1021/jp210720v**

64.) A.G. Milekhin, N.A. Yeryukov, L.L. Sveshnikova, T.A. Duda, **C. Himcinschi**, E.I. Zenkevich, and D.R.T. Zahn
Resonant Raman scattering of ZnS, ZnO, and ZnS/ZnO core/shell quantum dots
Appl. Phys. A 107, 275-278 (2012) **doi: 10.1007/s00339-012-6880-z**

63.) A. Talkenberger, **C. Himcinschi**, T. Weißbach, K. Vijayanandhini, I. Vrejoiu, C. Röder, D. Rafaja, and J. Kortus
Raman spectroscopic and X-ray diffraction investigations of epitaxial $BiCrO_3$ *thin films*
Thin Solid Films 520, 4590–4594 (2012) **doi: 10.1016/j.tsf.2011.10.196**

62.) J. Seibt, F. Hanzig, R. Strohmeyer, H. Stoecker, **C. Himcinschi**, B. Abendroth and D. C. Meyer
Influence of near-surface and volume real structure on the electronic properties of SrTiO3 MIM structures
MRS Symposium Proceedings 1368, 8-13 (2011) **doi: 10.1557/opl.2011.892**

61.) A.G. Milekhin, N.A. Yeryukov, L.L. Sveshnikova, T.A. Duda, E. Zenkevich, S. Kosolobov, A. Latyshev, **C Himcinschi**, N.V. Surovtsev, S.V. Adichtchev, Z.C. Feng, C.C. Wu, D.S. Wuu, and D.R.T. Zahn
Surface Enhanced Raman Scattering of Light by ZnO Nanostructures
J. Exp. Theo. Phys. 113, 983-991 (2011) **doi: 10.1134/S1063776111140184**

60.) **C. Himcinschi**, I. Vrejoiu, T. Weißbach, K. Vijayanandhini, A. Talkenberger, C. Röder, S. Bahmann, D. R. T. Zahn, A. A. Belik, D. Rafaja, and J. Kortus
Raman spectra and dielectric function of $BiCrO_3$*: Experimental and first-principles studies*
J. Appl. Phys. 110, 073501_1-8 (2011) **doi:10.1063/1.3642985**

59.) A. Vladescu, S. Mican, **C. Himcinschi**, and R. Tetean
Magnetocaloric effect in La(1.2)R(0.2)Ca(1.6)Mn(2)O(7) compounds
Journal of Optoelectronic and Advanced Materials 13, 263-267 (2011)

58.) J. Hanzig, B. Abendroth, F. Hanzig, H. Stöcker, R. Strohmeyer, D. C. Meyer, S. Lindner, M. Grobosch, M. Knupfer, **C. Himcinschi**, U. Mühle, and F. Munnik
Single crystal strontium titanate surface and bulk modifications due to vacuum annealing
J. Appl. Phys. 110, 064107_1-9 (2011) **doi:10.1063/1.3638692**

57.) M. Tcaci, **C. Himcinschi**, R. Nastas, O. Petuhov, T. Lupascu, and D. R. T. Zahn
Non-destructive Characterization of Modified Activated Carbon
Rev. Chim. 7, 727-731 (2011)

56.) V. Dzhagan, I. Lokteva, **C. Himcinschi**, J. Kolny-Olesiak, M. Ya. Valakh, S. Schulze, and D.R.T. Zahn
The influence of pyridine ligand onto the structure and phonon spectra of CdSe nanocrystals
J. Appl. Phys. 109, 084334_1-8 (2011) **DOI: 10.1063/1.3569741**

55.) V. Dzhagan, I. Lokteva, **C. Himcinschi**, X. Jin, J. Kolny-Olesiak, D. R. T. Zahn
Phonon Raman spectra of colloidal CdTe nanocrystals: effect of size, non-stoichiometry and ligand exchange

Nanoscale Research Letters 6, 79_1-10 (2011) **DOI: 10.1186/1556-276X-6-79**

54.) A. G. Milekhin, L. L. Sveshnikova, T. A. Duda, N. V. Surovtsev, S. V. Adichtchev, Yu. M. Azhniuk, **C. Himcinschi**, M. Kehr and D. R. T. Zahn
Resonance effects in Raman scattering of quantum dots formed by the Langmuir-Blodgett method
J Phys.: Conf. Series 245, 012045_1-4 (2010) **DOI: 10.1088/1742-6596/245/1/012045**

53.) **C. Himcinschi**, I. Vrejoiu, M. Friedrich, E. Nikulina, L. Ding, C. Cobet, N. Esser, M. Alexe, D. Rafaja, and D.R.T Zahn
Substrate influence on the optical and structural properties of pulsed laser deposited $BiFeO_3$ *epitaxial films*
J. Appl. Phys. 107, 123524_1-5 (2010) **DOI: 10.1063/1.3437059**

52.) **C. Himcinschi**, I. Vrejoiu, M. Friedrich, L. Ding, C. Cobet, N. Esser, M. Alexe, and D.R.T Zahn
Optical characterisation of $BiFeO_3$ *epitaxial thin films grown by pulsed-laser deposition*
physica status solidi c 7, 296-299 (2010) **DOI: 10.1002/pssc.200982414**

51.) P. Schäfer, **C. Himcinschi**, V. Chis, and D. R. T. Zahn
In situ Raman growth monitoring of Indium / Copper Phthalocyanine interfaces
physica status solidi c 7, 232-235 (2010) **DOI: 10.1002/pssc.200982484**

50.) L. Ding, **C. Himcinschi**, M. Friedrich, and D.R.T. Zahn
Optical investigation of CuPc thin films on vicinal Si(111)
physica status solidi c 7, 312-315 (2010) **DOI: 10.1002/pssc.200982455**

49.) F. Seidel, M. Fronk, **C. Himcinschi**, V. Chis, and D.R.T. Zahn
Spectroscopic ellipsometry and reflection anisotropy spectroscopy of Lu diphthalocyanine films on Si
physica status solidi c 7, 222-226 (2010) **DOI: 10.1002/pssc.200982464**

48.) C. Keil, O. Tsaryova, L. Lapok, **C. Himcinschi**, D. Wöhrle, O.R. Hilde, D.R.T. Zahn, S.M. Gorun, and D. Schlettwein
Growth and characterization of thin films prepared from perfluoro-isopropyl-substituted perfluorophthalocyanines
Thin Solid Films 517, 4379-4384 (2009) **DOI: 10.1016/j.tsf.2009.01.070**

47.) K. Fujii, **C. Himcinschi**, M. Toader, S. Kera, D.R.T. Zahn and N. Ueno
Vibrational properties of perfluoropentacene thin film
J. Electron Spectrosc. Relat. Phenom. 174, 65-69 (2009) **DOI: 10.1016/j.elspec.2009.01.002**

46.) R. Scholz, L. Gisslen, **C. Himcinschi**, I. Vragovic, E.M. Calzado, E. Louis, E.S.F. Maroto, and M.A. Dıaz-Garcıa
Asymmetry between Absorption and Photoluminescence Line Shapes of TPD: Spectroscopic Fingerprint of the Twisted Biphenyl Core
J. Phys. Chem. A. 113, 315-324 (2009) **DOI: 10.1021/jp806939q**

45.) M. Reiche, O. Moutanabbir, **C. Himcinschi**, S. Christiansen, W. Erfurth, U. Gösele, S. Mantl, D. Buca, Q.T. Zhao, Q.T. Zhao, R. Loo, D. Nguyen, F. Muster, and M. Petzold
Strained Silicon on Wafer Level by Wafer Bonding: Materials Processing, Strain Measurements and Strain Relaxation
ECS Transactions 16, 311-320 (2008) **DOI: 10.1149/1.2982883**

44.) **C. Himcinschi**, R. Sing, O. Moutanabbir, R. Scholz, M. Reiche S.H. Christiansen, U. Gösele, and D.R.T. Zhan
Etching-back of uniaxially strained silicon on insulator investigated by spectroscopic ellipsometry
physica status solidi (a) 205, 841-844 (2008) **DOI: 10.1002/pssa.200777753**

43.) S. Rudra, T. Wächtler, M. Friedrich, S.J. Louis, **C. Himcinschi**, S. Zimmermann, S.E. Schulz, S. Silaghi, C. Cobet, N. Esser, T. Gessner, and D. R. T. Zahn
Spectroscopic ellipsometry study of thin diffusion barriers of TaN and Ta for Cu interconnects in integrated circuits

physica status solidi (a) 205, 922-926 (2008) DOI: 10.1002/pssa.200777831

42.) I. Vragovic, E.M. Calzado, M.A. Diaz García, **C. Himcinschi**, L. Gisslén, and R. Scholz
Modelling absorption and photoluminescence of TPD
J. Luminescence 128, 845-847 (2008) DOI: 10.1016/j.jlumin.2007.11.063

41.) R. Tetean, **C. Himcinschi**, and E. Burzo
Magnetic properties and magnetocaloric effect in $La_{1.4-x}R_xCa_{1.6}Mn_2O_7$ *compounds with R=Ho or Yb*
Journal of Optoelectronic and Advanced Materials 10, 849-852 (2008)

40.) **C. Himcinschi**, M. Reiche, R. Scholz, S.H. Christiansen, and U. Gösele
Compressive uniaxially strained silicon on insulator by prestrained wafer bonding and layer transfer
Applied Physics Letters 90, 231909 (2007) DOI: 10.1063/1.2747182

39.) M. Reiche, **C. Himcinschi** , U. Gösele, S. Christiansen, S. Mantl, D. Buca, Q.T. Zhao, S. Feste, R. Loo, D. Nguyen, W. Buchholtz, A. Wei, M. Horstmann, D. Feijoo, and P. Storck
Strained Silicon-On-Insulator - Fabrication and Characterization
ECS Transactions 6, 339-444 (2007) DOI: 10.1149/1.2728880

38.) **C. Himcinschi**, I. Radu, F. Muster, R. Singh, M. Reiche, M. Petzold, U. Gösele, and S.H. Christiansen
Uniaxially strained silicon by wafer bonding and layer transfer
Solid State Electronics 51, 226-230 (2007) DOI: 10.1016/j.sse.2007.01.018

37.) R. Singh, I. Radu, M. Reiche, **C. Himcinschi**, B. Kuck, B. Tillack, U. Gösele, and S.H. Christiansen
High-density-plasma (HDP)-CVD oxide to thermal oxide wafer bonding for strained silicon layer transfer applications
Applied Surface Science 253, 3595-3599 (2007) DOI: 10.1016/j.apsusc.2006.07.077

36.) **C. Himcinschi**, R. Singh, I. Radu, A.P. Milenin, W. Erfurth, M. Reiche, U. Gösele, S.H. Christiansen, F. Muster, and M. Petzold
Strain relaxation in nanopatterned strained silicon round pillars
Applied Physics Letters 90, 021902 (2007) DOI: 10.1063/1.2431476

35.) M. Reiche, I. Radu, **C. Himcinschi**, R. Singh, S.H. Christiansen, and U. Gösele
Comparison of SiGe Virtual Substrates for the Fabrication of Strained Silicon-On-Insulator (sSOI) Using Wafer Bonding and Layer Transfer
ECS Transactions 3, 317-324 (2006) DOI: dx.doi.org/10.1149/1.2355829

34.) I. Radu, **C. Himcinschi**, R. Singh, M. Reiche, U. Gösele, S.H. Christiansen, D. Buca, S. Mantl, R. Loo and M. Caymax
sSOI fabrication by wafer bonding and layer splitting of thin SiGe virtual substrates
Materials Science and Engineering B 135, 231-234 (2006) DOI: 10.1016/j.mseb.2006.08.025

33.) **C. Himcinschi**, I. Radu, R. Singh, W. Erfurth, A. Milenin, M. Reiche, S.H. Christiansen, and U. Gösele
Relaxation of strain in patterned strained silicon investigated by UV Raman spectroscopy
Materials Science and Engineering B 135, 184-187 (2006) DOI: 10.1016/j.mseb.2006.08.023

32.) V. Sivakov, G.Andrae, **C. Himcinschi**, U. Gösele, D.R.T. Zahn, and S. Christiansen
Growth peculiarities during vapor-liquid-solid growth of silicon nanowhiskers by electron beam evaporation
Applied Physics A 85, 311-315 (2006) DOI: 10.1007/s00339-006-3675-0

31.) R. Singh, I. Radu, R. Scholz, **C. Himcinschi**, U. Gösele, and S. H. Christiansen
Investigation of helium implantation induced blistering in InP
Journal of Luminescence 121, 379-382 (2006) DOI: 10.1016/j.jlumin.2006.08.073

30.) R. Singh, I. Radu, R. Scholz, **C. Himcinschi**, U. Gösele, and S. H. Christiansen
Low temperature InP layer transfer onto Si by helium implantation and wafer direct bonding
Semiconductor Science and Technology 21, 1311-1314 (2006) DOI: 10.1088/0268-1242/21/9/016

29.) H. J. Fan, B. Fuhrmann, R. Scholz, **C. Himcinschi**, A. Berger, H. Leipner, A. Dadgar, A. Krost, S. Christiansen, U. Gösele, and M. Zacharias
Vapour-transport-deposition growth of ZnO nanostructures: switch between c-axial wires and a-axial belts by indium doping
Nanotechnology 17, S231-239 (2006) **DOI: 10.1088/0957-4484/17/11/S02**

28.) A. G. Milekhin, **C. Himcinschi**, M. Friedrich, K. Hiller, M. Wiemer, T Gessner, S. Schulze, and D.R.T. Zahn
Infrared Spectroscopy of Bonded Silicon Wafers
Semiconductors 40, 1304-1313 (2006) **DOI: 10.1134/S1063782606110108**

27.) G. Salvan, S. Silaghi, M. Friedrich, **C. Himcinschi**, and D.R.T. Zahn
Structural and morphological properties of perylene derivatives films on passivated semiconductor substrates
Journal of Optoelectronic and Advanced Materials 8, 604-610 (2006)

26.) O.D. Gordan, **C. Himcinschi**, D.R.T. Zahn, C. Cobet, N. Esser, and W. Braun
Reduced intermolecular interaction in organic ultrathin films
Applied Physics Letters 88, 141913 (2006) **DOI: 10.1063/1.2189153**

25.) S. Fruehauf, **C. Himcinschi**,, M. Rennau , K. Schulze , S.E. Schulz , M. Friedrich , T. Gessner , D.R.T. Zahn , Q.T. Le , and R. Caluwaerts
Scaling down thickness of ULK materials for 65 nm node and below and its effect on electrical performance
Microelectronic Engineering 82, 405-410 (2005) **DOI: 10.1016/j.mee.2005.07.023**

24.) **C. Himcinschi**, O. Gordan, G. Salvan, F. Müller, D.R.T. Zahn, C. Cobet, N. Esser, and W. Braun
Stability of tris(8-hydroxyquinoline)-aluminum(III) films investigated by vacuum ultraviolet spectroscopic ellipsometry
Applied Physics Letters 86, 111097 (2005) **DOI: 10.1063/1.1883314**

23.) **C. Himcinschi** and D.R.T. Zahn
Low-k xerogel films studied by ellipsometry and IR-spectroscopy,
New Trends in Advanced Materials, published by West University of Timisoara, 94-99 (2005)

22.) **C. Himcinschi**, N. Meyer, S. Hartmann, M. Gersdorff, M. Friedrich, H.-H. Johannes, W. Kowalsky, M. Schwambera, G. Strauch, M. Heuken, and D.R.T. Zahn
Spectroscopic ellipsometric characterization of organic films deposited via organic vapor phase deposition,
Applied Physics A 80, 551-555 (2005) **DOI: 10.1007/s00339-004-2973-7**

21.) **C. Himcinschi**, S. Hartmann, A. Janssen, N. Meyer, M. Friedrich, W. Kowalsky, D.R.T. Zahn, and M. Heuken
Thin organic heterostructures deposited via Organic Vapor Phase Deposition: spectroscopic ellipsometry characterisation
J. Cryst. Growth. 275, e1035-1040 (2005) **DOI: 10.1016/j.jcrysgro.2004.11.127**

20.) S. Hartmann, A. Janssen, M. Gersdorff, N. Meyer, M. Reinhold, M. Schwambera, G. Strauch, B. Marheineke, M. Heuken, H.-H. Johannes, W. Kowalsky, **C. Himcinschi**, D. Zahn
First Hybrid OLED by Organic Vapor Phase Deposition and Its Advantages in Deposition Rate Control for OLED Manufacturing,
SID Symposium Digest of Technical Papers 35, 1388-1391 (2004) **DOI: 10.1889/1.1821353**

19.) **C. Himcinschi**, M. Friedrich, S. Frühauf, S. E. Schulz, T. Gessner, and D. R. T. Zahn
Contributions to static dielectric constants of low-k xerogels films derived from VASE and IR spectroscopies,
Thin Solid Films 455-456, 433-437 (2004) **DOI: 10.1016/j.tsf.2003.11.241**

18.) M. Friedrich, **C. Himcinschi**, G. Salvan, M. Anghel, A. Paraian, Th. Wagner, T. U. Kampen, and D. R. T. Zahn
VASE and IR Spectroscopy: Excellent Tools to Study Biaxial Organic Molecular Thin Films: DiMe-PTCDI on S-passivated GaAs(100),
Thin Solid Films 455-456, 586-590 (2004) DOI: 10.1016/j.tsf.2003.11.224

17). A.G. Milekhin, M.Y. Ladanov, W.V. Lundin, Andrei I. Besulkin, A.N. Smirnov, V.Y. Davydov, **C. Himcinschi**, M. Friedrich, and D.R.T. Zahn
IR reflection of optical phonons in GaN/AlGaN superlattices,
physica status solidi (c) 1, 2733-2736 (2004) DOI: 10.1002/pssc.200405306

16). **C. Himcinschi**, M. Friedrich, K. Hiller, T. Gessner and D.R.T. Zahn
Infrared spectroscopic investigations of the buried interface in silicon bonded wafers,
Semicond. Sci. Technol. 19, 579-585 (2004) DOI: 10.1088/0268-1242/19/5/005

15.) D.R.T. Zahn, **C. Himcinschi**, M. Friedrich, A. Paraian, M. Heuken
OVPD and Applications of Optical Spectroscopic Methods to Growth Control (in german: OVPD und Anwendung optischer Spektroskopiemethoden zur Wachstumskontrolle),
Vakuum in Forschung und Praxis 15, 312-314 (2003) DOI: 10.1002/vipr.200300197

14.) M. Friedrich, G. Gavrila, **C. Himcinschi**, T. U. Kampen, A. Yu. Kobitski, H. Méndez, G. Salvan, I. Cerrilló, J. Méndez, N. Nicoara, A. M. Baró and D. R. T. Zahn
Optical properties and molecular orientation in organic thin films,
J. Phys.: Condens. Matter 15, S2699-S2718 (2003) DOI: 10.1088/0953-8984/15/38/009

13.) T.U. Kampen, G. Salvan, A. Paraian, **C. Himcinschi**, A. Kobitski, M. Friedrich, D.R.T. Zahn
Orientation of Perylene Derivatives on Semiconductor Surfaces,
Appl. Surf. Sci. 212-213, 501-507 (2003) DOI: 10.1016/S0169-4332(03)00390-8

12.) S. Fruehauf, I. Streiter, R. Puschmann, S.E. Schulz, **C. Himcinschi**, C.M. Flannery, T. Gessner, D.R.T. Zahn
Modified silica xerogel as a low-k dielectric with improved mechanical properties, Advanced Metallization Conference (AMC) 2002, San Diego, USA,
Conference Procceedings ULSI XVIII (published by Materials Research Society), 507-512 (2003)

11.) **C. Himcinschi**, E. Burzo, R. Tetean, D. Ristoiu, V. Pop
Magnetic Properties of $Ca_xLa_{1-x}MnO_3$ *(x>0.5) perovskites,*
Modern Physics Letters B 7, 263-266 (2003) DOI: 10.1142/S0217984903005214

10.) **C. Himcinschi**, M. Friedrich, S. Frühauf, I. Streiter, S.E. Schulz, T. Gessner, M.R. Baklanov, K.P. Mogilnikov, and D.R.T. Zahn
Ellipsometric study of the change in the porosity of silica xerogels after surface chemical modification with hexamethyldisilazane,
Analytical and Bioanalytical Chemistry 374, 654-657 (2002) DOI: 10.1007/s00216-002-1392-x

9.) **C. Himcinschi**, M. Friedrich, K. Hiller, T. Gessner, D.R.T. Zahn
Investigation during annealing of the interface in Si-Si bonded wafers by multiple internal transmission infrared spectroscopy,
International Semiconductor Conference (CAS) 2002, 8-12 october, 2002, Sinaia, Romania,
CAS 2002 Proceedings vol. 2 (published by IEEE), 271-274 (2002) 10.1109/SMICND.2002.1105847

8.) S. Fruehauf, I. Streiter, S.E. Schulz, E. Brendler, **C. Himcinschi**, M. Friedrich, T. Gessner, and D.R.T. Zahn
Hydrophobisation process for porous low K dielectric silica layers,
Advanced Metallization Conference (AMC) 2001, Toronto, Canada,
Conference Proceedings ULSI XVII (published by Materials Research Society), 287-294 (2002)

7.) C. Murray, C. Flannery, I. Streiter, S.E. Schulz, M.R. Baklanov, K.P. Mogilnikov,
C. Himcinschi, M. Friedrich, D.R.T. Zahn, T. Gessner
Comparison of Techniques to Characterise the Density, Porosity and Elastic Modulus of Porous Low-k SiO_2 *Xerogel Films*,
Microelectronics Engineering 60, 133-141 (2002) DOI: 10.1016/S0167-9317(01)00589-5

6.) **C. Himcinschi**, M. Friedrich, C. Murray, I. Streiter, S. Schulz, T. Gessner, D.R.T. Zahn
Characterisation of silica xerogels films by variable angle spectroscopic ellipsometry and infrared spectroscopy,
Semiconductor Science and Technology 16, 806-811 (2001) **DOI: 10.1088/0268-1242/16/9/312**

5.) **C. Himcinschi**, A. Milekhin, M. Friedrich, K. Hiller, M. Wiemer, T. Gessner, S. Schulze, and D.R.T. Zahn
Silicon oxide in Si-Si bonded wafers,
Applied Surface Science 175-176, 716-721 (2001) **DOI: 10.1016/S0169-4332(01)00146-5**

4.) G. Salvan, **C. Himcinschi**, A.Yu. Kobitski, M. Friedrich, H.P. Wagner, T.U. Kampen, and D.R.T. Zahn
Crystallinity of PTCDA films on silicon derived via optical spectroscopic measurements,
Applied Surface Science 175-176, 364-369 (2001) **DOI: 10.1016/S0169-4332(01)00069-1**

3.) **C. Himcinschi**, A. Milekhin, M. Friedrich, K. Hiller, M. Wiemer, T. Gessner, S. Schulze, and D.R.T. Zahn
Growth of buried silicon oxide in Si-Si bonded wafers upon annealing,
J. Appl. Phys. 89, 1992-1994 (2001) **DOI: 10.1063/1.1338512**

2.) **C. Himcinschi**, E. Burzo, and J.P. Deville
Magnetic and Magnetocaloric Properties of $La_{1.4-x}Yb_xCa_{1.6}Mn_2O_7$,
Materials Science Forum 373-376, 521-524 (2001) **doi:10.4028/www.scientific.net/MSF.373-376.521**

1.) I. Ardelean, G. Salvan, M. Peteanu, V. Simon, **C. Himcinschi**, and F. Ciorcas
EPR and magnetic susceptibility studies of B_2O_3*-SrO-*Fe_2O_3 *glasses*,
Modern Physics Letters B 13, 801-808 (1999) **DOI: 10.1142/S0217984999000993**

Acknowledgements

First of all I want to thank Prof. Dr. Jens Kortus who supported me through the Habilitation process.

Many thanks to Prof. Dr. Johannes Heitmann (TU Bergakademie Freiberg), Prof. Dr. Marin Alexe (Warwick University) and Prof. Dr. Jean Geurts (Julius-Maximilians-Universität Würzburg) for refereeing my cumulative Habilitation Thesis.

A big "thank you" I'd like to express to the people who provided the very nice and interesting multifunctional oxide samples: Dr. Ionela Lindfors-Vrejoiu, Prof. Marin Alexe, Prof. Kathrin Dörr, and their research groups!

A big thank goes to the people from the Freiberger Raman Laboratory who were involved in part of the measurements, simulations or technical assistance: Christian, Andreas, Birgit, Jan, Gert, Simon B. Thanks to Gabi for the administrative support.

Particular thanks I would like to express to the people from the wafer bonding group during my Postdoc at MPI Halle: Ionut, Rajendra, Silke, Dr. Manfred Reiche and deepest gratitude to Prof. Ulrich Gösele.

Thanks to Prof. Dr. David Rafaja and his group for their continuous XRD support. Thanks also go to Prof. Dr. Dietrich Zahn, who made possible my ellipsometry measurements in Chemnitz.

I would like to take this opportunity to thank all other authors who contributed to the 16 papers which are part of the Habilitation Thesis.

A warm word of thanks to all (actual or former) other members of the ITP group in Freiberg in the last 10 years for the nice time spent together (I hope I will not forget anyone…): Wolfgang, Sebastian, René, Jakob, Jonas, Simon Li., Silvia, Claudia, Lillit, Nebahat, Ronald, Steve, Torsten H., Torsten W., Simon La., Rico, Thomas, Kai, Lenz, Charlotte, Tobias and Johannes.

Last by not least a big "thank you" to my family: to my wonderful wife Georgeta for all the support, and to my wonderful children Vlad and Darius, even for correcting sometimes my German.

Erklärung

Hiermit erkläre ich, Dr. Cameliu Constantin Himcinschi, geboren am 29.06.1974, an Eides statt, dass ich die vorliegende Arbeit selbstständig und nur unter Verwendung der angegebenen Quellen und Hilfsmittel angefertigt habe. Die wörtlich oder inhaltlich übernommenen Stellen wurden als solche gekennzeichnet. Ein Habilitationsverfahren wurde von mir bislang an einer anderen Fakultät oder Universität weder eröffnet noch beantragt. Frühere Habilitationsverfahren an der TU Bergakademie Freiberg sind meinerseits nicht unternommen worden.

Freiberg,

Ort, Datum ……………………………….

Unterschrift